PNC TJ8627 90-001

FEL用高反射率・高耐力ミラーの試験
および
FELの開発状況調査

(動力炉・核燃料開発事業団　委託研究成果報告書)

1990年3月

電気通信大学 新形レーザー研究センター
植田憲一

動力炉・核燃料開発事業団 (Power Reactor and Nuclear Fuel Development Corporation)

PNC TJ8627 90-001

１９９０年３月

ＦＥＬ用高反射率・高耐力ミラーの試験
および
ＦＥＬの開発状況調査

植田憲一※

要旨

自由電子レーザーにおける光共振器およびそのための光学素子の技術的課題と、その解決のための研究の方向を明らかにすることを目的として本研究は行われた。代表的な成果を以下にあげる。

１）ＦＥＬと同等な波長、パルス幅を持つ超短パルス色素／エキシマレーザーシステムが開発された。

２）高感度な光音響法による光学材料の損失測定が行われた。

３）反射率分布の重要性が実験的に確かめられた。

４）リング共振器の特性、アライメント精度について定量的に検討した。

５）ＦＥＬ共振器における斜入射光学素子の重要性を指摘した。

６）海外の光学技術、ＦＥＬ研究の動向を調査し、検討した。

本報告書は、電気通信大学が動力炉・核燃料開発事業団の委託により実施した研究の成果である。

※　電気通信大学新形レーザー研究センター　教授

PNC TJ8627 90-001
March, 1990

Investigation of High Reflectance and High Damage Threshold Mirrors for FEL and Research of the FEL Developments -

Ken-ichi Ueda

Abstract

This work has been carried out for the investigation of the engineering for the optical resonator and the optics for free electron lasers. Several important issues obtained in this research are shown as follows;

1) A dye/excimer laser system which can produce ultra-short pulses equivalent to the FEL pulses has been developed.
2) A photo-acoustic method with ultra-high sensitivity has been developed for the measurements of absorption and laser induced damage of optical components.
3) The measurements of the uniformity of reflectors have been demonstrated experimentally.
4) The characteristics of ring resonators including the alignment accuracy have been examined quantitatively.
5) The importance of the grazing incidence optics for FEL resonators has been pointed out clearly.
6) The optical engineering and FEL researches in the foreign countries have been investigated widely and intensively.

Work performed by University of Electro-Communications under contract with Power Reactor and Nuclear Fuel Development Corporation.

* Professor, Institute for Laser Science,
University of Electro-Communications

受託研究

「ＦＥＬ用高反射率・高耐力ミラーの試験及びＦＥＬの開発状況調査研究」
研究報告書

電気通信大学　新形レーザー研究センター

研究代表者

教授　　植田憲一

研究協力者

助手　　西岡　一

助手　　米田仁紀

助手　　佐々木明

平成２年３月３１日

目　次

１．はじめに

自由電子レーザー研究の現状とそれに関係した光学素子および共振器技術について、広い範囲から調査、研究することで、今後の研究の指針を与えることを目的として研究を行った。

以下のような研究を中心として研究を行った。

① 国際会議、研究所訪問によって、海外における自由電子レーザー研究の現状を調査した。
② 低損失、高反射率の共振器ミラーが必要な自由電子レーザーのために、高感度な光音響法を開発して、光学素子の吸収、レーザー損傷を測定した。
③ さらに新しいレーザー損傷検出法として２次元画像解析を利用した方式を提案、装置をデザインし、試作を開始した。
④ 光学薄膜の吸収とレーザー損傷の関係を研究した。
⑤ 超短パルスによる多光子吸収を観測した。
⑥ 自由電子レーザーと同等のパルス幅をもつ超短パルス可視光レーザーを開発した。

これまで検討されることの少なかった自由電子レーザーの光学部分についての技術的課題とその研究方向を見いだすことに研究の主眼をおき、今後の自由電子レーザー研究に寄与することを意図して本研究報告書はまとめられた。

２．自由電子レーザーの研究動向

本研究は自由電子レーザーにおけるレーザー共振器および光学素子の開発方向を明らかにすることを目的とした。自由電子レーザー研究の現状を把握することから始めよう。現在、研究中の自由電子レーザーの発振波長を図２－１にまとめたので、参考にされたい。

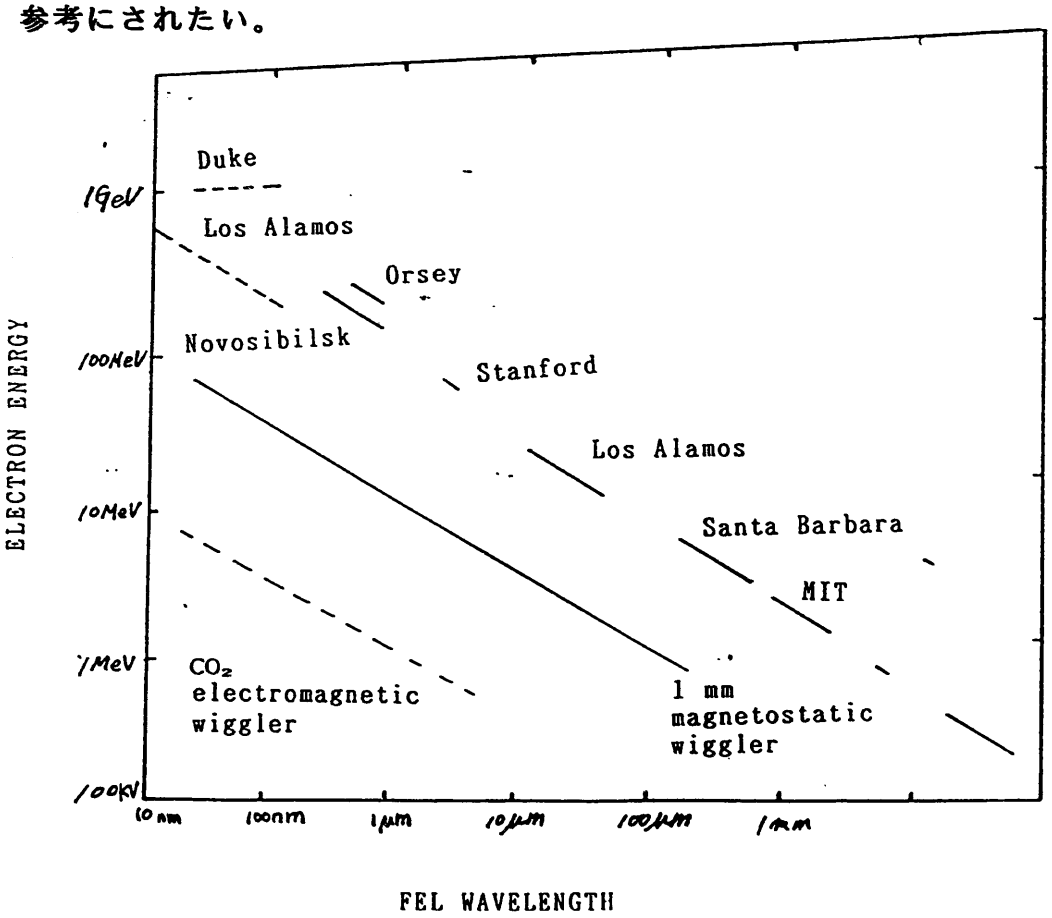

図２－１　自由電子レーザーの発振波長（計画中は破線）

２．１　自由電子レーザーの開発状況

２．１．１　ＲＦライナックＦＥＬ

もっとも代表的な自由電子レーザーの形式で、スタンフォード大学の超伝導ライナック、ロスアラモス研究所のＬ－バンド・ライナック、ボーイング社の自由電子レーザーなどがその代表的なものである。ロスアラモス研究所では１０～４０μｍの波長域における高出力、高効率動作を目標に実験が進められ、最近ではレーザー

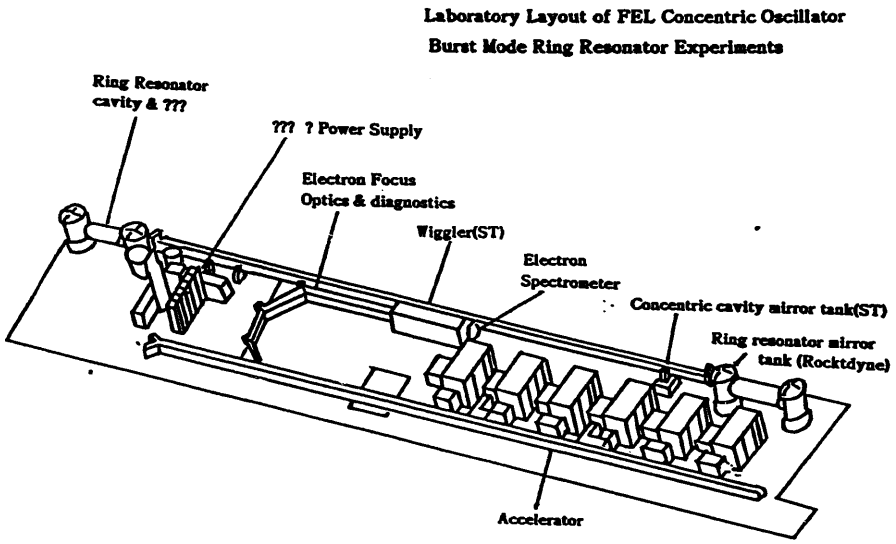

図２－２　ボーイング可視光発振ＦＥＬ

照射光電子放出電子ビームダイオードで大きな成果をあげている。また、高効率動作のためのエネルギー回収実験でも、６０％以上のエネルギー回収に成功した。ロスアラモス研究所やスペクトラ・テクノロジー、ロケットダインと共同したボーイング社は０．５μm、０．６μmの可視域発振で高出力発振を実現している。図２－２にボーイング製可視光自由電子レーザー、図２－３にロスアラモス研究所のＨＩＢＡＦ（High Brightness Accelerator FEL）の外観図を示した。

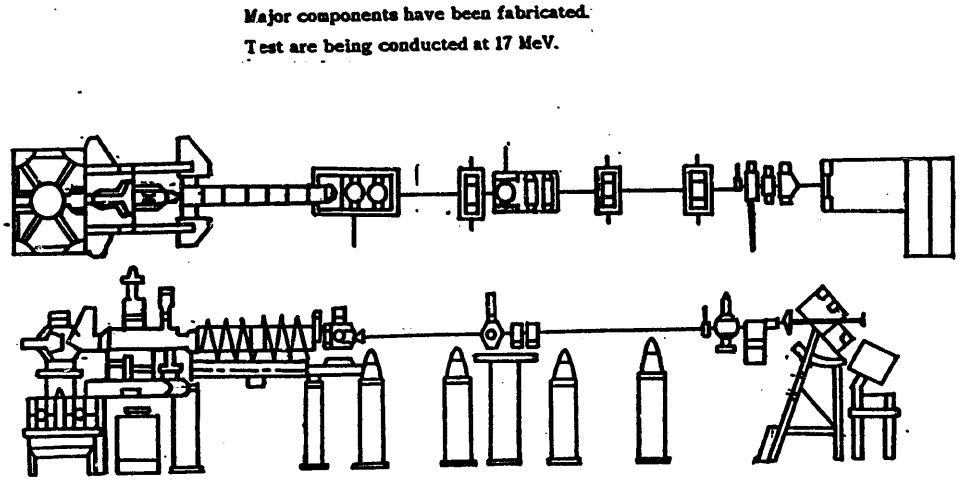

図２－３　ロスアラモスＨＩＢＡＦ自由電子レーザー

２．１．２　電子蓄積リングＦＥＬ

電子蓄積リング型自由電子レーザーは紫外線などの短波長の発振にもっとも適した装置である。ソ連ノボシビルスクの原子核研究所では、バイパスをもつ電子蓄積リングで世界最短波長（２４０ｎｍ）の発振に成功した。Optical Klystron を用いており、ウィグラーの長さは７．８ｍである。ビームエネルギー３５０ＭｅＶで２４０ｎｍから６９０ｎｍにわたる発振に成功した。２４０ｎｍにおける増幅利得は２．５％という高い値を示した。

２．１．３　誘導加速器型ＦＥＬ

ローレンスリバモア研究所、大阪大学、日本原子力研究所で増幅実験が進められているパルスパワー応用大電流線形加速器をもった装置である。リバモア研究所のＥＴＡ(Experimental Test Accelerator)は、発振波長９ｍｍのミリ波を増幅し、ピーク出力１ＧＷ以上を実現している。電子の減速に同調させたテーパー付きウィグラーによって３５％のエネルギー引き出し効率を達成している。この形式の自由電

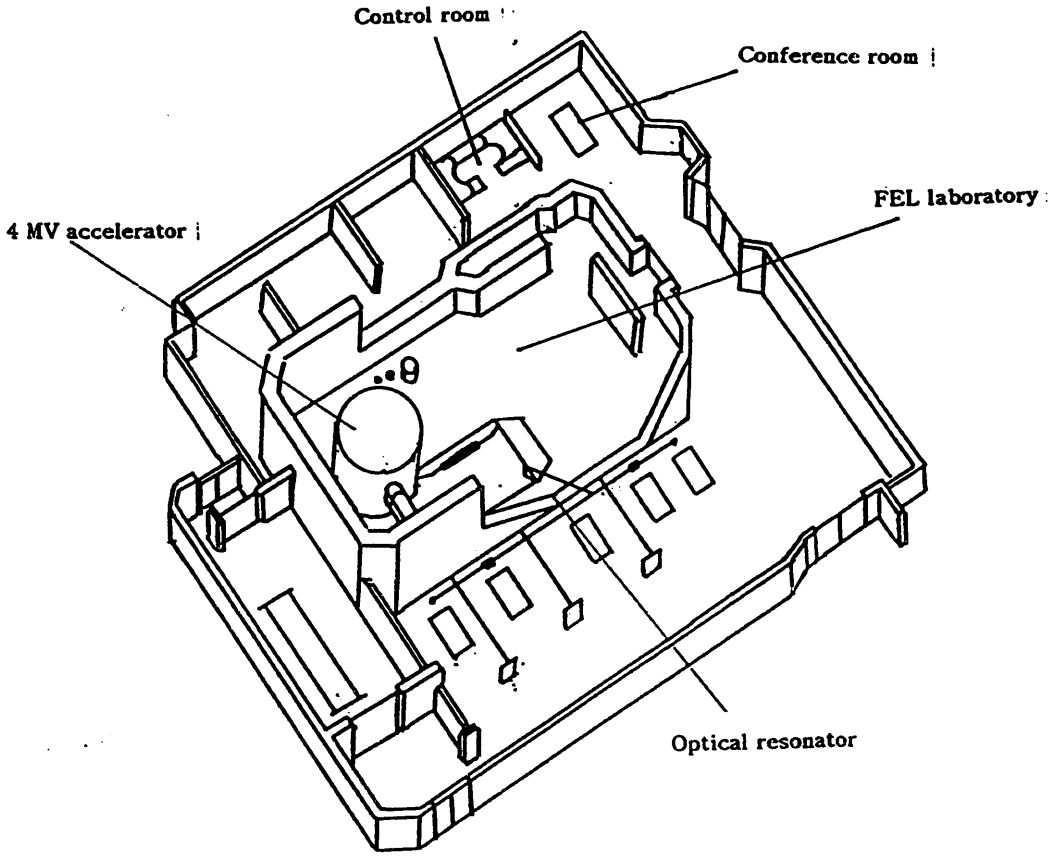

図２－４　静電加速器によるＦＥＬ実験施設（サンタバーバラ）

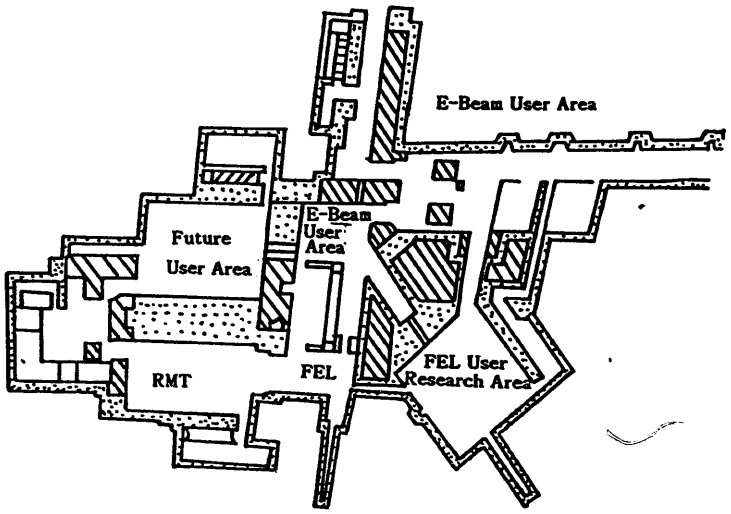

図２－５　ＮＩＳＴ／ＮＲＬ　ＦＥＬ共同利用研究施設

子レーザーは高出力のマイクロ波レーザーである特長を活用して、トカマク型プラズマ装置の加熱実験に使われている。

２．１．４　静電加速器型ＦＥＬ

カリフォルニア大学サンタバーバラ校では、図２－４のように遠赤外レーザー利用の研究センターで自由電子レーザーの応用研究が進んでいる。発振波長は１２０μｍ～４００μｍの遠赤外線である。静電加速器の電子ビームは高品質で、ビームエミッタンスは１８ｍｍ－ｍｒａｄ，エネルギー広がりは０．１％である。数１００μｓのパルス幅で単一モード発振に自由電子レーザーとしてはじめて成功した。

２．１．５　マイクロトロン型ＦＥＬ

米国ＮＩＳＴ／ＮＲＬ、イタリア・フラスカッティ研究所で開発が進められている自由電子レーザーで、加速されるにつれて電子の軌道が変わるレーストラック・マイクロトロンの特長を利用して、多波長の発振をすることを目的としている。このため、医学、生物関係など幅広い応用が考えられ、共同利用研究センターとしての準備が進められている。特にＮＩＳＴ／ＮＲＬは米国の国立共同研究センターである。図２－５にＮＩＳＴ／ＮＲＬの自由電子レーザーシステムを示す。

２．２　自由電子レーザー用光学系の意味

いうまでもなく、自由電子レーザーの構成は

１）高エネルギー電子を発生する電子加速器

２）電子を偏向させて電磁波を放出させるウィグラー磁場

３）レーザー発振させるための光共振器

の３つの部分に大別することができる。わが国の自由電子レーザーの研究は、主として１）と２）の部分に集中していた感があり、光共振器の設計およびそのための光学素子の開発はほとんど行われていない。現在のところ、高品質の電子ビームを発生させて利得を確認することを目的にした研究が主体であったが、実際に利得が観測されても発振が容易でないことが明らかになってきた。実際、わが国において、大阪大学、電総研、分子科学研究所、理化学研究所などで利得は観測されているものの、共振器を用いたレーザー発振は成功例がない。特に波長が短くなると利得が小さいために、共振器損失の方が大きくて、実際的な発振に到達しないのが現状である。

このような事情は海外でも同様で、多数の研究グループが自由電子レーザーの研究を展開しているが、実際に発振しているのは限られたグループである。自由電子レーザーの研究を指導してきた集団は基本的に加速器を専門とするグループであり、光学やレーザーの専門家が少ないことも、これらの現状を生み出した原因の一つである。

本研究ではこのような事情を鑑みて、自由電子レーザー研究における光学素子および光学系の開発のために、どのような問題点が存在し、それを解決するための研究方向を探ることを主眼とした。

２．３　ＦＥＬ研究の動向

研究の手法としては、

１）従来のレーザー、特に紫外線レーザー用光学素子の開発で有用であった手法を再検討し、

２）２次元画像計測を応用した新しい光学素子のための計測法の開発を目

指した。

3）海外および国内で開催された国際会議に出席し、海外の研究者と意見を交換する。

などの方法を用いて、総合的な研究を行った。

実際に出席、調査した国際会議の一覧を表２－１に示す。

表２－１　調査した自由電子に関係した国際会議

会議の名称	主催者	開催場所	日時	出席者
1 Paticle Accelerator conference	ＩＥＥＥ	Chicago USA	Mar.1989	植田憲一
2 American Physical Society (APS)	米国物理学会	Anaheim USA	Oct.1989	米田仁紀
3 LASER'89	米国レーザー学会	New Orleans USA	Dec.1989	西岡　一
4 OE/LASE'90	SPIE 国際光学機器学会	Los Angeles USA	Jan.1990	植田憲一
5 国際自由電子レーザーシンポジウム	日本原子力研究所	東京	Jan.1990	植田憲一

従来から自由電子レーザー研究の中心であった米国では、ロスアラモス研究所、ローレンスリバモア研究所、スタンフォード大学、カリフォルニア大学サンタバーバラ校、など従来から研究が盛んな研究所、大学に加えて、ＭＩＴ、ＮＩＳＴ／ＮＲＬ、ボーイング社、フロリダ中央大学、バンダービルト大学、デューク大学、など野心的な研究が新しく計画されている。新しい研究の方向の特長は、生物物理や医学応用、個体の表面物理や光化学などの具体的応用と直接結びついて、実際に利

用者を含んだ研究計画となっていることである。また、もうひとつの大きな特長は、短波長自由電子レーザーの目標がＸ線レーザーの開発を含んでいることである。

米国における研究動向の背景には、これまで研究の推進力であった戦略防衛構想（ＳＤＩ）が、世界の平和傾向、軍縮を求める潮流のために、大幅に縮小されることが確実なことがあげられる。同時に、米国においては自由電子レーザーはすでに実用段階に入っていることに注目しなければならない。実際、最近カリフォルニアにシエラ・レーザーという自由電子レーザーを受注、設計、製作、輸出をする企業が設立され、活動を開始している。

さらに、自由電子レーザーによるＸ線レーザーの開発計画の示すところは、現在の自由電子レーザー研究の地位をよく反映したものである。すなわち、これまで有力な光源のなかった遠赤外線では自由電子レーザーは十分な価値をもっているが、他のレーザーが多数存在し、応用研究が活発な近赤外、可視、紫外線領域では、巨大な装置を必要とする高価な自由電子レーザーの存在意義を認めさせることが困難である。このことが先進的な自由電子レーザーの研究を、真空紫外光を飛び越して一挙にＸ線領域にまでジャンプさせた理由のひとつであることは間違いがない。したがって、非常に短い波長で発振させることが目標であると同時に、一方で小型、低コスト、高効率なシステムの開発が、自由電子レーザーの将来を左右するということも明確に認識されなければならない。

２．４　ＦＥＬに関係した技術動向

２．４．１　高輝度電子ビームの発生　－　光電子発生ダイオード　－

加速器技術に関する最近のもっとも大きな進歩は図２－６に示したレーザー照射光電子ダイオードによる低エミッタンス電子ビームの発生である。研究の中心となったのはロスアラモス研究所で、それ以外にもアルゴンヌ研究所、ローレンスバークレイ研究所、フェルミ研究所など超大型の加速器計画を持っている研究所でも、基礎的な研究が進められている。この分野では、理化学研究所の河村らの先駆的な研究を忘れてはならないだろう。

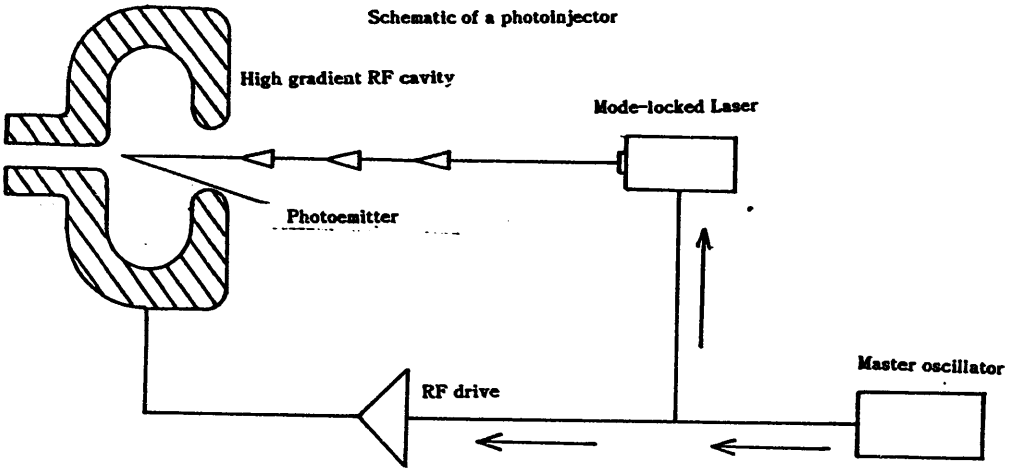

図２－６　光電子放出低エミッタンスダイオード

表２－２　光電子陰極に関する研究例

Lab.	Cathode Material	Quant. Eff.	Current Density	Pulse Width	Rep. Rate	Beam Current Micro	Beam Current Macro
LANL	Cs_3Sb	1 %	>600 A/cm²	15 ps	108 MHz	400 A	3 mA
	CsK_2Sb	4 %	>600 A/cm²	22 ps			
Duke	LaB_6	0.01 %		2 ps	95.2 MHz	85 A	15 mA
Argonne	Y, Metal						
LBL, USA	?						
Germany	?						

線形加速器における光電子陰極の研究は自由電子レーザーと密接に結びついて研究されているが、他の巨大加速器研究所の動機は新型巨大加速器の設計に関係している。最近のように加速器のエネルギーが際限もなく上昇すると、研究予算の制限から加速器利用の高エネルギー科学を存続、発展させることが困難になってくる。この限界を突破するための技術として、粒子発生部のエミッタンスを画期的に低下させ、実質的なビーム電流を向上させることが望まれている。いずれもきわめて切実な要求から出発しているだけに、今後大きく発展すると期待される。

自由電子レーザーに戻ると、最初に光電子陰極を自由電子レーザーに応用した結果を体系的に発表したのは Duke大の J.Maday らである。スタンフォード大学の Mark Ⅲ に応用した結果を表２－３および表２－４にまとめた。

表２－３　レーザー照射光電子陰極を用いた自由電子レーザー

Curtis (Rocketdyne) and Maday (Duke Univ.)

Photo cathode	LaB_6
Laser	3ω of mode licked YAG (355 nm)　rep rate 95.2 MHz
	100 ps, rep rate = 95.2 MHz
Quantum efficiency	10^{-4}
Accelerator	Stanford Mark Ⅲ
Wiggler	Stanford Mark Ⅲ
	+ Rocketdyne 2 m wiggler power amplifier
FEL wavelength	3.1 μm
Typical macropulse	
energy	0.35 mJ
Peak intra-cavity	
power	200 MW
e-Beam	
macro pulse	15 mA, 3 μs
micro pulse	80 A, 2 ps
B_{ry}	< 2 pi mm mrad
B_{rx}	< 10 pi mm mrad
energy	38.5 MeV
energy spread	< 1 %

表２－４　光電子陰極による特性向上

	Thermionic	Photo Cathode	
	Typical	Typical	Maximum
g_0	60 %	100 %	150 %
macro pulse	70 pC	170 pC	250 pC
	35 A	60 A	85 A
normalized emittance			
$\gamma \beta \varepsilon_y$	10π	8π	
$\gamma \beta \varepsilon_x$	4π	4π	
peak			
brightness	1.8×10^{11}	3.8×10^{11}	5.4×10^{11}

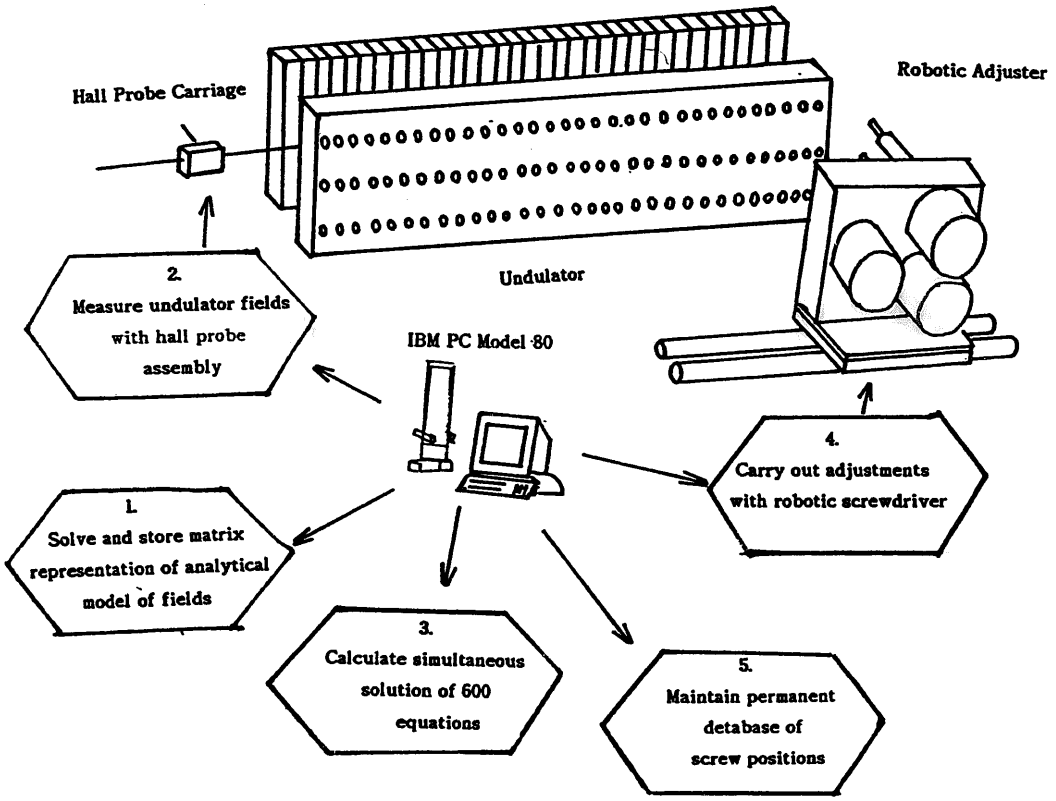

図２－７　計算機による高精度ウィグラーの調整

２．４．２　高精度ウィグラー

ウィグラーに関する研究動向は、高ピッチ、高精度による短波長化の方向である。実験が進むにつれて、ウィグラー磁場をもっと強くしたり、磁場強度の均一性を高める必要がいずれの研究所でも高まっている。このため、新しいウィグラー設計、製作が進められている。意外に感じたのは永久磁石を用いたウィグラー磁場の均一度が予想外に悪く、そのため自由電子レーザーの出力が制限されていることであった。現在では磁場の精密測定を行いながら、ウィグラーの組立調整をしているようだが、新しい方式でどの程度改善の効果がでるか、興味がもたれるところである。カリフォルニア大学サンタバーバラの高精度ウィグラー調整の様子を図２－７に示した。ここではロボット技術の応用が考えられている。

２．４．３　高安定低損失光共振器

自由電子レーザーに用いられている光学素子の製造技術および光学調整技術は電子ビーム技術などに比べて、平和的な技術に見えるので、公開されていると誤解しがちである。米国における光学技術は深く軍事技術と結びついており、且つ米国が世界を大きくリードしていると意識している分野だけに、公開されていない情報が非常に多い。最近、レーザー核融合関連で、研究競争が激しくなるにつれて、従来接することのできなかった光学技術について、意見交換したり、議論することが可能になってきた。

超高反射率を持った光学素子の製造技術はわが国が遅れている分野である。しかし、この分野における技術の差は、米国の光学技術の先端的研究向上を見学、議論した感じでは埋められないものではない。基本的には経験の差がギャップを生み出していると考えるべきであろう。ただし、工場におけるオンサイト計測やコンピュータを駆使した非球面光学素子の製作、さらに大口径光学素子のためのハニカム構造とアクチュエータによる曲率自動制御には大きな技術ギャップを感じる。さらに、超精密姿勢制御はアライメントに不可欠の技術であり、コンピュータによる自動アライメントもわが国には欠けている。しかし、これらを構成している基礎技術はいずれもわが国で盛んであり、研究に方向を与え、組織さえすれば、自由電子レーザー用の光学システムのための研究基盤は十分にある。

３．自由電子レーザー用光学系

自由電子レーザーの増幅利得は低いので、損失に打ち勝って発振するために要求される共振器ミラーの反射率は非常に高くなくてはならない。可視域の発振を得ようとする場合、９９．９９％以上の反射率が必要であると考えられている。自由電子レーザーにおける共振器設計、光学素子開発の重要性は、改めて真剣に考えなければならない。もしも光学素子の性能が悪く、反射率が９９．９％に低下したことを考えれば、光学系の重要性は明らかである。９９．９９％の反射率を９９．９％に低下させるということは、損失が１０倍に増大したということを意味する。反射率の低下を利得の増大で補償しようとする場合、利得を１０倍にしなくてはならない。元来、大きな利得を発生することが困難だから、低損失共振器が強く要求されることからすれば、利得を増大することと、損失を低下させることのいずれが合理的な方向であるか、自ずから明らかである。

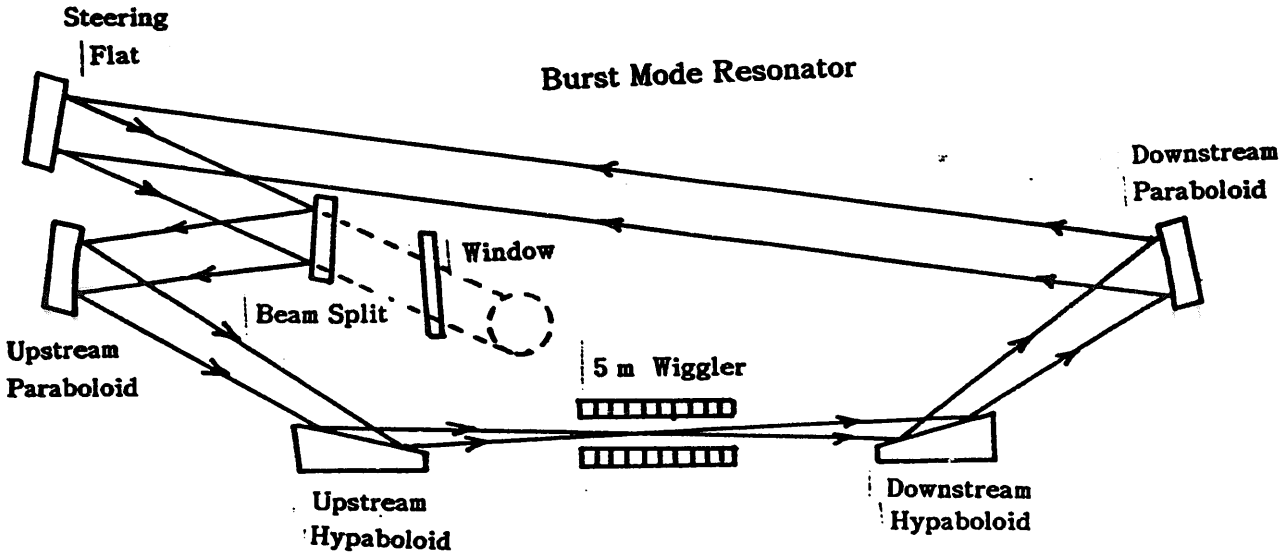

図３－１　斜入射光学系リング共振器

３．１　自由電子レーザーの光共振器

３．１．１　光共振器の実際

現在稼働しているボーイング社の可視光自由電子レーザーに用いられた光共振器の構成を図３－１に示す。この光共振器の特長は

①発振波長　０．６μｍ

②リング共振器（周回距離２００ｍ）

③斜入射シリコン双曲面鏡；８７°入射　長さ６４ｃｍ

④軸外しシリコン放物面鏡；口径２８ｃｍ

などである。

３．１．２　回折広がりと共振器長

自由電子レーザーの発振波長が短くなると、利得係数が小さくなるので、ウィグラーの長さを長くとらないと発振が困難になる。この為、本装置ではウィグラー長を５ｍにとってある。ウィグラーの全長にわたって電子ビームとレーザー光の相互作用体積を確保するためには、レーザー光の収束半径が１ｍｍ以下である必要がある。利得が低い自由電子レーザーでは、共振器内にレンズ光学系などを挿入して損失を増加させることを避けなければならない。このため、レーザーのビーム径の拡大は、回折による自然の広がりと反射光学系によるテレスコープを利用する。

ガウスビームを収束光学系で集光した場合、回折効果のために集光点付近では近似的な平行ビームをつくることができる。ビームの収束点付近で長い平行ビームをつくるためには焦点距離の長い光学系で集光する必要があり、ミラー間隔が長くなる。このため、ボーイング社の装置では、２枚の収束用双曲面鏡の間隔は５０ｍに設計されている。必然的に共振器長は長くなり、同時に共振器のアライメント精度がきびしくなることが避けられない。

３．１．３　進行波励起とリング共振器

波長可変レーザーでは空間的ホールバーニング効果による不連続的な波長同調を防止するために、リング共振器が用いられることが多い。自由電子レーザーでは光速に近い速度で運動しているバンチされた電子がウィグラーの周期磁場と相互作用して利得を発生するので、励起は本質的に進行波励起である。このため、ファブリペロー型の共振器では利得方向と逆の方向のリターンパスで利得を得ることはできない。結果的には、入射される電子ビームパルスに同期した周回時間をもつリング共振器が、もっとも合理的な共振器である。

３．１．４　斜入射シリコン双曲面鏡

ウィグラーにもっとも近い部分におかれた反射鏡はシリコン製の斜入射型の双曲面鏡である。

ａ．斜入射光学系である。

ｂ．双曲面鏡である。

ｃ．シリコン基板を用いている。

ｄ．表面は銀鏡としている。

などの特長を有している。斜入射光学系を用いる理由は、レーザーや制動輻射光による光損傷を避けるためと、広い波長範囲にわたって高反射率を獲得するためである。斜入射光学系で波長範囲を広げるために、表面には銀が蒸着されており、熱負荷を考慮して熱伝導の良いシリコンが使用されている。

３．１．５　軸外し放物面鏡

双曲面鏡で反射され、なお拡大されたビームを反射してリング共振器に構成するミラーで、共振器のアライメント調整を中心的に負担する役割をもつ。同時に、リング構成によって生じる軸外し光学系の収差を最小限にとどめるような光学設計がなされている。入射角が垂直入射に近いので、誘電体多層膜によって高反射率を達成している。

３．２　自由電子レーザーの波長可変性

自由電子レーザーの為の共振器や光学素子が要求される条件は、通常のレーザーに比べて必ずしも緩いものではなく、むしろ非常にきびしい。それらは自由電子レーザーそのものの特徴と深く関連づけられている。自由電子レーザーの特徴を表３－１にまとめてみよう。

図３－２に示した通り、従来の波長可変レーザーでは幅広いスペクトルで利得を発生できる媒質の発光を、波長可変性をもった共振器で波長同調をする。すなわち、広帯域の利得に波長依存性のある損失を組み合わせることで、発振波長を制御するのである。一方、自由電子レーザーの場合は波長同調範囲に対応するような広帯域のスペクトルで発振させることは原理的にできない。自由電子レーザーの発振波長

表３－１　自由電子レーザーと他のレーザーの比較

	他のレーザー	自由電子レーザー
電子の状態	束縛電子	自由電子
エネルギー状態	離散的	連続的
レーザー媒質	気体、液体、固体 プラズマ	真空
励起方法	光励起、電子衝突	電子加速
吸収損失	物質の固有吸収	なし
波長可変の方法	波長分散共振器	加速電圧変化

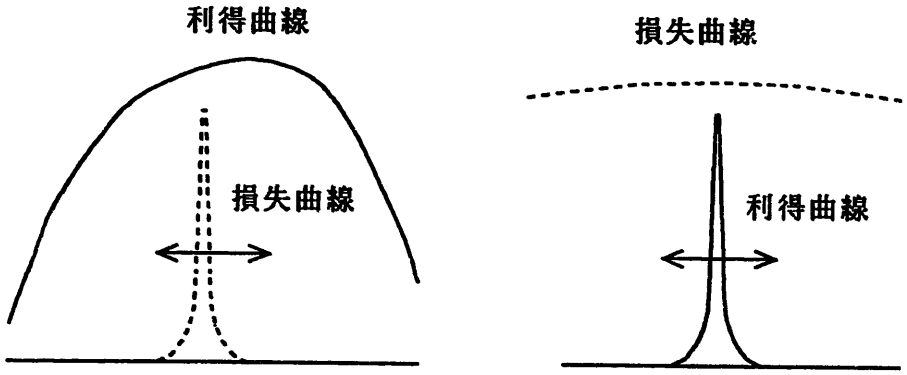

図３－２　波長可変レーザーの利得と損失の関係

は、電子の運動エネルギー、ウィグラー磁場の強度と周期などで決定され、決して外部の共振器損失の波長依存性で発振波長を同調することはない。自由電子レーザーの発振は与えられた条件では常に狭いスペクトルであり、その狭いスペクトルの発振条件が広い範囲で制御できるのである。このように自由電子レーザーには利得

条件と損失条件の関係が従来のレーザーと逆転している特長がある。この為、共振器光学系の帯域は、従来のレーザー以上に広帯域であることが要求される。斜入射光学系は広帯域の高反射率を達成するためにも有利な方式であることに注目しておく必要があるだろう。

3．3　長光路リング共振器

自由電子レーザーの共振器のひとつの形が長い光路長をもったリング共振器であるとして、問題点を検討してみよう。

3．3．1　共振器損失の影響

レーザー発振における共振器損失の影響は、レーザー媒質自身に吸収損失があるかどうかで、大きく事情が異なってくる。簡単な解析を行ったみよう。

単位長さあたりの利得係数、吸収係数、利得長をおのおのg_0，α_0、Lとおき、共振器の出力鏡の反射率をR，透過率をT＝1－Rとする。レーザー出力は共振器からみれば共振器損失として表現できるので、出力損失を共振器内に分布した損失として表現する。損失係数をγとすると

$$\exp(-\gamma L) = R$$

である。

レーザー発振の定常状態を表現する式はレーザー光強度をI、利得飽和強度をIsとして、次の式で表される。

$$\frac{dI}{dz} = \left(\frac{g_0}{1+I/I_s} - \alpha - \gamma\right) = 0 \qquad (3-1)$$

したがって

レーザー出力 $I_{out}=\gamma I_{in}$の関係を考慮すると、飽和強度で規格化したレーザー出力は

$$I_{out} = \frac{g_0\gamma}{\alpha+\gamma} - \gamma \qquad (3-2)$$

である。最大の出力を与える反射率は、$dI_{out}/d\gamma=0$の条件から

$$\gamma^2=\alpha(g_0-\alpha) \qquad (3-3)$$

の関係が成立する。このように、最適損失係数は吸収係数の関数である。図３－３に示した通り、吸収係数がほとんどゼロである自由電子レーザーでは、共振器の結合効率が低ければ低いほど、レーザー出力を増大させることができる。

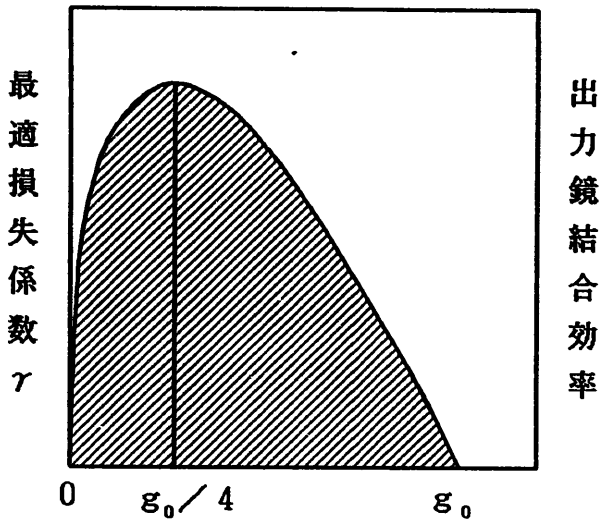

図３－３　レーザーの吸収と最適結合の関係

以上の簡単な解析から、低損失、高反射率の反射鏡で構成される共振器の必要性は、単に低い利得を克服して発振を可能にするといった消極的なものではなく、自由電子レーザーを最適条件で動作させ、もっとも効率よく出力を取り出すために必要な条件であることが示された。

３．３．２　透過光学系と反射光学系

長い光路長をもった共振器を構成するためには、共振器内にイメージ転送を可能にする結像系を導入することが必要である。共振器内にビームの収束光学系、すなわち結像光学系がない場合には、光の回折現象によってレーザービームは大きな損失を受けるからである。共振器損失を極力避けるべき自由電子レーザーでは、回折損失、光学系の吸収損失、表面散乱などの損失要素を可能な限り避けなければならない。レンズおよび反射鏡の損失要素を図３－４に示す。レンズは反射鏡に比較して、吸収、反射、表面散乱のすべての点で損失が多い。さらに高出力の超短パルスで色中心ができることを考えると、自由電子レーザーの共振器は反射光学系のみで構成すべきである。

一方、反射鏡では表面加工精度が波面ひずみとして直接的に反映されるので、高精度光学素子の製作技術の重要性はますます高まることに注意しなければならない。

３．３．３　軸外し光学系における光学損失

ビーム伝送系を有する長光路リング共振器は必然的に軸外し光学系を含まざるを得ない。このため、通常のレーザーの場合のファブリペロー型共振器と違って、共振器内の光学モードの解析は相当複雑な問題となる。中でも、軸外し光学系から生じるコマ収差は光線追跡の計算機システムなどを駆使して、解析しなければなら

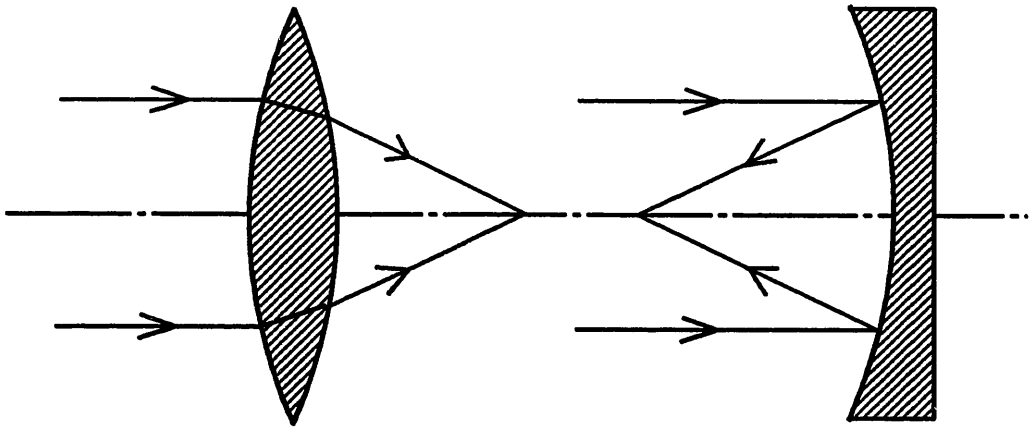

＊吸収損失
＊反射面　２面
＊散乱損失

＊表面吸収
＊散乱損失

図３－５　光学系の損失要素

ない。幸い、電通大レーザー研究センターでは核融合用大出力ＫｒＦレーザー増幅システムの光学システムの設計のために、軸外し光学系を含む光線追跡法に基づいた計算機シミュレーションコードを開発した。大出力ＫｒＦレーザーシミュレーションの解析結果を、レーザーの集光能力を例として、図３－５に示した。ここでは軸外し光学系に球面鏡を用い、入射角によって生じる収差を定量的に計算している。

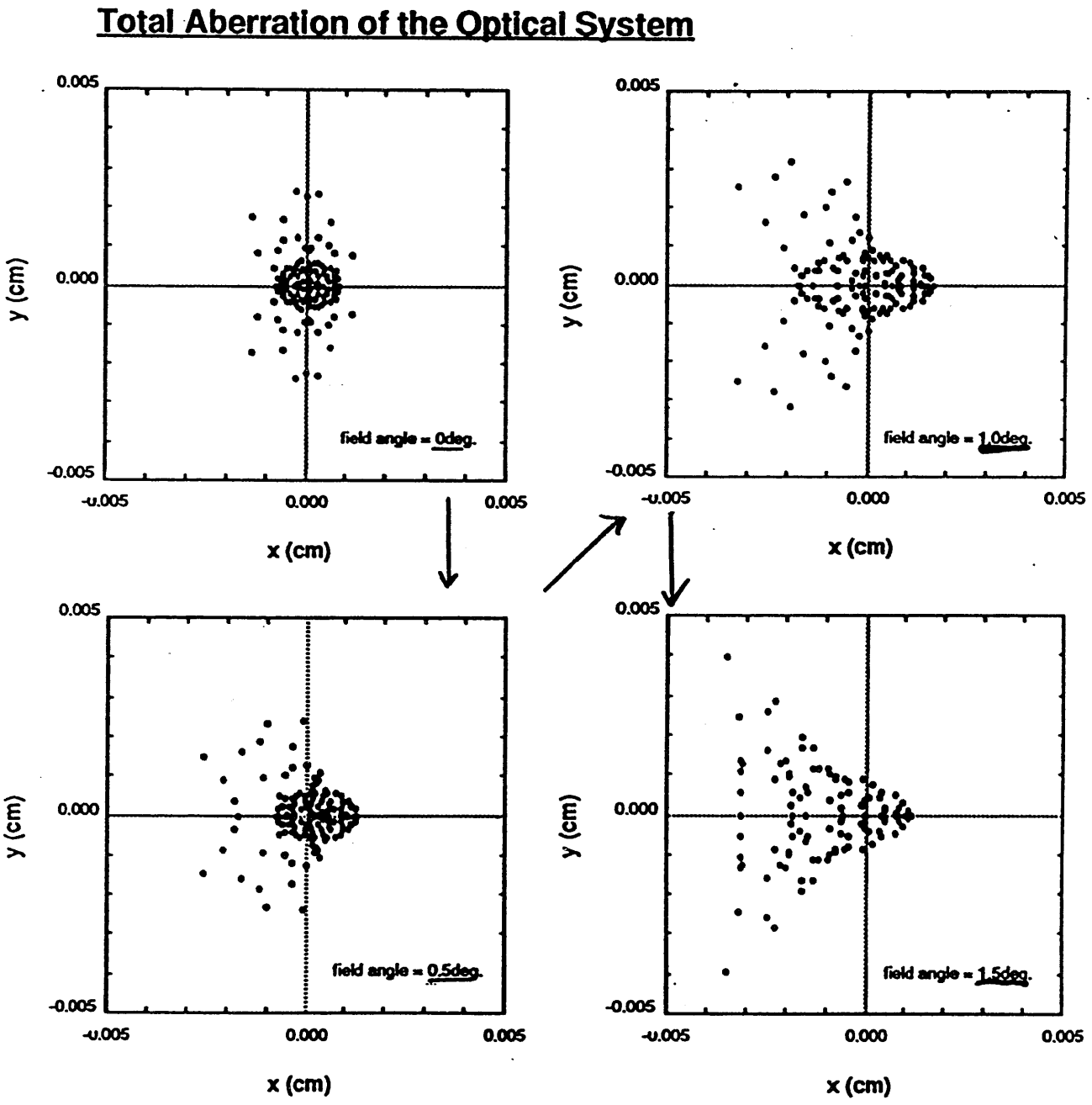

図３－５　大出力ＫｒＦレーザー増幅システムにおける光線追跡シミュレーション

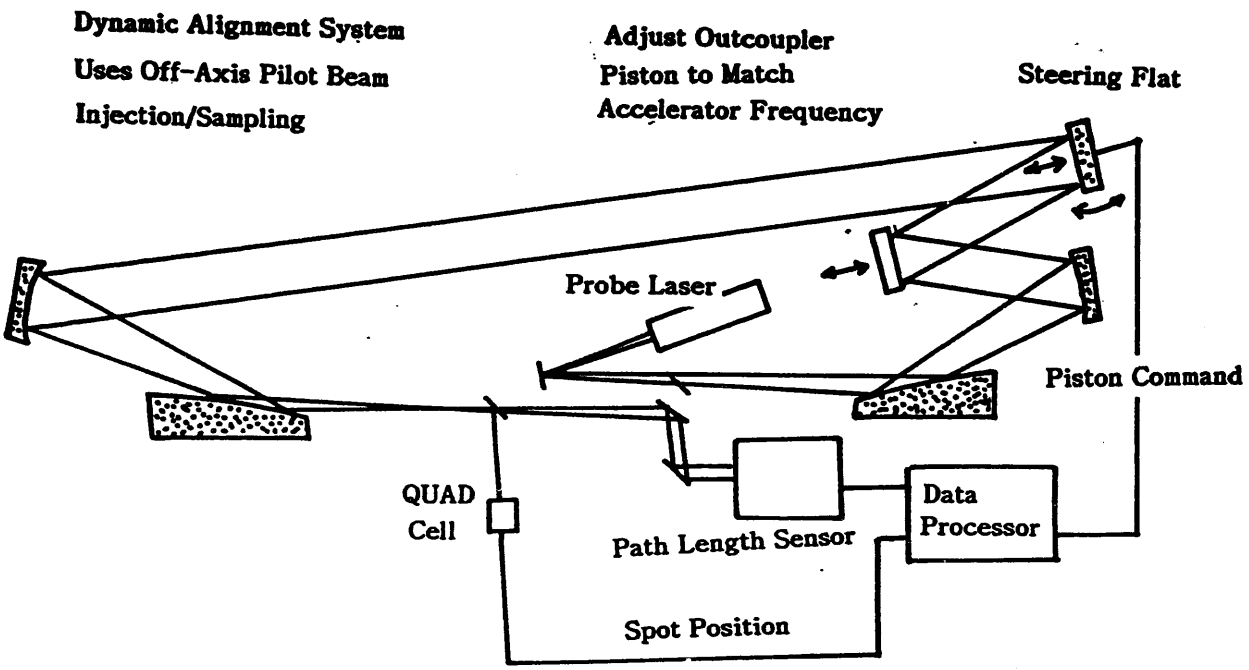

図３－６　斜入射リング共振器のダイナミック・アライメント

３．４　共振器のアライメント精度

３．４．１　自動アライメントの条件

ボーイング社の自由電子レーザーのリング共振器の周回長さは２００ｍであるが、さらに高出力を計画しているレーザーでは、利得を稼ぐためにウィグラー長さが１０ｍ必要だとされている。この場合、共振器長は実に６００ｍ必要だとされており、共振器調整はきわめて困難な課題となる。S.A.Mani らの計算によれば、８００ｎｒａｄ（ナノラジアン）のミスアライメント、λ／３０のコマ収差、λ／３０の非点収差によって、出力が１０％低下する。これは、きわめて厳しい条件であり、従来のレーザーでこのように精密な共振器調整を行った例はおそらくないだろう。この意味で、自由電子レーザーの光学調整は、全く新しい技術を開発する必要があるのである。

さらに、自由電子レーザーに特有の条件として、すべての光学系は真空系の中にあり、外部から遠隔操作によって、最終段階の光学調整をすることがあげられる。

これらの事情を考えると、自由電子レーザーの光学系は

ａ．きわめて高精度の光学調整を

ｂ．計算機による自動的アライメントシステムを

ｃ．真空系の中で遠隔操作を行う

ものだということが結論される。ひとつの例として、ロケットダインのダイナミックアライメントシステムの構成を図３－６に示した。共振器にいっさいの光学素子を挿入することを避けたシステムで、プローブ用ビームを軸外しで注入し、位置センサー（QUAD Cell）、光路長センサーからのデータを計算機処理することで共振器の軸合わせアライメントを行っている。このシステムの開発にはロスアラモス研究所が協力しており、同研究所が核融合用レーザーの自動アライメントのために開発した計算機コードが利用されていると思われる。すなわち、自由電子レーザーのように長い光路長をもち、きわめて厳密な調整精度を必要としたレーザー装置は、従来は核融合用レーザーしかなかったという事情を反映しているのである。ちなみに、ロスアラモス研究所の核融合用ＫｒＦレーザーシステム”オーロラ”は、図３－７に示したように全長４００m弱の光路長をもち、９６本のレーザービームをターゲット上の一点に２００μmの精度で同時に照射しようとするものである。この点からすると、これまで核融合用ＫｒＦレーザーの開発を行ってきた電通大新形レーザー研究センターの研究成果を有効に活用することができる素地が大きい。

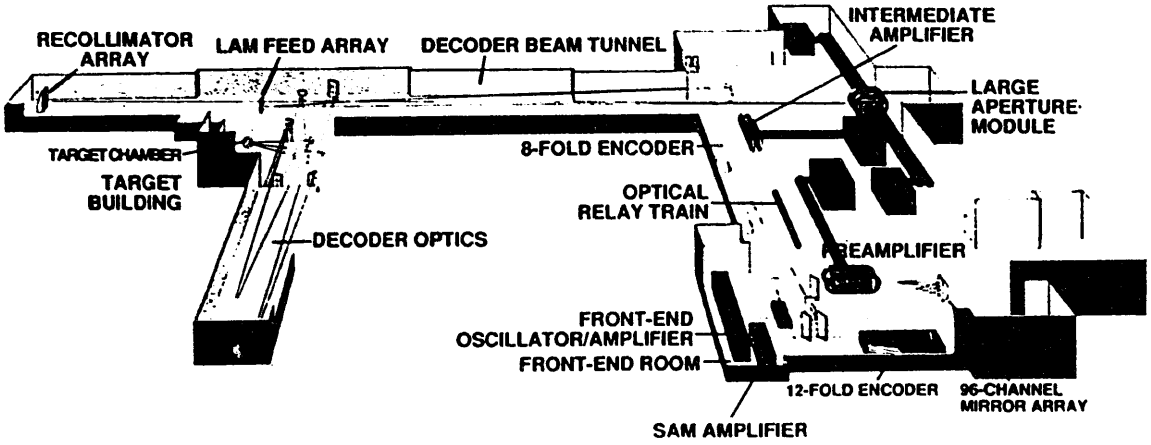

図３－７　核融合用エキシマレーザーシステム　”オーロラ”

DOUBLE CORNER CUBE RESONATOR (concentric equivalent)

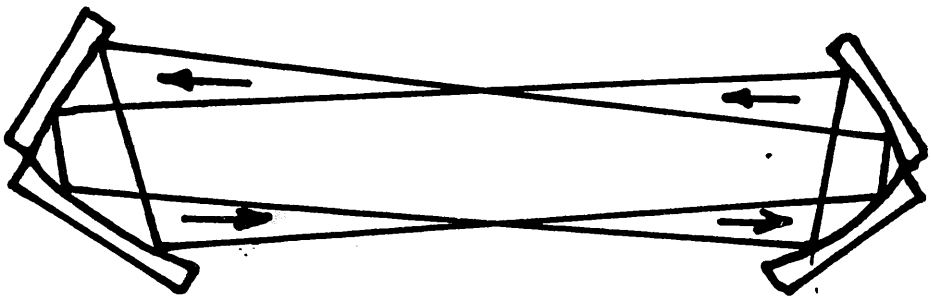

図３－８　コーナーキューブを用いたリング共振器

３．４．２　角度鈍感型光共振器

ひとつの可能性として、共振器自身の構造を反射鏡の角度精度に鈍感に設計することが有効であろう。よく知られているように、コーナーキューブは光を入射方向に正確に反射して帰す性質をもっている。もちろん、全く同じ光軸に反射することはできず、わずかに平行移動した反射光となることが避けられない。図３－８のような共振器構成を利用して、光学調整の精度を少しでも緩和することは、短波長自由電子レーザーの開発のために、非常に重要な課題である。わが国ではコーナーキューブをもったリング共振器の実際的な光学精度、ミスアライメントに対する感度、非点収差、コマ収差の定量的な検討がなされたことはない。今後、急いで研究を組織しなければならない分野である。

３．４．３　位相共役光学系の応用可能性

このような考え方をさらに発展させたものに、位相共役光学系の利用が考えられる。位相共役ミラーとは、たとえば光強度に依存した屈折率をもつような物質、（Photo-refractive material）にレーザー光を照射すると、物質内にレーザー光の干渉によって誘起された密度変動が生じる。密度の規則的な変動は実時間回折格子が形成されるために、入射レーザー光の伝播方向のみが逆転した”位相共役光”が発生して、図３－９のようにどこから照射しても正確に入射方向に光を反射するという光学系である。最近では９０％以上もの高い反射率も報告されるようになっているので、自由電子レーザーに適用することも不可能ではないかも知れない。ただし、位相共役ミラーを形成するためには、レーザー自身のコヒーレンスが高いレー

ザーでなくてはならない。いずれにしても、従来の技術にこだわることなく、新しい発想に基づいた画期的な方式が期待される分野である。

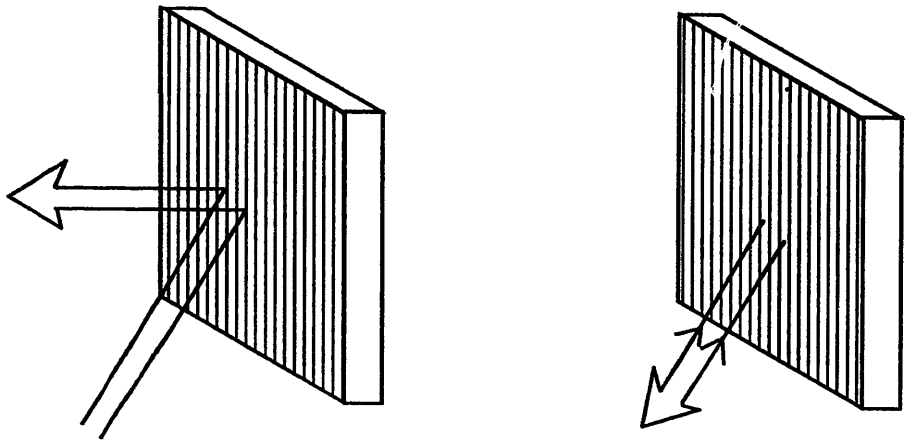

鏡の反射　　位相共役反射鏡

図３－１０　位相共役反射鏡の振る舞い

４．自由電子レーザーの光学素子

自由電子レーザーの共振器に用いられる光学素子は、自由電子レーザーの特徴を反映して、他のレーザーのために開発された光学素子に比べて過酷な条件に耐えなければならない。各々の特徴を吟味してみよう。

ａ）きわめて高い反射率を持つ必要がある。（反射率）

ｂ）高いレーザー損傷強度をもつ必要がある。（レーザー損傷）

ｃ）斜入射光学系に必要な非球面ミラーである。（形状）

ｄ）短波長の高調波、制動輻射光に耐える。（雑音光損傷）

前章で述べたように自由電子レーザーの光学素子は、低利得で発振するためと同時に最適結合の条件から、非常に高い反射率をもつことが必要である。特に、はじめて発振させる場合には通常９９．９９％以上の高反射率ミラーが用いられる。ここでは光学素子の実際の例に即して、自由電子レーザーに必要な条件を検討することにする。

４．１　光共振器のアライメント

高利得を得ようとするとウィグラー長が長くなり、必然的に光共振器の光路長が長くなければならないことは前章で述べた。現在稼働中および計画中の自由電子レーザー用のリング光共振器の周回距離は２００ｍから６００ｍに達している。このように長い光路長をもった光共振器用の光学素子として、いくつか特長的な光学素子が提案されている。必要な光学調整精度の例をＳＰＩＥにおける発表からあげてみよう。図４－１～図４－３は斜入射リング共振器におけるミスアライメント、非点収差、コマ収差のレーザー出力に与える影響を計算機シミュレーションしたものである。結論的には

①　８００ナノラジアンのミスアライメント

②　λ／３０の非点収差

③　λ／３０のコマ収差

があれば、レーザー出力は１０％低下すると計算されている。

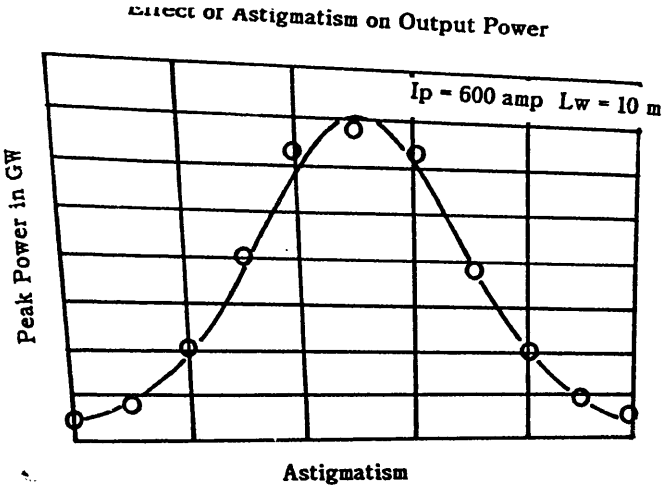

図４－１　ミスアライメントの影響

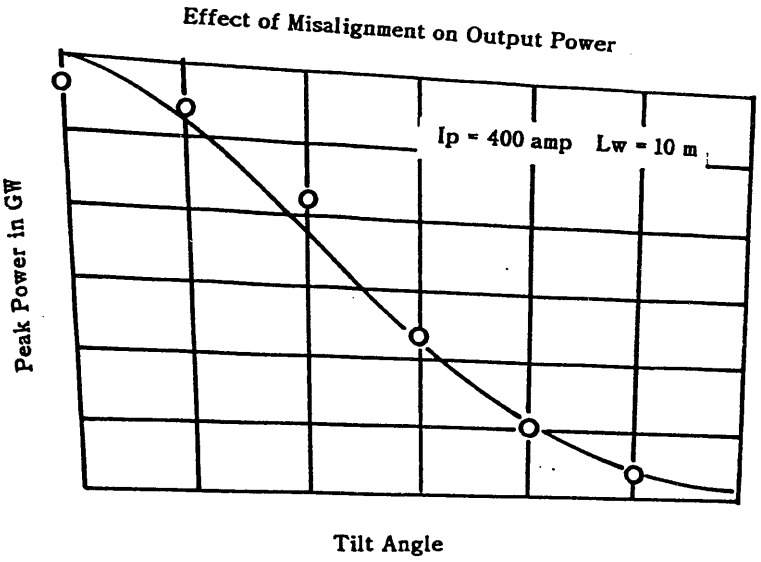

図４－２　非点収差の影響

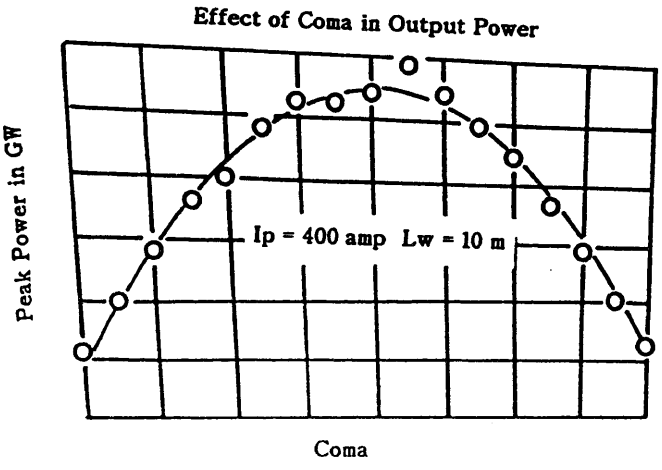

図４－３　コマ収差の影響

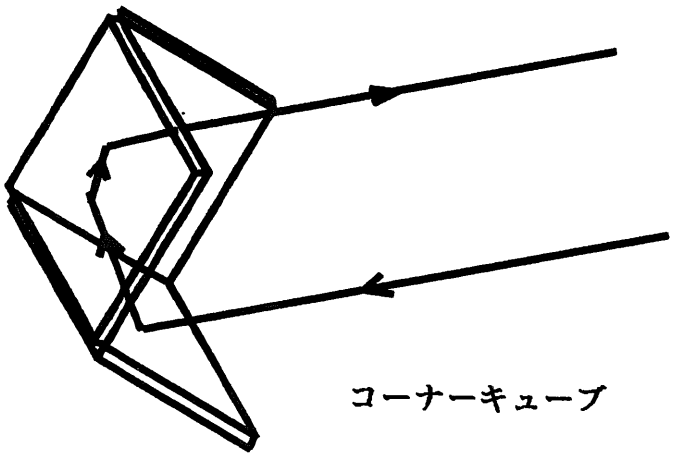

図４－４　コーナーキューブの構成

このため、共振器調整の精度を緩和するような光学素子が望ましく、コーナーキューブの利用がまず考えられている。

４．１．１　コーナーキューブ

アライメント条件を緩和する光学素子として考えられているコーナーキューブは、反射鏡３枚で構成される。図４－４に構成を示した。高精度の平面鏡を３枚組み合わせてつくったコーナーキューブの平面鏡相互間の直角度は微調装置によって調整される。コーナーキューブは入射した方向と同じ方向に光線を反射する性質をもっているので、長い光路長をもった共振器における光学調整の困難さを逃れることができる。長い光路長では反射鏡の軸が$\delta\theta$だけ傾くと、$\delta x = L\delta\theta$の光学像のズレが生じる。このため、光路長に比例した調整精度が要求されるので、このようなシステムは重要である。

一方、コーナーキューブの角度が$\delta\theta$振れた場合、$\delta\theta$がマイクロラジアンの領域では、図４－５のように$\delta x = \delta\theta$の感度で光軸が平行移動する。電子ビームの直径が１ｍｍ以下の自由電子レーザーでは、このような光軸の平行移動も大きな損失となる。角度制御ほどの鋭敏さはないものの、何らかの対処が必要である。

コーナーキューブ反射鏡の問題点は反射率にある。コーナーキューブでは光線がもとの方向に反射されて戻るには、３回の全反射をしなければならない。共振器内における反射回数が通常の全反射鏡に比べて多くなるので、ミラーの損失は他の反射鏡システムの１／３以下にする必要がある。

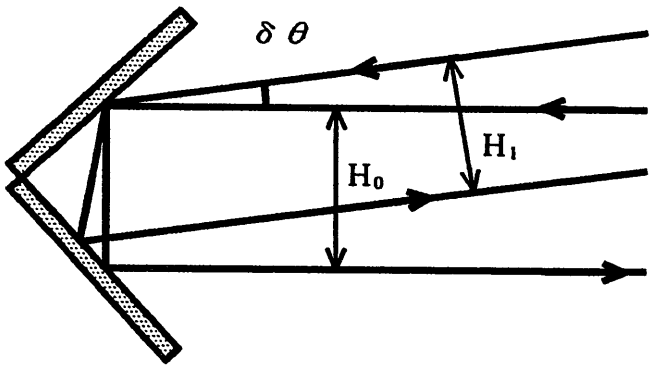

$$\frac{\delta H}{H_0} = \frac{H_0 - H_1}{H_0} = \frac{\cos 45^\circ}{\cos(45^\circ - \theta)} \cos 2\theta - 1$$

図４－５　コーナーキューブにおける光線の平行移動

４．１．２　穴開きミラーによるレーザー出力

共振器内部に蓄えられている共振エネルギーを外部に取り出すためには、共振器の内部と外部を結合する光学素子が必要である。結合光学系には誘電体多層膜による半透鏡が用いられることが多かったが、きわめて厳しい反射率制御が必要とされることに加えて、前述のような光学軸の変動に対処することも、ひとつの要素となり得る。実際に検討されている共振器構成を図４－６に示そう。ここではレーザー出力鏡としてスクラバーミラーすなわち穴開きミラーが検討されている。穴開きミラーの利点は以下の通りである。

①反射率は全反射鏡でよく、反射率制御がない。

②穴は空間フィルターの役割をするので、反射鏡による軸のズレを利得領域との相互作用で補正する機能が期待できる。

③共振器の光軸中心のビームに対してほとんど損失を与えない。

④将来高出力化した場合、冷却光学素子を適用することができる。

特に、光学系のミスアライメントが生じた場合のモード修復機能については、計算機シミュレーションで確かめる必要があるだろう。透過光学系では光学素子の内部から水冷することができない。高出力光学系は反射系で考える方が合理的であり、将来の発展製を考慮すると穴開きミラーが必要となる所以である。

表４－１　自由電子レーザーに用いられる光学素子の特性

Mirror	Coating Material	Reflectivity	Absorption	Wavefront Destortion
Silicon Hypaboloid	Bare Silver	98.5% at 0° 99.92% at 87°	1.5% at 0° 0.06% at 87°	λ /? for
Silicon Paraboloid	$ZrO_2/SiO_2/TiO_2$	99.99%	0.001%	λ /27 for 1.5″ witness
Silicon Steering Flat	$ZrO_2/SiO_2/TiO_2$	99.99%	0.001%	λ /22 for 1.5″ witness λ /20 for 11″ mirror
Fused Silica Outcoupler	HfO_2/SiO_2	variable with wavelength	0.002%	λ /30 for 1.5″ witness λ /30 for 11″ mirror
Fused Silica Window	ZrO_2/SiO_2	< 0.1%	0.001%	λ /30 for 12″ window

λ = 0.6328 μm

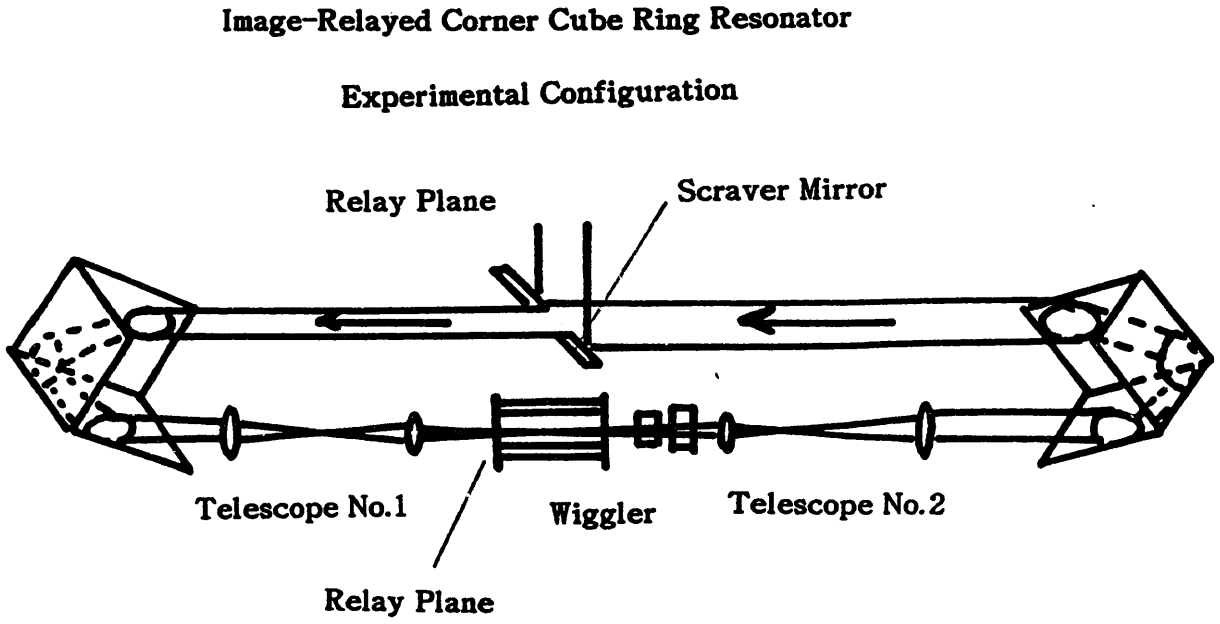

図４－６　コーナーキューブ／穴開きミラー型リング共振器

４．２　高反射率・低損失反射鏡

光共振器に用いられている光学素子の例を表４－１に列挙した。この例はボーイング社の０．６μｍ発振ＲＦライナック型自由電子レーザーである。電子のエネルギーは１４０ＭｅＶでウィグラー長は５ｍである。斜入射リング共振器の光学素子で、共振器の光路長は周回距離で約２００ｍである。現在、１０ｍウィグラーを設置中で、その場合の共振器長は６００ｍ程度になると予想されている。

表４－１に例示された光学素子から分かる自由電子レーザー用光学素子の反射、吸収特性は以下の通りである。

①　反射率は９９．９９％が必要である。

②　吸収は０．００１％以下である。

③　平面度はλ／３０以下である。

④　出力鏡に誘電体多層膜を用いる場合は、レーザー出力の波長に合わせて製作する必要がある。

⑤　出力窓の無反射コーティングは０．１％以下の反射率に抑える。

⑥　光学素子の寸法が大きい。

⑦　非球面光学系が必要である。

これらの要求は光学素子製造技術として非常に厳しい。①②は反射鏡の損失に関するもの、③④⑤は光学素子の精度に関するもの、⑥⑦はサイズ、形状に関するものである。

４．３　反射鏡の損失

反射鏡の損失原因は

①反射層内の吸収

②表面散乱による損失

③光透過

である。

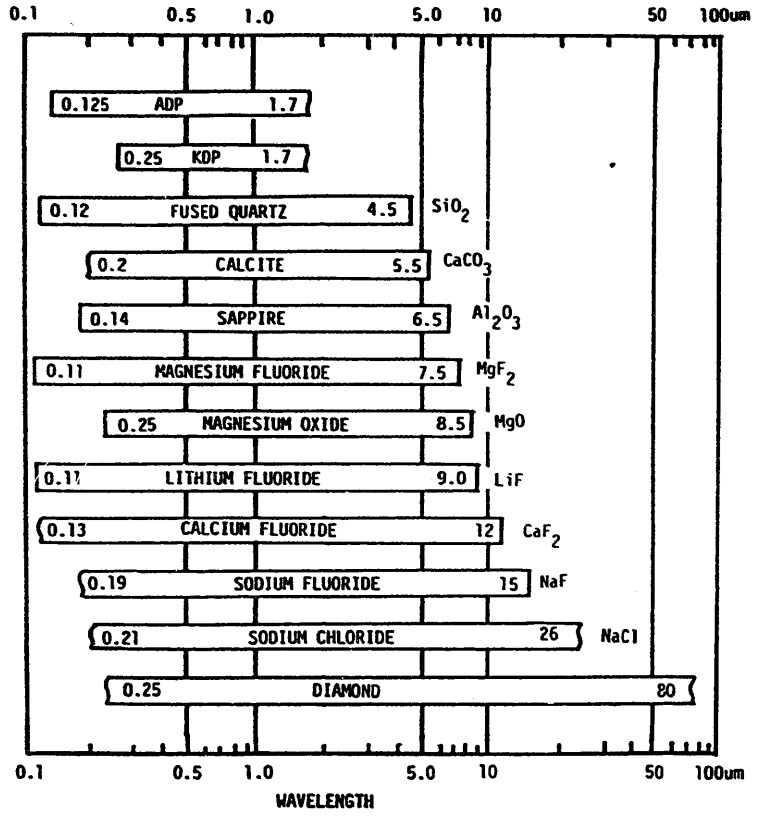

図４－７　光学材料の透過波長域

４．３．１　光吸収による損失

光を反射すべき反射鏡の表面物質が光を吸収すれば、損失することは自明である。しかし、０．００１％オーダーの微小吸収を問題にする限り、吸収の全くない物質を考えることは困難である。物質の吸収機構の基本はバンドギャップエネルギーで決定されるので、光子のエネルギーが高くなるほど、すなわち光の波長が短くなるほど吸収が増大することが避けられない。理屈の上では、バンドギャップエネルギーより小さな光子エネルギーの波長では吸収がないはずだが、格子欠陥、構造不整、不純物吸収のために、可視域でもわずかな吸収を示す。一般には、吸収端波長が短波長であればあるだけ、可視域の吸収損失が小さいと考えても間違いはない。代表的な光学材料の有効な波長域を図４－７にまとめた。赤外材料として優秀な特性を示す光学材料の多くが、紫外域でも良い光学材料であることが分かる。

４．３．２　表面散乱による損失

低吸収物質を用いて吸収損失を減少させてゆくと、もっとも大きな損失要素は表面散乱になる。表面散乱には、基板表面の凹凸に起因するもの、表面物質の屈折率の不均一によるもの、表面に付着した微粒子によるもの、などがある。光学基板の表面粗さ以外の問題は比較的初歩的で、注意深く作成、使用すれば現在の技術で解決済みである。

一方、表面粗さに起因する散乱損失を０．００１％に減少させることは、簡単ではない。自由電子レーザー用反射鏡では、数オングストローム、すなわち波長の１０００分の１以下の微少な凹凸しか持たないような超平滑面に研磨しなければならない。このような技術はレーザージャイロ用光学部品の研磨技術、超安定レーザー用光学部品の開発など、軍事技術と結びついて欧米で発達したので、わが国が比較的遅れている分野である。しかし、最近民間企業の中にも、このような超先端的光学技術に挑戦しようとする機運が盛り上がりつつあるので、大いに協力して開発すべきであろう。

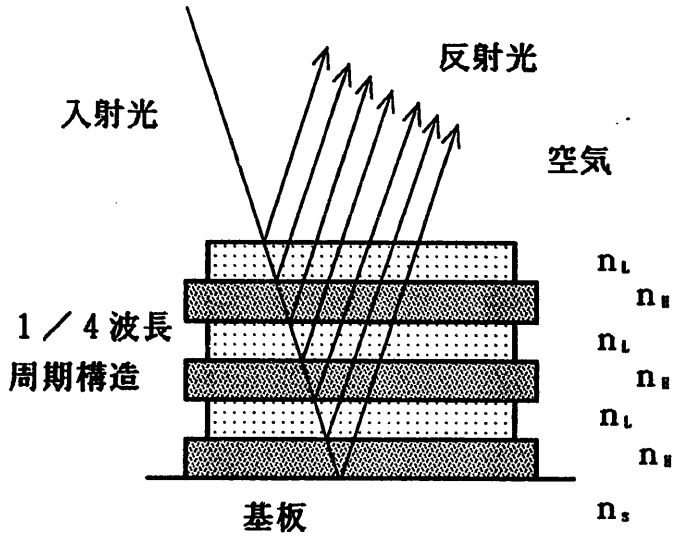

図４－８　誘電体多層膜反射鏡

４．３．３　光透過による損失

金や銀、アルミニウムのような反射金属の固有の反射率は９８％程度であって、さらに高い反射率を得るためには、誘電体多層膜による多重干渉効果を利用しなければならない。図４－８に示したように、n_Hとn_Lの高低２種類の屈折率をもつ光学薄膜を各々１／４波長間隔で積層すると、偶数層の場合の最高反射率と反射帯域は屈折率比　$f = n_H / n_L$の関数となって、

$$R_{max} = \left\{ \frac{(n_s f^{2N} - 1)}{(n_s f^{2N} + 1)} \right\}^2 \qquad (4-1)$$

$$\Delta\lambda = \frac{4\lambda_0}{\pi} \sin^{-1} \left\{ \frac{(1-f)}{(1+f)} \right\} \qquad (4-2)$$

となる。ただし、n_sは基板の屈折率で、層数は２Ｎである。ここに示した式から分かるとおり、多層膜を構成する誘電体の屈折率の比が高いほど、少ない層数で広帯域のスペクトルに対して高い反射率を達成することができる。したがって、高反射率ミラーをつくるためには

①　屈折率の差が大きく

②　吸収率の小さな

２種類以上の光学材料を使用することが重要な要素である。

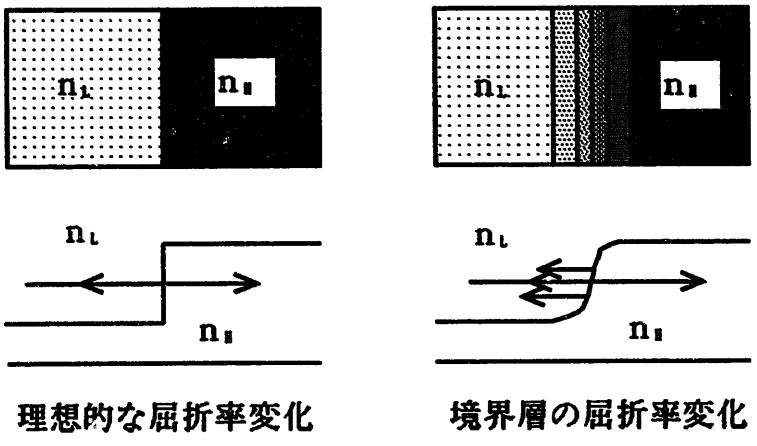

図４－９　不鮮明な境界層による反射率の減少

１）膜厚不整合による光透過

上記の反射率は各薄膜の厚みが厳密に１／４波長で、かつ吸収がゼロで位相変化が理論通りの場合に達成される。しかし、もし蒸着過程の制御が不完全で、膜厚が理想状態からはずれると、反射率が低下し、低下した分は光学薄膜を透過することになる。このとき、わずかな量の透過光が基板に到達したとしても、レーザー損傷には決定役割を果たすことが多い。

２）膜間境界面の影響；蒸着方法の影響

もうひとつの問題は多層膜間の境界層である。理論的には２枚の誘電体層の境界はステップ的に屈折率が変化していることが望ましい。しかし、実際は図４－９に示したように厚みは非常に狭いが両者が混ざりあった境界層が存在する。このため反射率は理想状態よりも低下する。境界層の状態は蒸着方法に依存している。従来一般的であった電子ビーム加熱真空蒸着法は、もっとも境界が不鮮明になるといわれている。同時に、電子ビーム蒸着法で生成した光学薄膜はもっとも密度が低い。鮮明な境界層をつくるには、スパッタリング法、イオンビーム・デポジション法が適している。米国その他で自由電子レーザー用の光学素子をつくっている方法はイオン・デポジション法だと言われている。

４．４　斜入射非球面反射鏡

４．４．１　斜入射反射鏡の高反射率

ウィグラーにもっとも近い鏡はレーザーのパワー強度が高く、もっとも過酷な条件にさらされる。ビーム半径が小さな条件で、反射鏡に与えられる照射強度を軽減できる光学素子は斜入射光学系である。表４－１に示した通り、入射角が８７度の場合、照射強度は１／１９に低下させることができる。斜入射光学系のもうひとつの利点として反射率を高くできる。垂直入射では９８．５％の反射率の銀鏡も８７度入射では９９．９２％にも達するのである。誘電体多層膜の反射鏡に比べると、反射率の波長依存性が少ないことも重要である。

４．４．２　非球面光学素子のサイズ

ただし、斜入射光学系は光学素子のサイズが非常に大きくなる。入射角が８７度の場合２０倍以上の光学素子の大きさが必要になる。同時に、軸外れのために発生する収差を補正する必要がある。このために、双曲面鏡と放物面鏡を組み合わせたデザインなども考案された。ただし、放物面鏡もまた、光路長が短い場合には同軸放物面鏡ではありえなくなる。この点からすれば、リング共振器の光路長が長い方が波面の歪は少なくなるだろう。

実際に製作された非球面光学素子を図４－１０に示した。双曲面鏡は長さ６４ｃｍに達する大きなシリコン・ウェッジを研磨整形したものである。放物面鏡も直径２８ｃｍのものが製作された。研磨加工の精度からいえば、光学ガラスの方が優れており、同時に大きな基板を用意することも簡単なのに、シリコン・ウェッジを用いた理由は、反射鏡に与えられる熱負荷にある。

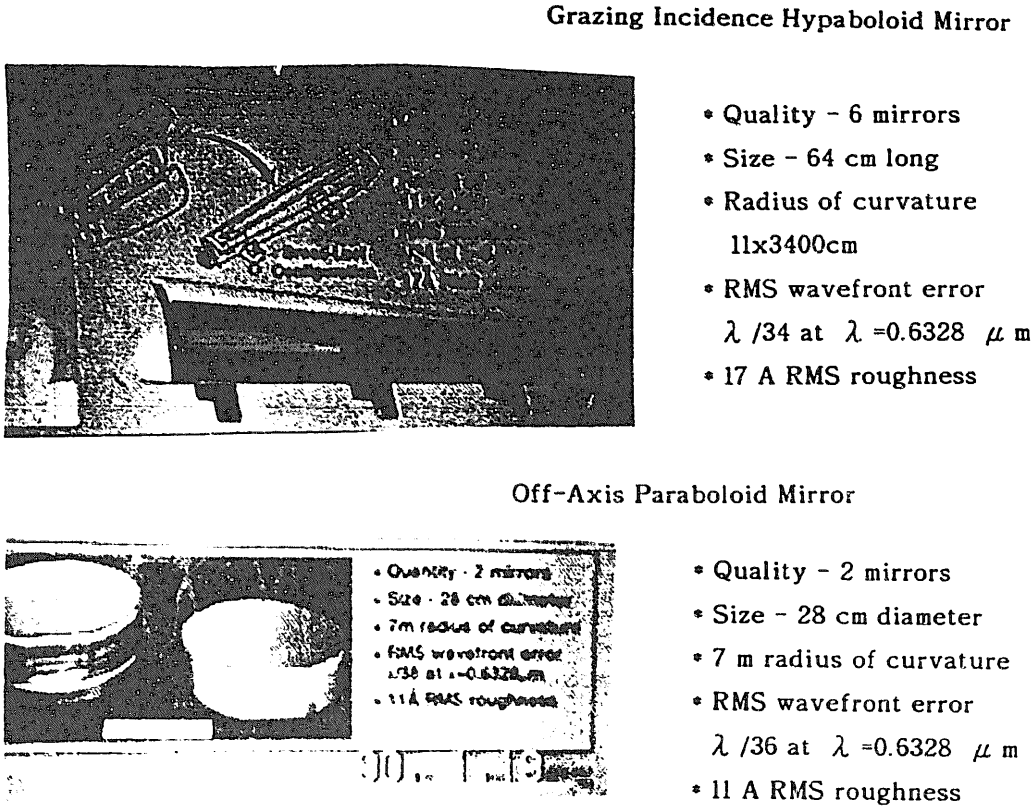

図４－１０　斜入射双曲面鏡と軸外し放物面鏡

４．５　高入力・高耐力光学素子

自由電子レーザーのレーザー媒質は真空である。通常のレーザーではレーザー媒質の自己吸収とつりあう条件で発振出力が制限される。しかし、自由電子レーザーでは自己吸収がないので、共振器損失とつりあう条件まで上昇する。９９．９９％以上の高反射ミラーで構成される共振器では、共振器内のパワーフローはレーザー出力の１００００倍にも達するのである。しかも、非常に繰り返しが高く、ほぼ連続的な発振をするのだから、共振器用ミラーに対する入力パワーの要求は非常に高い。

４．５．１　光学素子の熱負荷と損傷機構

光学素子の損傷機構には、

①連続発振レーザーおよびナノ秒以上のパルスに対応する熱破壊

②ピコ秒パルスに対応する電界破壊

の２種類が存在する。通常のレーザーではどちらかの現象のみに対応すればよいのだが、自由電子レーザーの場合は両者が同時に存在している。自由電子レーザーの発振は、発振パルスが高出力のピコ秒パルスで、繰り返し周波数は１００ＭＨｚ以上にも達するからである。短パルス高出力パルスレーザーでありながら、平均出力もまた大きいという従来のレーザーでは経験しなかった条件に対処するため、レーザー損傷の研究はさらに重要性を増すことだろう。

まず最初に対応しなければならないのは機構が単純な熱的レーザー損傷である。高い平均出力を持つレーザーでは、連続発振レーザーと同様の考え方を適用できる。そこで非球面光学素子を冷却なしに用いる場合には、形状を工夫して温度上昇に安定な形状を選ぶことが重要である。熱負荷に対して安定な形状で、同時に研磨工程における機械強度を保証するために工夫された三角形断面（図４－１１）、六角形断面（図４－１２）のシリコン母材が用いられたケースもある。

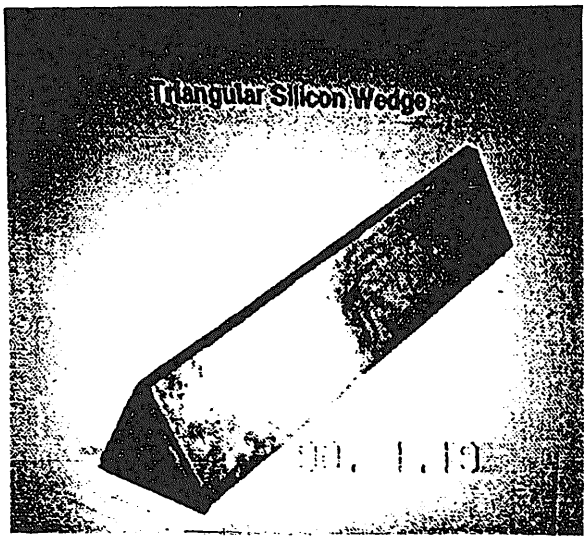

図４－１１　３角断面光学素子

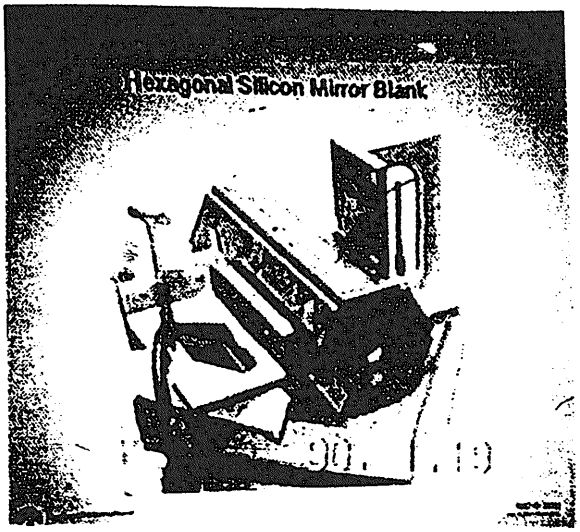

図４－１２　６角断面光学素子

４．５．２　光学素子の水冷

自由電子レーザーの開発が進めば、レーザーの効率は数１０％にも達すると予想される。１００ＭｅＶ、１００ｍＡのマクロパルス平均電流を仮定すると、数ＭＷの定常発振に対応しなければならない。このため、実用的には冷却する必要がある。各国で開発中の自由電子レーザーで、冷却光学素子が用いられた例は少ないと思われるが、早晩必要になる条件である。前述の非球面ミラーの母材がシリコンであった理由は、むしろ冷却のためではないかと推察される。

表４－２　光学素子材料の特性

母材材料	熱伝導率	サイズ	研磨	蒸着
光学ガラス	×	○	◎	◎
結晶	△	×	◎	◎
シリコン（半導体）	○	△	○	◎
金属	◎	◎	×	△

冷却のためには光学素子材料の熱伝導率が重要である。表４－２でも分かるようにガラスは熱伝導率が低く、結晶は大きな光学素子用の材料育成が困難である。一方、金属の母材は超平滑面をつくることが困難で、多層膜を蒸着することにも余り適していない。結果として、熱伝導率の良い半導体結晶のシリコンならば、将来母材そのものの中に水冷部をくり抜けば、もっとも良い組み合わせとなると考えられる。

４．６　高精度非球面曲面の計測

大型の非球面光学素子の計測はわが国では未経験の分野である。従来の光学素子の検査項目は

① 面精度
② 平面度
③ 波面歪み
④ 反射／透過特性

程度であった。追加すべき項目として

⑤ 表面粗さ
⑥ レーザー損傷強度
⑦ 超低損失光学素子の損失測定
⑧ 曲面形状の精密測定
⑨ 実負荷または環境試験

などを挙げることができる。

これらの課題のうち、表面粗さの測定については最近、ザイゴ社製、ワイコ社製の表面粗さ計が多くの企業、研究所に導入され、計測データをつけることが始まっている。レーザー損傷強度および超低損失光学素子の反射率測定は、企業のみで行うことが困難で、レーザーを専門的に研究している大学、研究所と共同研究を行うことが望ましい分野であろう。

一方、⑧⑨の課題は計測装置や試験装置の開発が重要で、かなりの研究投資が必

要な一方、実用レベルの製造技術と結合しなければ意味がない。実際、今回の訪米調査でも判明したように、研磨、蒸着工場内でのオンサイト測定が重要である。さらに厳しい環境における耐力を測定するための環境試験装置などは、わが国にないので、今後考えなければならない方向である。

このような３次元曲面形状の測定には、原器による干渉計測を用いることができない。各国でコンピュータを駆使した新しい曲面研磨、曲面計測の装置が開発され、実用化されている。図４－１３に斜入射光学素子の曲面計測の用いられた装置の一例を示す。レーザー干渉計を駆使して、２次元の曲面形状を正確に測定することができる。原理的には、表面粗さ計を広範囲に適用したものと同等であるが、高精度を発揮するための技術は非常に高いものがある。

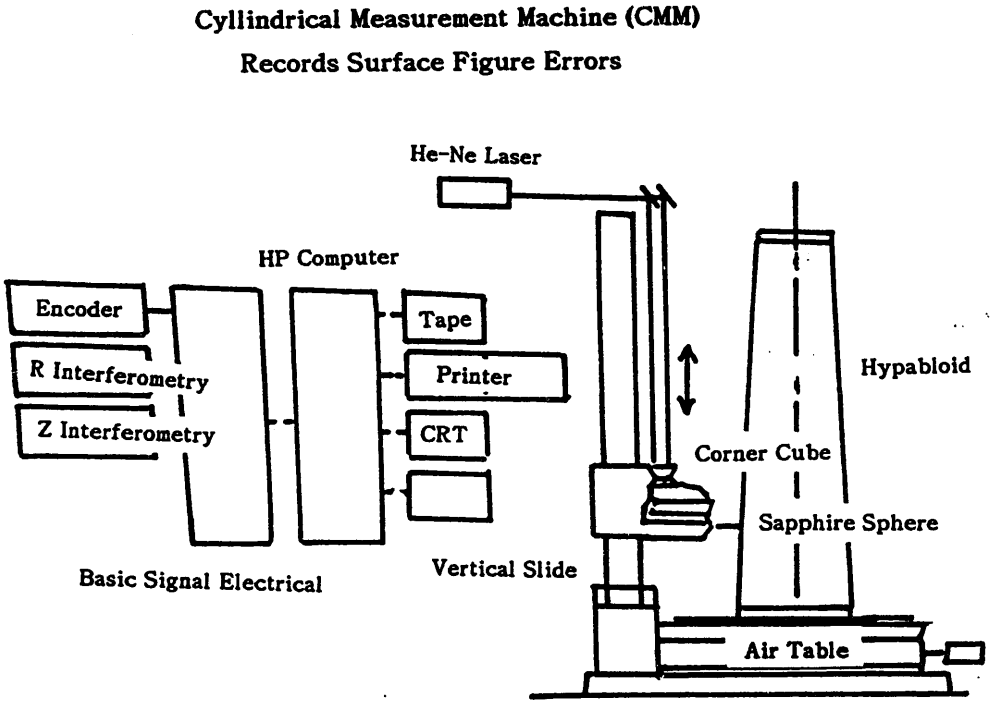

図４－１３　３次元形状計測装置

５．　光学素子の特性測定

自由電子レーザーにおける光学系、光共振器、光学素子が重要であることを、これまで述べてきた。光学系、光学素子を開発するためには、光学素子の特性を正確に測定することが不可欠である。この章では、光学素子の微少吸収、多光子吸収、レーザー損傷強度、反射率分布などの測定法について検討する。新しく開発している光音響法、ピコ秒パルスによる共振器損失法、画像計測応用反射鏡測定などについても記述する。

５．１　高反射ミラーの反射率測定法

自由電子レーザーで要求されるような低損失ミラーの反射率や損失係数を正確に測定することは容易でない。まったく吸収がなくても通常のミラーの場合には、０．２％程度の表面散乱が避けられないと考えられている。また、誘電体多層膜の薄膜内吸収を測定することも困難な課題である。このように微少な損失を測定するのに適した方法は光共振器に閉じ込められた光の閉じ込め時間、すなわち共振器内の光子寿命を測定する方法である。光共振器としてファブリペロー共振器が用いられる。わが国においても、色素レーザー出力にＥＯ変調器で変調をかけ、ファブリペローエタロンの透過光の矩形波立ち上がり時間を検出して、高反射率ミラーの反射率測定を行った例がある。

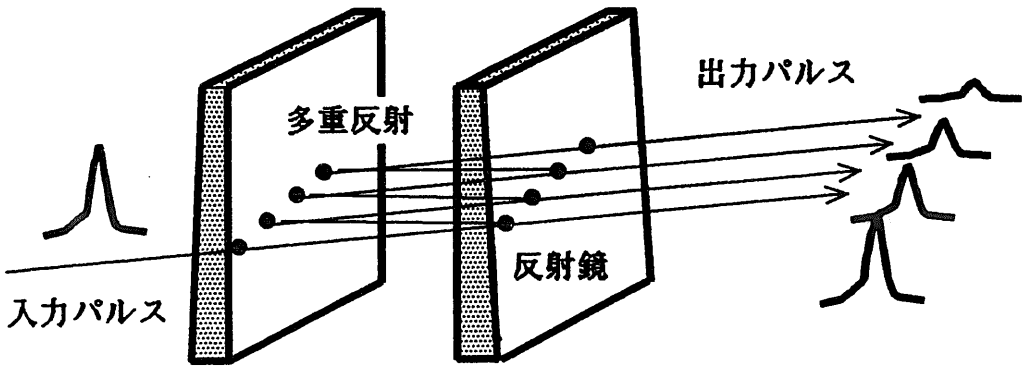

ファブリペロー共振器

図５－１　ファブリペロー共振器と共振器寿命測定

５．１．１　共振器の光子寿命による損失測定

ミラーの損失計測に用いるファブリペロー共振器の特性を簡単にまとめてみよう。ファブリペロー型の共振器はファブリペロー干渉計とも呼ばれ、図５－１のように互いに平行に配置された２枚の反射鏡で構成された光共振器である。入射した光は、２枚の反射鏡の多重反射によってある時間だけ光共振器の中に閉じ込められる。閉じ込められる時間のことを光共振器の寿命と呼び、共振器の損失で決定される量である。入射光として超短パルスを考えて、多重反射しているパルス同士が同一進行方向では互いに重ならないと仮定する。この場合は干渉効果を考える必要がないので解析は容易である。鏡の反射率をＲ，入射光強度をI_0とすると、Ｎ回往復した後の光強度は

$$I = I_0 (1-R)^2 R^{(2N-1)} \qquad (5-1)$$

で表される。透過パルスの強度は$R^{(2N-1)}$に比例するのであるから、パルス強度の変化を測定すれば直ちにミラーの反射率を求めることができる。この方式の利点は、パルス同士を分離して計測するので、光のコヒーレンスの影響を受けないことである。実際予想される高反射率の条件で、ファブリペロー共振器の透過光量の理論計算結果は図５－２のようになる。反射回数１０００回程度で10^{-4}オーダーの微少な損失を正確に測定できることがわかる。

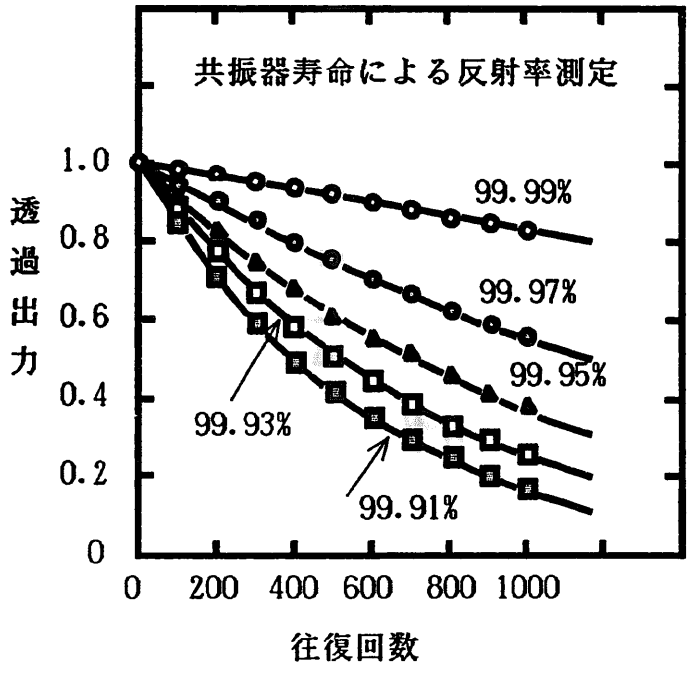

図５－２
反射率と共振器寿命

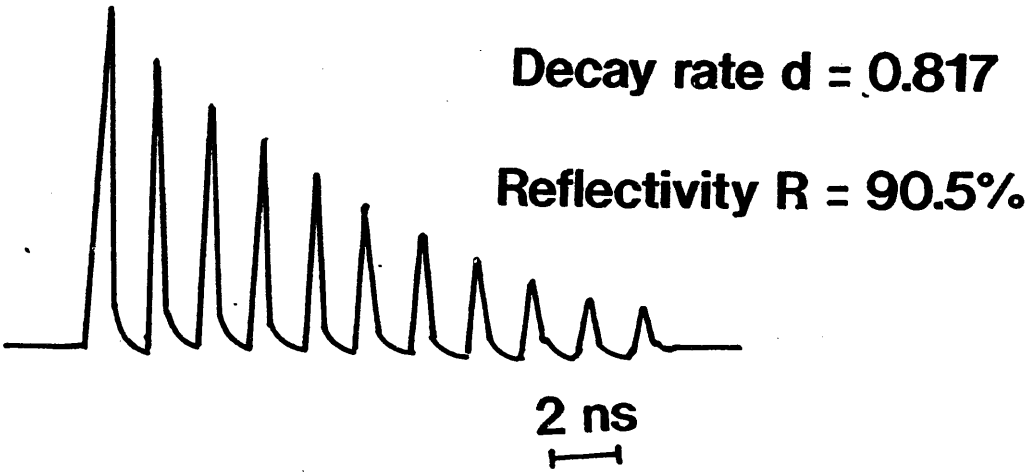

図５－３　ピコ秒レーザーによる反射率の実測例

実際に新しく開発した超短パルスレーザー光を用いて光子寿命を測定した実験結果を図５－３に示した。用いたレーザー装置の詳細は６章で詳しく説明する。用いた試料は２４８ｎｍで９０％の反射率を持つ鏡で２４８ｎｍ、１ｐｓのパルスで測定した。共振器の間隔を３０ｃｍとしたので、透過パルスの間隔は２ｎｓである。パルス幅の変化などは考える必要がないので、透過光強度はフォトダイオードでエネルギー検出すれば十分である。高速オシロスコープ（Tektronix 7104）で記録された減衰時定数から、試料の反射率を測定したところ、９０．５％であることが分かった。この値は分光光度計で測定した値と一致した。今回の測定は反射率が低いので、反射回数が少なかったが、超高反射率ミラーの損失測定も全く同様に行うことができる。高反射率の試料を測定する場合は、減衰時定数が長くなるので測定系の応答が不必要になるので、より容易な測定となる。断っておくが、減衰時定数の測定には、図５－３に示したようにパルスを独立させて測定する必要はない。測定系の時定数が減衰時定数より早いという条件を満足さえすれば良い。したがって、９９．９９％の反射率を測定する場合には、減衰時定数を表現する曲線が直接オシロスコープ上に記録されるだろう。

５．１．２　干渉縞の幅から測定する方法

従来、わが国で測定された方法は、連続波の可視光レーザーを用い、チョッパーで整形された矩形波の波形ひずみを位相検波方式で測定するものであった。連続波

または共振器内で光が多重に重なるパルス幅を持つ場合は、光の干渉を考慮しなければならない。

入射光としてパルス幅の十分長い単色光を仮定すると、２枚の反射鏡の間で多重反射した光が互いに干渉しあって、透過光強度は

$$\frac{I_t}{I_i} = \frac{\left(\frac{T}{1-R}\right)^2}{1+\frac{4R}{(1-R)^2}\sin^2\left(\frac{\delta}{2}\right)} \qquad (5-2)$$

となる。ただし、I_tは透過光強度、I_iは入射光強度、Ｔは干渉計の透過率、Ｒはミラーの反射率、γは光共振器の１往復あたりの位相遅れである。フィネス係数Ｆ、エアリー関数Ａ（δ）をおのおの

$$F = \frac{4R}{(1-R)^2} \qquad (5-3)$$

$$A(\delta) = \{1+F\sin^2(\delta)\}^{-1} \qquad (5-4)$$

と定義すると、光の透過率は

$$\frac{I_t}{I_i} = \left(\frac{T}{1-R}\right)^2 A(\delta) \qquad (5-5)$$

と表現することができる。したがって、干渉縞の半値全幅をγとすると、エアリー係数Ａ（$\gamma/2$）＝１／２から

$$\gamma = 4\sin^{-1}(1/\sqrt{F}) \qquad (5-6)$$

となる。

ただし、ここで用いたフィネス計数はファブリペロー干渉計の性能を表現するときによく用いられるフィネスとは異なり、コントラスト比を表している。ちなみに、通常用いられることの多いフィネスの定義は

$$F' = \frac{\pi}{2}F = \frac{\pi R}{1-R} \qquad (5-7)$$

である。

導出された経過から明らかなように、ファブリペロー干渉計の出力光強度は、ミラーの反射率だけでなく、光共振器内のわずかな位相の変化が関係してくる。実際の計測条件では、レーザー光を完全な単色光とみなすことはできない上に、可干渉性すなわちレーザー光のコヒーレンスは常に一定ではありえない。通常の条件ではこれらの効果は無視できるほど小さいが、０．０１％以下の微少な損失を測定しようとするときには、重大な誤差の原因となる。

原理的にはコントラスト比を表すフィネス係数から反射率を計測することは可能だが、０．０１％の損失を区別して測定するためには、γ＝０．２ｍｒａｄという非常に狭いスペクトル線幅を定量的に測定しなければならない。実際の計測条件で、このような線幅から反射率を導出することはきわめて困難で、大きな誤差を伴うことになる。

５．１．３　連続チョッパー光立ち上がり時間測定

したがって、実際に応用される場合には、チョップされた連続光の位相敏感検波が用いられる。立ち上がり時間の位相変化から、時間領域における損失計測を行うのだが、光チョッパーの立ち上がり時間はそれほど早くないのでこの方法には本質的な困難がある。その上、時間的干渉効果の時間的変化の影響を受けるので、好適な測定法とは言いがたい。

結果として、ビームの干渉を受けることのない超短パルスで共振器の光子寿命を測定する方法が、もっとも高感度で信頼がおける測定法だと結論でできる。

５．２　レーザー損傷強度の測定

レーザー損傷強度には吸収、光透過、基板の表面状態、蒸着条件、均質性など光学素子の特性のすべてが反映している。このため、レーザー損傷強度の測定は光学素子の品質測定の最終的な判定基準という意味を持っている。

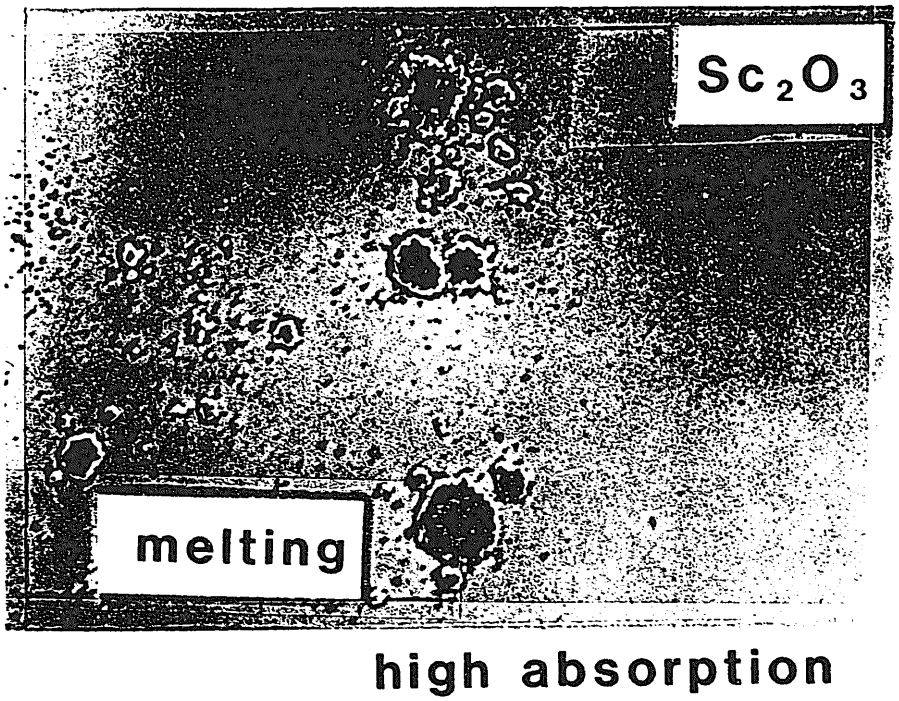

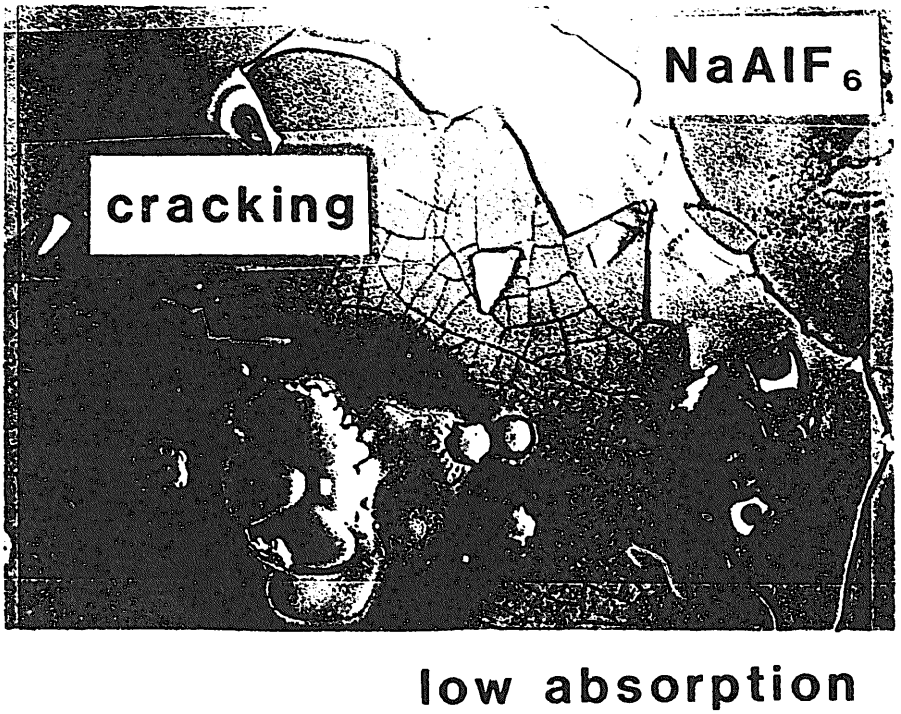

図５－４　レーザー損傷のノマルスキー顕微鏡写真

５．２．１　ノマルスキー顕微鏡法

これまでのレーザー損傷強度の測定法は、ノマルスキー顕微鏡による肉眼観察が中心であった。レーザー損傷の検出感度そのものはＨｅ－Ｎｅレーザーなどのレーザー散乱を用いた方法の法が高いと報告されているものの、米国リバモア研究所、ロチェスター大学、ロスアラモス研究所、ニューポートその他の光学メーカーなどこれまでに訪問した研究所のすべてが顕微鏡法を用いている。これには米国およびヨーロッパで、高耐力ミラーの開発の重要性がレーザー開発の早い段階で認識され、当時に確立できた検出方法で研究所間の相互比較を行うラウンドロビン方式が実施されているという事情が反映している。わが国においても事情は同様で、ほとんどの研究所はノマルスキー顕微鏡でレーザー損傷を検出している。

ノマルスキー顕微鏡法は微分干渉効果を用いるので、通常の顕微鏡では観測困難なわずかな損傷を、色の違いとして検出できる利点を持っている。しかしながら、レーザーのショットごとに顕微鏡下に移動するために、高倍率にして視野を狭くすることはできない。１００倍以下の低倍率の観測では、きわめて初期的な微少損傷を見逃すことがある。同時に、レーザー損傷の検判定は個人差があることも指摘されている。損傷強度を求めるだけでなく、損傷の機構を解明しようとするとき、損傷状態の顕微鏡観察は重要な情報を与えてくれる。たとえば、図５－４に示すように同じレーザー損傷でも、薄膜の性質によって損傷の様子が大きく異なる。このような損傷の差異は顕微鏡で観察すれば一目瞭然である。この意味で、たとえより鋭敏で信頼性の高い損傷検出法が開発されたとしても、顕微鏡法が需要で欠くことのできない研究手段であることに変わりはない。

５．２．２　レーザー散乱測定法

高出力レーザーの集光点にＨｅ－Ｎｅレーザーなどを照射しておき、その散乱光のレベルが変化することを検出してレーザー損傷強度を測定する方法である。実際、論文で報告されている検出感度は顕微鏡法よりかなり高い。しかし、レーザー損傷の種類によっては必ずしも高くない場合もある。特にクラックや欠損が生じないような内部的破壊の場合には、むしろ顕微鏡法の法が感度が高いこともあるので注意しなければならない。経験からすると、実験環境の影響を受け易いので、感度は高

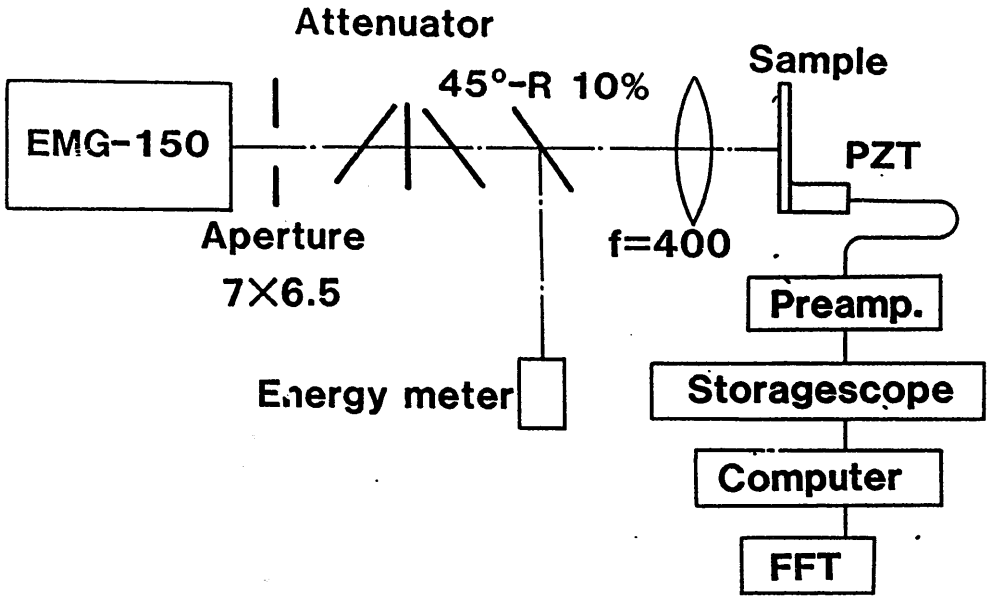

図５－５　光音響法による吸収測定、レーザー損傷検出の実験配置

いものの信頼性が高いとはいえない。

５．２．３　光音響法

光音響法はレーザー損傷が生じる際に発生する超音波を機械／電気変換器ＰＺＴ（Piezo-Electric Transducer）で検出する方法である。機械的破壊の場合に大きな超音波が発生することは自然な現象で、それを用いた損傷の検出は原理的に優れた点を持っている。それらの利点は

①　検出感度が高い。

②　損傷以外の原因による信号を容易に区別できる。

ということに集約される。代表的なレーザー損傷では光学素子の微少な部分が破壊され、飛び出すことがふつうである。この様な場合には、吸収とは比較にならない大きな衝撃力を光学素子に与えるから、破壊現象を検出することはきわめて容易で個人差が生じない。

光音響法が高感度であることは、光学薄膜内の微少吸収を直接計測することができることからも明らかである。光音響法による吸収およびレーザー損傷強度の測定に用いられた装置の構成を図５－５に示す。各種薄膜材料の吸収係数（屈折率の虚数部、消衰係数ともいう）を測定した結果を図にしたものが図５－６である。光学

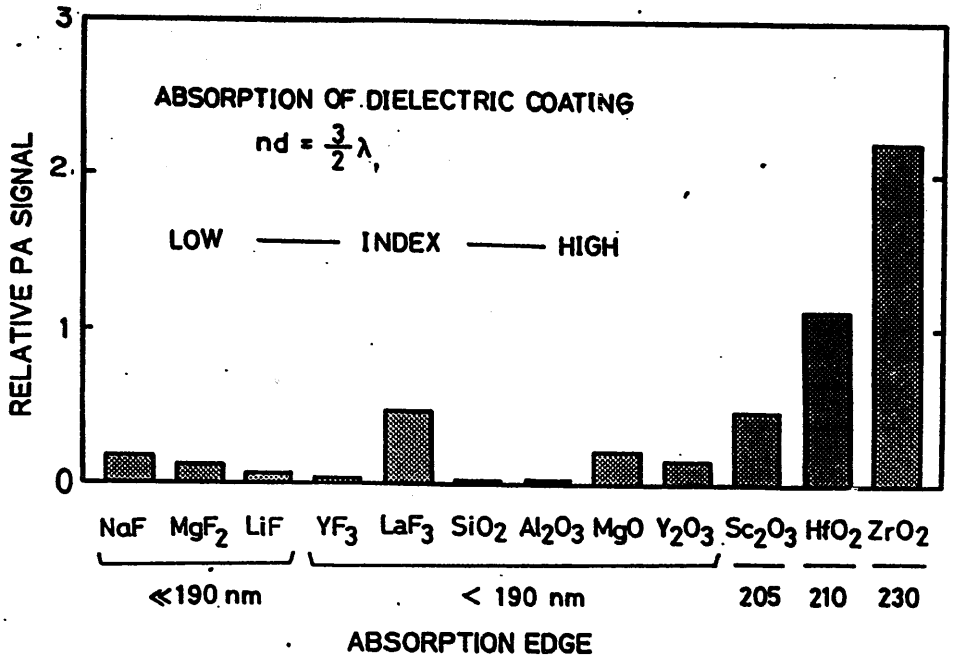

図５－６　光学薄膜の屈折率と吸収係数

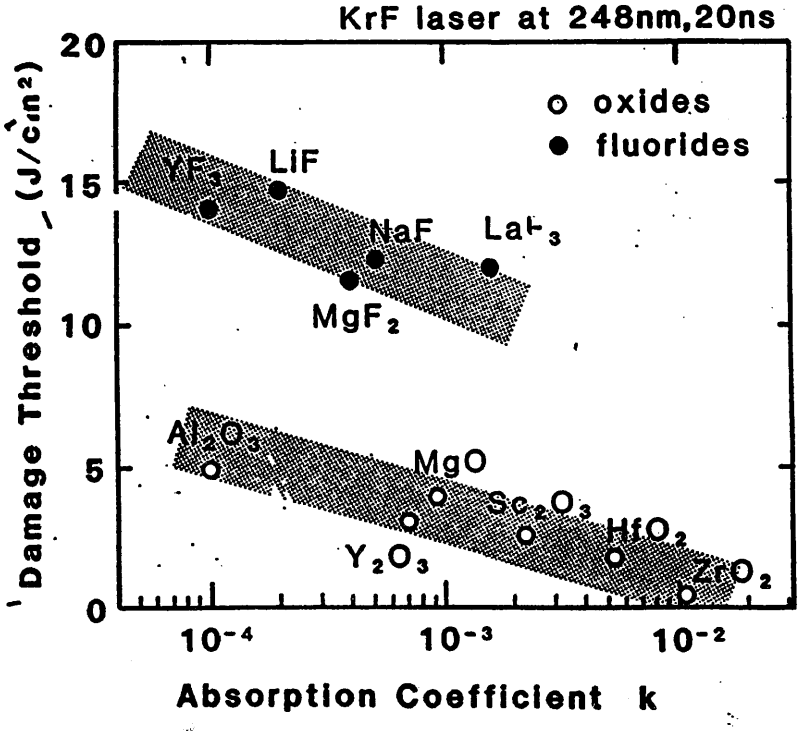

図５－７　光学薄膜の吸収係数とレーザー損傷強度の相関

厚さが１．５λの光学薄膜の吸収係数が10^{-4}のオーダーまで測定することができた。

レーザー損傷が発生すると、吸収で発生していた光音響信号の数１０倍の大きな信号が検出されるので、間違うことはない。単層膜の光学損傷しきい値と吸収係数の関係をグラフにすると図５－７のようになる。同じ吸収係数を持つものでも酸化物薄膜とフッ化物薄膜では損傷機構が異なることが、両者の相関からはっきりと理解される。

５．３　光学素子の均質性

以上述べてきたような測定法はすべてレーザーを集光して損傷を発生させる局所的光学特性の測定である。しかし、実際のレーザー動作条件ではレーザービームは光学素子の全面を照射し、レーザー損傷ではもっとも弱い部分が破壊される。平均値で損傷強度が決定されるわけではない。本来からいえば光学素子全面を照射した損傷強度測定が理想的であるが、そのためには巨大なレーザーが必要になり現実的ではない。光学素子の均質性について、従来は測定することなく信じていたが、実際に測定した結果は、検査する必要があることを証明した。以下に、均質性の悪い反射鏡を検査で選び出した例を示そう。

５．３．１　反射率均一性の測定

レーザーミラーの反射率は通常蒸着装置に挿入されたテストピースの反射率を測定して行われる。今回我々は１ロットの全反射鏡のすべてについて、反射率分布を測定した。実験装置は図５－８に示した構成である。レーザーを拡大して試料用反射鏡の全面を照射し、その反射像をＣＣＤカメラで撮影した。映像情報はイメージ・プロセッサーを通して計算機で処理される。反射鏡の反射率分布の一様性、不均一性の程度とそのパターンは解析され、ワイヤーメッシュ、等高線表示、カラーコード、などで表示される。また、反射率のヒストグラムから光学素子としての均質性を定量的に示すことができる。

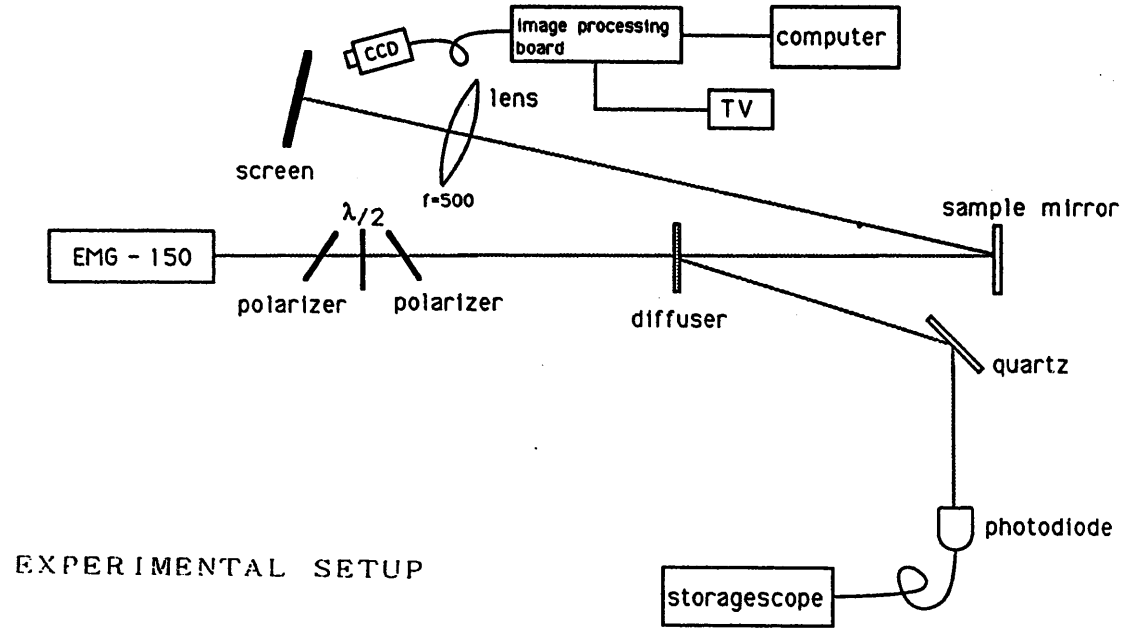

図５－８　２次元反射率分布の測定

実験結果を図５－９、図５－１０に示した。おのおの（ａ）はワイヤーメッシュ表示、（ｂ）は等高線表示、（ｃ）は反射率のヒストグラムである。本来均質だと思われていた反射鏡の中に、少数ではあるが図５－１０のように大きな反射率分布をもつものが存在することが明確に示された。

５．３．２．　波長掃引２次元反射計測法

上述の実験結果をふまえて、新しい光学素子の特性計測法を開発中である。本年度はその基礎的部分の検討を行ったので、今後実際に開発、応用を行う予定である。ここではその原理と構成を示しておこう。

誘電体多層膜の反射特性は図５－１１に示すとおり、層数が増えるにしたがって高反射率を示す領域が拡大してゆく。同時に干渉に関係する境界面が増えるにつれて反射域のエッジは急峻になっていく性質がある。中心波長は膜生成の影響や光照射による変質の影響を受けにくいが、反射率が急峻に変化する波長は、膜厚精度や膜の性質に非常に敏感に影響される。空気中に長時間放置しておくだけで、空気中の水分の影響で反射スペクトルがわずかにシフトするほどである。レーザー波長ではなく、光学的性質がもっとも急峻に変化している波長で、光学素子の均一性、レ

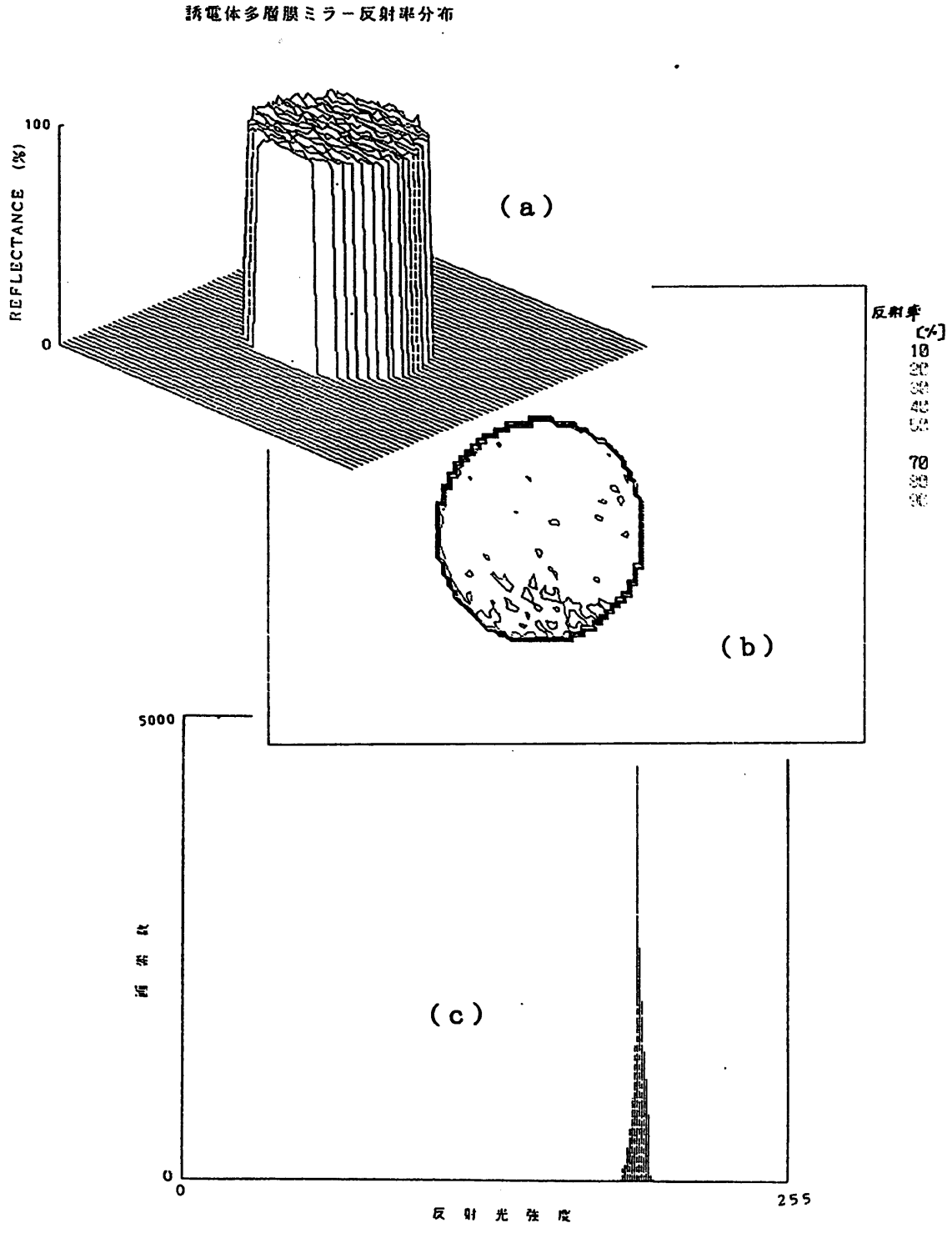

図５－９　反射率分布（均一分布反射鏡）

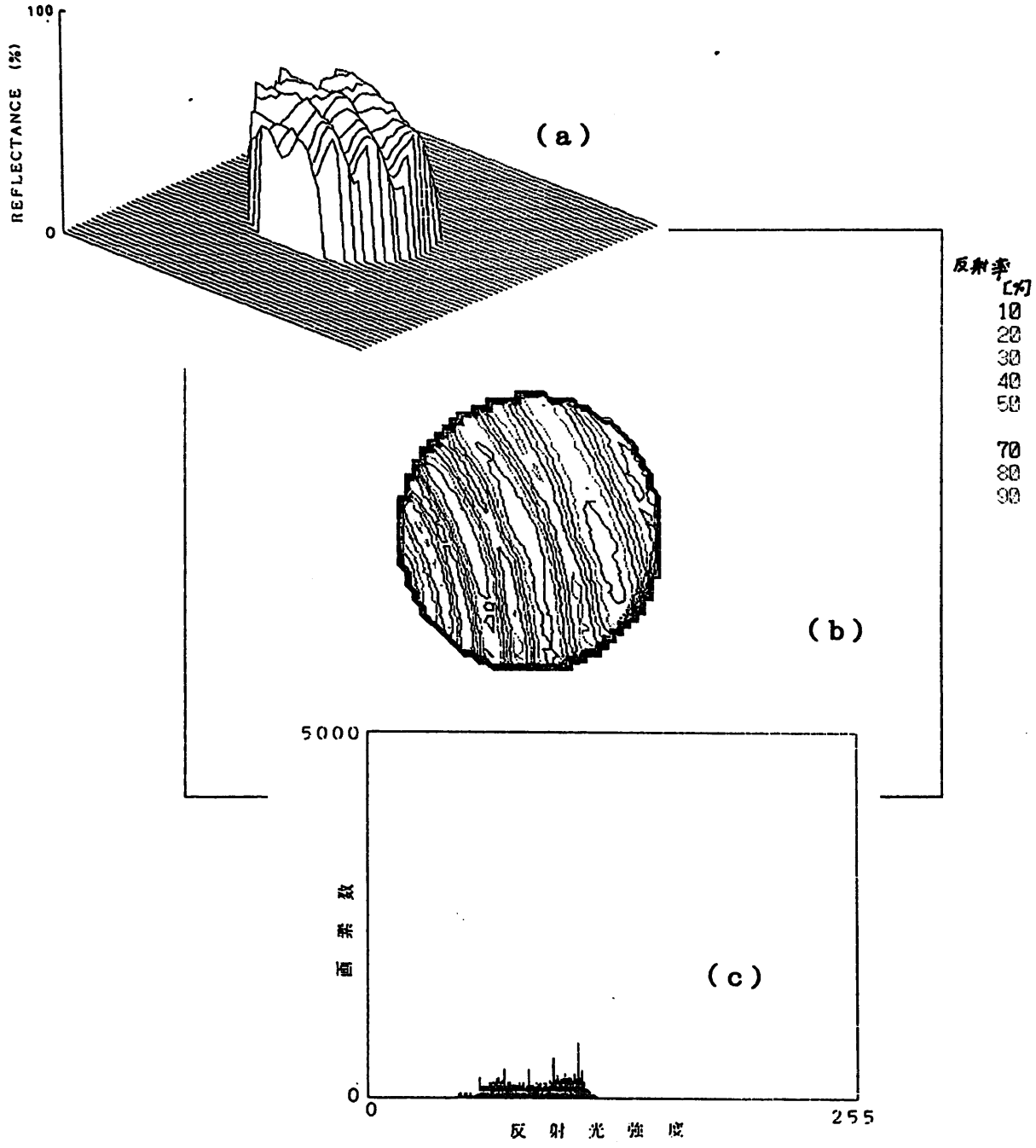

図５－１０　反射率分布（不均一分布鏡）

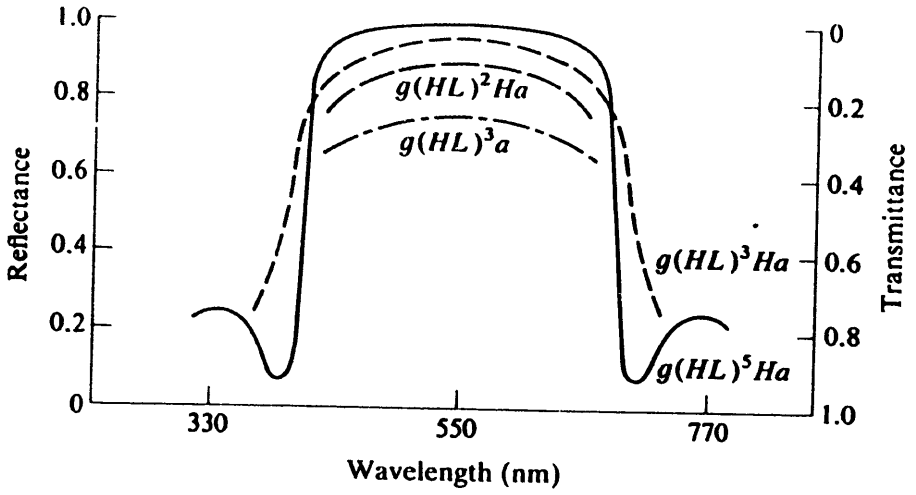

図５－１１　誘電体多層膜の反射スペクトル特性

ーザー損傷の影響を測定することは、新しい鋭敏な計測法となると期待できる。

実際に開発中の装置は図５－１２に示すように、分光器で波長を掃引した光で試料を照射して、その反射像をＣＣＤカメラで計測するシステムである。微弱な光を拡大するので、マイクロチャンネル・プレートを使用する必要があるだろう。しかし、このシステムでは、反射率分布の一様性のみならず、誘電体多層膜の均一性に関する精密な２次元分布が測定できる予定である。予備実験とはことなりタングステンランプや重水素ランプなど連続光源を用いるので、測定精度が向上する。これらの波長掃引２次元反射分布像はイメージプロセッサを通じて、ビデオレコーダに記録される構成になっている。

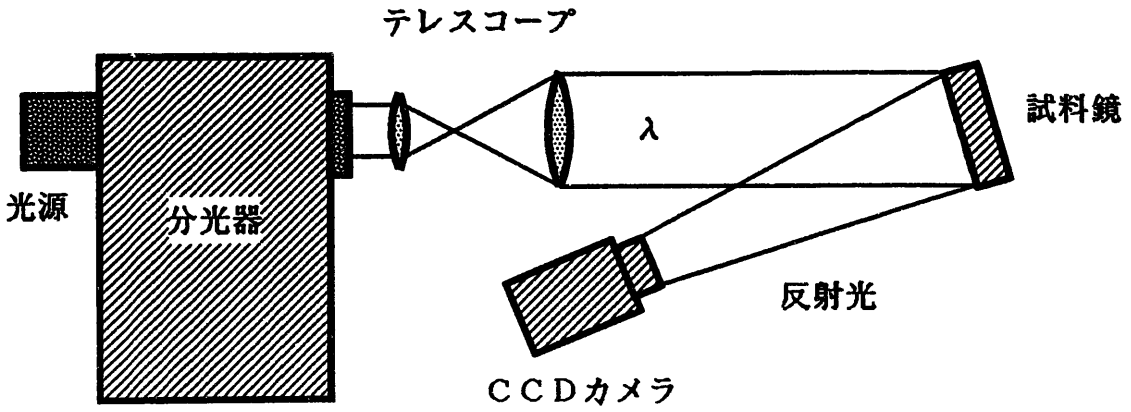

図５－１２　波長掃引２次元反射率測定装置

５．４　色中心の形成と多光子吸収

５．４．１　雑音高の発生と色中心の形成

高出力のレーザーパルスを長時間照射し続けると、光学材料の内部の構造不整が原因になっていろ中心が生まれることが知られている。図5－１３に示したのは、合成石英の窓材にＫｒＦレーザーを照射した場合に発生する色中心の発光スペクトルである。５８５ｎｍに観測される赤色の蛍光ははじめから観測されることはない。高出力短パルスのレーザー光を照射すると、照射スポットから赤い発光が次第に強くなってくるのである。この様な色中心の発生は、繰り返し周波数の高いピコ秒レーザーである自由電子レーザーで大きな問題となる可能性がある。すなわち、一旦形成された色中心は吸収係数を増大させる役割をし、高反射率ミラーを短時間に劣化させると考えられるからである。

自由電子レーザーに特有の問題として、ウィグラーにおける高調波の発生と短波長の制動輻射光による光学損傷がある。高い利得を得るためには、電子の蛇行の程度が多くなる必要がある。一方、大きな蛇行運動をした場合、電子ビームに垂直な面内における電子の運動は完全な正弦波的運動からずれて、高調波が発生することが避けられない。ｎ次高調波の波長は基本波の１／ｎであるので、短波長に強い雑音光が発生することになる。また、レーザーのようにコヒーレントな性質を持たな

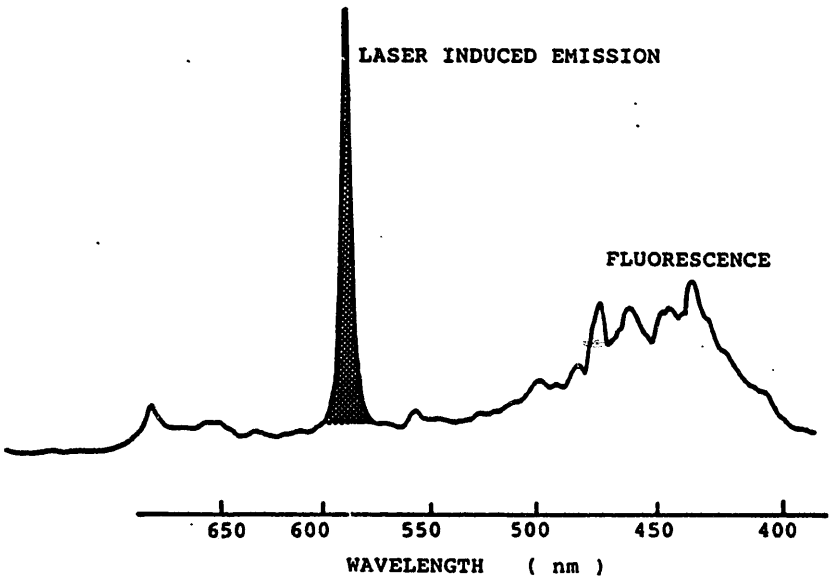

図５－１３　紫外線レーザー照射で形成された色中心の発光スペクトル

い自然放出光が、偏向させられた電子から放出される。制動輻射に起因する自然放出光は幅広いスペクトルを持つ。高エネルギー電子加速器を用いる自由電子レーザーでは制動輻射光は真空紫外から軟X線におよぶ。この様な制動輻射光、高調波成分はたとえその強度は低くても、①反射鏡に完全吸収される可能性があり、②波長が短いので、光学素子の損傷、色中心の形成に決定的重要性を持つ。ウィグラー設計で、どの程度高調波発生を抑制できるか、また自然放出光を制御できるかは、自由電子レーザーの研究の指名を製する重要課題であろう。同時に自由電子レーザー用光学素子の開発では、レーザー発振波長のみならず、広範囲な短波長領域に対して超高反射率を持った光学素子が必要になることが明らかである。この点からして、本報告で強調した斜入射光学素子の開発に力を傾注しなければならない。

５．４．２　多光子吸収の測定

ピコ秒レーザーの場合、色中心の形成には多光子吸収が大きな役割を果たすと考えられている。光学材料の多光子吸収の正確な測定はかなり困難な問題で、研究者間で激しい論争が行われる場合も多い。多光子吸収の観測には数１０ＧＷ以上の高強度レーザー光が必要である一方、この様に高い光強度では自己収束など別の種類の非線形現象が発生する危険があるからである。しかも、図５－１４に示した実測データを見れば分かるとおり、わずかな吸収量から多光子吸収の成分を分離計測するのは困難で、高精度の測定とはなり得ない。この様な危険を避けるには、もっと低い光強度で測定が可能で、しかも吸収量のみを測定できる方法が望ましい。

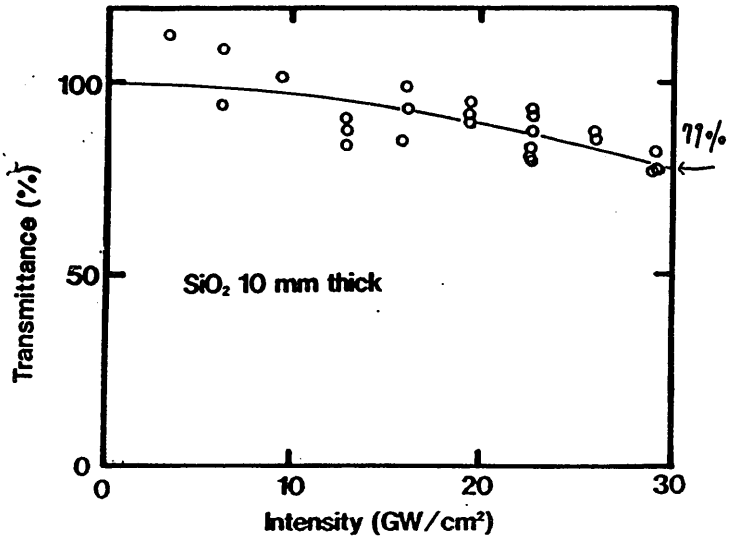

図５－１４　合成石英による非線形吸収透過率

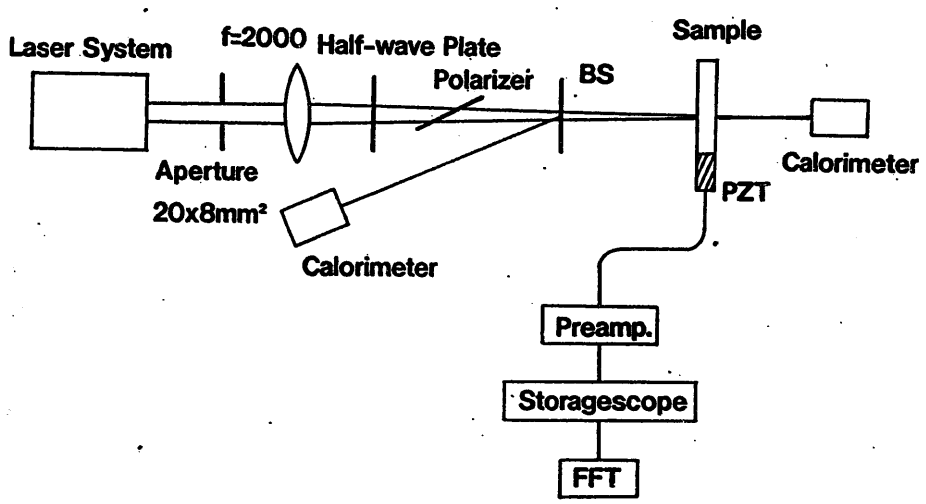

図５－１５　光音響法による多光子吸収の測定

光音響法は光学薄膜の吸収測定で、他の方法よりもはるかに高感度で、且つ吸収エネルギーに比例していることを確かめた。そこで光学材料のピコ秒パルスに対する吸収を測定するのに応用した。ピコ秒パルスでは吸収エネルギーそのものが微少なので、従来法では測定困難である。実験配置は図５－１５である。長焦点レンズでピコ秒レーザーのパルスを集光し、集光点にサンプルをおいて光音響信号を観測した。用いたパルス幅は１ｐｓである。合成石英、CaF_2，MgF_2について測定した結果を図５－１６から図５－１８に示した。照射レーザー強度に対して、光音響信号が何次の非線形性を示すかによって２光子過程か、または３光子過程かを判定することができる。この実験結果が証明するのは、合成石英は１GW／cm^2以上ではすでに２光子吸収が支配的であり、CaF_2は１０GW／cm^2を越えた段階で線形吸収から２光子吸収に移行するということである。また、MgF_2の場合はバンドギャップエネルギーが大きいので，１００GW／cm^2で非線形吸収が大きくなるが、傾きからすると３光子吸収過程である。この様に光音響法は光学材料の非線形吸収を測定する上でも、高感度であった。

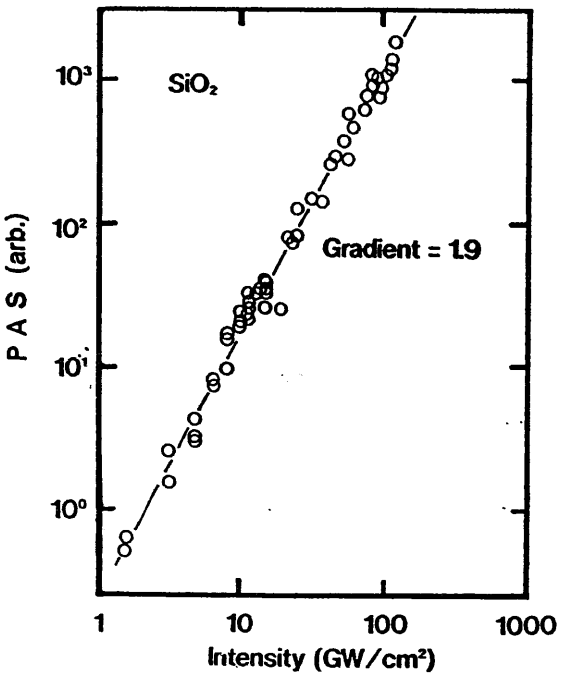

図５－１６　合成石英の吸収特性

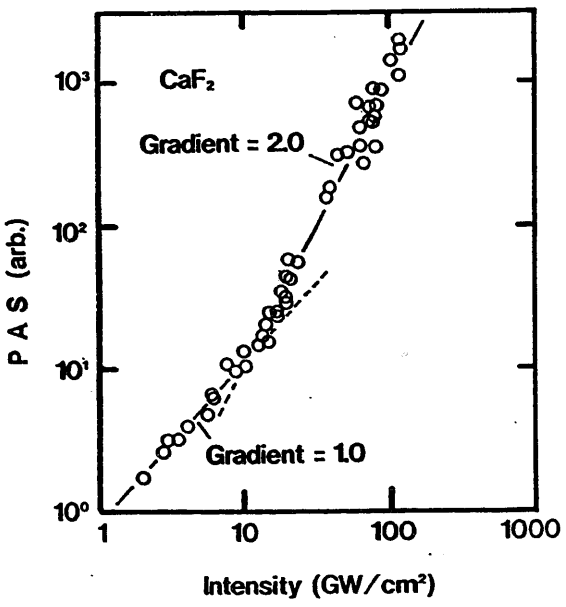

図５－１７　ＣａＦ₂の吸収特性

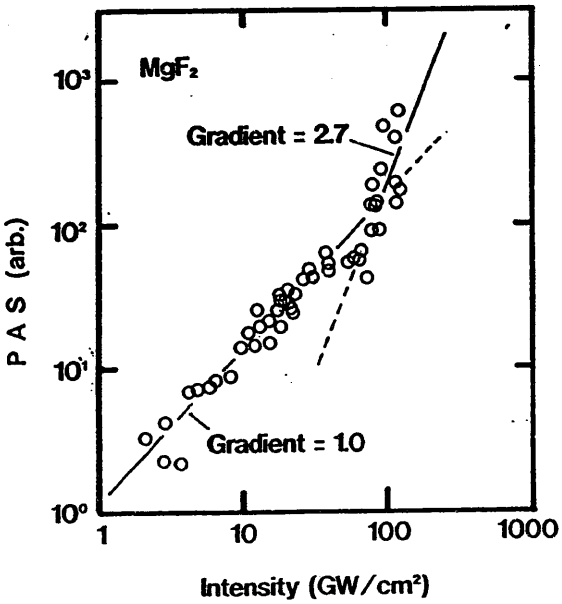

図５－１８　ＭｇＦ₂の吸収特性

６．　ピコ秒レーザーパルスの発生

自由電子レーザー用の光学素子の特性を評価するためには、自由電子レーザーと同等の性質のレーザー出力を発生する光源を開発しなければならない。レーザー用反射鏡の損失を最終的に決定する要素は薄膜吸収、表面散乱である。これらの要素はレーザーの発振波長が短くなればなるほど大きくなる波長特性を持っている。したがって、機動性に富む小型の可視光から紫外線領域のピコ秒パルス発生レーザーは、自由電子レーザーが実用化された場合でも、光学素子の試験、開発用に重要な役割を果たすであろう。同時に、このようなレーザーは自由電子レーザーに注入するための高品質の種レーザーとしても有用になる。今回、図６－１に示すような超短パルス発生レーザーシステムを開発した。

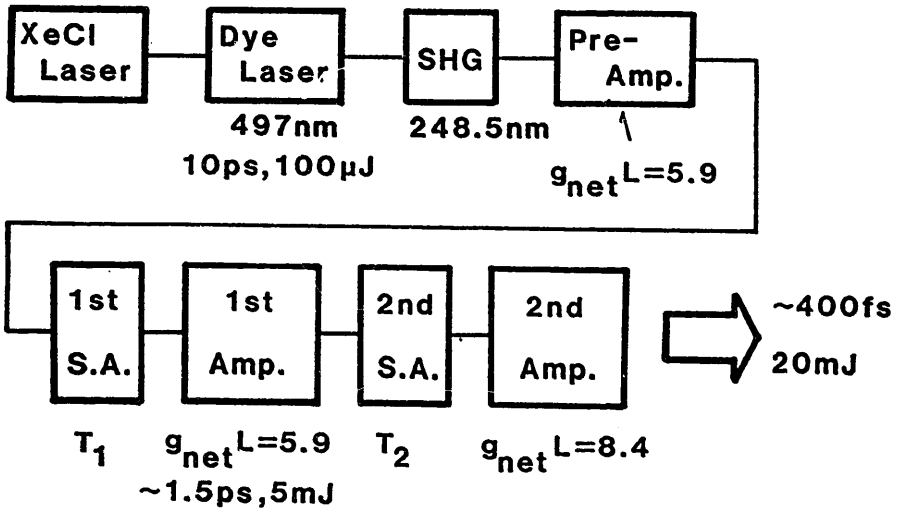

図６－１　超短パルス発生レーザーシステム

６．１　ピコ秒色素レーザー発振／増幅システム

電通大新形レーザー研究センターで開発中の超短パルス色素レーザーは、実験室において自由電子レーザーの実験的シミュレーションを行うのに最適である。外観と色素レーザーの発振／増幅部の写真を図６－２、図６－３に示した。

同装置の特性を表６．１にまとめる。

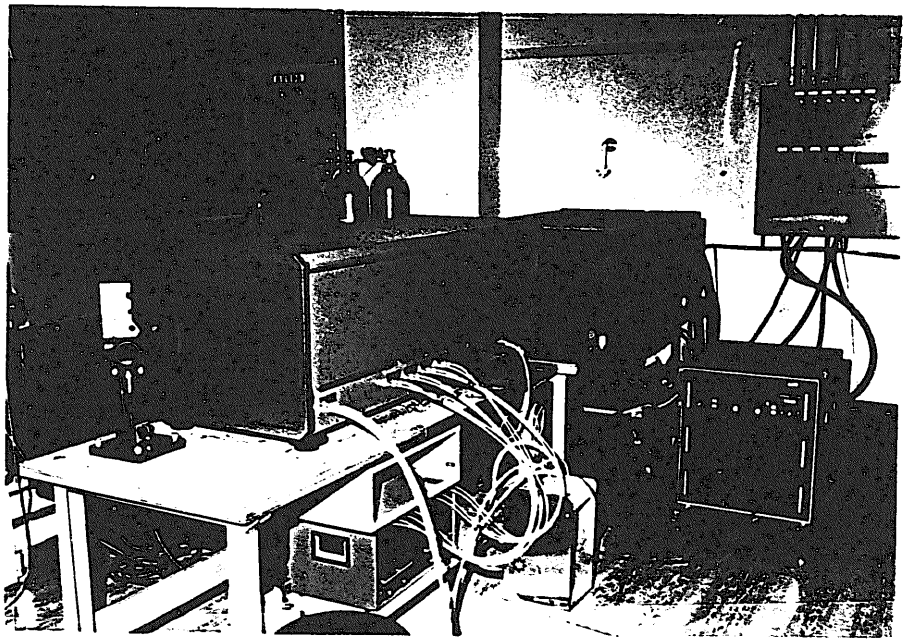

図６－２　ピコ秒発生色素レーザーの外観

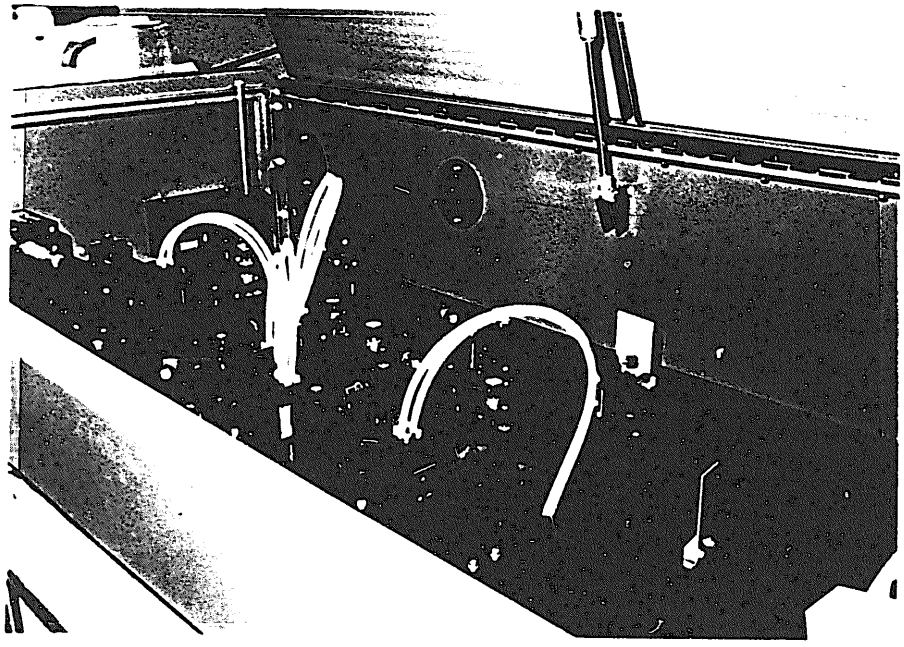

図６－３　色素レーザーの発振／増幅部

表６．１　ピコ秒発生色素レーザーの構成と特性

エキシマレーザー励起色素レーザー

短パルス発振器　；　過渡消光型短共振器発振器

QTDL(Quenched Transient Dye Laser)

励起方式　；　ＸｅＣｌ励起ＰＴＰ色素レーザー

増幅システム　；　ＸｅＣｌレーザー励起３段増幅システム

出力特性	改良前	改良後
出力パルス幅	５０ｐｓ	１０ｐｓ
パルスエネルギー	３００μＪ	１００μＪ
出力パワー	６ＭＷ	１０ＭＷ
レーザー発振波長	４９７ｎｍ	同左
波長可変範囲	＜１０ｎｍ	同左
背景雑音	＜１０％	＜０．１％
繰り返し	２５Ｈｚ	同左
高調波発生	なし	ＢＢＯにて可能
高調波波長	なし	２４８．５ｎｍ
紫外用増幅器	なし	放電型ＫｒＦレーザー
紫外出力パルス幅	なし	４００ｆｓ
紫外レーザー出力	なし	２０ｍＪ
ピーク出力	なし	５０ＧＷ

開発した超短パルス可視／紫外レーザーシステムの原型は、ラムダフィジックス社のＦＬ４０００である。構成は図６－４のとおりである。色素レーザーの励起には発振波長３０８ｎｍのＸｅＣｌレーザーを用いた。超短パルスレーザーの発振のために、非常に短寿命の短波長色素レーザー（ＰＴＬレーザー）を発振させ、クマリン３０７をレーザー色素とする発振器を励起した。サブナノ秒の立ち上がり時間をもつＰＴＬレーザーは、低い反射率からなる短共振器と、高い反射率の長共振器

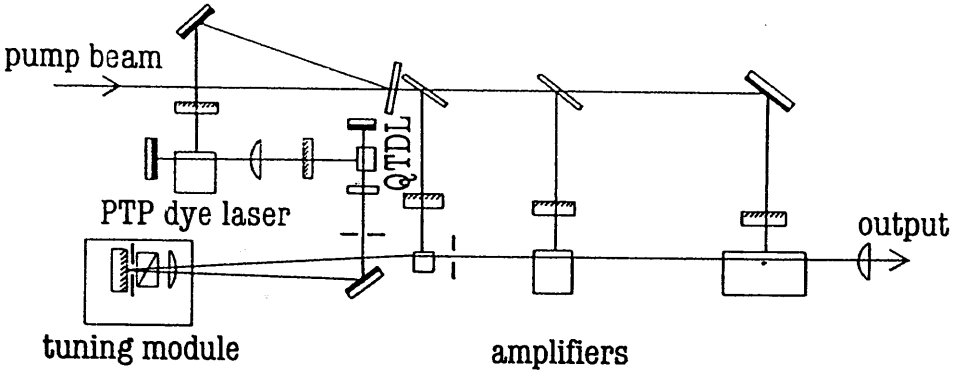

図６－４　ＦＬ－４０００の構成

で構成された軸外し２重共振器の色素レーザー発振器を光励起する。励起された色素レーザー発振器では、非常に強い励起が行われるので短時間で発振が立ち上がる。当初は共振器の往復時間が短く、高い増幅利得を有効に利用できる短共振器で発振が立ち上がり、その後低損失の長共振器内の光子密度が高まるにつれて、短共振器

の発振は停止する。このようにして、簡単な構成から広帯域のピコ秒パルスを発生させるものである。広帯域発振をしたレーザー出力から、外部の小型の分光器（Tuning Module）によって波長を選択し、３段の色素レーザー増幅器で増幅する。

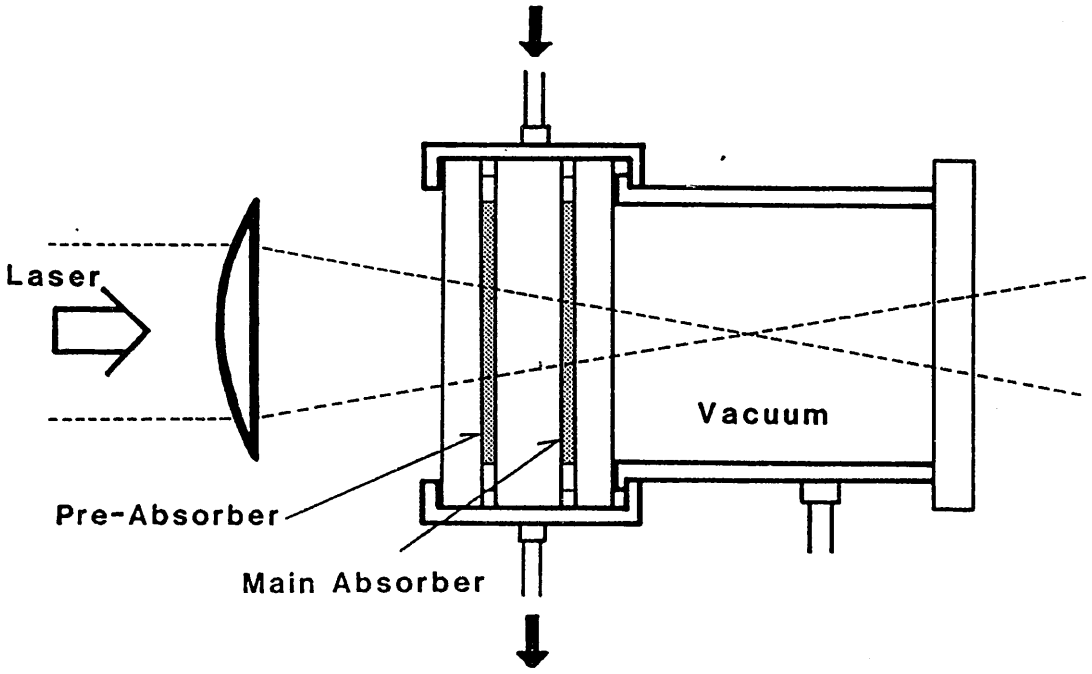

図６－５　超短パルス発生用２段階可飽和吸収セル

６．２　フーリエ限界ピコ秒パルスの発生
－　２段階可飽和吸収法　－

ＦＬ４０００のシステムは非常にシンプルなので、複雑な装置を組み合わせる必要がない利点があるが、同時に安定な動作をさせることが非常にむずかしい。実際、わが国で購入した研究施設においても、元来の装置性能を発揮させることがほとんどできなかった。レーザー動作の不安定の原因は、最初のレーザー発振そのものが、急速励起で短パルスを発生させる機構なので、雑音効果らの立ち上がりにおけるモードの選択性が不十分なことに起因している。電通大レーザー研では、紫外線の超短パルス発生のために有効な可飽和色素を世界ではじめて開発し、その特性を詳しく測定、解析を行ってきた。その結果、超短パルスレーザー発振／増幅システムを安定に動作せる方式として、集光強度の大きく異なる２種類の可飽和吸収セルを直列に結合させた図６－５のような２段可飽和吸収システムを開発した。このシステムでは可飽和吸収セルの役割を、パルスの前端部を除去する前置吸収セルと、パルスの整形、短縮を行う主吸収セルの２つの部分に分離し、各々の条件を最適化することで、超短パルス発生を安定化することに成功した。原理的な説明は図６－６を参考にされたい。

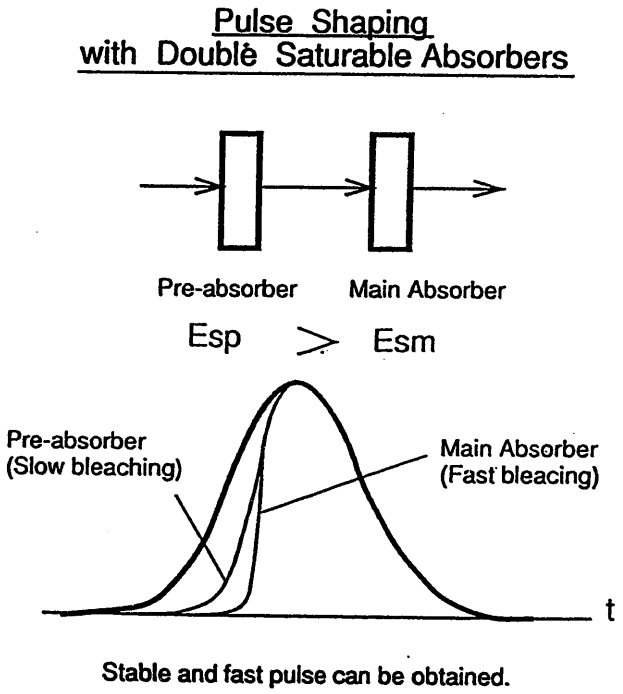

図６－６　２段階可飽和色素の原理

その成果をピコ秒色素レーザーに応用して、フーリエ限界パルスを安定に発生させること試みた。色素レーザー用の可飽和吸収体としては、ショット社製のＯＧ－５３０色ガラスフィルターを用いた。図６－７に与えられたＯＧ－５３０の吸収特性とレーザー用色素の蛍光スペクトルから分かるように、５００ｎｍの近傍で用いるのが適当である。図６－８のように２段階可飽和吸収フィルターを挿入し、熱的

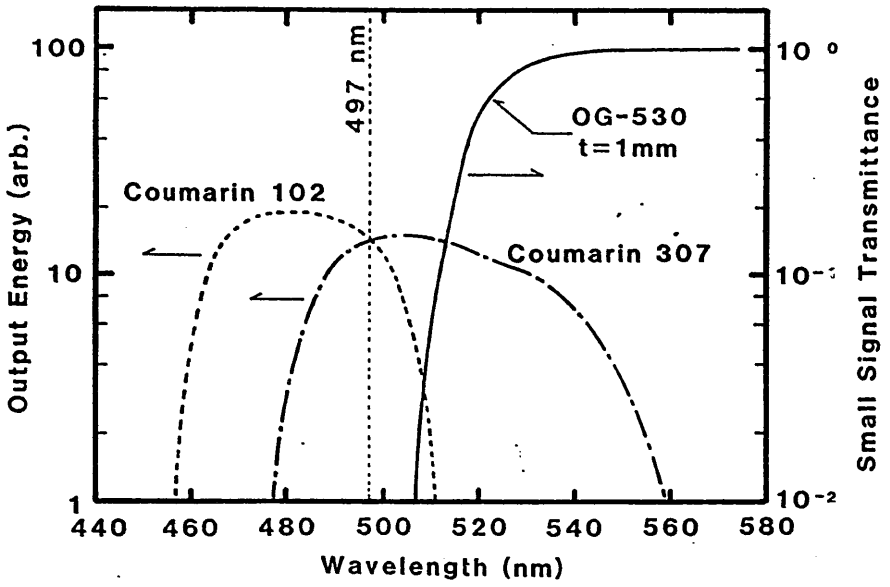

図６－７　ＯＧ－５３０の吸収スペクトル

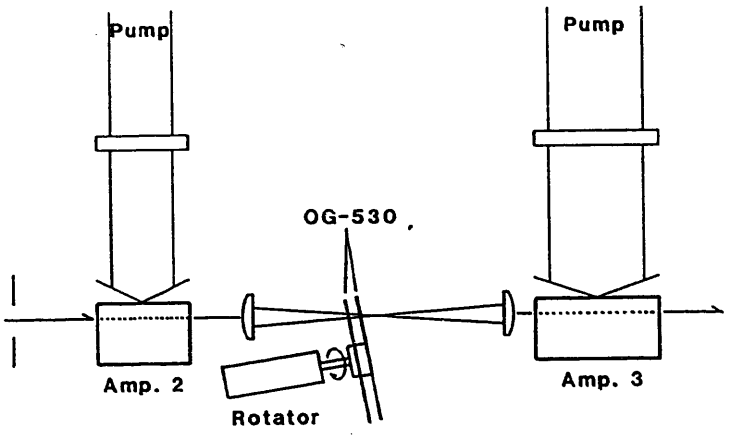

図６－８

２段階可飽和フィルターの配置

図６－９

パルス幅とスペクトルの

同時計測

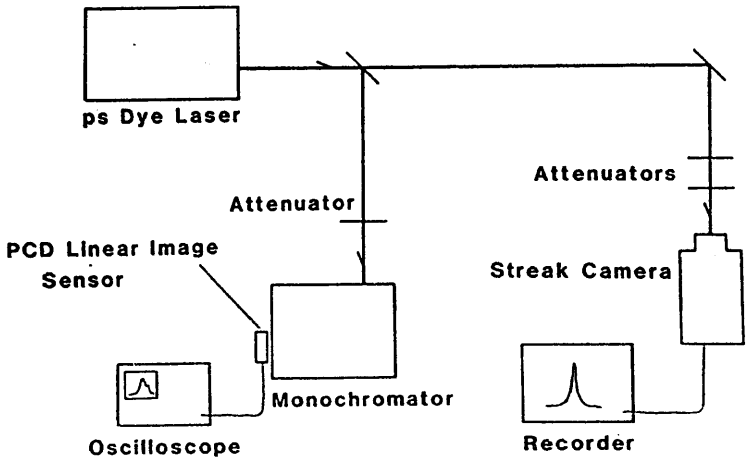

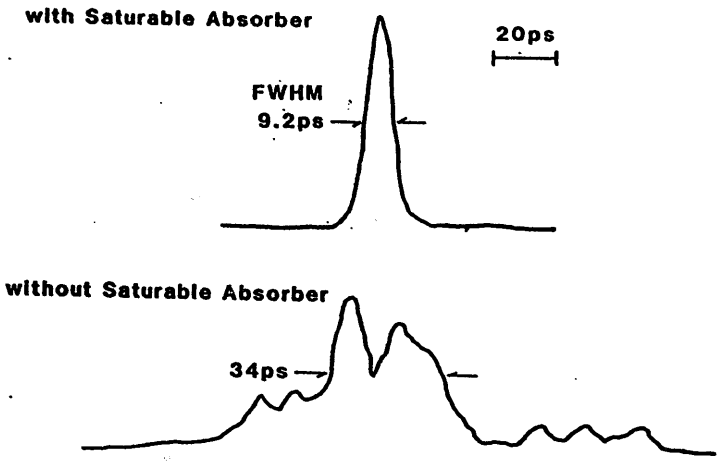

図６－１０　ピコ秒色素レーザーの発振波形

破壊を避けるためにフィルターを回転しながら実験を行った。

図６－９の実験配置を用い、高速ストリークカメラ（浜松ホトニクスＣ９７９）でピコ秒パルスのパルス幅の計測を行った。パルス幅とスペクトル幅を同時に計測することで、フーリエ限界パルスにどの程度近いか判定できる。実際のパルス波形を例示しよう。図６－１０はこの様な改良を加える前後のパルス波形の変化を示している。５０ｐｓのパルス幅仕様を持っているＦＬ－４０００では、調整を精密にしてパルス幅を４０ｐｓ以下にしたとしても、図６－１０のようにパルスの内部に細かい構造を持ち、再現性にも乏しい。一方、２段可飽和吸収システムを導入した結果、パルス幅は１０ｐｓ以下に短縮されたのみならず、パルス波形が非常にスムーズになったことに注目しなければならない。同時に計測された発振スペクトル幅とパルス幅の積をとると、

$$\Delta\nu\Delta t \approx 0.5$$

となる。ガウス型パルスのフーリエ限界パルス条件は

$$\Delta\nu\Delta t \approx 0.44$$

であるから、ほぼフーリエ変換の限界パルスを発生させることに成功している。

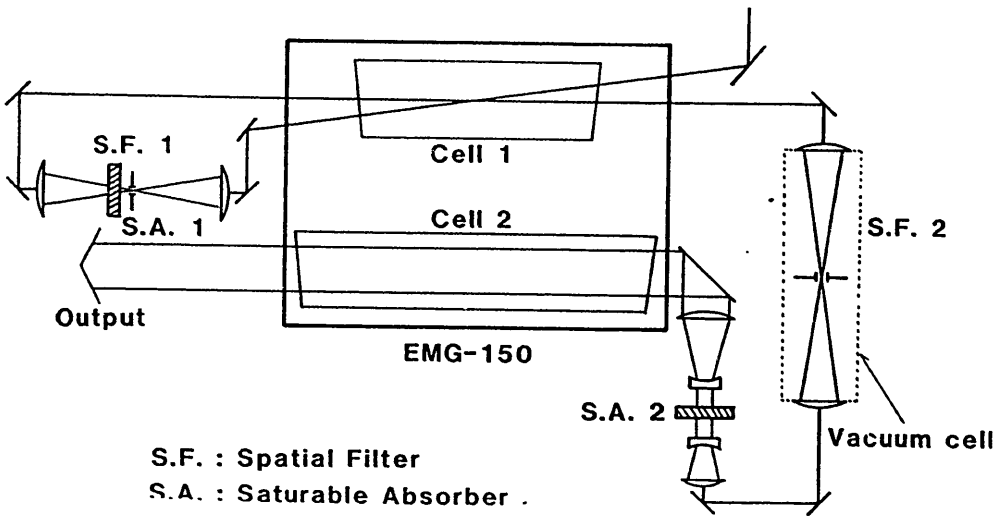

図６－１１　超短パルスエキシマ増幅器／パルス圧縮器

６．３　紫外線ピコ秒／サブピコ秒発生レーザーシステム

ピコ秒色素レーザーの出力パルスの第２高調波をエキシマレーザーで増幅する方式で、ピコ秒／サブピコ秒の紫外線レーザーパルスを発生させることに成功した。将来、自由電子レーザーの波長が短くなり、紫外線を発生するようになった場合の、等価実験システムとして有用である。前述のシステムに図６－１１の増幅システムを付加し、各段間の可飽和吸収色素アクリジンの濃度を調整することで、出力パルスのパルス幅を変えることができる。図６－１２は結果の１例である。結果を表６－２に示したように、本超短パルス発生色素／エキシマレーザーシステムは

① 色素レーザーとして、１０ｐｓ、１０ＭＷの０．５μｍパルスを発生する。

② 第２高調波をエキシマレーザーで増幅することで

４００ｆｓ、５０ＧＷの紫外線（０．２５μｍ）パルスを発生する。

③ 繰り返し周波数は２０Ｈｚである。

小型のテーブルトップ装置で、以上のような性能を出すことができた。自由電子レーザー用光学素子の開発、計測に十分有用な装置であると結論することができる。

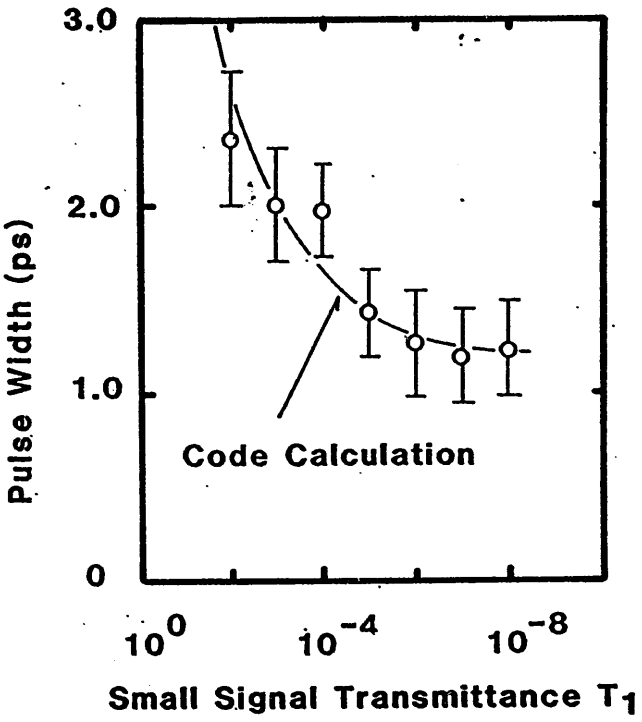

図６－１２　可飽和色素の濃度とパルス幅の関係

表６－２　超短パルス色素レーザー／エキシマレーザーシステムの特性

Position	Pulse Width	Energy	Peak Power
Dye Laser Output (497nm)	10 ps	100 μJ	10 MW
after SHG (248.5nm)	(10ps)	~3 μJ	~300 kW
1st Amp. Output	~1.5 ps	5 mJ	~3.3 GW
2nd Amp. Output	400 fs	20 mJ (ASE <0.1%)	50 GW

7．光学素子技術の動向調査報告

本章では海外の光学技術について行った調査研究の報告書を2編まとめる。海外出張の報告書をそのまま掲載するので、若干形式がずれるが、出張直後の報告書がもっとも適当であるので、あえてそのままの形で掲載する。

出張報告書の内訳は以下の通りである。

1）タイトル　「自由電子レーザー調査報告」

内容	シカゴ	高エネルギー粒子加速器国際会議
	ケンブリッジ	Science Research Laboratory
	ニューヨーク	Quantronix Co.
	サンフランシスコ	Stanford Univ. High Energy Lab.

2）タイトル　「海外出張報告」

内容	ロサンゼルス	SPIE OE/LASE'90
		Newport Inc.
		Rocketdyne/Rockwell International
	ロチェスター	KODAK/Federal System Division

7．1　自由電子レーザー調査報告

自由電子レーザー調査報告

電通大新形レーザー研究センター
植田憲一

日程　　１９８９年3月２０日－３０日
訪問先　アメリカ合衆国
　　シカゴ　　粒子加速器国際会議
　　ケンブリッジ　　Ｓｃｉｅｎｃｅ　Ｒｅｓｅａｒｃｈ　Ｌａｂ.
　　ニューヨーク　　Ｑｕａｎｔｒｏｎｉｘ　Ｃｏ.
　　サンフランシスコ　　スタンフォード大学高エネルギー物理研究室

自由電子レーザー調査報告

電通大新形レーザー研究センター
植田憲一

日程　１９８９年３月２０日－３０日

訪問先　アメリカ合衆国

シカゴ　粒子加速器国際会議

ケンブリッジ　Ｓｃｉｅｎｃｅ　Ｒｅｓｅａｒｃｈ　Ｌａｂ.

ニューヨーク　Ｑｕａｎｔｒｏｎｉｘ　Ｃｏ.

サンフランシスコ　スタンフォード大学高エネルギー物理研究室

１．概要

米国における自由電子レーザーの研究状況とその応用について上記訪問先と、その他研究者との意見交換を通じて調査を行った。全体を簡単にまとめると

※稼働中または稼働を開始しようとしているＦＥＬは順調である。

※ＦＥＬの潜在能力を基礎に応用が検討されている。このため、応用研究の具体性に難が　ある。

※光電子型陰極の最新データが良好な結果を与えた。

２．粒子加速器国際会議（シカゴ・ハイアット・ホテル）　３月２０日－２３日

大型加速器の計画は、計画の概要のみでデータがなく面白くない。自然の秘密を探るという高邁な目的のためか、技術的話題のみにもかかわらず、基礎学問的雰囲気を失っていない。一方、現実的には米国、欧州共同体の蓄積リングの応用として、Ｘ線リソグラフィーなどを強調しなければならない状況も見られた。同時に、日本の研究発表の比重と評価が以外に低い感じがしたのが予想外の印象であった。

ＦＥＬ研究の現状

２－１　ＫＡ１　ＬＬＮＬ　ＥＴＡ－Ⅱ　（Ａ．Ｌ．Ｔｈｒｏｏｐ）

２５０ＧＨｚＦＥＬ　＞１２ＧＷ（９７％ＴＥＭ$_{01}$）　１０ＭｅＶ，３ｋＡ

引出し効率　４４％　トラッピング効率　７０％　バーストモード５００Ｈｚ

Ｂｒｉｇｈｔｎｅｓｓ　４．０－２．０ｘ１０^{9}Ａ（ｍｒ）^{2}

磁気圧縮　４μｓ　→　７０ｎｓ

ウイグラー　３．７５ｃｍ／５．５ｍ／４．７ｋＧ／可変範囲３７％

フルーエンス　０．０７Ｊ／ｃｍ^{2}（損傷強度の１／１０）

３．８ＧＷ出力（６．６ｋＪ／バースト）

２－２　ＫＡ２　Ｂｏｅｉｎｇ　可視域ＦＥＬ（Ｄ．Ｓｃｈｏｆｆｓｔａｌｌ）

共振器長　２００ｆｔ　ウィグラー　４０ｆｔ　ソレノイド　Ｂ＝２．５ｋＧ

出力　１４ＭＷ（パルス出力）／４ＭＨｚ／０．７ｋＷ（平均出力）８９年２月１日

ＦＥＬ特性

マクロパルス	９０μｓ	波長	６６２ｎｍ
共振器内パワー	１．２ＧＷ	スペクトル幅	７ｎｍ
１パス利得	２０－３０％	エネルギー	１０８．９ＭｅＶ
小信号利得	１００％　（不安定性に依存）		
パワー効率	０．２３％		

２－３　ＫＡ３　マイクロトロン（ＮＩＳＴ／ＮＲＬ）（Ｐ．Ｄｅｂｅｎｈａｍ）

５ＭｅＶ　ｉｎｊｅｃｔｏｒ　／　１７－１８５ＭｅＶ　出力

１００ｋＷ出力予定　サイズ　５ｘ６ｍでコンパクト

ウィグラーはＭａｘｗｅｌｌ　Ｌａｂ．　１９９１年完成予定

医用応用ＦＥＬと称しているが、具体的にどの様に応用するかは知らないとのこと。

２－４　その他

その他、ＬＡＮＬのＦＥＬ（Ｊ．Ｍ．Ｗａｔｓｏｎ）も医用応用であるが、そ

ちらは

１５ＭｅＶの加速器で、１－３ｍｍの短い周期のウィグラーを用いる。さらに３次、　５次の高調波を発生させて短波長化している。

Ｅｌｉａｓの発表はコンパクトＦＥＬに関するレビューで、目新しいことはない。

Ｐｈｏｔｏ－ｉｎｊｅｃｔｏｒによる高輝度電子ビームの発生と応用

新しく注目された結果は紫外線レーザー照射による高輝度電子ビームを発生である。ＬＡＮＬ，ＬＢＬ，アルゴンヌ、デューク／ロケットダイン、西ドイツなど多くの研究所で行われている。６０－９０ＭＶ／ｍの高いＲＦ電界をかけた光電子陰極にモードロックＹＡＧレーザーの３倍高調波を照射して、高輝度の電子ビームを発生させている。

電極材料は、ＬＡＮＬがＧａＡＳ，ＣｓＩ、アルゴンヌはイットリウム金属電極、デューク／ロケットダインはLaB_6である。最大電流は６００Ａ／ｃｍ^{2}以上、カソード直径０．４ｃｍ，パルス幅１５ｐｓ－１００ｐｓなどの結果が得られている。

実際に、光電子を用いたＦＥＬの動作例がデューク－ロケットダインから発表された。但し、ポストデッドラインにも間に合わなかった様子で、アブストラクトその他の資料はない。

波長　３．１ミクロン　マクロパルス　３μｓ　ミクロパルス　２ｐｓ

ＲＦ　２８５７ＭＨｚ　ＦＥＬ　９５．２ＭＨＺ　繰り返し　１０Ｈｚ

エネルギー広がり　＜１％

	熱陰極	光電子陰極	
	通常	通常	最高
小信号利得	６０％	１００％	１５０％
マクロパルス	７０ｐＣ	１７０ｐＣ	２５０ｐＣ
	３５Ａ	６０Ａ	８５Ａ
ピーク輝度	1.8×10^{11}	3.8×10^{11}	5.4×10^{11}

加速器のＲＦパワーとモードロックＹＡＧレーザーの同期をとるためには、後にニューヨークで訪問したＱｕａｎｔｒｏｎｉｘのＹＡＧレーザーシステムが好都合で、使用しているレーザーはすべて同システムであった。

３．スタンフォード大学高エネルギー物理研究室訪問

Ｄｒ．Ｔｏｄｄ　Ｓｍｉｔｈ

米国のＦＥＬの応用研究　：　予算で決定されており、ゆがんだ姿である。

現状はすべてＳＤＩ予算である。特別な医用応用などはない。但し、何か新しいものがでるかも知れないという期待と、何かに使わなくてはならないという必要性で主張しているに過ぎず、積極的な研究者はいない。

スタンフォードの現状

０．８ミクロン／１から２５ミクロンの計画

利得１０％／パスで出力ミラーの反射率は９９％である。共振器長の調整は精密さが　必要でＨｅ－Ｎｅレーザーによる干渉計を組んでいる。

目標　　光化学　　２波長ＦＥＬ（励起・検出プローブ）

材料物性、生体物理　（ｐｓ時間分解能）

Ｒｅ－ｃｉｒｃｕｌａｔｉｏｎによる効率改善のため（２７％）運転コストの低減が期待できる。個人としては光電子陰極は必要ないという主張である。理由は、熱陰極の方が連続動作に向いていること、問題は加速器技術にあるので電子ビーム発生に転嫁するのは賛成でない、などの理由による。

その他、光電子陰極用のモードロックＹＡＧレーザーなどについて調査を行った。

以上

７．２　海外出張報告

海外出張報告

報告者　；　電通大　レーザー　　植田憲一

日時；１９９０年1月１０日－２３日

用務；ＳＰＩＥ　ＬＡＳＥ’９０　出席、論文発表

訪問、情報交換　；　ニューポート、コダック、ロケットダイン

海外出張報告（ＳＰＩＥ　ＬＡＳＥ’９０、米国光学技術調査）

報告者　；　電通大　レーザー　　植田憲一

日時；１９９０年１月１０日－２３日

用務；ＳＰＩＥ　ＬＡＳＥ’９０　出席、論文発表

訪問、情報交換　；　ニューポート、コダック、ロケットダイン

１１日　　ニューポート

Ｎｅｗｐｏｒｔにおける高反射率ミラーについて

１．基板の材質、研磨方法、温度安定性

２．平面度、表面粗さ、平行度などの検査方法

３．多層膜の蒸着方法、方法による損失差、損傷強度との関係

４．レーザー損傷強度と測定方法ｈｏｓｔ；Allan Iguchi,Jeff Parker,?.Amano (tour conductor)

Francis J.Boero(Director of component products),

Keith Bennet(vibration)

基板の表面粗さ；６Ａ－２Ａ　研磨方法は通常のリングポリッシャーのみである。研磨材はアルミナ、仕上げの研磨工場は紫外線のよくでる単色性のよい蛍光灯で、ニュートンリングを観測しながら仕上げている。蒸着装置は電子ビーム蒸着で、イオンビームアシストはしていない。層数は４９層で膜厚計測は振動法でやっている。スーパーキャビティーのミラー用にはイオンビームデポジションを使っているような話がでた。理由は完全なアモルファス膜になるからである。スーパーキャビティー用のミラーの損傷強度は Quanta Ray のＹＡＧレーザーを用いたダメージテスト装置で測定し、通常ミラーの２倍以上である５０Ｊ／ｃｍ^{2}以上の値を得ている。損傷を起こし易い場所は基板と薄膜の界面である。（これはこちらの誘導質問に乗った感じで、正確に計測したりしていない感じがした。）いずれにしても、共振器内の電界強度が非常に高いスーパーキャビティー用ミラーとＦＥＬ用ミラーはその特性上、損傷強度についても多くの共通点を持っているという点で意見が一致した。興味が集中している波長は１．３－１．５μｍであった。しかし、日本の市場はそれほど大きくないという印象を持っているようだった。

反射損失の測定については、１）高フィネスキャビティーでサイドバンド測定など共振条件を求めて、損失を算出する方法、２）短パルスレーザーによる共振器寿命を求める方法、の２種類を用いているとのことであったが、実際は装置の関係から前者のみであると考えられる。

損傷実験の条件は、照射面積はφ０．８ｍｍである。損傷の計測は正確に移動できるノマルスキー型の顕微鏡である。レーザー散乱その他の鋭敏な計測法、エキシマレーザーなどの他の波長に対する損傷実験の設備はない。２４８ｎｍにおける損傷強度は１Ｊ／ｃｍ^{2}と低い値である。

ダイヤモンドターニングマシーンは持っていない。そのため、レンズなどは球面光学系のみを製作している。最大２８インチまで研磨できる研磨機が２台あるのみである。ただし、蒸着装置はそれほど大きな基板に蒸着することはできないので、製作可能な光学ミラーの最大は１２インチである。もし、さらに大きなミラーが必要な場合は、コーティングは外注するのである。また、最短波長は１９３ｎｍである。研究用の光学素子、光学ホルダーのみであり、それ以外の展開の用意はされていない。外見上、研磨工程には特別の工夫があるようには見えない。スーパーキャビティー用のミラーの研磨は、この工場ではやっていないように見える。

基板にはゼロデュアーと、石英を用いているが石英の方が面精度の良い研磨ができる。これは材質の均質性によっている。スーパーキャビティーに用いるのは基本的にゼロデュアであるが、何を用いるかはユーザーに依存した問題である。ジャイログレードではあるが、米国では、ジャイロ用ミラーは国防省の認めた少数の企業のみが、ジャイロ用ミラーを製作することができる。ニューポートは作ることができない。

新しい分野として Ti:Sapphire の広帯域ミラーについて聞いたところ、現在は開発していないとのことであった。現状の技術では銀鏡がよいのではないかとの意見で、本当に検討していない印象を持った。広帯域ミラーの技術はスーパーキャビティーミラーに通じているので、もう少し具体的な検討結果を期待したのだが。

防振台ではすべてが着磁性ステンレス鋼の表面板で、内部は鉄性のハニカムである。アルミを用いないのは、剛性に起因する共振周波数の点で鉄の方が優れて

いるからで、アルミハニカムを使用する考えはまったくない。規格品でもっとも大きいのは２．４×６ｍ程度である。東大桜井先生の研究室を卒業した近藤真通氏がアクティブ防振機構の研究を行っていた。 Keith Bennet が聞きたがったのは、Newport が直接日本で会社を展開した場合に、丸文を通じて商売しているのと同等以上の信用が得られるかどうかという点であった。

１１日－１２日 John Wayne Airport - Las Vegas - Pittsburgh - Rochester
mid-night flight

１２日　Eastmann KODAK　Dan Shirkey(absent),Benjamin B.Snavely

Advanced Technology Development,Federal Systems Division

Dr.Benjamin B.Snavel (Assistant General Manager)

(716)253-2394

Robert P.Locke　(716)253-2591 Large Optics Development

Dave ; presentation and tour conductor

人物に関する解説　B.B.Snavely

以前はＬＬＮＬの研究員で、同意体分離、光学素子の開発などの仕事に従事していた研究者である。ＡＶＬＩＳでは１９７４年に論文を出しており、非常に初期に基礎的な研究を行った学者である。当然、ガラスレーザーの開発には深く関与しており、現在も関係が深い。

ＯＨＰによる説明；Dave

平面研磨

リング型平面研磨機　ＮＯＶＡ用光学素子の研磨

最大１６０インチ（４ｍ）（２台）２．５ｔの石英板で平面制御をしている。その他、１００インチ級のものは８から１０台程度並んで運転中であった。主としてＬＬＮＬのミラー、レーザーディスクを研磨中である。最大の研磨機と同じ部屋にフィゾー型の干渉計が２台設置され、研磨状態を検査している。ザイゴ社製の市販品（４インチ）と別に３５インチのフィゾー干渉計が稼働中である。ＬＬＮＬの３２インチより大きく、おそらく世界最大だろう。温度制御は数度だということだが、研磨に関しては環境の影響はそれほど大きくないそうだ。研磨材、粒子サイズ、研磨液の温度制御などでＯＫだとのことである。

通常研磨　；　８０インチ（２ｍ）、１／２０λ　４０インチ（１ｍ）

表面粗さ　１０－５Å

材料はコーニング社の担当であるとのことであったが、一見しただけでいろいろな光学材料を研磨していた。非常に薄いハニカム表面のガラスは石英だが、その他ゼロデュア、不明などの材料が研磨されていた。日本の工場と違う点は、石英以外のほとんどの光学材料に色がついていることである。現にＬＬＮＬ用ミラ

一も薄いピンクがかった色をしていたし、干渉計用光学アームはもっと濃い赤をしていた。

計算機制御型研磨機　ＯＡＧＭ２５００；ハッブル望遠鏡、ＳＤＩ用光学素子
　　非円形、被対称光学素子、ハニカム光学素子、adaptable optics

ＸＹ軸制御　平面計測／研磨の繰り返し工程

７２時間（２週間）程度かけて研磨しているようだ。時間とともに面精度が向上するデータからすると、時間をかければ、さらに面精度が向上しそうである。研磨部分が回転していないのは、回転をかけると平均化されてしまうので、曲面研磨などの精度が低下するからだそうだ。固定された研磨状態で、どのような研磨パターンでどのような面のアンジュレーションが発生するのか、データベースに基づいた制御を行っている。このようなシステムは米国内の他のメーカー、欧州のメーカーで共通であるが、コダックほど大きなシステムはない。基板を保持する台は自由に移動することが可能で、そのまま計測タワーに移動することができる。研磨液の注入を自動的にするノズルがついているが、現場では作業員が手動で補給していた。

非球面整形用イオンビームエッチング装置

現在、装置のテスト中で、実際に設置するサイトの近傍で動作テストを行っている。重量２００ｔ以上の巨大な真空チャンバーで真空度は10^{-6}Ｔｏｒｒ以上である。中和化されたアルゴンイオンビームを照射してくれたが、ビーム径は５－１５ｃｍで元来がイオンロケットの技術を応用している。イオン源は真空チャンバー内を３次元的に移動し、上部から吊るされた基板をエッチングするのである。表面粗さは０．００３８－０．０１λである。従来の研磨方法と比べて大きく優れている点の一つは面ダレのないことで、１００インチの光学素子の端から１ｃｍ以下まで、設計された面精度に制御される。

コダックでは２０年以上も前にプラズマエッチングで基板加工をする技術を開発しており、イオンビームエッチングはその延長である。真空チャンバーの内部は広く、一つの部屋を構成しているので、基本的にスペースチャンバーとして使用され、宇宙環境における光学素子の検査を行うのではないかと思わせた。別項の検査能力に関する説明で、液体窒素温度から１００℃までの温度条件で、真空環境試験ができると言明していた。設置サイトは１２ｍ×１２ｍ×２ｍ程度の巨

大なプールのように見えた。天井も異常に高く、単に表面整形装置を設置するだけではなく、それを含んだシステムを考えているように思えた。

原理的な説明では、イオンビームエッチングは基本的に面の整形であり、それ自身には研磨性能を期待していないとのことであった。電解研磨のようにエッチング速度の差を利用した平滑化機能が期待できるのではないだろうか。

検査用タワー　大口径用　垂直軸、水平軸　各１台　高さ約１５ｍ

１００インチ反射鏡の計測可能、空気保持による無重力環境試験

反射望遠鏡のような構成（垂直軸型）、

３角形の光学パス（別の姿勢）Ritchey Test? <82-inch

参照光学ミラーは４０インチのものがついていた。実際に試験していたものもハニカム形状で、大口径はすべてハニカムを使用しているようだ。adaptive optics の場合も、実際に検査用タワーに取り付けて、アクチュエータによる曲率変化の特性をとっている。このような検査装置を用意することは、もっとも重要で、検査能力なしに光学素子の開発はない。

検出器としては、写真フィルム、ＣＣＤ素子などがあるが、基本的にはホログラフィー計測と同じフィルム計測が用いられる。光源は巨大な干渉系にも関わらず、５ｍＷのＨｅ－Ｎｅレーザーで、コヒーレンス長からすれば安定化Ｈｅ－Ｎｅレーザーに勝るものはない。この点からもフィルムによる計測が必要である。

ハニカムミラー　；　重量密度は単一素子光学ミラーの３％

ハニカム構造の製作；高圧水ジェットによるハニカム製作

大きなガラス基板からハニカム構造を切り出している。ガーネット微粒子を含む高圧水をチタンノズルから噴出させて、任意形状のハニカムを切り出す。基本形状は３角形で、異なった大きさのハニカムを多層に重ねることでいろいろな要求に応じることができる。ノズルの寿命を延ばすためにシースビームなどを用いているかと質問したが、適当な間隔で取り替えれば問題ないとの答えであった。ハニカムと表面用ガラス基板の接着はコーニングの担当で、熱膨張率や機械的ストレスを生じさないような接着剤のようなもののようだ。低い温度で融着できる感じであるが、詳細は不明である。このようなハニカムミラーの研磨にはＸＹ軸制御型の研磨機が必要である。

高出力レーザー用ベリリウム光学系の工場は毒性の問題で見学できなかったが、その周辺は完全にみることができた。毒性対策として、いたるところで減圧環境が用いられていた。材料の粉末化、その他の処理はＫＯＤＡＫ独自で行っているようだ。

ジャイロ用光学工場や蒸着工場は場所が違うことで見学できなかった。しかし、全体に非常に丁重で、何も隠すことなくオープンに見学が許され、質問にも正確に答えていたように思える。宇宙空間で用いる adaptive optics や、地上ベースのＳＤＩ用光学系であることも、格別隠す様子がなかった。こちらが不思議に感じるほどオープンに見学・議論ができたのが収穫である。日本の会社ではこんなにオープンな議論ができないように思う。

ロチェスターは基本的に工場であり、研究所ではないので、レーザー損傷実験などの施設はない。それらはＬＬＮＬ，ＬＡＮＬ，ロチェスター大、アリゾナ大などとの共同研究である。

１５日 － １９日　ＳＰＩＥ　ＬＡＳＥ’９０

ＳＰＩＥ開会、論文発表　午前中　ＫｒＦ　午後　ＲｂＦ

自由電子レーザーに関する調査

T.T.Yang(Rocketdyne) on Lunch

ＦＥＬ研究

光学設計に関しては８０人のＰｈＤを擁する米国最大の研究グループの一つである。（ただし、勿論ＦＥＬだけではない。）

C.Turner (Rocketdyne)

Rockedyne はＦＥＬ用光学系の設計製作に参加できるかどうかに興味がある。詳しい仕様が必要だ。中心人物としては

Ｄｒ．Ｋ．Ｃ．Ｓｕｎ　技術的なリーダー　from 望月　Ｓ．Ｖ．Ｇｕｎｎ

Ｗｉｌｌｓｏｎ　マネージャー　Ｂｉｌｌ　Ｍｏｗｅｒ

１８日

Introduction to FEL　D.Prosnitz(LLNL)

ＬＬＮＬのＦＥＬ研究は中止になった。（tentatively と表現したが、会場から笑いが漏れた。）ボーインググループとの競争に負けた結果である。

Tapered Wiggler が非常に効果的なことを実証したのが大きい。通常のレーザーではエネルギーが光に変換された場合、原子の量子的エネルギーは一定で、原子の分布数が変化するのに比べ、ＦＥＬでは分布数が不変で電子のエネルギーが連続的に変化することが、Tapered Wiggler に反映している。この意味で、ＦＥＬは拘束電子を利用した通常のレーザーとは根本的に異なっている。

FEL research for microwave frequency　G.Bekefi (MIT)

非常な高電界で小型化する案くらいが新しいところか？

Boeing/USASDC rf free-electron laser　j.l.adamski (Boeing)

本命のＦＥＬ　グループは　加速器；ボーイング、理論、計測；ＬＡＮＬ，ウィグラー；ＳＴＩ、光学系；ロケットダイン　のチームで構成されている。

共振器には grazing incidence mirror を用いたリング共振器を用い、共振器長は６２ｍで、ＦＥＬの建屋のもっとも長いパスを占めている。光学系はすべて真空系の中に納められるので、大きなミラー格納部分がみられる。研究としては計測がしっかりしているのが特徴的であった。それでも、ＦＥＬは非常に不安定なものらしく、ショットごとの利得のばらつきのデータは印象的である。特に画像計測技術が重要である。計測されたパラメータ；ビームパターン、ウィグラーと電子ビームのマッチング、自然放出光の遠視野像（高調波計測を含む）、干渉像、利得のばらつき、デチューニング効果、サイドバンド計測、電子エネルギーの減速効果、エネルギー広がりの変化　など

Los Alamos high brightness FEL　W.D.Cornelius

フォトインジェクタによる低エミッタンス電子の発生

ＮＩＳＴ－ＮＲＬ

全米の共同利用として装置の設置、調整が進んでいる。バイオ関係への応用が多いようだ。

バイオ医学関係の応用が多い理由のひとつは、レーザーとし手厳しい要求がされずに、ａ単純に波長可変であれば便利だというところにあるかもしれない。なぜなら、よく知っているように、医学応用のほとんどは土木工事のような応用が多いからである。

ＵＣＳＢ　Ｇ．Ｒａｍｉａｎ

ハイブリッド・ウィグラーによって高精度のウィグラー磁場をつくっている。ウィグラーの製作は西ドイツの会社のように聞こえた。

ＦＥＬ用共振器

共振器調整が非常に大変で２００ｎｒａｄ程度の精度は必要になるようだ。このため、コーナーキューブを用いた光学系で、調整を容易にしようとする提案がほとんどであった。日本でもコーナーキューブを含むリング共振器の設計コードを開発する必要がある。

実際に開発・応用されているロケットダイン（D. Sun）のシステムは違って、Siの大きな結晶（3×3×10インチ）を使った斜入射式の双曲線型のミラーである。最近では水冷型の結晶ミラーも開発した。双曲面の計測、研磨がむずかしそうだ。

コーティングを含めて99.99%の反射率はいろいろな材料で達成している。リング共振器では軸外しビームを多用するので、コマ収差やアスティグマティズムなどを正確に計算することが非常に重要である。同時に非球面光学系の製作技術が重要だ。

この辺の計算コードの開発は適当なテーマのように思える。

19日　FELの応用と短波長FEL

応用として考えられているのは、主として短波長、中でもX線の応用である。これは米国におけるFELの現状の反映である。vuv、xuv領域の計画はレーザー研究の社会から拒否されたようだ。テーブルトップの短波長レーザーの計画が多数進行している環境では、FELの研究が予算を食いすぎるので、一挙にX線領域、それも40Åまでジャンプせざるをえないようだ。

短波長化のための新しいアイデアは提案されていない。基本的に従来の延長で、高エネルギー、低エミッタンス・高輝度電子ビーム、高精度ウィグラーで実現しようとするものである。高輝度ビームの発生では、LANLの実験で数10ピコ秒のレーザー照射で、輝度の高いビームを600A／cm^{2}の電流密度で発生させたという情報をえた。これにより、バンチャーが不要になるとともに、ナノ秒パルスのような熱効果によるエミッタンスの低下がなくなると期待される。ただし、照射レーザーの波長は仕事関数と同じか、多光子吸収で仕事関数に一致する必要がある。なぜなら、余剰エネルギーは方向性を持たないため、初期エネルギーの分散から熱的に広がったビームを発生するからである。（しかし、加速された電子のエネルギーからすれば、初期エネルギーの広がりなどどうでもよいように思えるのだが。）このあたりは、プラズマを発生しない最大強度、引き出し電流量、金属、誘電体の電界破壊との関係からもおもしろいテーマとなるようだ。

いずれにしても短波長レーザーにすると、高反射ミラーがないので、50%反射でも発振可能な設計をしなけらばならないので大変である。逆にいえば、FE

Ｌは、加速器、ウィグラー、共振器光学系、で構成されているにも関わらず、加速器に集中しすぎていることに問題がある。光学系の重要性は、加速器によって利得を１０％向上させるのも、共振器損失を１０％減少させるのも同じことで、損失を減少させる方がダメージその他でも有利であることに注目すべきである。

ＳＰＩＥの会議そのものはおもしろくない会議だったが、最後のまとめ的にＦＥＬのレビューがまとまってあったのは有意義であった。一方、初日から最終日までスケジュールが詰まってしまったので非常に疲れた。

８．まとめ

自由電子レーザー研究における光学系および光学素子の位置づけを、電通大レーザー研究センターの短波長レーザー開発の経験と、海外研究状況調査によって行った。その結果、

① 自由電子レーザーにおいて光学系、光学素子の研究が持つ重要性、

② 組織的光学技術研究の必要性、

③ 従来のレーザー用光学素子開発の手法が有効である。

ということが明らかになった。

個別の課題としては

① 長光路で光学調整に鈍感な共振器

② レーザー損傷に強い斜入射光学系

③ ３次元曲面光学素子の製作と計測

④ 高調波、制動輻射光による光学損傷

について新しく検討した。

自由電子レーザー研究のために有用と思われる

① 超短パルス色素／エキシマレーザーシステム

② 光音響法によるレーザー損傷、微少吸収測定法

③ 超短パルスレーザーによる超高反射率測定法

④ 超短パルス多光子吸収計測法

⑤ ２次元画像処理応用光学特性測定法

などを開発し、新しい光学素子開発の基盤を準備した。

以上のような基礎技術の上に組織的な研究開発を行うことが、自由電子レーザーの光学系の研究が進むべき方向であると結論された。

本研究の遂行に当たり、新形レーザー研究センターの宅間センター長はじめ職員各位、および学生諸君の多大の協力を得た。ここに記して感謝の意を表したい。

付録　米国におけるＦＥＬ研究の発表資料

付録１　ＳＰＩＥ　ＯＥ／ＬＡＳＥ’９０
関係試料

付録２　１９８９年高エネルギー粒子
加速器国際会議における自由電子
レーザーに関係した発表論文

付録１　ＳＰＩＥ　ＯＥ／ＬＡＳＥ’９０

１９９０年１月１５日－１９日、　ロスアンゼルス、米国

自由電子レーザーシンポジウム

光共振器セッションから　自由電子レーザーに関係する光共振器

付録１　ＳＰＩＥ　ＯＥ／ＬＡＳＥ’９０
自由電子レーザーシンポジウム　発表資料

１．ローレンスリバモア研究所の誘導線形加速器ＥＴＡ－Ⅱ

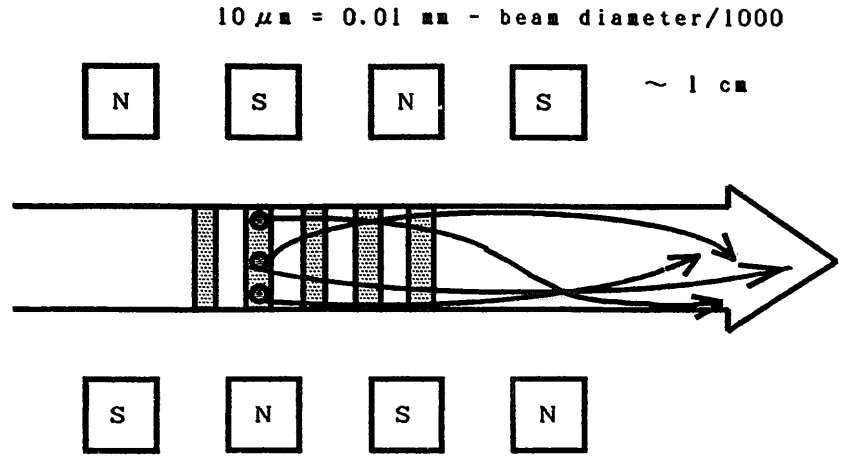

Electron beam envelope
* Trapped e
* Untrapped e

Representative e
Trajections from
Random transverse motion

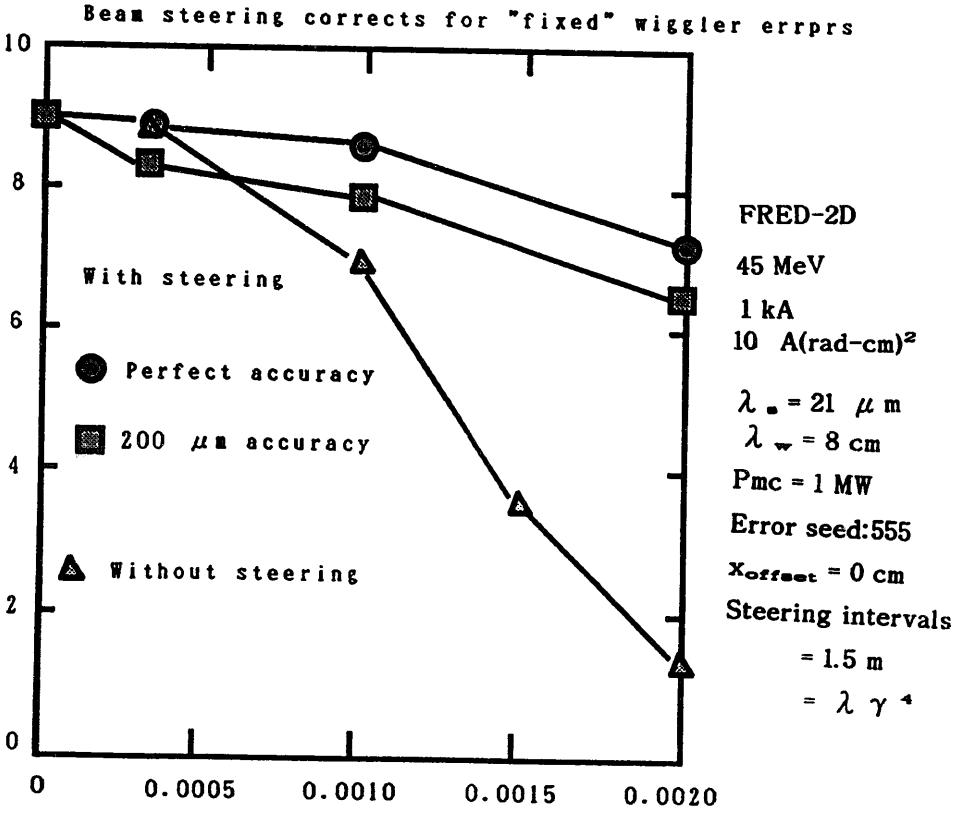

The accelerator must be chosen to match the desired applications

Accelerator	Nominal Energy	Nominal Pulse Length	Nominal Peak Current	Duty Factor
RF Linac	100 MeV	30 ps	300 A	Moderate
Storage Ring	500 MeV	50 ps	300 A	High
Induction Linac	50 MeV	50 ns	3 kA	Low
Van Der Graf	10 MeV	3 μs	3.0 A	High
	100 MeV	3 ps	3.0 A	High

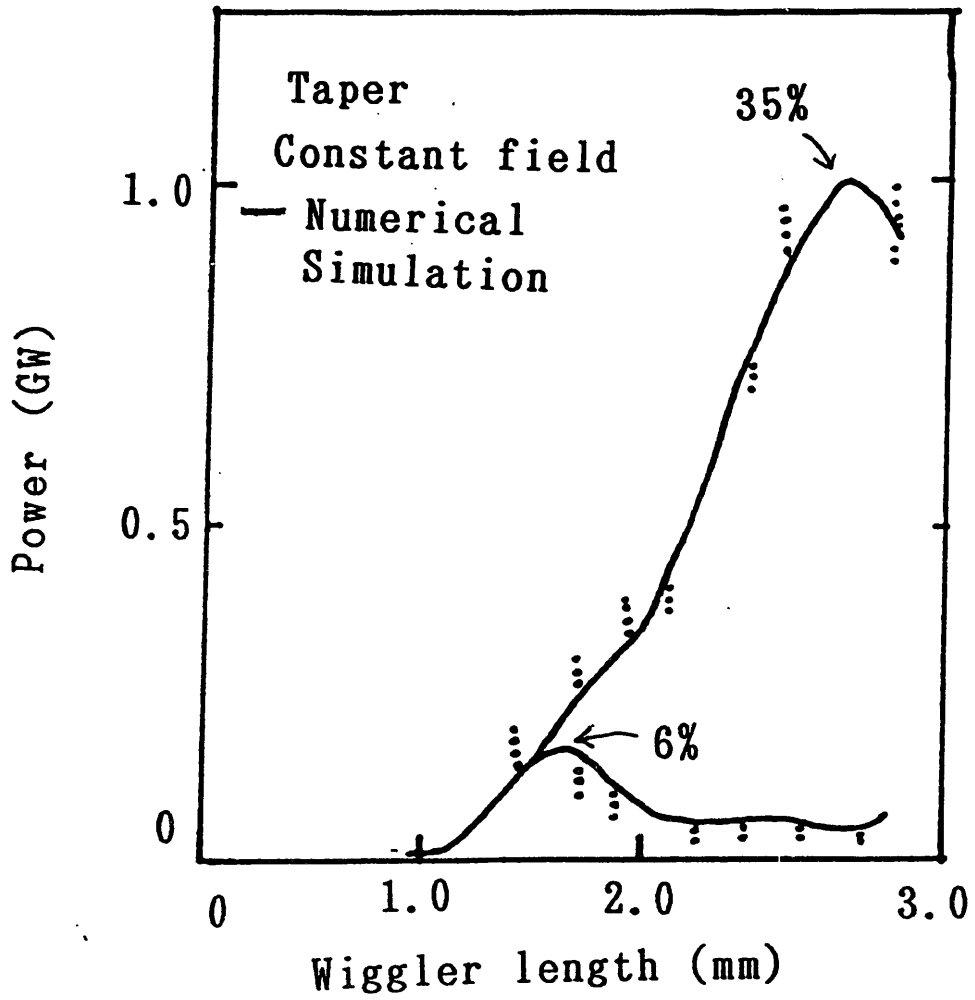

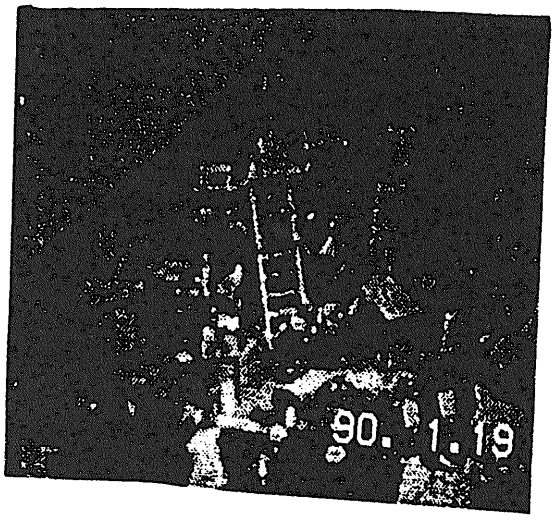
90. 1.19

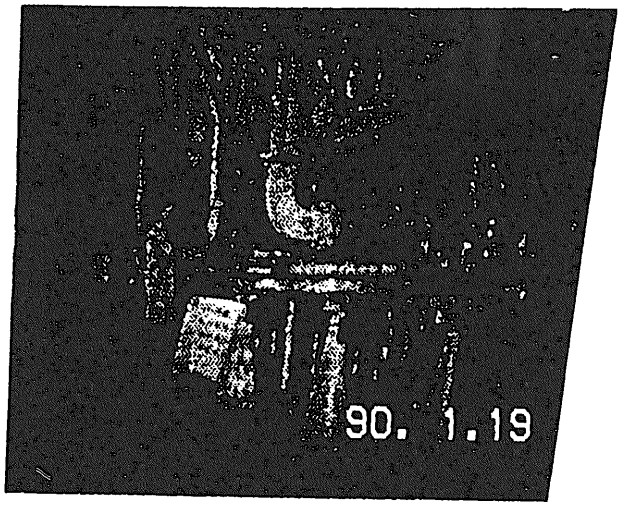
90. 1.19

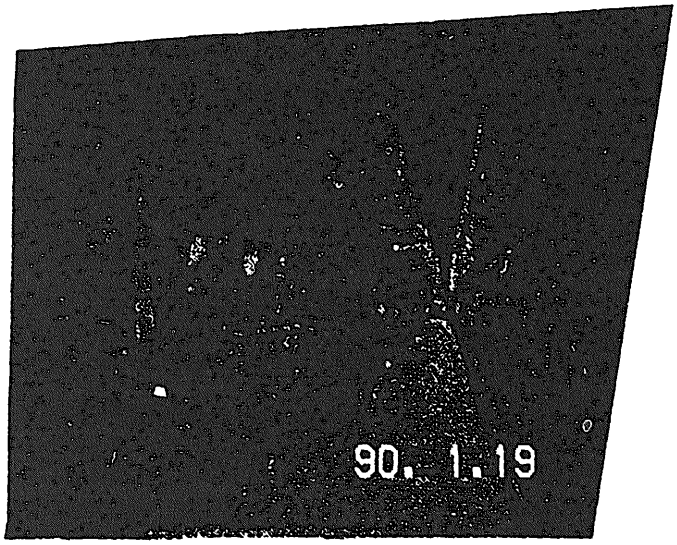
90. 1.19

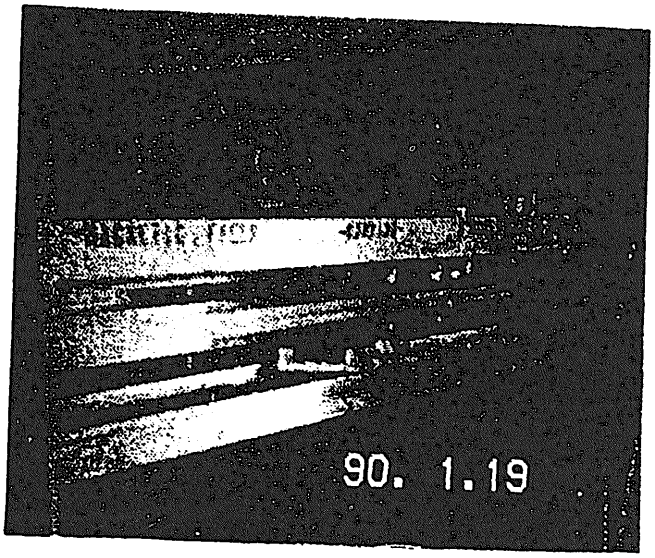
90. 1.19

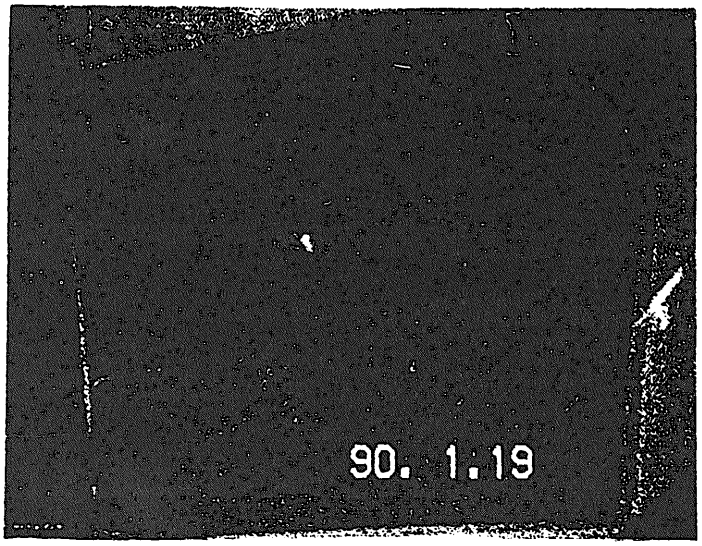
90. 1.19

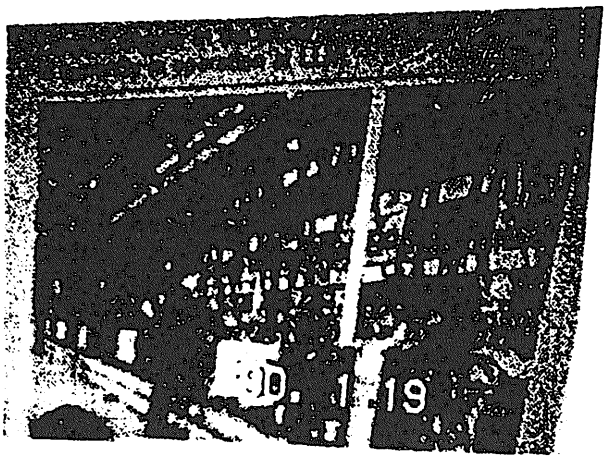
90. 1.19

Suppression of Feedback Oscillations

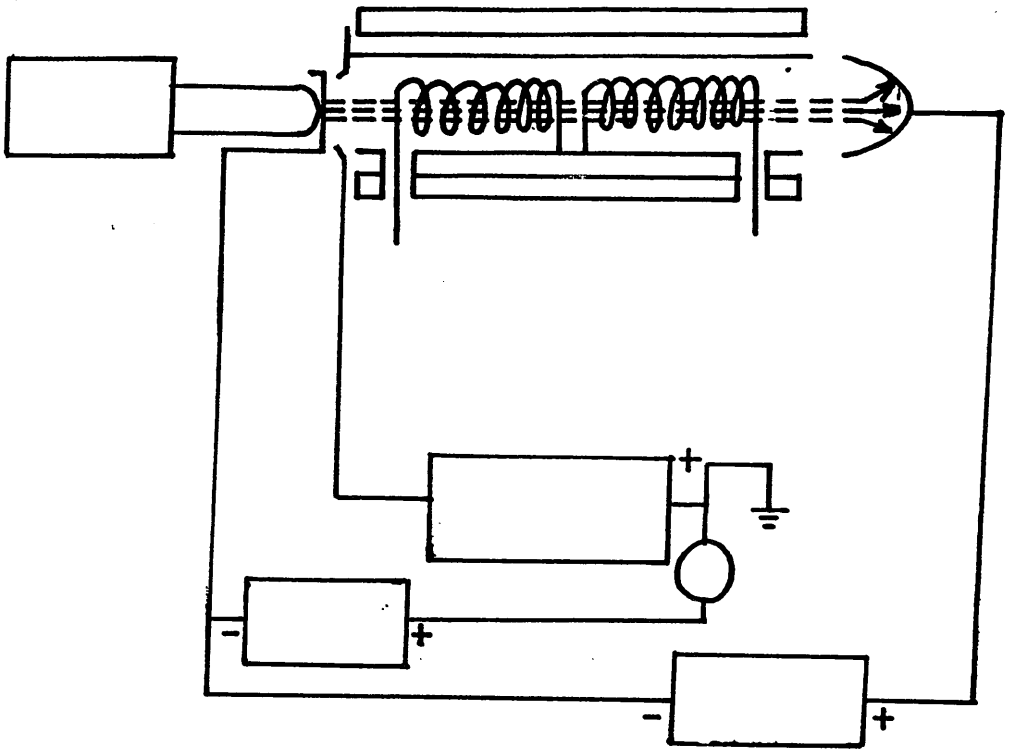

Prebunching

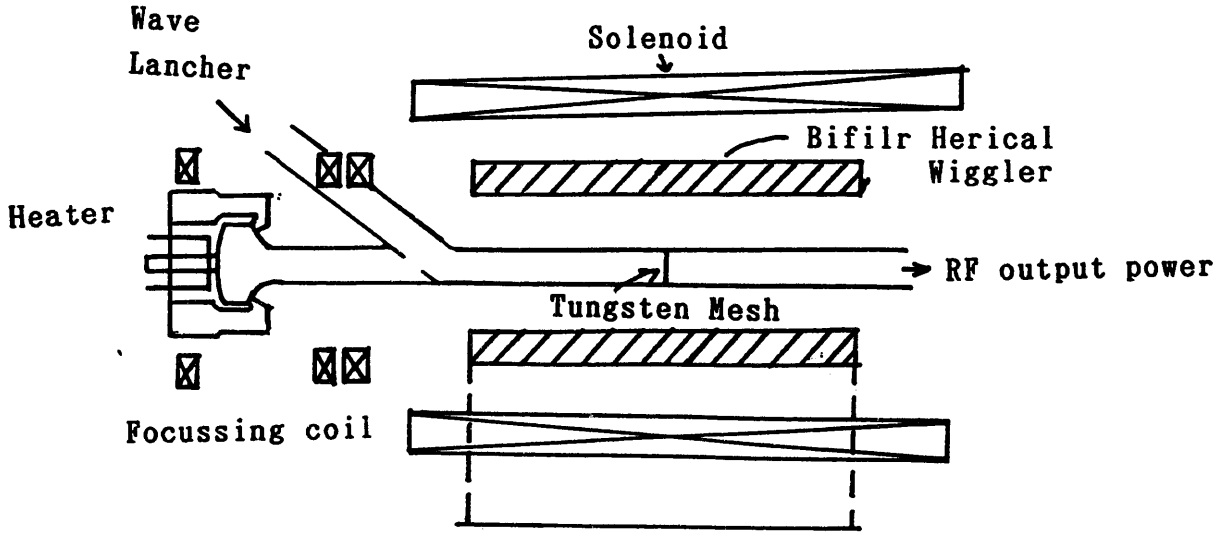

Effects of Prebunching

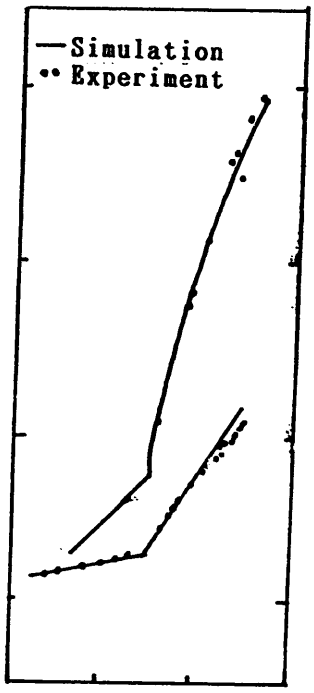

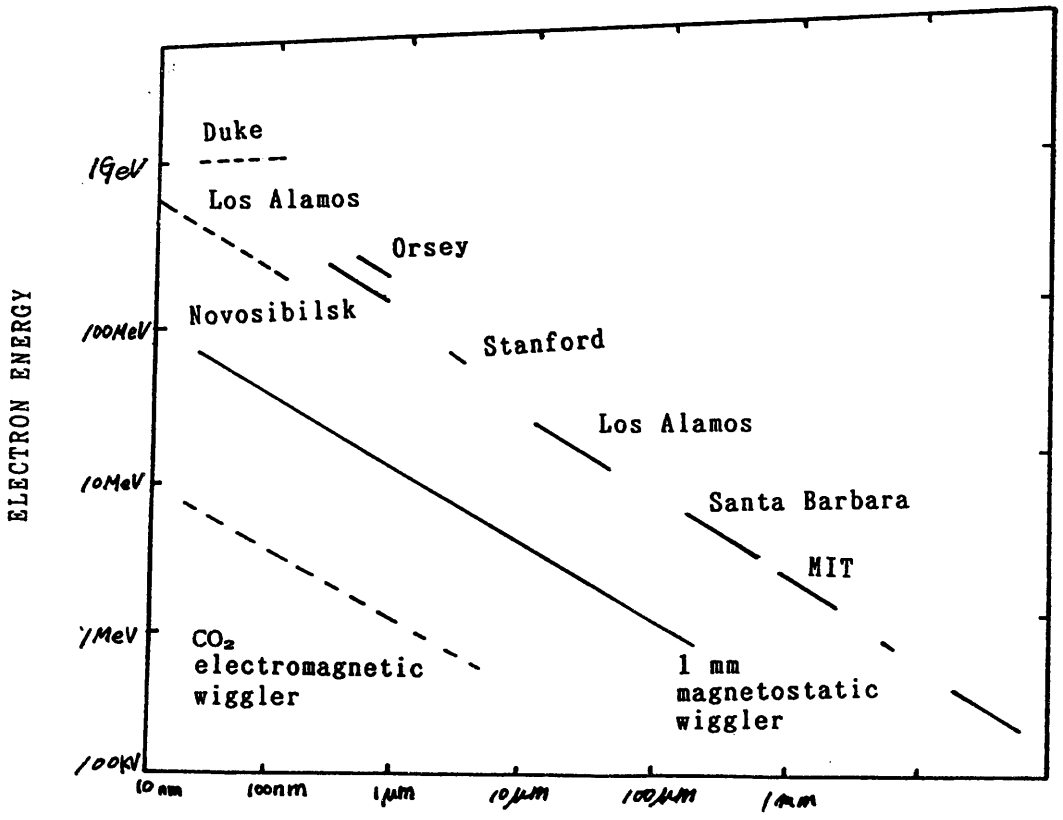

2．ＭＩＴプラズマ研究所におけるＦＥＬ（円形パルスパワー）

MIT Microwiggler

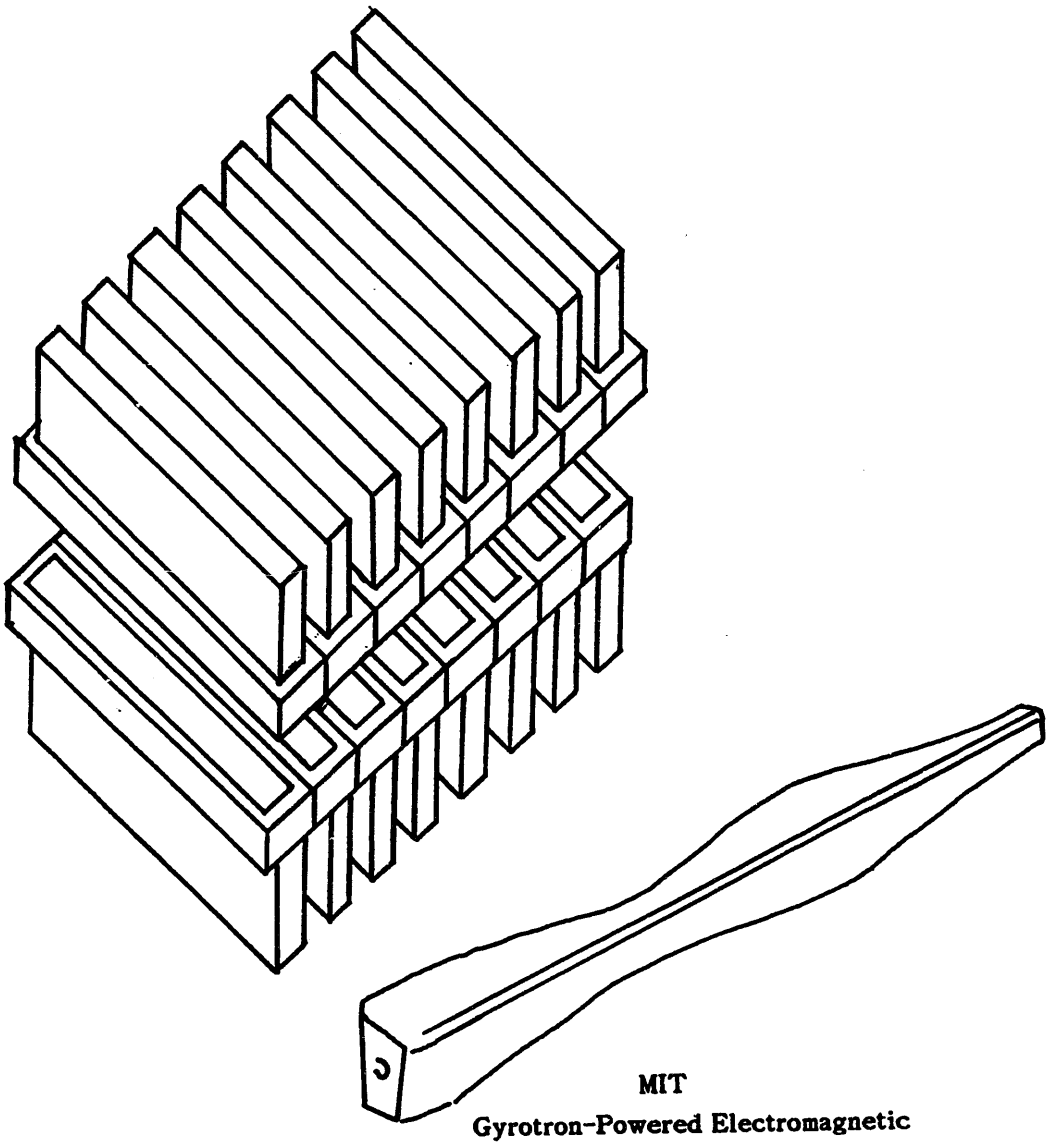

MIT
Gyrotron-Powered Electromagnetic
Wiggler Cavity
Cavity # 1
TE_{13} mode, 133 GHz
a_w = 0.003　300 kW
a_w = 0.05　4 MW

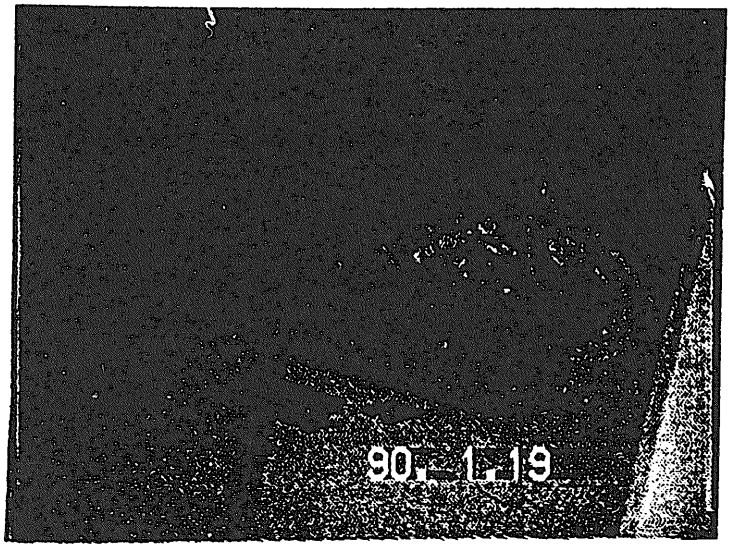

SUMMARY

- Goals　High peak power　High average power　High efficiency
- Applications　- Drivers for high gradient accelerators
  - Plasma heating　- Short wavelength communication
- New active area　Cyclotron autoresonance masers [CARM]

High gradient accelerating structure at LBL

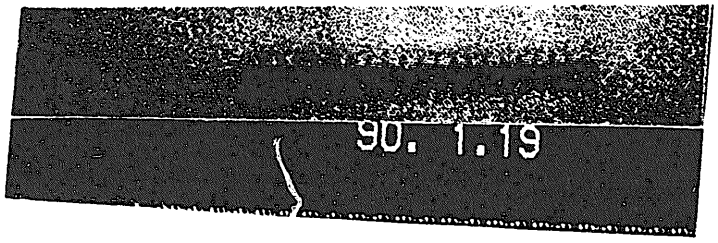

3．ボーイング可視光ＦＥＬ（ＲＦライナック）

Update on the Boeing USASDC RF Free Electron Laser
Technology Experiments

- **Boeing–Overall experiment architecture, experiment and test**
- **Los Alamos – Theory, diagnostic measurements**
- **Spectra Technology – Wiggler, concentric cavity**
- **Rocketdyne – Ring resonator**

Laboratory Layout of FEL Concentric Oscillator
Burst Mode Ring Resonator Experiments

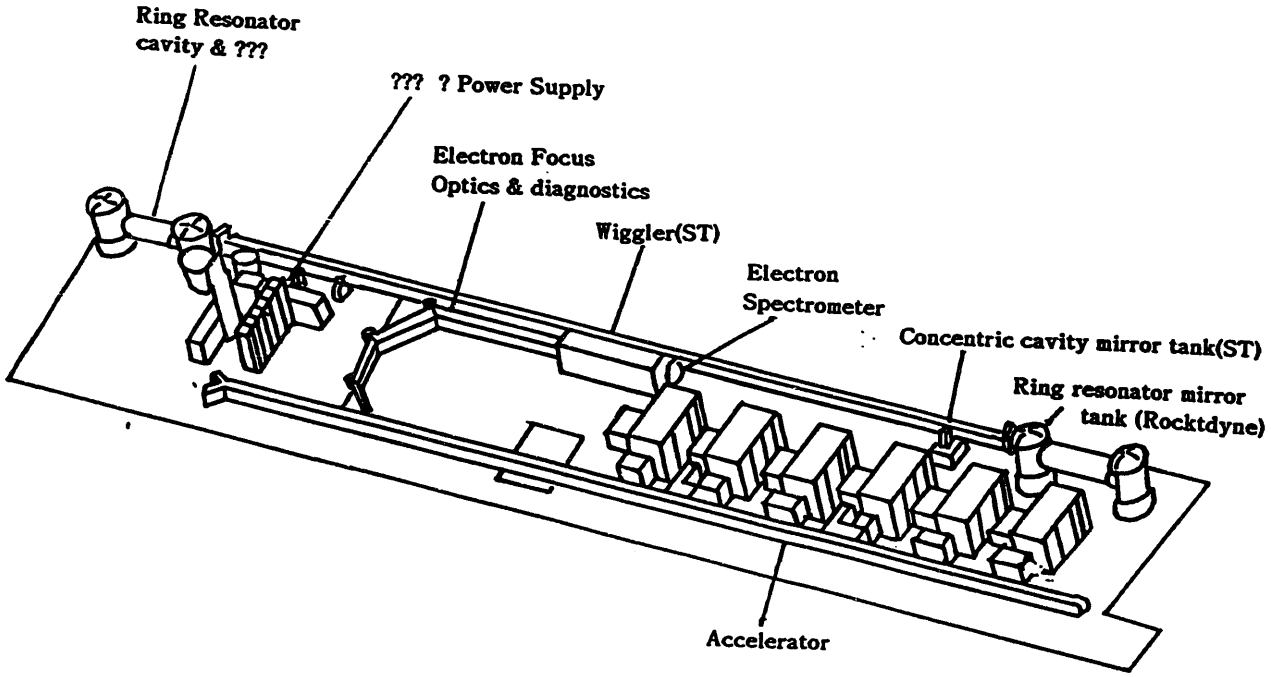

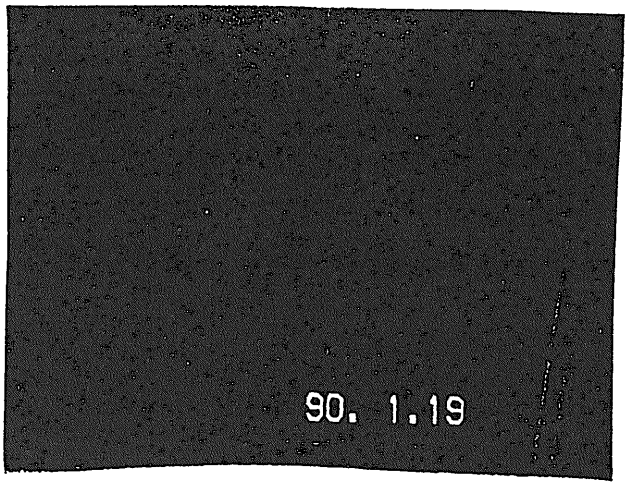
90. 1.19

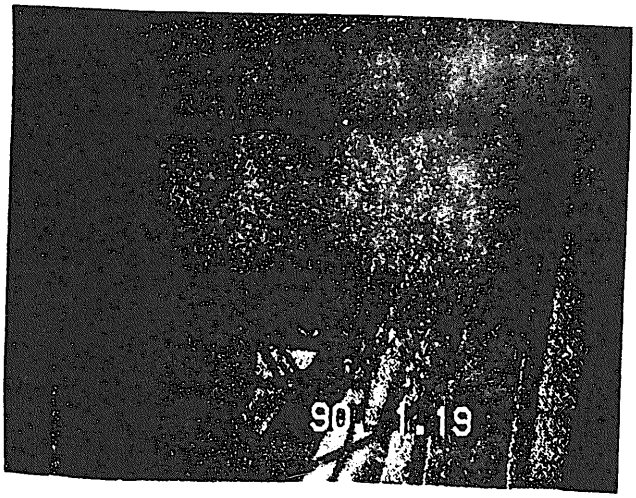
90. 1.19

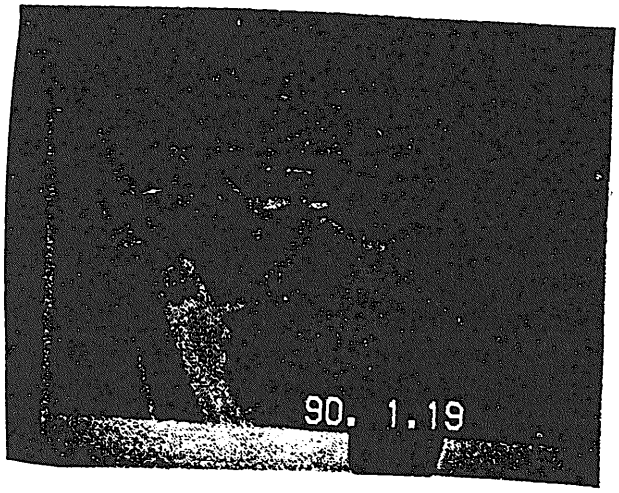
90. 1.19

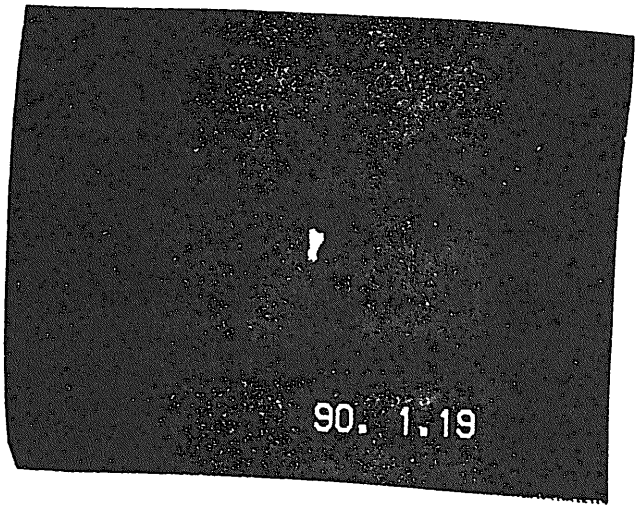
90. 1.19

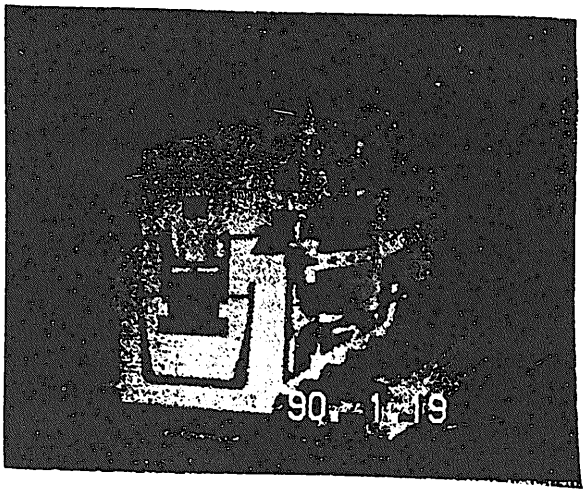
90. 1.19

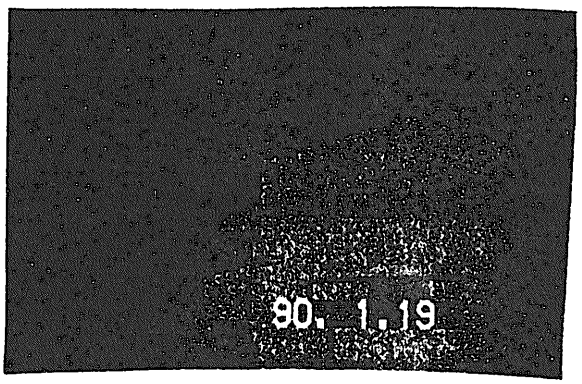
90. 1.19

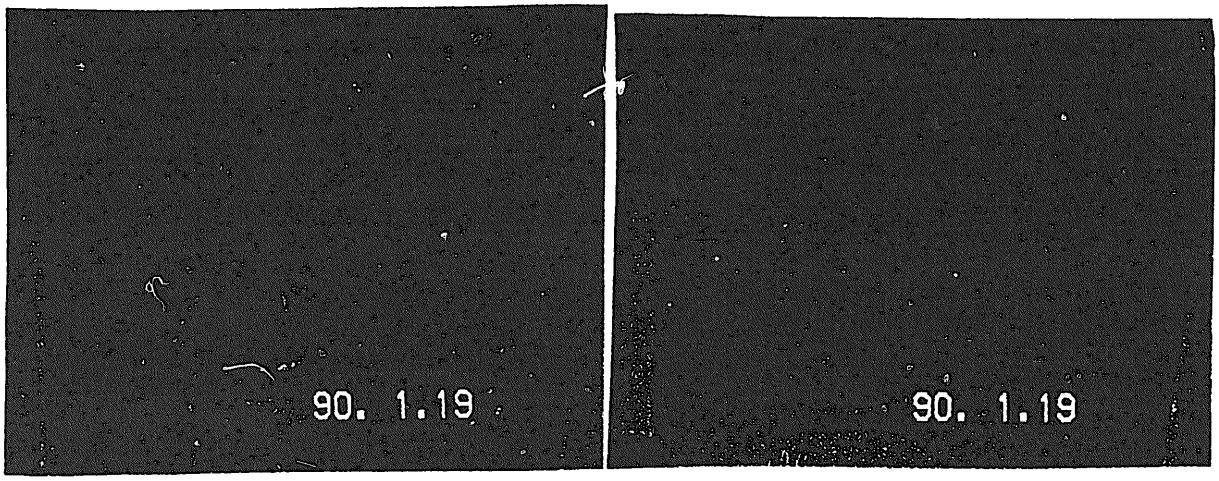

Boeing Los Alamos SDC 0.6 μ m FEL Experimental Status

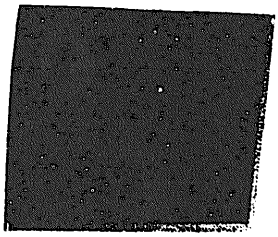

0.6 μ m FEL light recorded by video camera

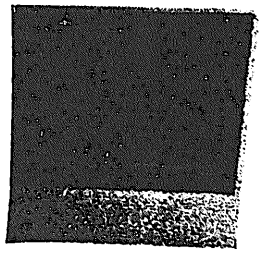

Laser output from photomultiplier

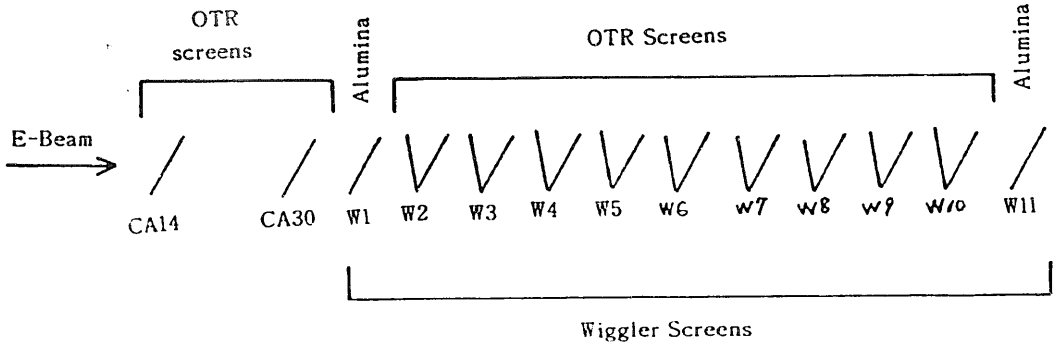

ELectron Beam Matching to Wiggler

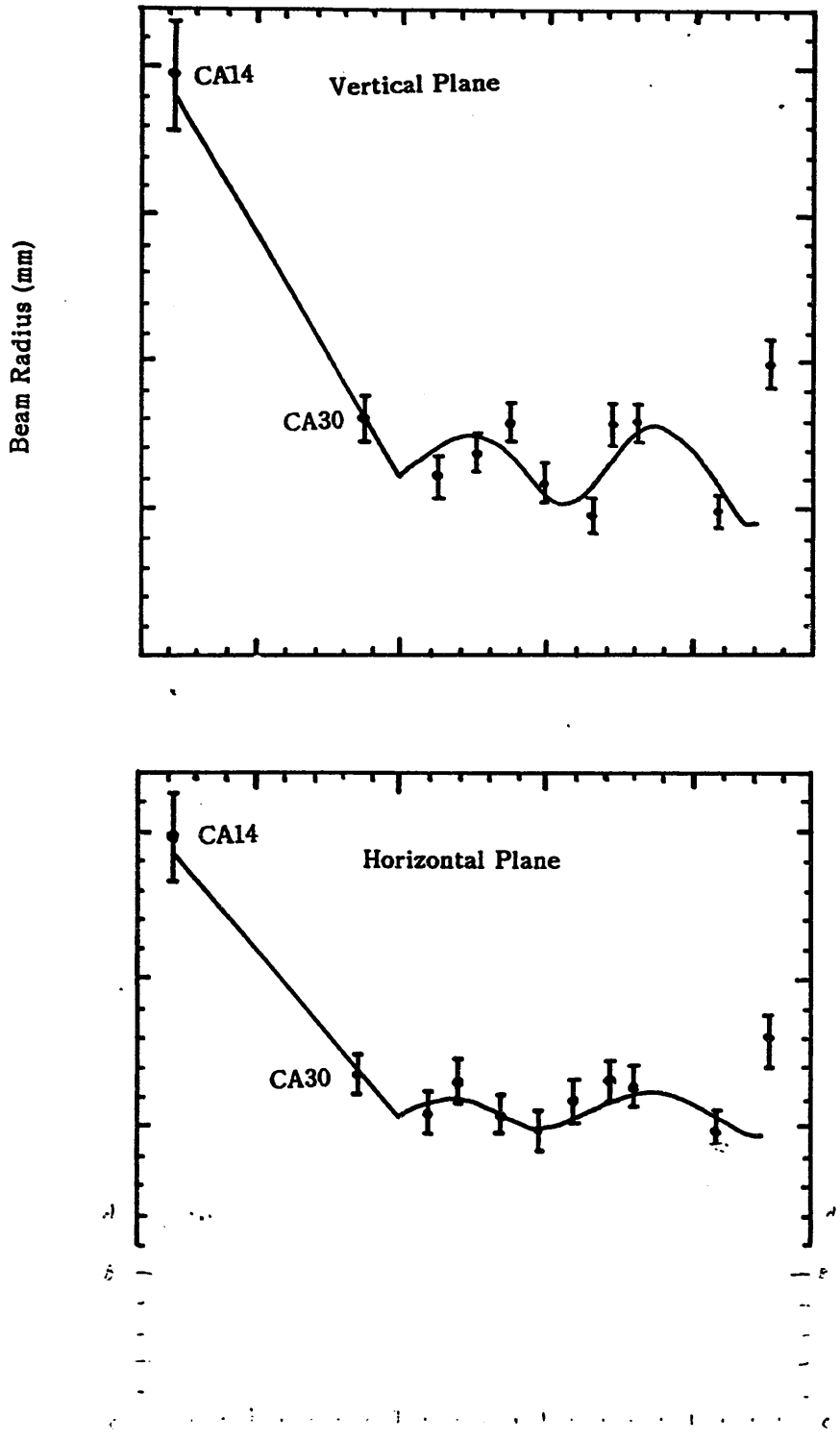

Far-Field Spontaneous Emission Patterns

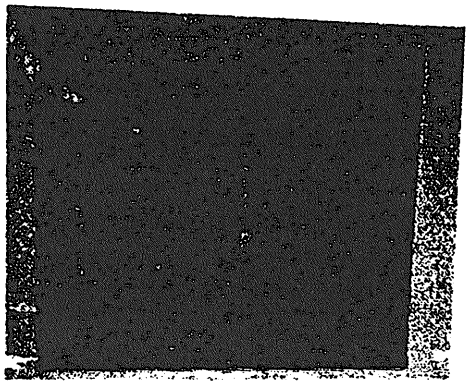

After 50 cm of wiggler

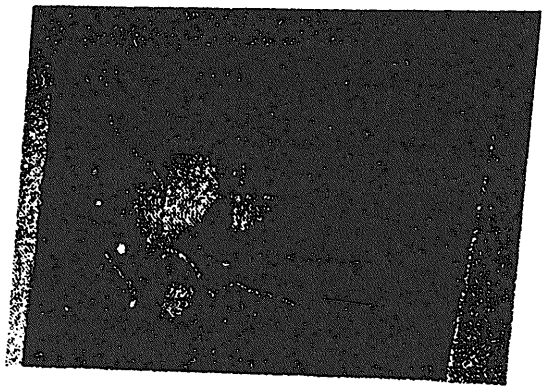

After 250 cm of wiggler

Angular Distribution of OTR Patterns

?????????? ?ing Angle and Divergence

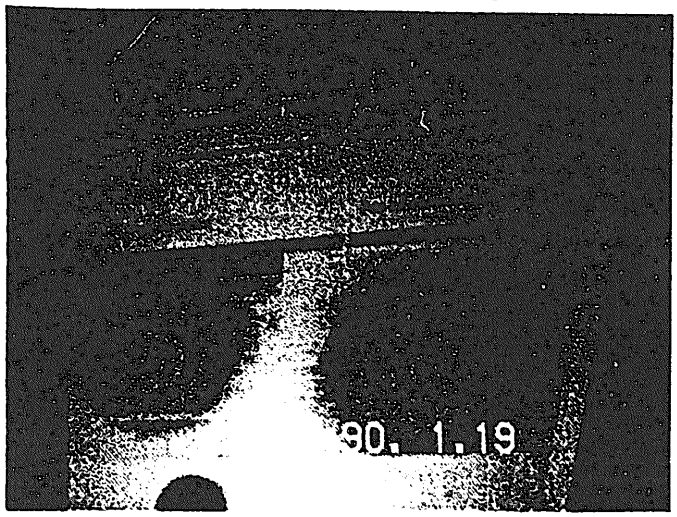

Horizontal and Vertical E-Beam Divergences

and Sideband Using a Polarizer

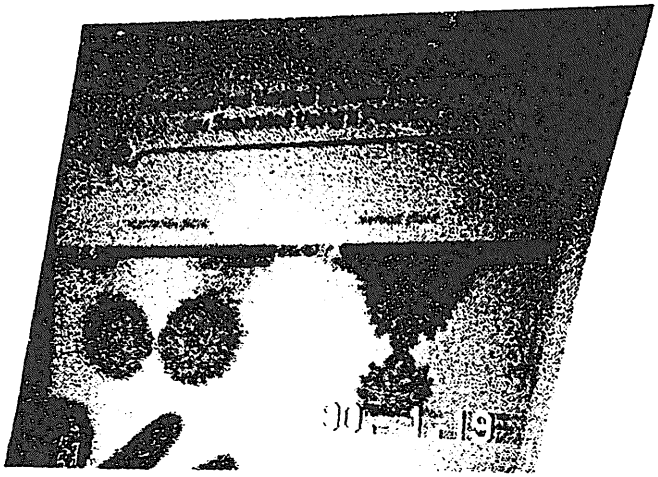

Small Signal Gain During 8 Hours on August 4,1989

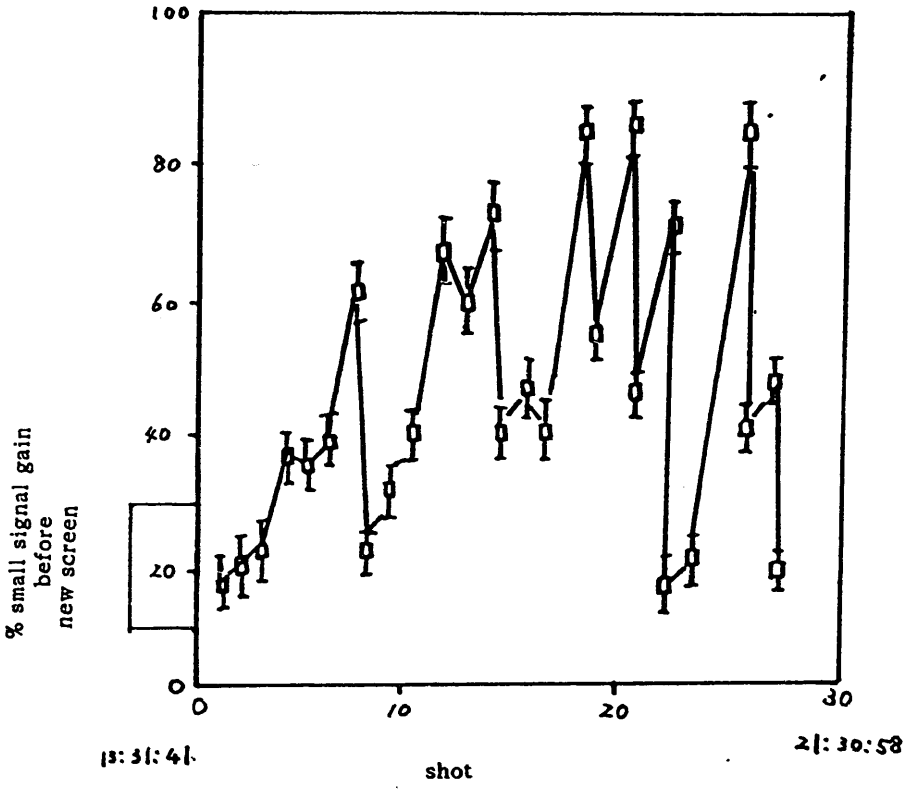

Detuning Optical Cavity Makes Sideband Disappear

Spectrometer Array Shows Some Electrons

Being Decelerated by 4%

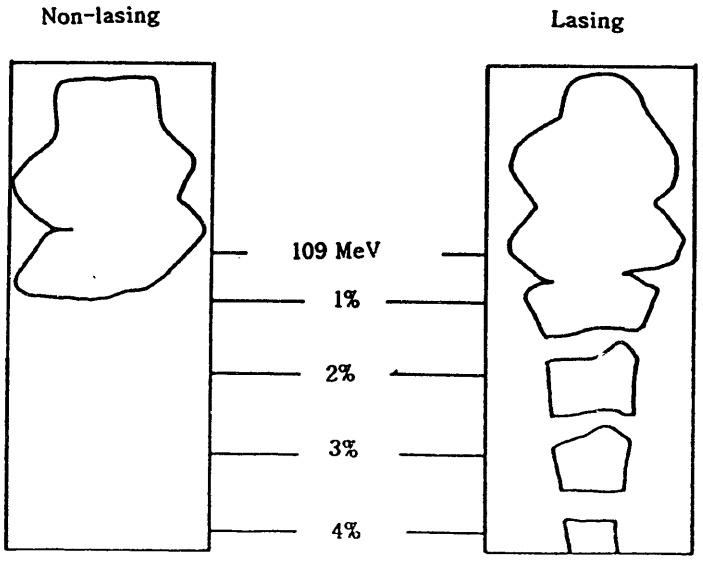

Single-Micropulse Energy Spread

Versus Time Into Macropulse

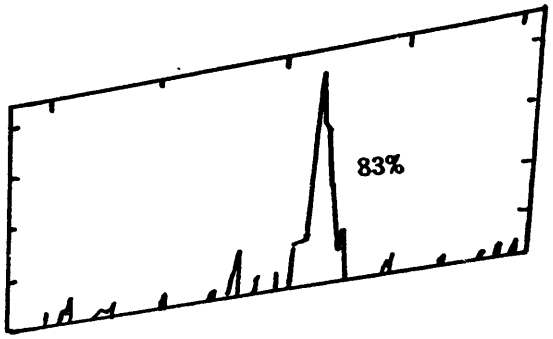

Time into macropulse 13.7 microseconds

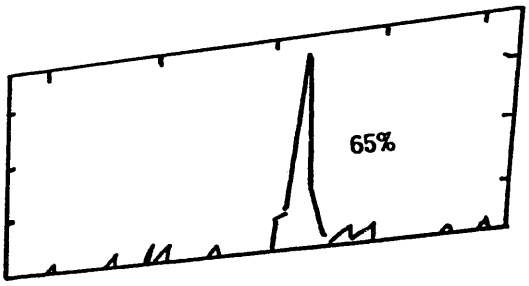

38.7

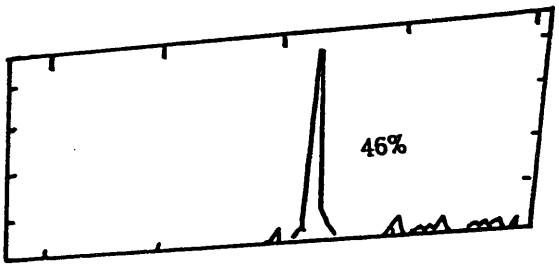

63.7

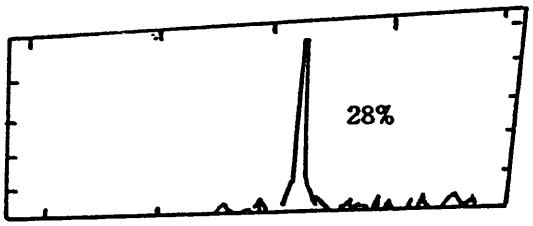

88.7

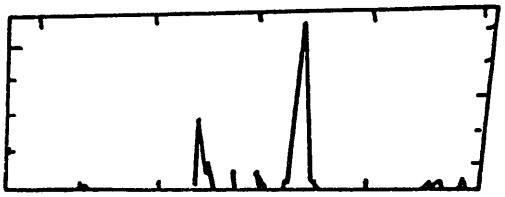

113.7

4．ロスアラモス研究所　高輝度加速器によるＦＥＬ（ＲＦライナック）

Los Alamos High Brightness Accelerator FEL

(HIBAF) Facility

W.P.Cornlius,S.C.Bender,L.E.Thode,H.L.Shefield

Los Alamos National Laboratory

Previous Los Alamos FEL Experiments

1981-82 Amplifier Experiment
- 4% extraction efficiency with tapered wiggler
- optical gain measured

1983-84 Oscillator Experiment
- 10 kW output at 10 μ m
- "Perfect" optical quality
- Tunable from 9-35 μ m

1985-88 Energy Recovery Experiment (ERX)
- 70% of electron beam energy recovered
- FEL operation stable during recovery
- 2% extraction efficiency in oscillator

1986-89 Photoelectric Injector Demonstrated
- 600 A/cm^2 emission from 1 cm^2 Cs_3Sb cathode
- 3 Amp average current produced at 1 MeV
- Good emittance demonstrated (40 π mm-mRad at 6 nCoul)

1987-89 FEL Experiments Demonstrated
- Sideband suppression using Littrow grating
- 5% efficiency using prebuncher
- Validation of computer codes
- Lasing on 3rd harmonics (4 μ m)
- Harmonic measured to 7th harmonics

1988-89 Photoelectric Injector
- Durability of CsK_2Sb cathode
- 3 MeV operation
- 600 Amp peak current in 22 ps pulses

Schematic of a photoinjector

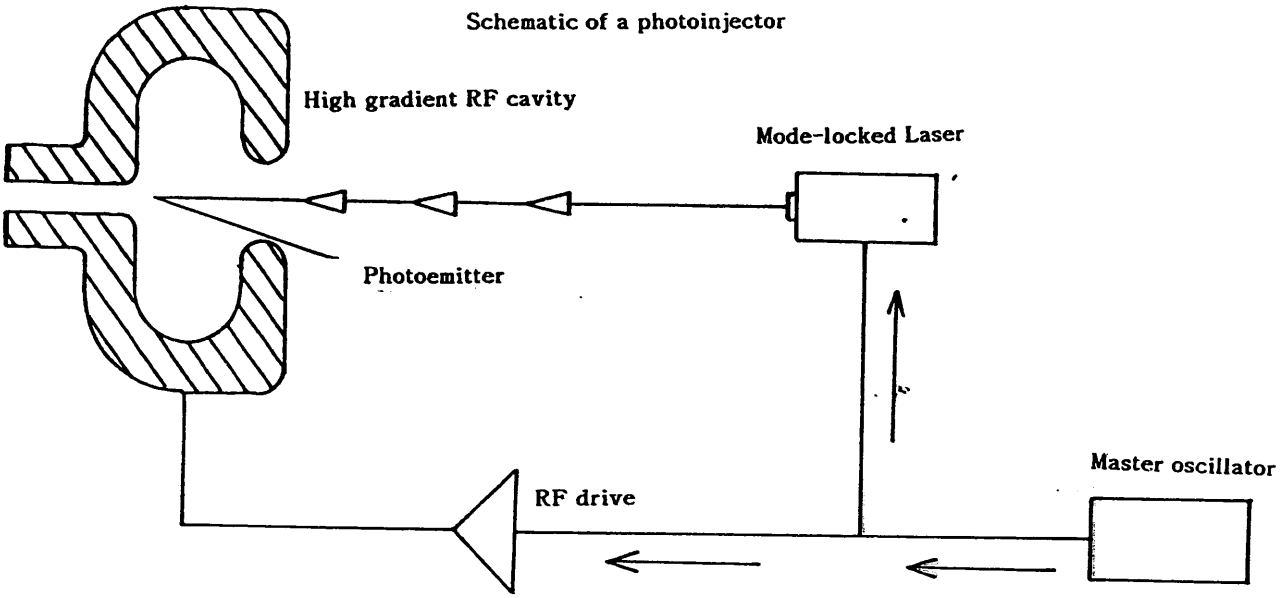

The Photoinjecter is an Internal Part of
the Accelerator Structure

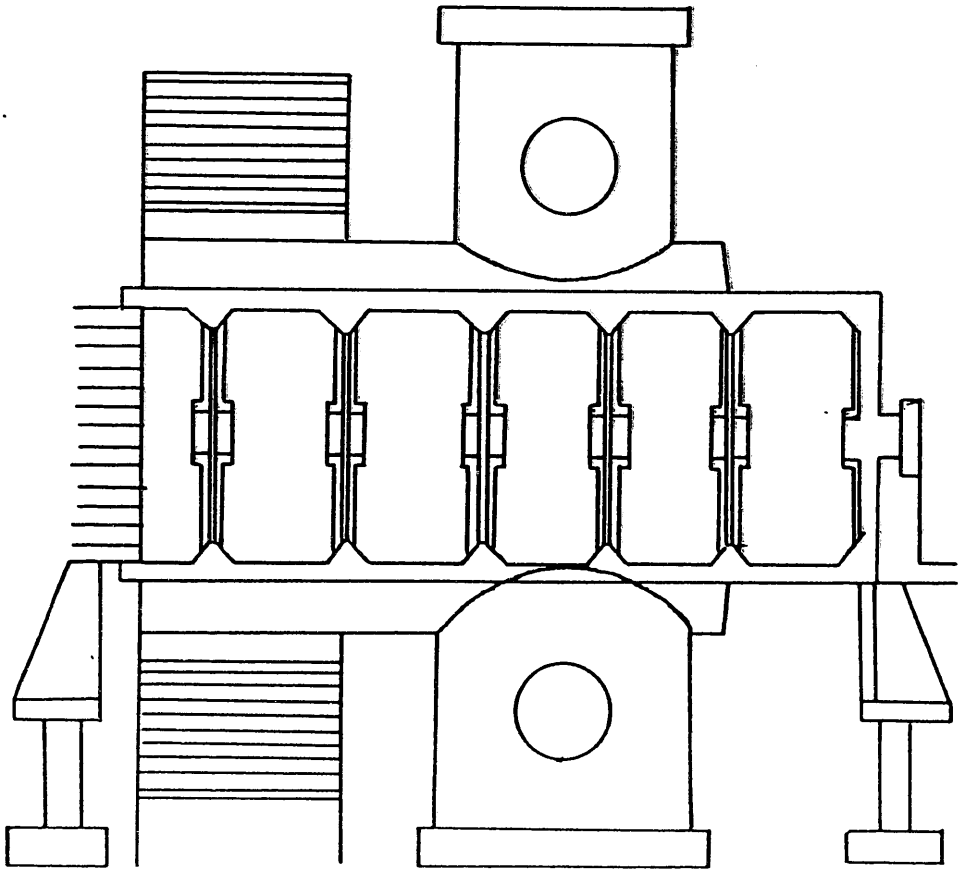

SUMMARY OF PHOTOINJECTOR PROPERTIES

Photoinjection laser

Nd-YLF Oscillator and Amplifier

Laser wavelength 525 nm

Laser Power 200 MW

Modulated frequency 10833 MHz

Micropulse repetition rate 2167 MHz

Macropulse repetition rate 100 Hz

Photocathode

Cs_3Sb quantum efficiency 1% at 525 nm

CsK_2Sb quantum efficiency 4% at 525 nm

Cathode area 1 cm^2

Electron macropulse

Pulse width

Average current

Output energy

Electron micropulse

Pulse width

Charge per Pulse

Peak current

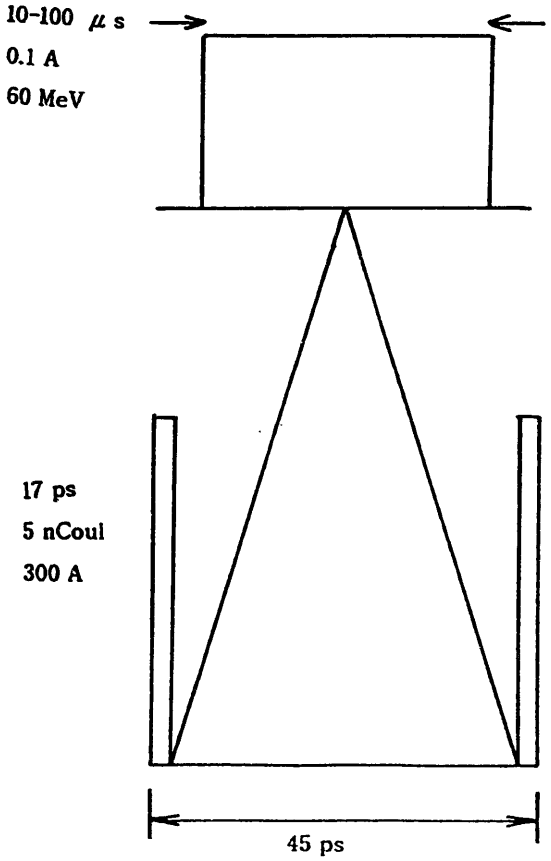

Acc field, cell #1	260 MV/m
Length	63.415 cm

==========

Output energy	6.0 MeV
μ pulse charge	5.0 nC
Beam current(avg)	0.1 A
(peak)	300 A
Emittance(90% norm)	50.0 ? mm-mr

Beam at Wiggler (Calc)

Beam energy	40.0 MeV
Energy spread	0.2 %
Macropulse rep rate	1.0 Hz
Macropulse length	10-100 sec
Micropulse rep rate	21.67 MHz
Micropulse length	16.6 ps
Emittance	$50.0% mm-mr
μ pulse charge	5.0 nC
Pulse current	300.0 A

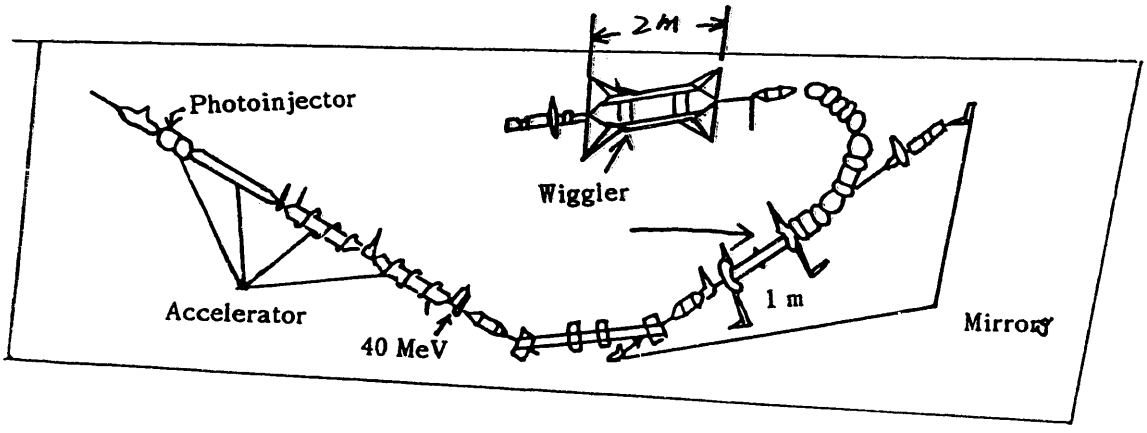

A. Small signal gain values.

Wiggler Case	Small Signal Gain	Wavelength (μ m)
W1	113	2.65
W2	43	2.70
W3	60	2.73

B. Power and efficiency for 20 % gain.

Wiggler Case	Wavelength (μ m)	Saturated Power (GW)	Efficiency (%)
W1	2.775	3.0	3.7
W2	2.800	3.5	3.7
W3	2.725	5.0	5.5

C. Power and efficiency for 10 % gain.

Wiggler Case	Wavelength (μ m)	Saturated Power (GW)	Efficiency (%)
W1	2.800	6.5	?
W2	2.800	9.0	?
W3	2.700	12.0	0.7

Expected HIBAF oscillator performance with a shortperiod wiggler (λ w=3 mm).
The measured electron beam parameters are: 40 MeV beam energy,
50 x mm-mRad emittance (90%), 0,25% energy spread, and 250 A peak current.
Calculations courtesy of J.C.Goldstein

	N=37 Periods (Lw=11 cm)	N=100 Periods (Lw=30 cm)
Rayleigh Range	25.0 cm	15.0 cm
Small signal Gain	15.5 %	64.0 %
Optical Wavelength	379.2 nm	375.0 nm
Power at Saturation	1.0 GW	0.6 GW
Saturated Gain	4.7 %	6.1 %
Saturated Wavelength	386.0 nm	386.0 nm
Extraction Efficiency	0.48 %	0.35 %

Predicted HIBAF SAMOPA operation gain parameters. The measured electron beam parameters are; 40 MeV beam energy and 50 ? mm-mRad emittance (90%). Calculations courtesy of J.O.Goldstein.

Present Status

Major components have been fabricated.

Test are being conducted at 17 MeV.

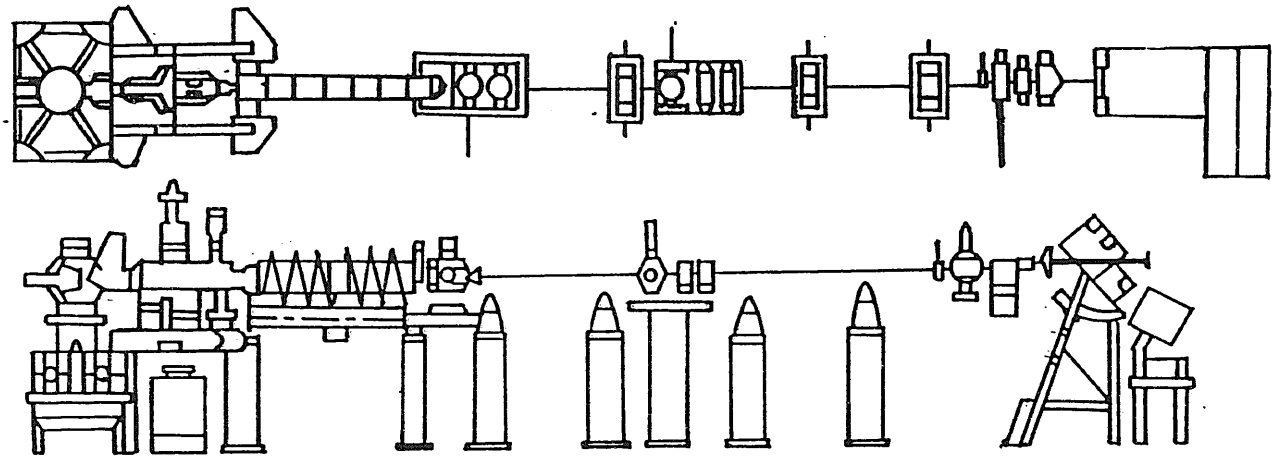

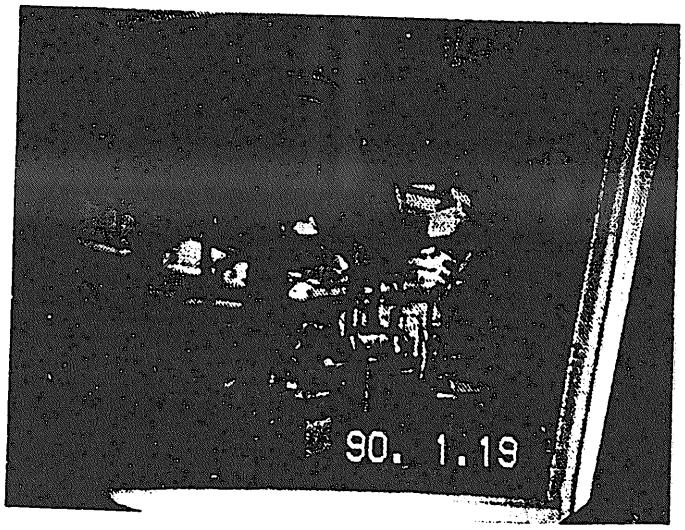

Conclusion

HIBAF will be a unique facility for continued development of
FEL technology.

1. High quantum efficiency photocathode rf gun.
2. Production and transport of high-current high-brightness electron beams.
3. Design mistake and ? electron beam diagnostics.
4. Update and calculate "integrated" numerical design code(NEX)
5. ? nw concepts.
6. Demonstrate maintenance of electron beam quality through large-angle bends.
7. ???

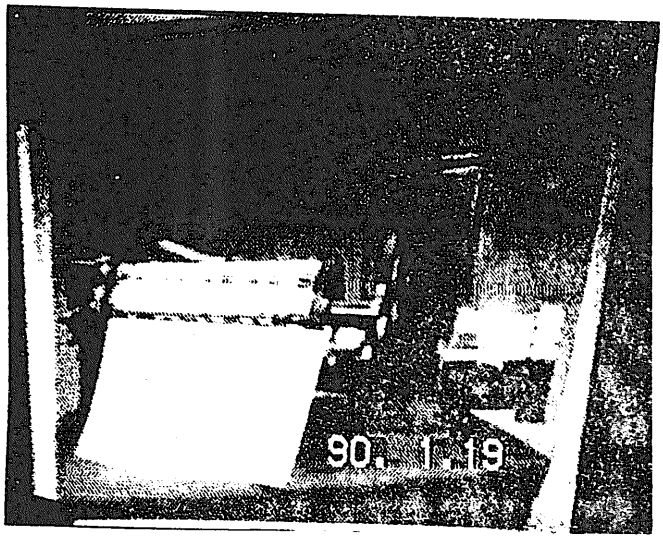
90. 1. 19

5．ＮＩＳＴ－ＮＲＬのＦＥＬ（レーストラック・マイクロトロン）

NIST-NRL FEL

Personnel

* NIST

R.G.Johnson FEL
R.L.Ayres
J.B.Broberg
R.L.Cutler
P.H.Debenham, Div.
B.C.Johnson
E.R.Lindstrom
W.A.Cassatt, GRR
D.L.Mohr
S.Penner*
J.E.Rose
J.K.Wittaker
N.D.Wilkin
M.A.Wilson, RTM
P.Liposky

* NRL

C.M.Tang
P.Sprangle
E.Esarey
W.Maratke
S.Pyoprulos

National Free-Electron Laser and electron Beam User Facility

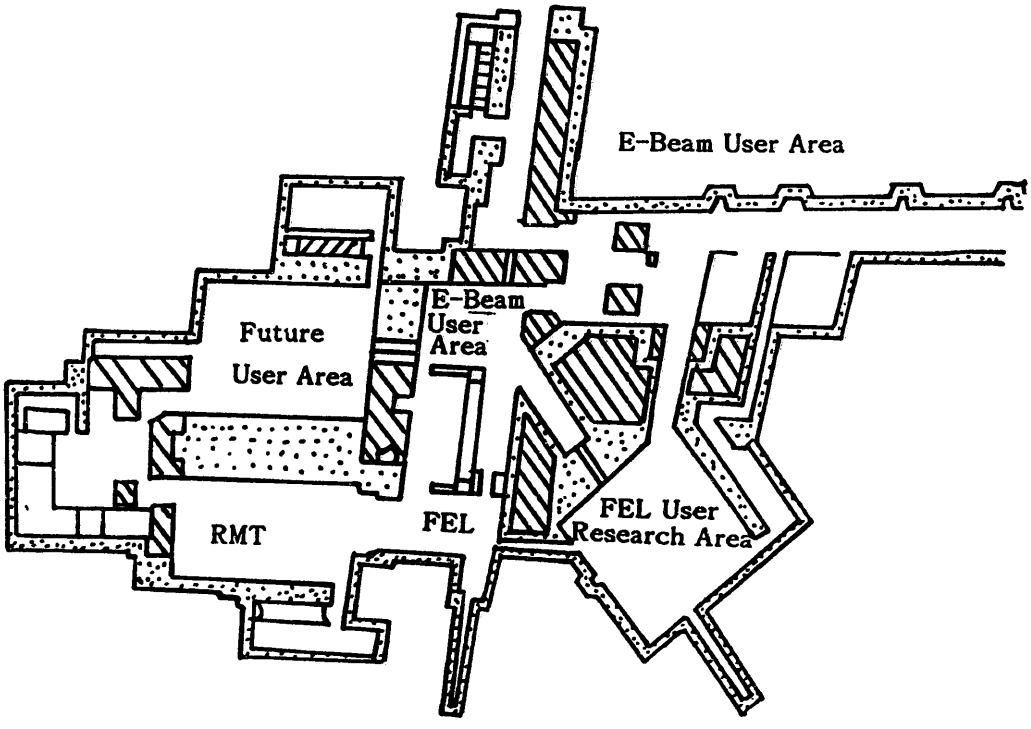

Output Light Properties

Wavelength	200 nm – 10 μ m
Average power	10 – 200 W
Pulse width	3 ps
Repetition rate	66.111 MHz
Peak power	40 – 1000 kW
Peak energy	0.1 – 3.0 μ J
Photon flux	10^{25} – $2 \cdot 10^{27}$ phot $cm^{-2}s^{-1}$
Photon density	$3 \cdot 10^{13}$ – $6 \cdot 10^{15}$ phot $cm^{-2}s^{-1}$
(3 mm-dis spot)	
Spectral resolution	$1.3 \cdot 10^{-6}$ – $6.7 \cdot 10^{-3}$
Polarization	Linear
Mode	TEM_{oo}
Beam diameter	0.6 – 1.6 mm
(1/e amplitude)	
Beam divergence	4.3 – 5 mrad

RTM

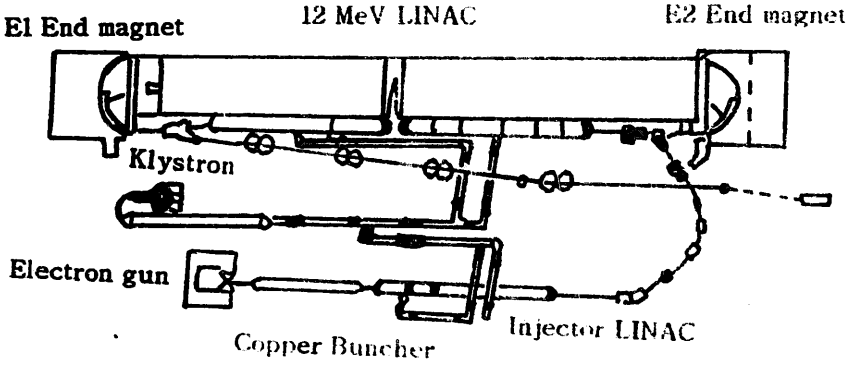

NIST_RTM Performance

	Original design	Measured 2/87	Measured 6/89	New gun design
Energy(MeV)	17-185	5.5	17	17-185
Average current (mA)	550 max	630	(300 in macropulse)	550 max
Average beam power (kW)	100 max	3.5	0.03	100 max
Peak current	0.07	-	-	2 - 4
Micropulse length (ps)	3.5	-	-	3.5
Micropulse frequency (MHz)	2380	2380	2380	65.1
Macropulse duty factor(%)	100	100	0.5	100
Energy spread(keV)	40 10	5 0.7	18 2.4	40 10

NIST-NRL FEL
Undulator Design

* Hybrid undulator (SmCo permanent magnets; vanadium permendur poles)
* Number of periods - 130
* Total length - 28 cm
* Maximum magnet field - 0.54 T
* Maximum gap - 10 cm
* Taper - 0.5 mm/m
* Vacuum chamber aperture - 0.85 cm(vertical)
  1.6 cm(horizontal)
* Operation in full or half length mode

Commercially Available Mirrors for NIST-NRL FEL

450 nm to 850 nm

Multi-layer Dielectric on Fused Silica

Bandwidth: ϕ 50 mm

Reflectivity: 0.9999

Absorption: 10-20 ppm

Distortion from Heating

* Observed to be negligible at 250 kW/cm^2 for CW dye lasers; we expect < 50 kW/cm^2, average
* Calculated distortion in steady state using finite element analysis method.

Dielectric Breakdown

* Damage threshold is 20 J/cm^2 in 1 μ s
* We expect 0.25 J/cm^2 in 1 μ s

Damage from Harmonics

* From experience at other FELs, we expect absorption to increase.
* We are calculating harmonic radiation.
* Deacon Research in Phase I of UV-induced damage study for multi-layer dielectrics that are designed for 240 nm.
* FEL operating parameters must be adjusted so that harmonic content is minimized.

NIST-NRL FEL

Research Program

* Experts in a broad range of research areas will set the direction of the research program initially through a series of workshop.
* Biomedical users workshop (13 - 14 September 1989).
  - Time-dependent fluorescence measurements for molecular dynamics and structure
  - Time-resolved spectroscopy of nucleic acids for DNA dynamics and protein-nucleic acid interactions
  - Time-resolved spectroscopy to study photon migration in tissue
  - Raman spectroscopy to study protein folding and conformation
  - Optical measurements of biomacromolecules stimulated by synchronous energy surface (e.g. microwaves, x rays)
  - Light penetration mapping; optical tomography
  - Tissue welding and ablation; cell penetration for protein infusion; optical interaction with drugs
* Other workshops planned
  - Surface and materials science
  - Fast chemistry
  - Fiber optics
  - Radiometry and

NIST-NRL FEL

Facilities Development

* Pump source to provide multiple frequencies (because of high average power)
  - Dye lasers including uv dyes; produce fs pulses
  - Optical parametric oscillators and amplifiers
  - Solid state lasers
  - Mixing schemes
* Dynamic studies of FEL physics (because of continuous lasing)
  - Frequency scanning by undulator gap adjustment
  - Various outcoupling to study saturation and maximum output power
  - Power and frequency stabilization by feedback

FEL-RTM

Milestone

• FEL User Area is cleared of old equipment	2/90
• Electron gun and chopping/bunching cavities for high-current injector are ordered	4/90
• Engineering design of FEL optical cavity is completed and major components are ordered	7/90
• Undulator is installed and tested at NIST	6/90
• Construction of RTM is completed	
• Construction of electron beam transport line is completed	7/90
• New power supply for RTM klystron is installed and tested	9/90
• Controls for complete RTM and electron beam line are tested	11/90
• First full-energy operation of RTM with present injector	1/91
• RTM performance tests with present injector are completed	4/91
• Present RTM injector is replaced with high-current injector	11/91
• Laser cavity, optical beam line, and diagnostics are installed	11/91
• Control for FEL and high-current injector are tested	12/91
• First lasing	2/92
• First FEL operation for users	5/92

The UCSB FEL Development Program;
Status and Plans

Gerald Ramian
Center for Free-Electron Laser Studies
Quantum Institute, University of California
Santa Barbara, CA 93106

Presentation to;
OE/LASE'90
Los Angels, CAlifornia, Jan.18,1990

6．カリフォルニア大学サンタバーバラ校　量子研究所　（静電加速器）

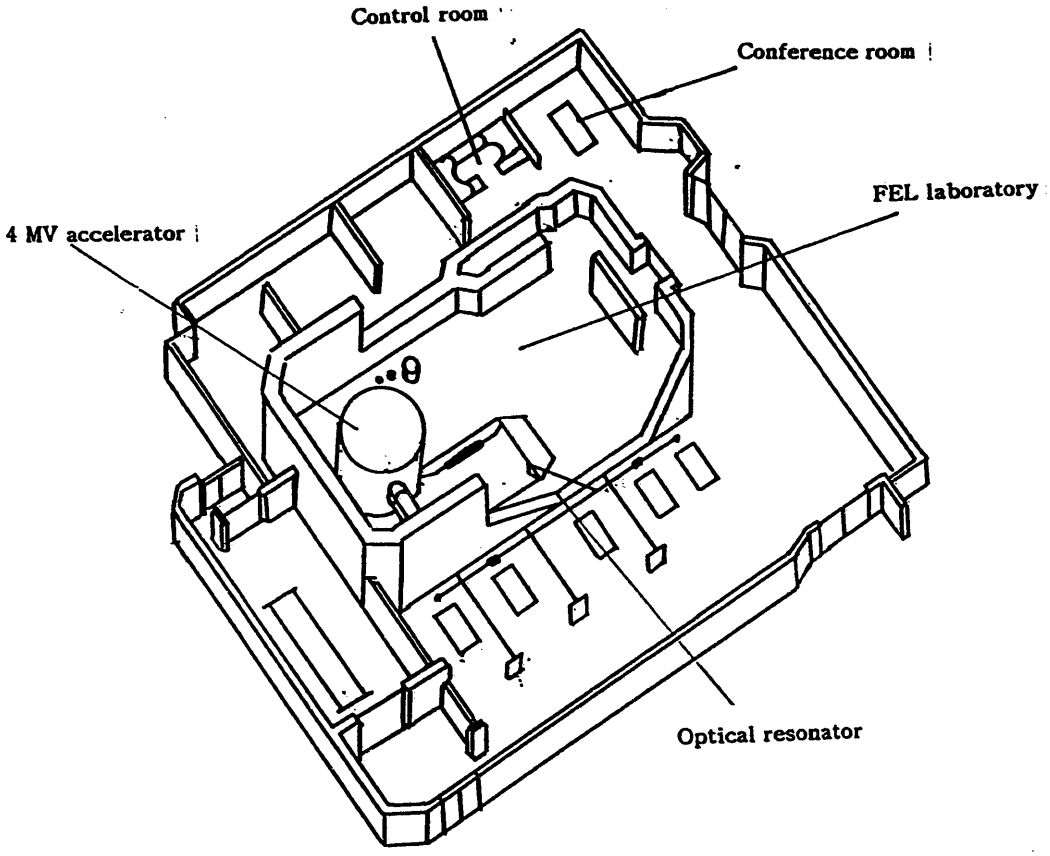

Optical resonator Research Center for Free Electron Laser Studies
University of California, Santa Barbara

The Electrostatic Accelerator has Significant
Advantages as an FEL Beam Source

* No Thermal Microstructure
  - Narrow linewidth - long coherent length
  - No damage to optics of samples by very high peak power

* Absence of strong time-dependent field gradient
  - acceleration with minimum beam degradation

* Recirculation
  - Static fields permit deceleration and collection of a beam with perfect efficiency

* Simple Reliable operation
  - Accelerator is a simple, self-contained mechanical device that can be switched on or off with a minimum of loss

Electron Beam	
Energy	2.0 - 6.0 MeV
Current	1.0 - 20.0 A
Emittance	$\approx$ 10 - 30 π -mm-mr
Energy spread	$\approx 10^{-3}$
Recirculation	$\approx$ 95%

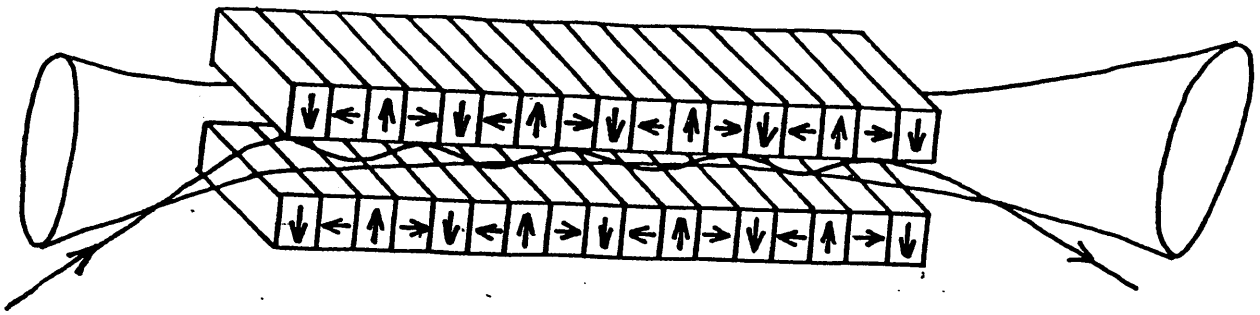

"HALBACH" Configuration of Original UCSB FEL

Field Homogeneity : $\Delta B/B_{av} = 2\%$

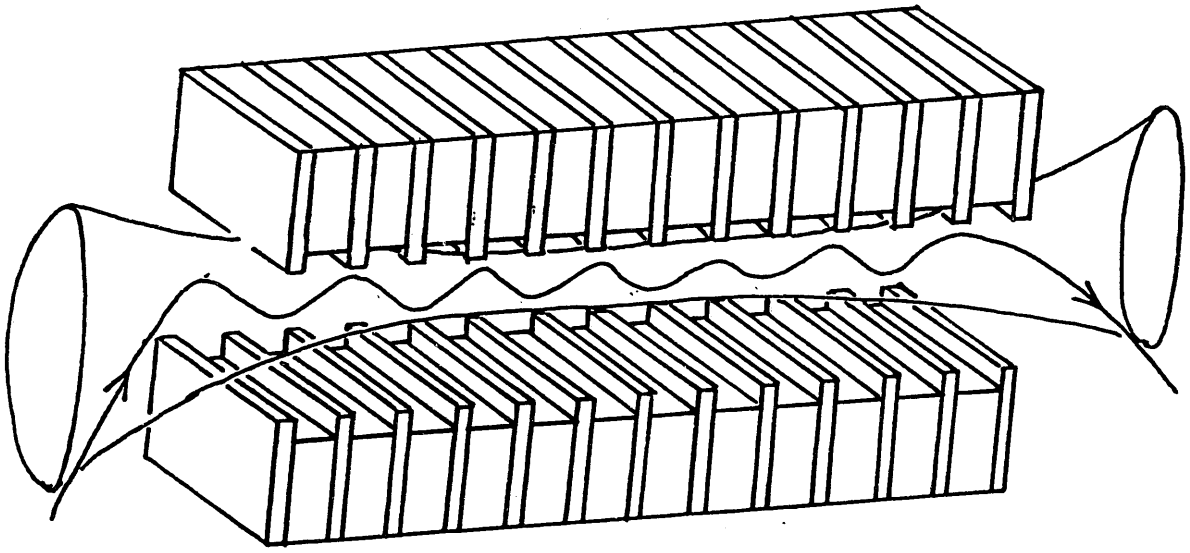

UCSB Wiggler HALBACH Configuration

* Fields in gap determined by pole tip geometry

The Computer Optimized Hybrid Undulator
is Based on Several Principles

1. A Small Attractive Force

$$F = \frac{1}{\mu_o} \int_{-} B\, ds$$

exists between magnets and pole tips that facilitates the sliding of pole tips as a positioning mechanism

2. The required pole tip positions can be determined by the small taneous solution of 2N equations in 2N unknowns

3. Elementary simple analytical model exists to determine the elements of J.

Computer Optimization of Undulator

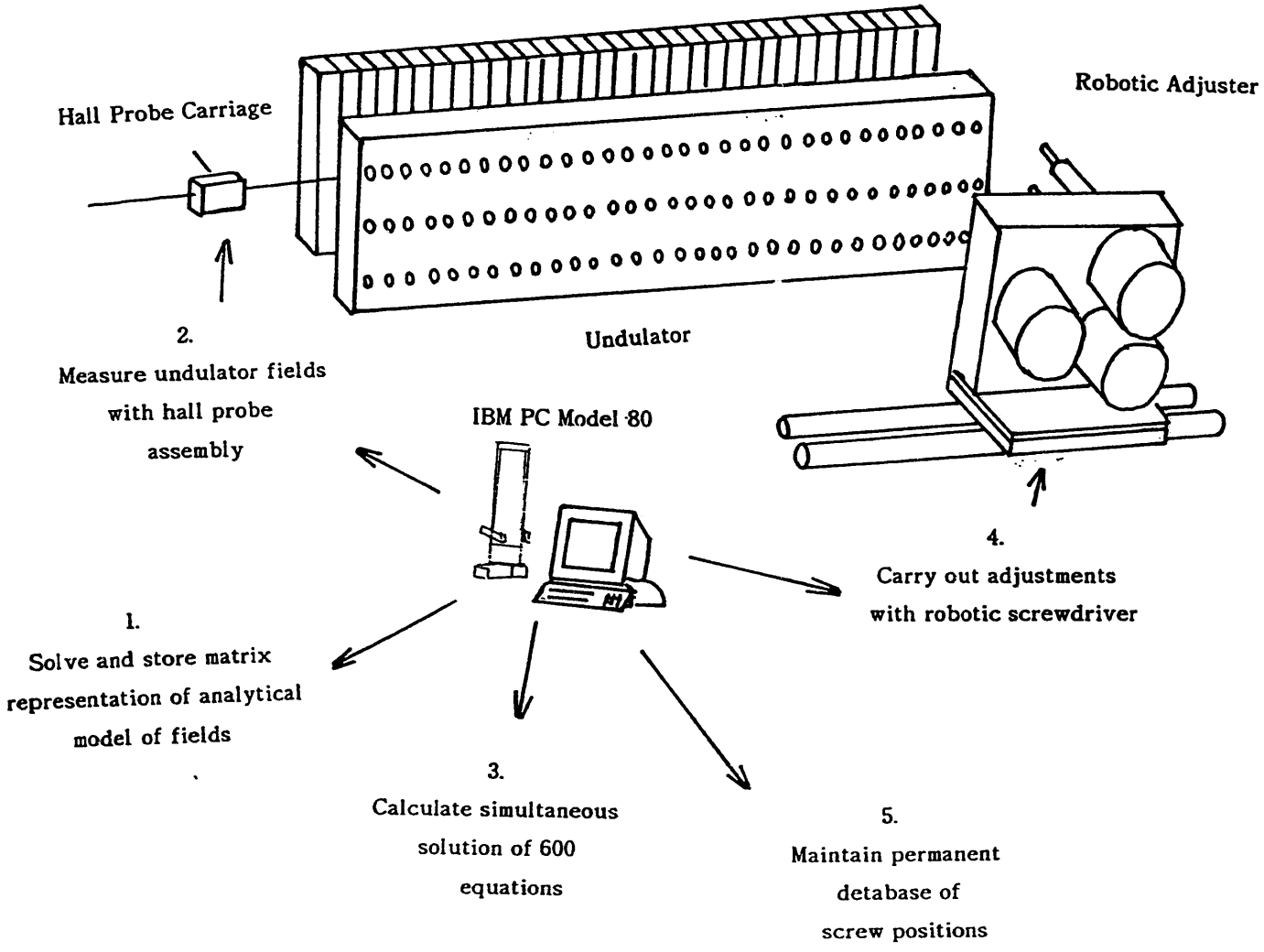

A New UCSB FEL Undulator Produces Fields
of Unprecedented Accuracy

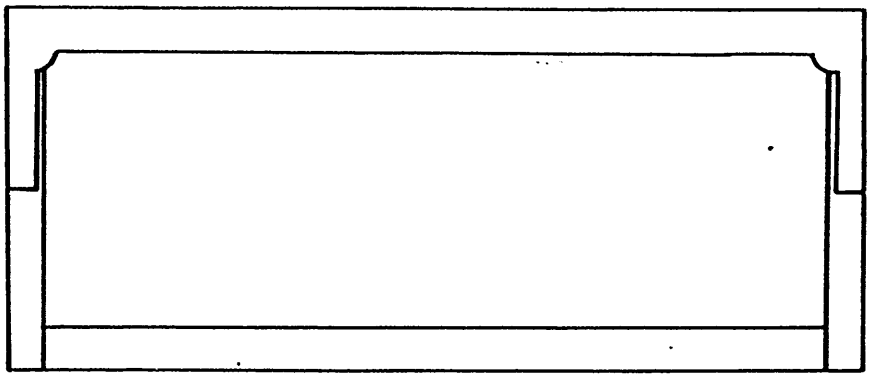

δ B/B = 0.11%

E = 49 MeV λ = 90 μm

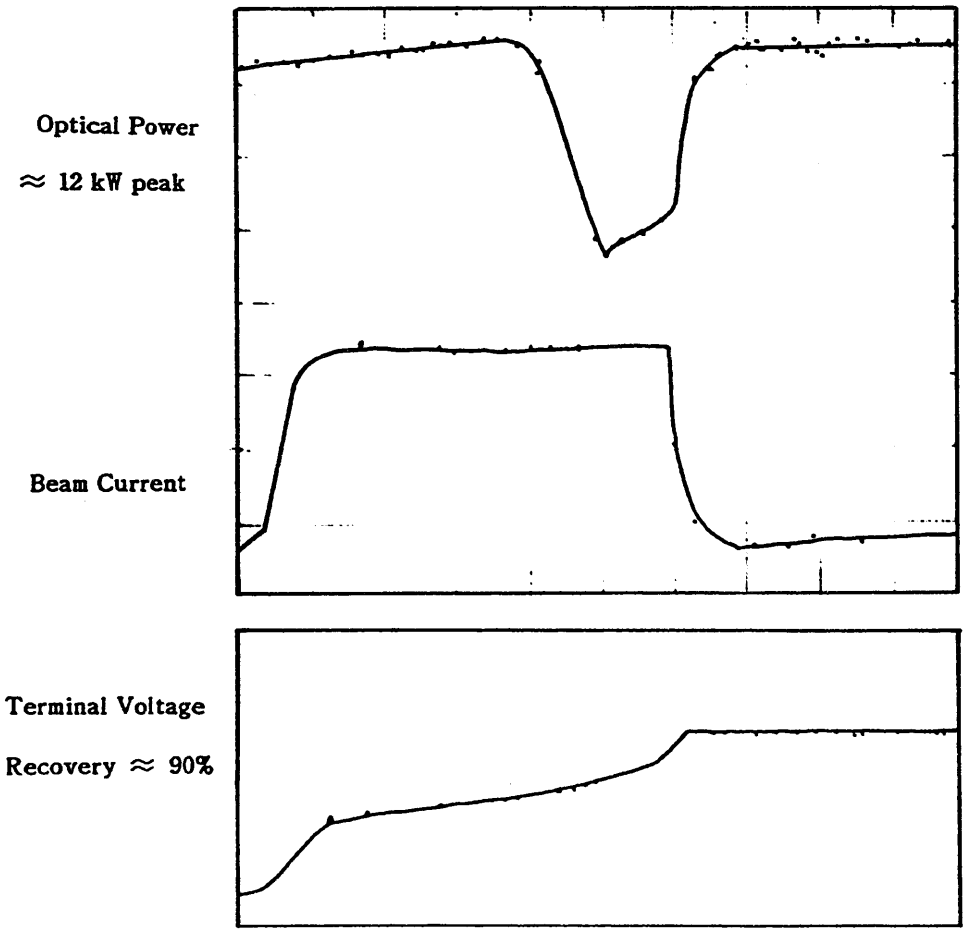

Silicon Cavity Dump Coupler

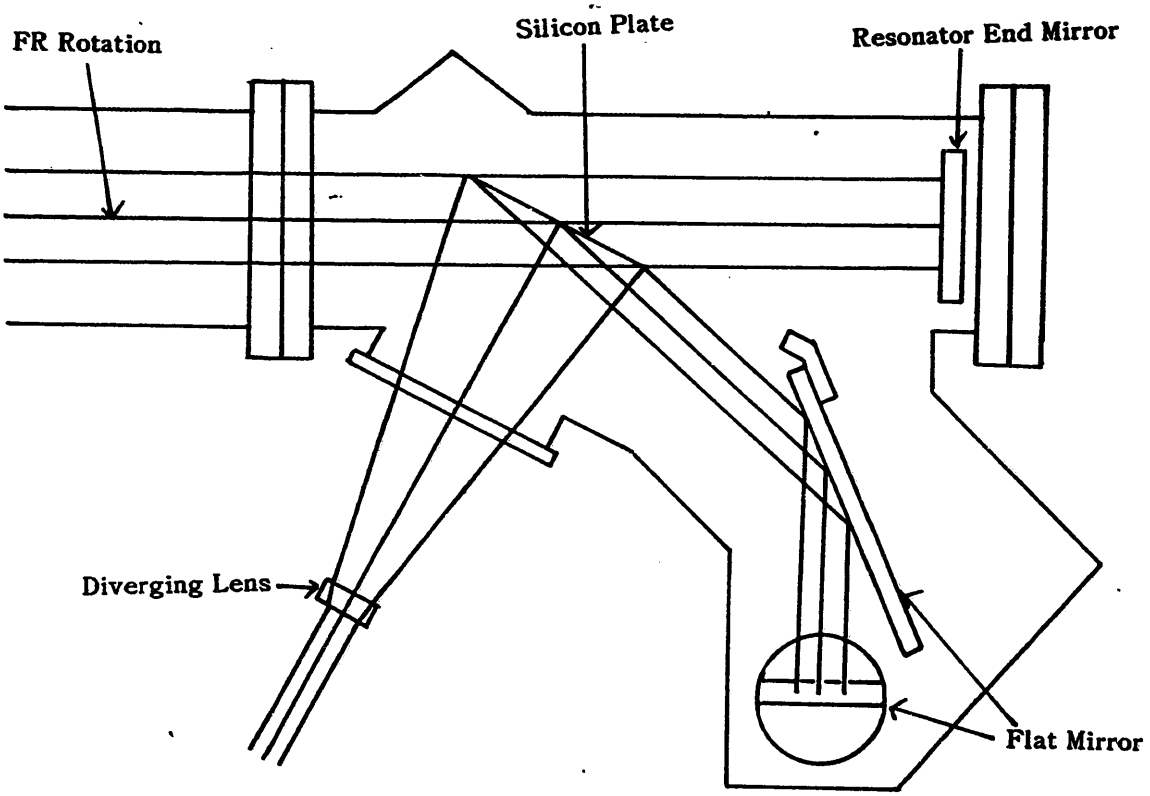

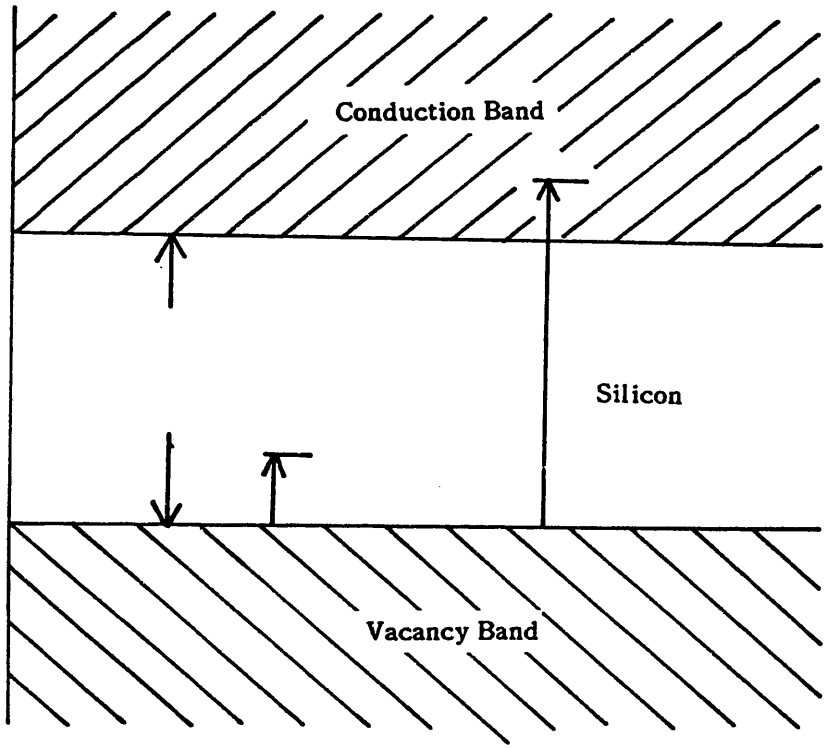

Planned FEL Development st UCSB

1. New Wavelength Extension FEL
   * Millimeter Wave
   * Mid-Infrared
   * EM-Undulator Experiment

2. Beam Switchyard

3. Control System Improvements

4. Other Development Projects
   * Average Linewidth Narrowing
     Injection locking
     Computerized Charging
     New GVM
   * Terminal Stabilizer
   * Free-Beam Optical link system
   * Collector Beam Spectrometer
   * New Spectrometer System
   * Transition Radiation Beam Diagnostics

Millimeter FEL

MM Wave FEL Parameters	
	Design
Energy	2.0 - 6.0 MeV
Current	2.0 A
λ_o	5.0 cm
λ	1.34 mm - 193 μm
P_{out}	4 - 37 kW

Features;

* 1.3 mm - 200 μ m wavelength coverage
* Uses new tunable undulator technology
* Use many components from original FEL

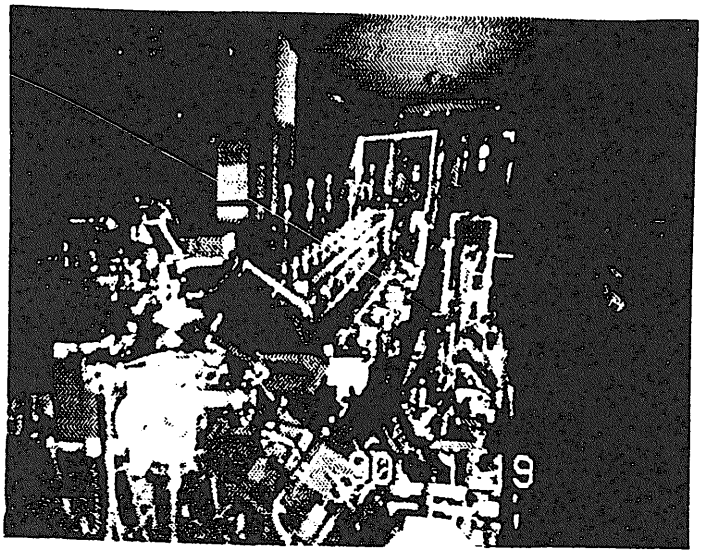

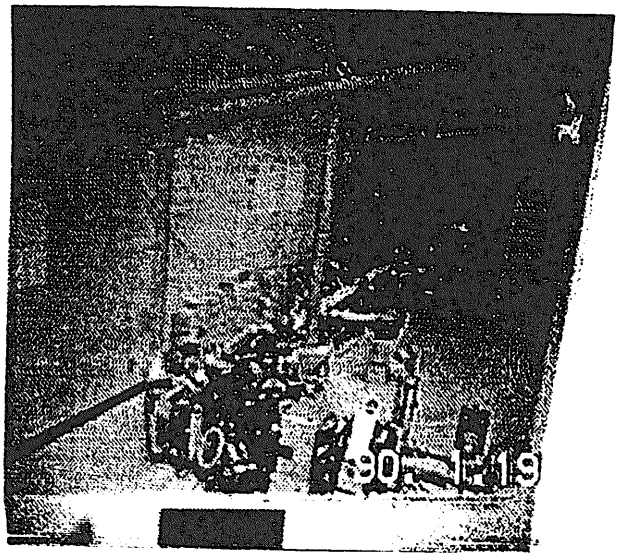

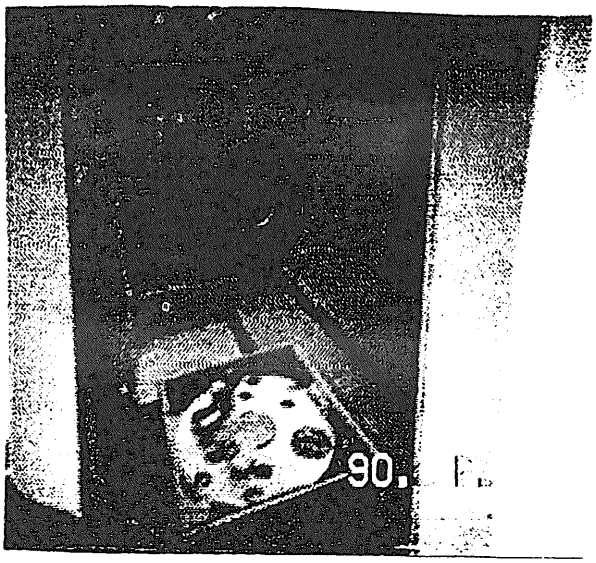

Mid-Infrared FEL

Mid-IR FEL Parameters	
	Design
Energy	4.0 - 6.0 MeV
Current	2.0 A
λ_o	1.85 cm
λ	64 - 30 μm
P_{out}	4 - 8 kW

Features;

- Wavelength coverage to 30 μ m
- Uses 3rd harmonic generation
- Uses new tunable undulator technology

Challenges;

- Undulator in vacuum environment
- Suppression of fundamental lasing
- Stringent electron beam quality requirements
- Diagnostics for small, high current-density beam

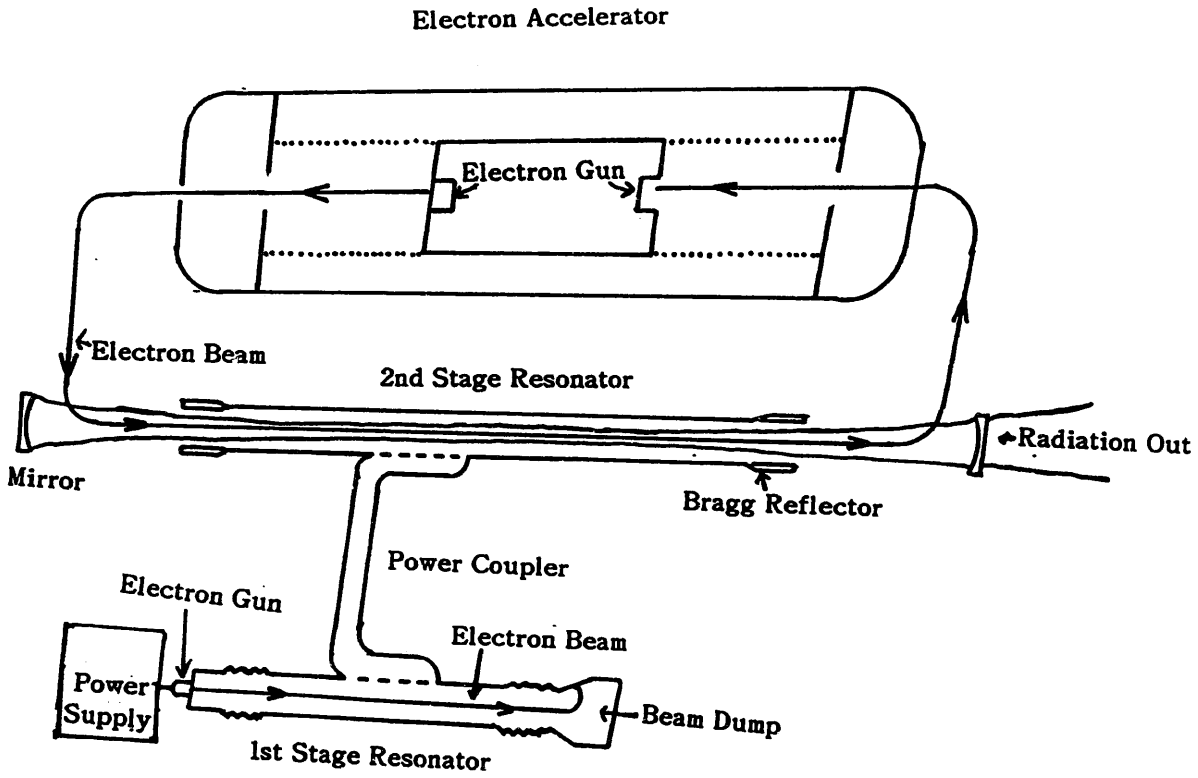

	FY '90	FY '91	FY '92	Future
λ	50 μm	16 μm	8 μm	5 μm
υ_1	30 GHz	30 GHz	60 GHz	90 GHz
P_1	500 kW	1 MW	2 MW	5 MW
E_2	3 MeV	6 MeV	6 MeV	6 MeV
I_2	5 A	10 A	20 A	20 A

Proposed Beam Switchyard

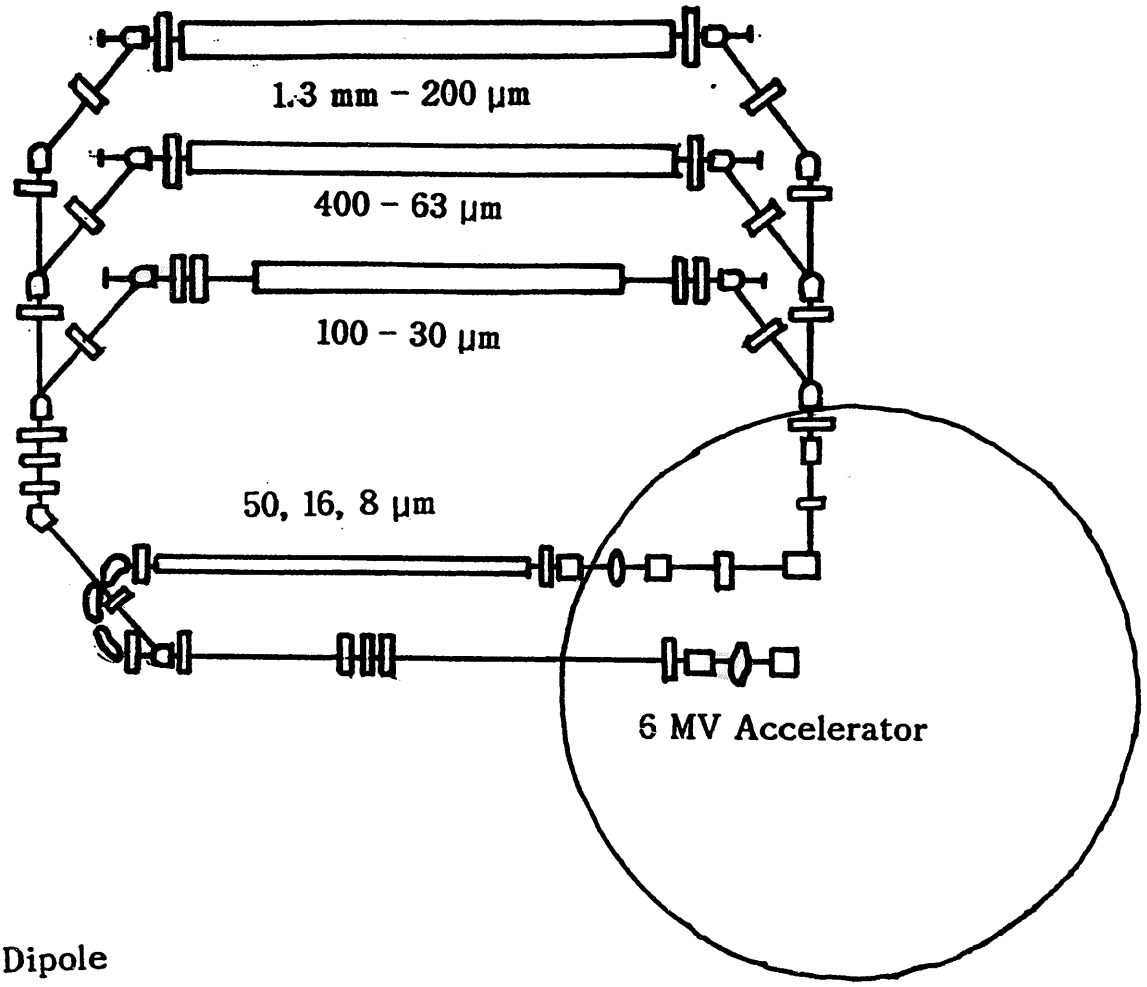

● Dipole

■ Quadrapole

* Major restructuring to accommodate four new FELs
* will use new higher quality dipoles
* will use a more sophisticated alignment system
* will require more sophisticated electronic control
* in house capability in beam line design and construction

A 2MV Test Accelerator is under Construction at UCSB

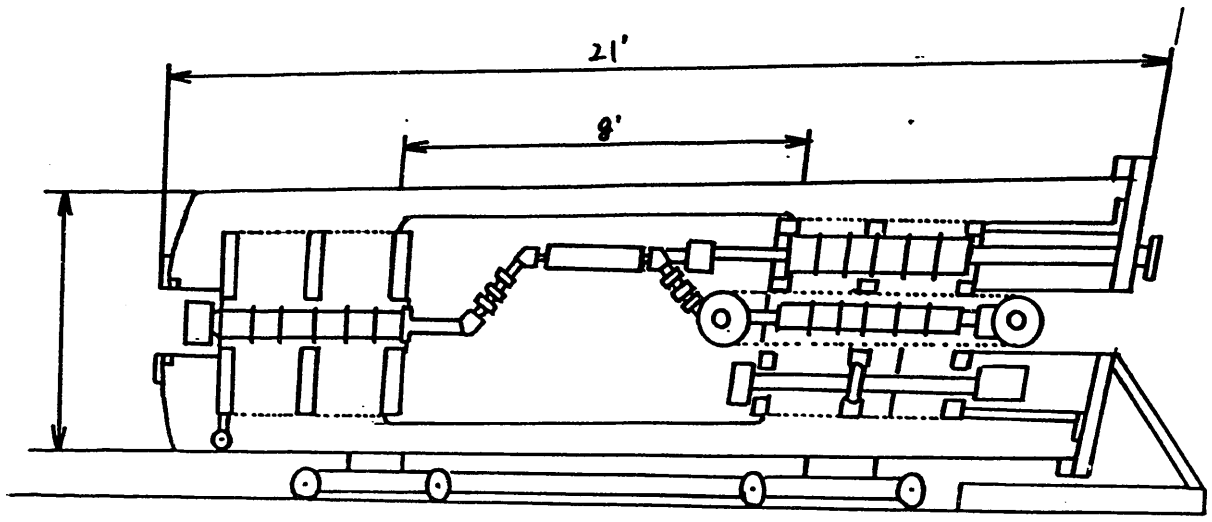

Illustration of 2MV Test Accelerator with Compact FEL Components ;

Applications;

- Development of high current-density beam diagnostics and technology
- Development of Phase 2 undulator and technology for the 6MV machine
- Demonstration of "next generation" FEL concepts
- Provide second source of radiation to user facility

Wavelength Available to Scientific Users

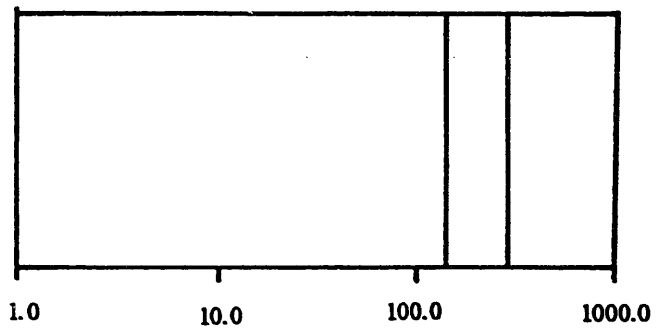

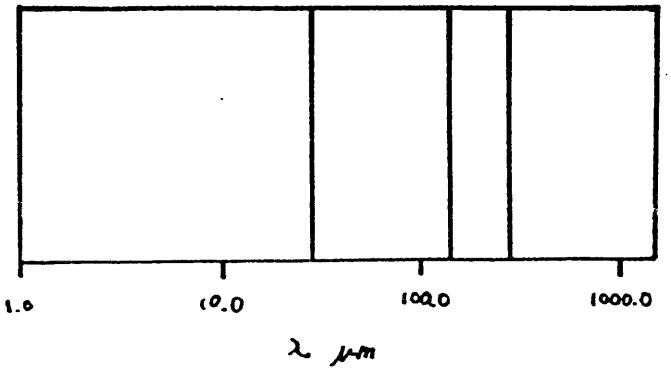

- Extend wavelength coverage from the Mid-IR out to the MM
- Extend the characteristics to cover microsecond to nanosecond pulse

1．2　FEL用光共振器

Grazing Incidence Ring Resonator for Visible Wavelength Free-Electron Laser(FEL)

Kennth C.Sun Rocktdyne Division , Rockwell International

- Grazing Incidence Ring Resonator
- Mirror Fabrication
  - Single Crystal Silicon
  - Grinding & Polishing
  - Profilometry
  - Interferometry
  - Coatings
- Alignment
  - Dynamic Alignment
  - Fast Steering Mirror
  - Outcoupler
- Summary

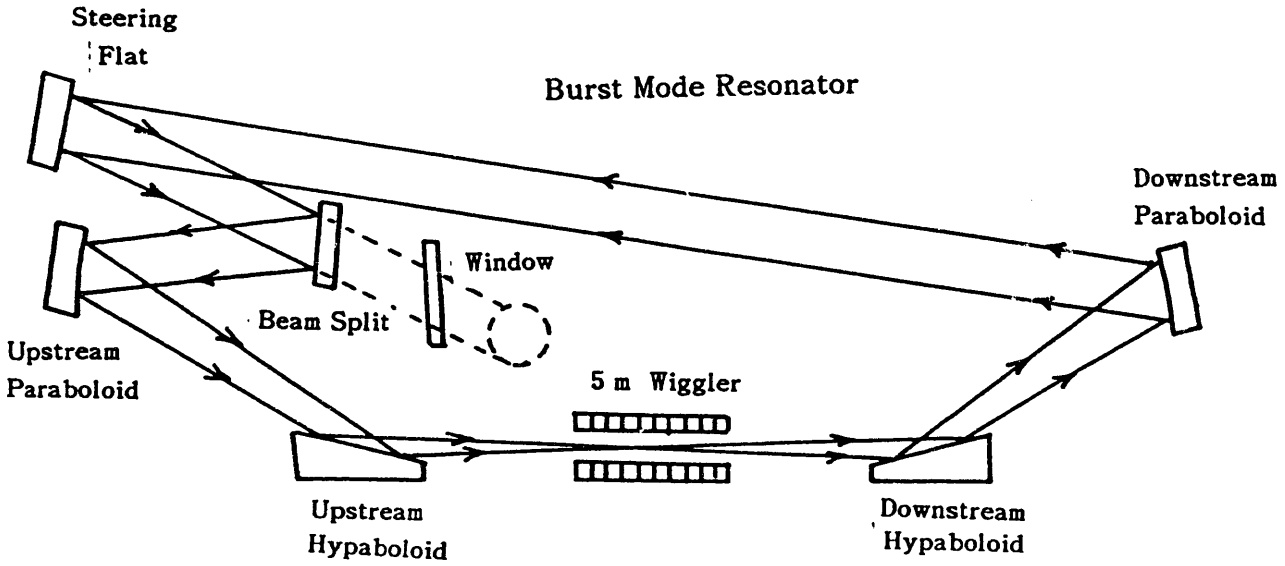

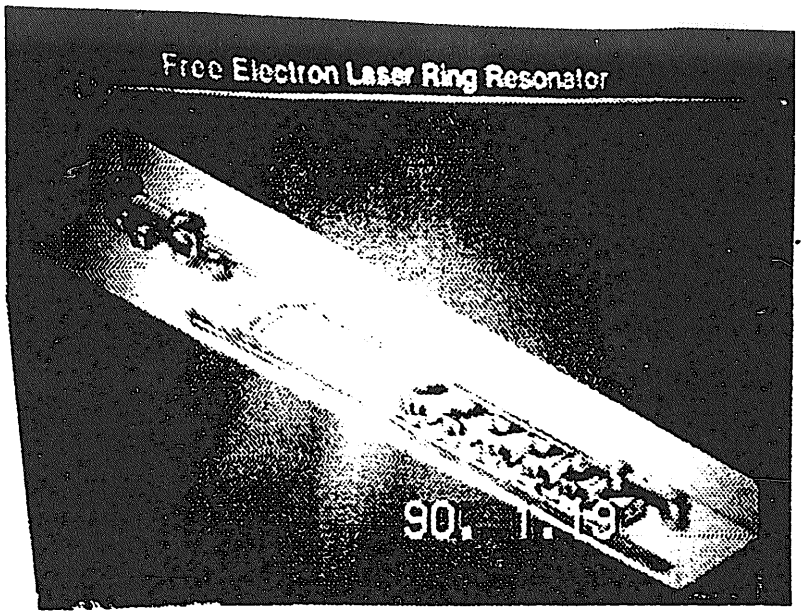
Free Electron Laser Ring Resonator

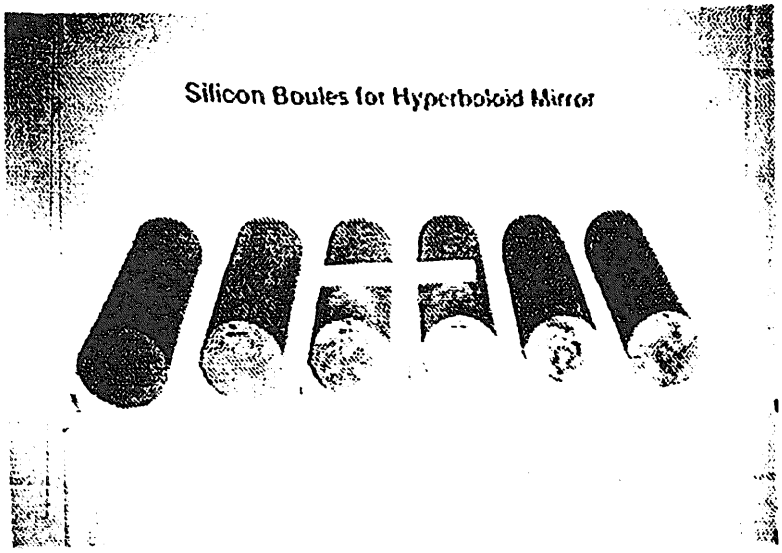
Silicon Boules for Hyperboloid Mirror

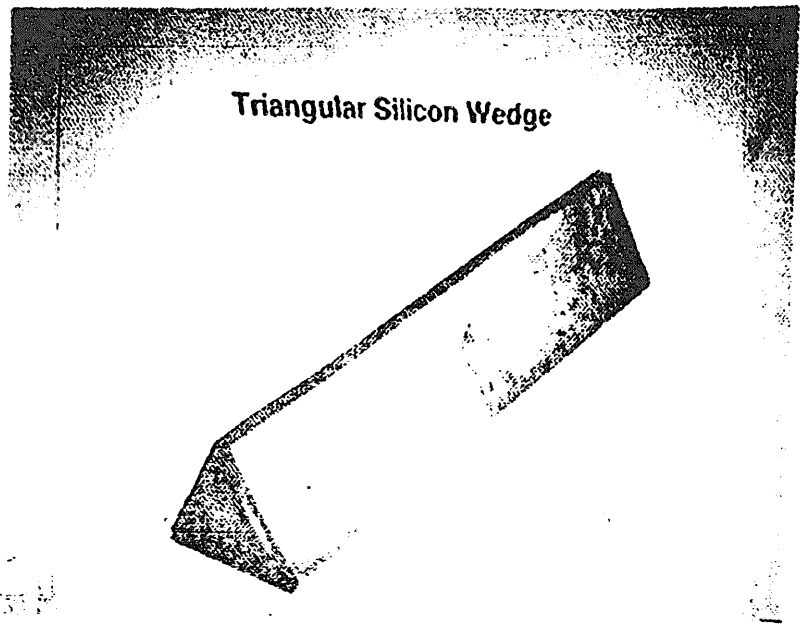
Triangular Silicon Wedge

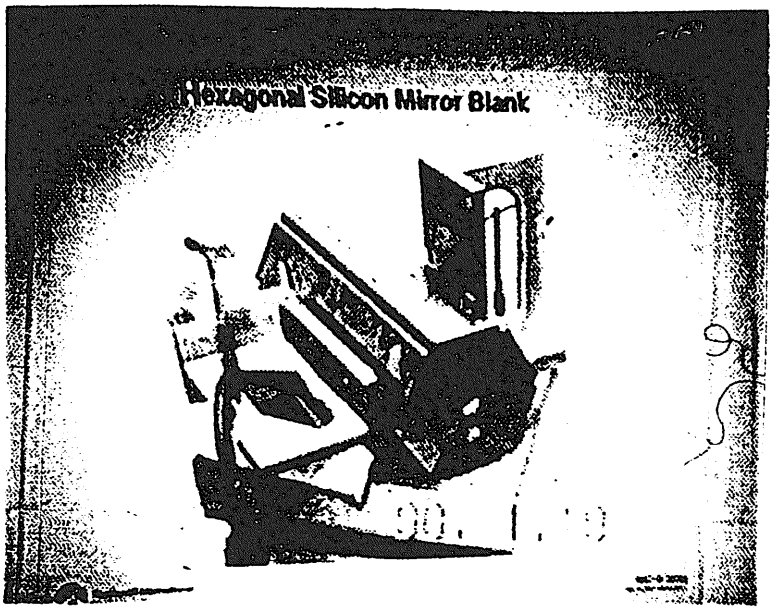
Hexagonal Silicon Mirror Blank

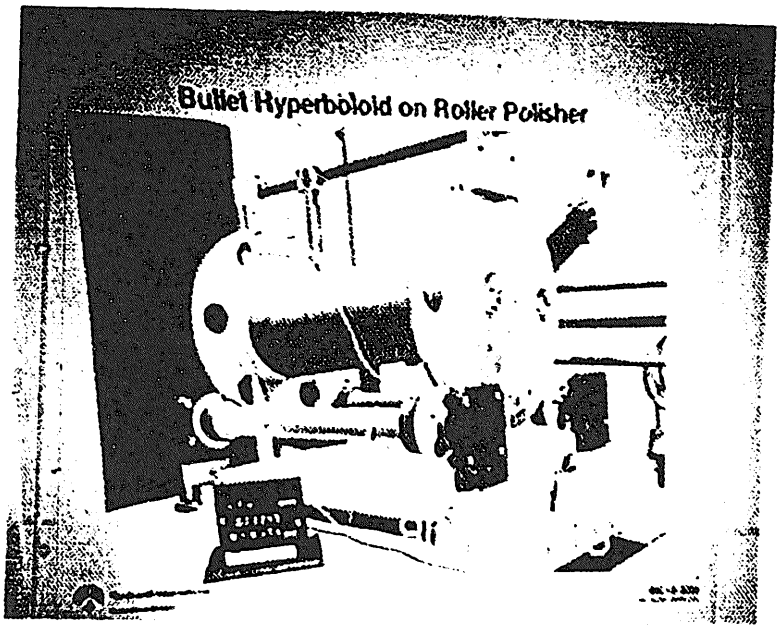
Bullet Hyperboloid on Roller Polisher

Cyllindrical Measurement Machine (CMM)
Records Surface Figure Errors

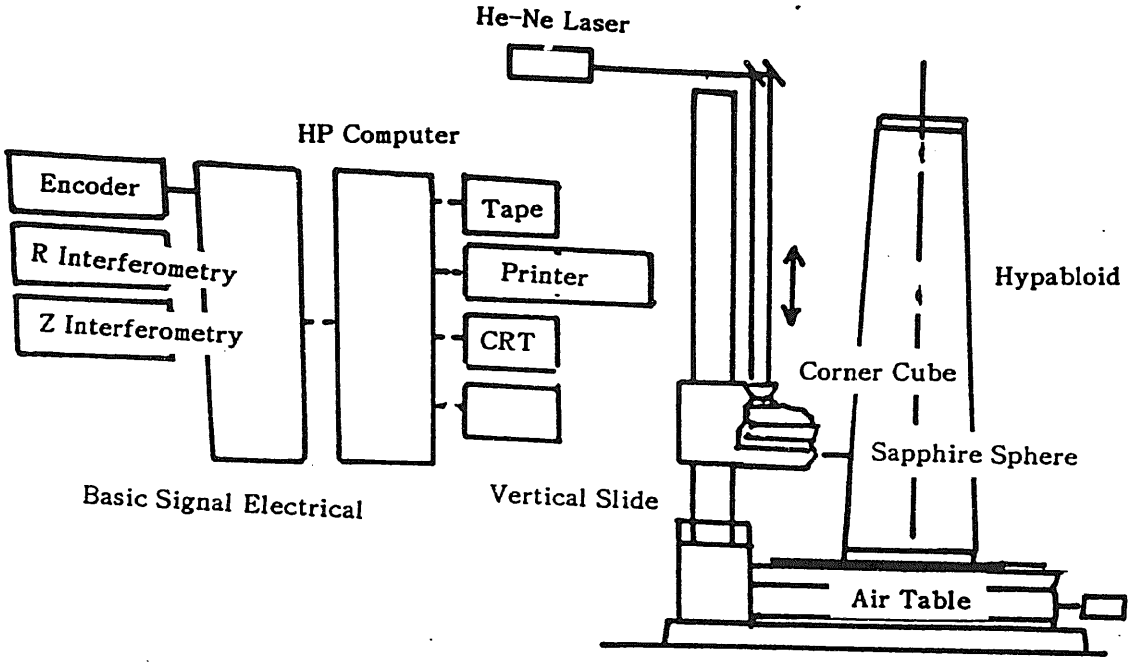

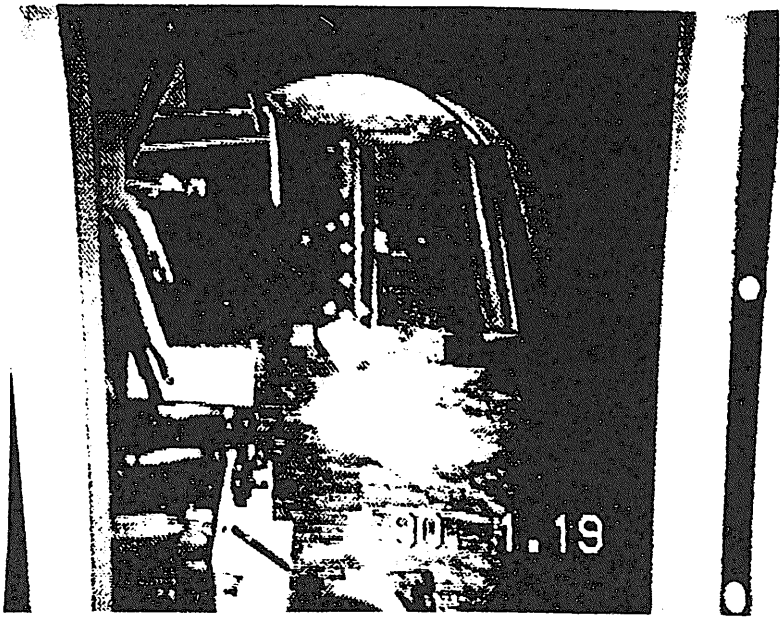

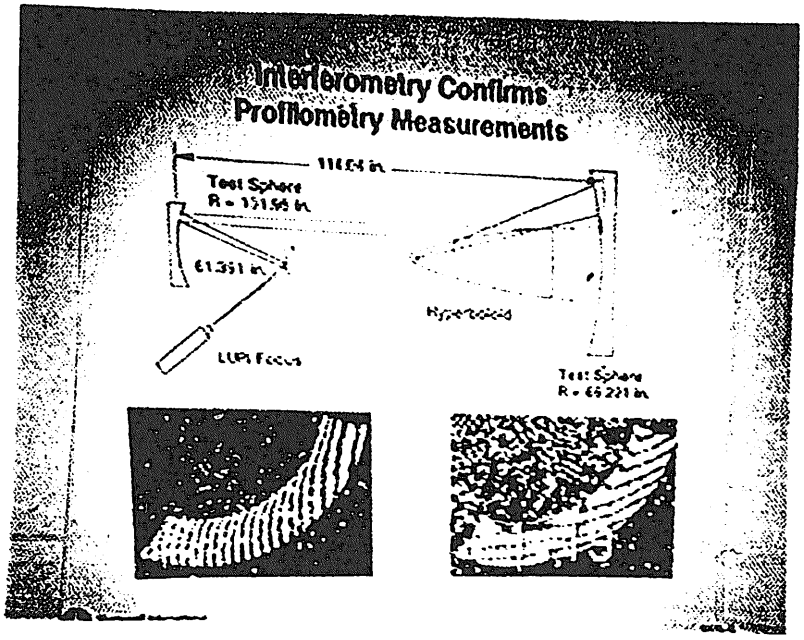

Full-Scale Aspheric Surface Figuring Has Been Successfully Demonstrated

Grazing Incidence Hypaboloid Mirror

* Quality - 6 mirrors
* Size - 64 cm long
* Radius of curvature
  11x3400cm
* RMS wavefront error
  λ /34 at λ =0.6328 μ m
* 17 A RMS roughness

Off-Axis Paraboloid Mirror

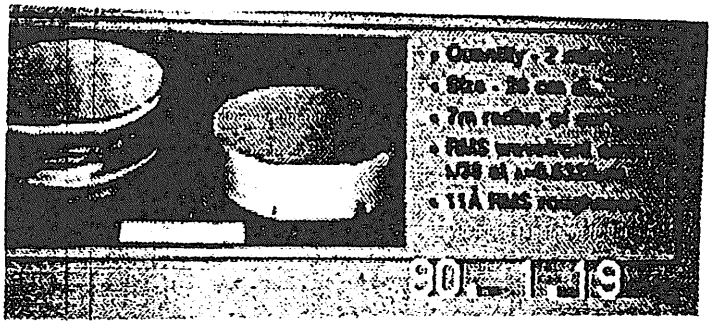

* Quality - 2 mirrors
* Size - 28 cm diameter
* 7 m radius of curvature
* RMS wavefront error
  λ /36 at λ =0.6328 μ m
* 11 A RMS roughness

FEL Coatings Have High Reflectivity & Low Absorption

Mirror	Coating Material	Reflectivity	Absorption	Wavefront Destortion
Silicon Hypaboloid	Bare Silver	98.5% at 0° 99.93% at 87°	1.5% at 0° 0.06% at 87°	λ /? for
Silicon Paraboloid	$ZrO_2/SiO_2/TiO_2$	99.99%	0.001%	λ /27 for 1.5" witness
Silicon Steering Flat	$ZrO_2/SiO_2/TiO_2$	99.99%	0.001%	λ /22 for 1.5" witness λ /20 for 11" mirror
Fused Silica Outcoupler	HfO_2/SiO_2	variable with wavelength	0.002%	λ /30 for 1.5" witness λ /30 for 11" mirror
Fused Silica Window	ZrO_2/SiO_2	< 0.1%	0.001%	λ /30 for 12" window

λ = 0.6328 μm

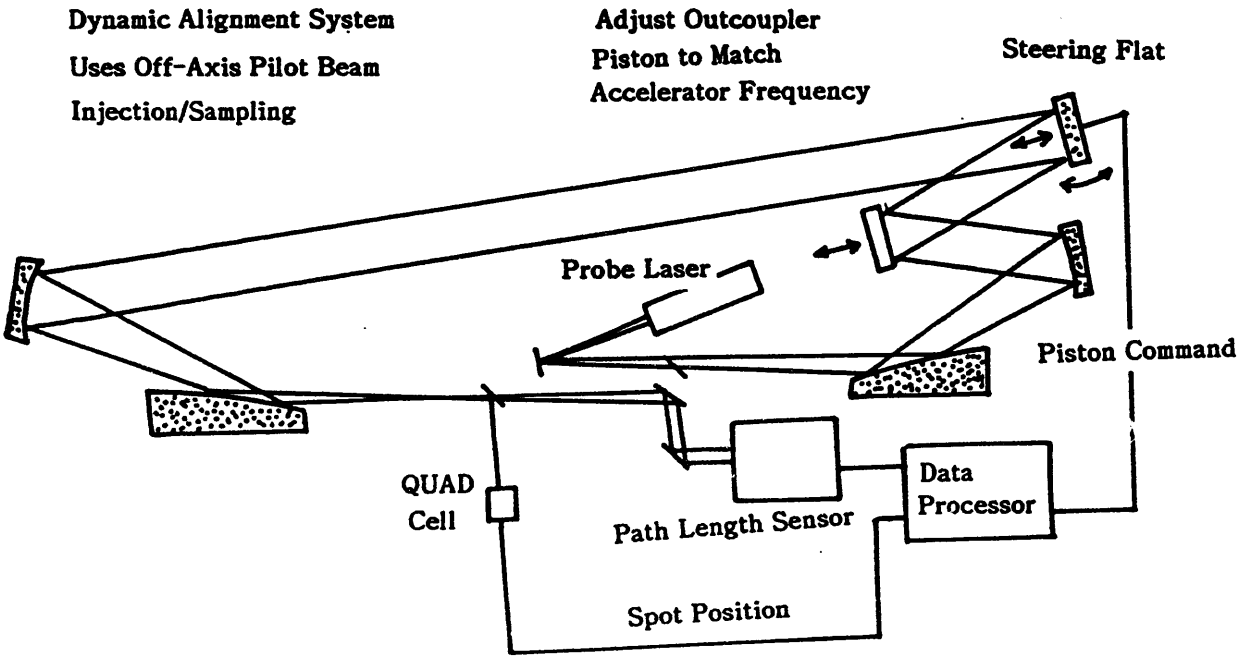

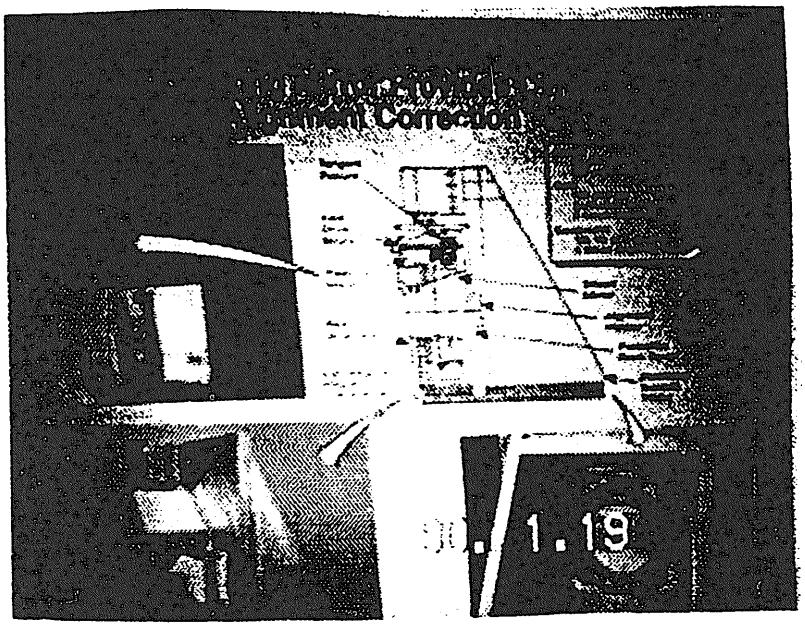

Fast Steering Mirror Provides
Dynamic Alignment Correction

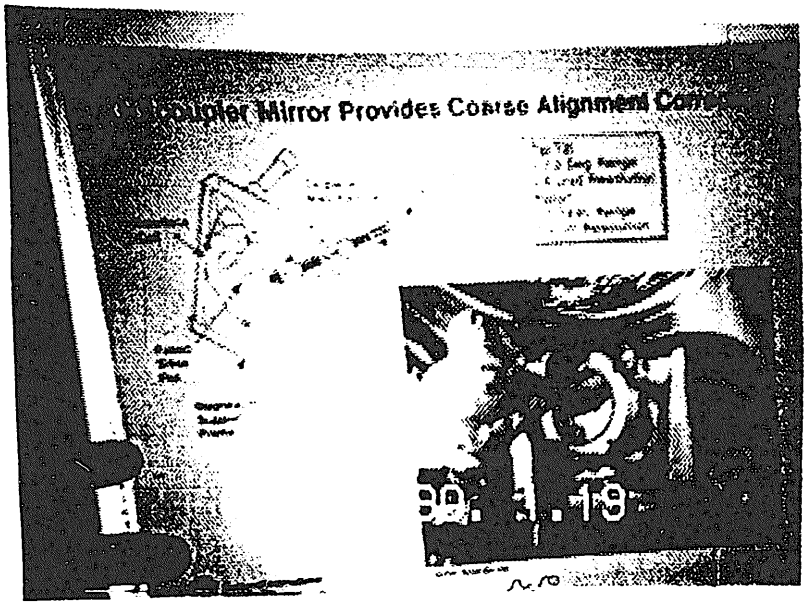

Outcoupler Mirror Provides
Coarse Alignment Correction

Summary

* Full Scale Grazing Incidence Ring Resonator
* High Quality Large Aspheric Silicon Mirrors
    * λ /30 rms wavefront error for six grazing incidence hypaboloid
    * λ /40 rms wavefront error for two off-axis paraboloid
* Rockwell Has Just Entered Water Cooled Silicon Mirror Business
    * Rocketdyne acquired Be? Coated Structure Group on Jan.4 1990.
* Resonator is currently aligned
    * Good wavefront
    * Good path length
    * First light hopefully within ? weeks.

Resonator Performance Analysis for a Ring Resonator FEL

S.A.Mani, J.E.Long, L.S.?

Global Coordinate System

Δ x = Translation along x axis	θ x = ?? about x axis
Δ y = Translation along y axis	θ y = ?? about y axis
Δ z = Translation along z axis	θ z = ?? about z axis

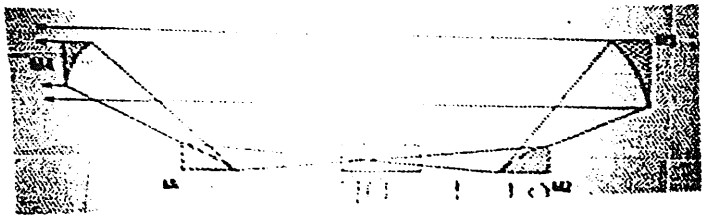

Rotation, Translation with respect to aligned optical axis intercept with optical surface
For propagation from M3 to M4 Coordinate ? system in ???

Resonator Code Description

* Wiggler is divided into n sections of length Δ z.
* Laser field is propagated to the center of first section.
* Complex gain is applied to the laser field.
* Electron equations of motion are integrated over Δ z.
* The betatron motion of the electrons is followed to determine their trajectory.
* Laser field is propagated to the end of the section.
* The above procedure is repeated until the entire wiggler length is travelled.
* The optical field is propagated through all the optical elements around the wiggler entrance.

Electron Equations of Motion

$$\frac{d\gamma}{d(ct)} = -\frac{e}{mc^2}\frac{aw(r)}{2\gamma}F_p E_o(r)\sin[\psi + \theta_o(r)]$$

$$\frac{d\psi}{d(ct)} = kw(z) - \frac{k_o}{2\gamma^2}[1 + \frac{a_w(r)^2}{2} + (\gamma\beta_x)^2 + (\gamma\beta_y)^2 - a_w a_y \cos(\psi + \theta_o)]$$

$$\frac{d(\gamma\beta_x)}{d(ct)} = -\frac{a_w^2 k_{wx}^2}{2\gamma}x$$

$$\frac{d(\gamma\beta_y)}{d(ct)} = -\frac{a_w^2 k_{wy}^2}{2\gamma}y$$

with

$$\frac{dx}{d(ct)} = \beta_x \quad \text{and} \quad \frac{dy}{d(ct)} = \beta_y$$

No.5 Optical Field Equation

$$2ik_o\frac{E}{z} + \frac{2E}{x^2} + \frac{2E}{y^2} = S(r)$$

where

$$S(r) = <\frac{-4zk_o}{c} J \frac{a?(r)}{\gamma} F_p e^{-i???}>$$

$$F_p = J_v(\mu) = J_1(\mu)$$

$$\mu = k_o a_z???$$

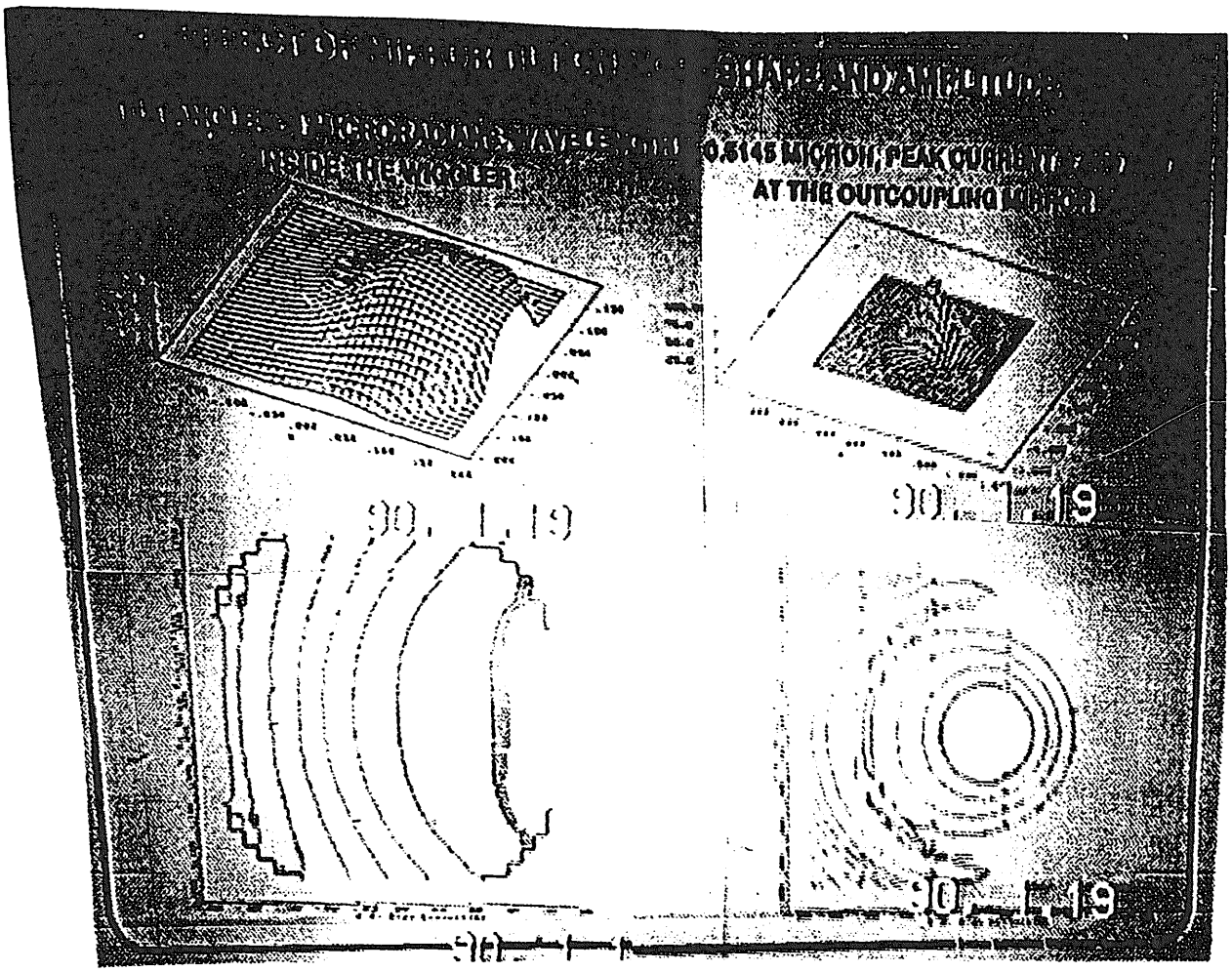

Effect of Misalignment on Output Power

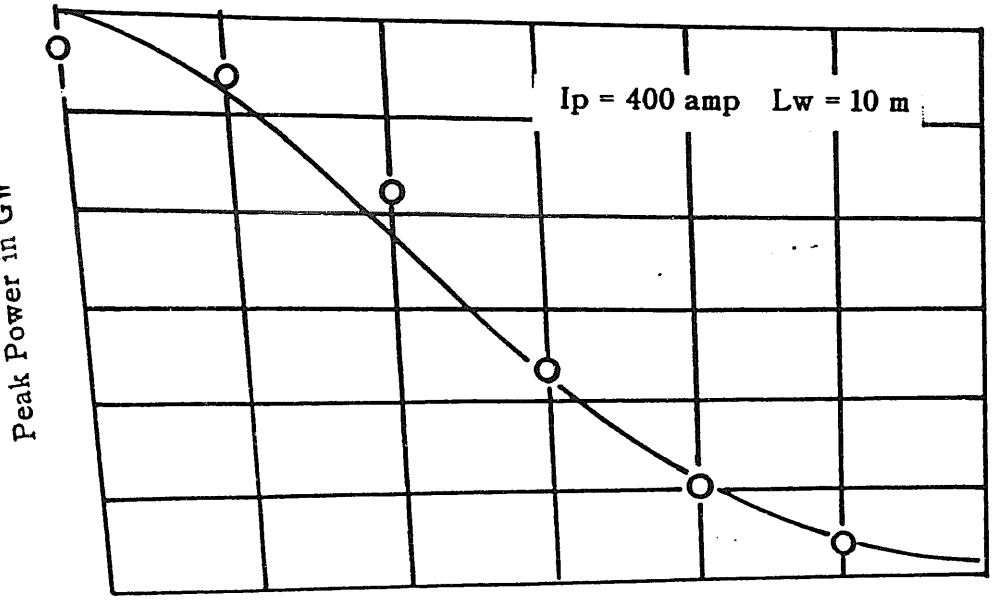

Effect of Astigmatism on Output Power

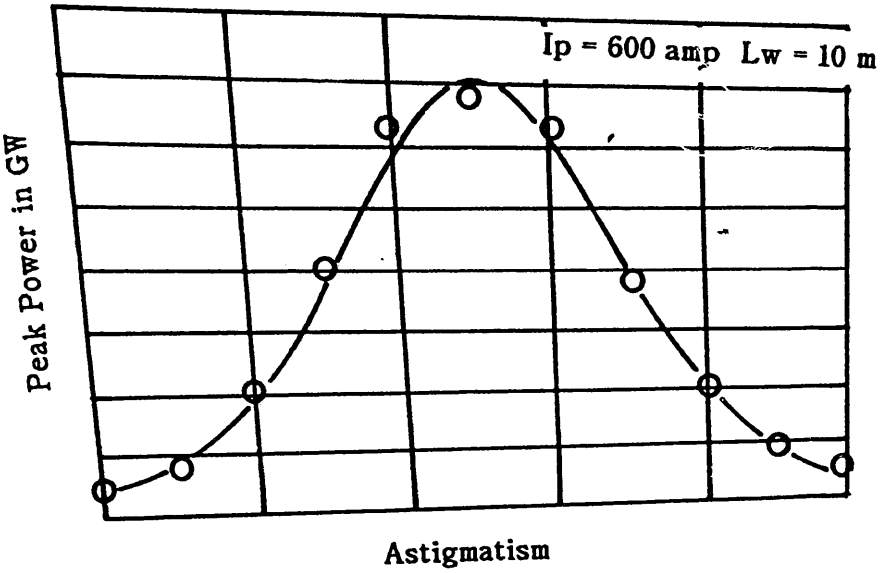

Effect of Coma in Output Power

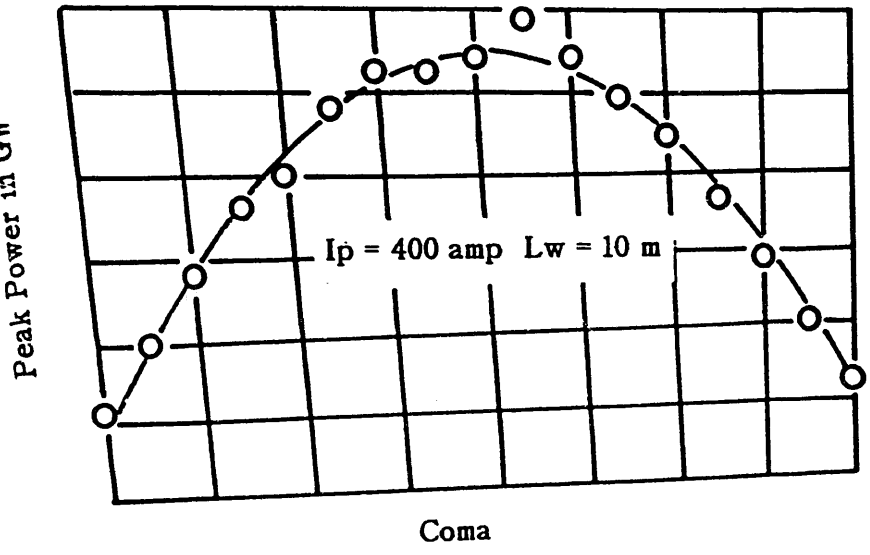

10% Power Loss Occurs For

* ～800 nanoradian Mirror Misalignment
* ～ λ /30 Residual Coma
* ～ λ /30 Residual Astigmatism

Summary

* FEL Resonator Code Developed in Cartesian Coordinated

* FEL Performance Dependence on the Following Can be Studied
  - Misalignment
  - Defocus
  - Coma
  - Astigmatism

* Cam be Used to Establish Fablication Torelance on Optical Components

Alignment-insensitive resonators using optically-powered corner cubes

J.A.Macken et al, Rockwell International

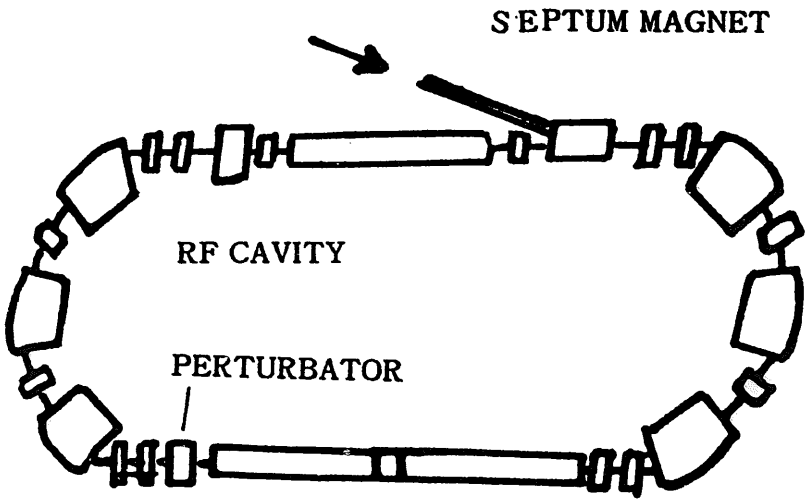

OPTICAL KLYSTRON(～6.2m)

DOUBLE CORNER CUBE RESONATOR (concentric equivalent)

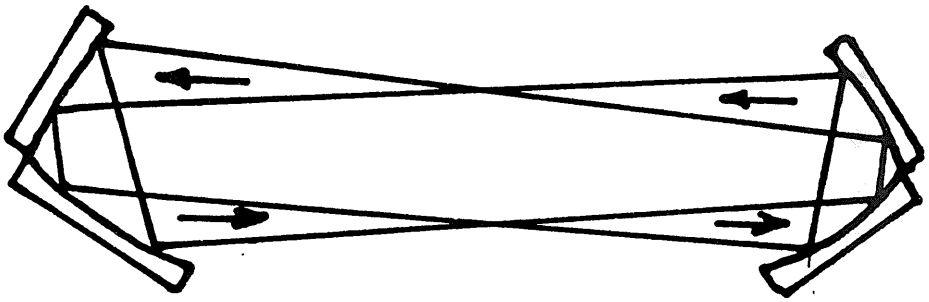

Assumption in Calculations

FEL Resonator 600 m long
1 μ m wavelength
Beam 30 cm diameter at each corner cube
Gain region 10 m long
Minimum distortion alignment for corner cube
Corner cube made with 3 spherical mirrors
(1038 m radius for concentric configuration)
(2077 m radius for confocal configuration)
Forward and return beams separative optics

Conclusion

Corner cubes made with three long radius spherical mirrors;

a. can produce diffraction-limited performance
b. exhibit insensitivity to tilt
c. retains sensitivity to misalignment of individual mirrors.

Laser resonators made with focusing corner cubes;

a. exhibit greatly reduced alignment ?
b. have unique properties in the confocal configuration.

IMAGE-RELAYED CORNER CUBE RING RESONATOR

C.? FORD, S.W.OUDN? TRW

Image-Relayed Corner Cube Ring Resonator

Experimental Configuration

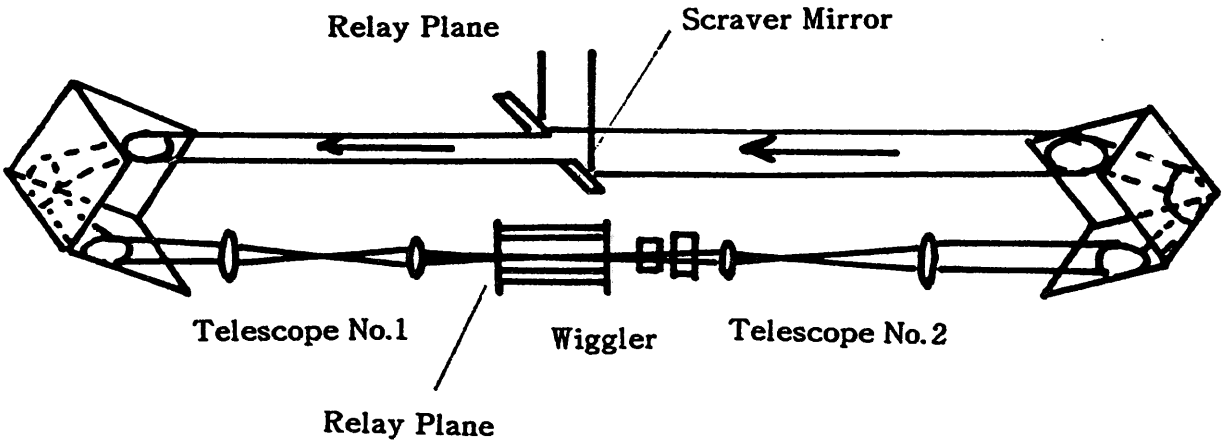

Image-Relayed Corner Cube Ring Resonator

Experimental Configuration

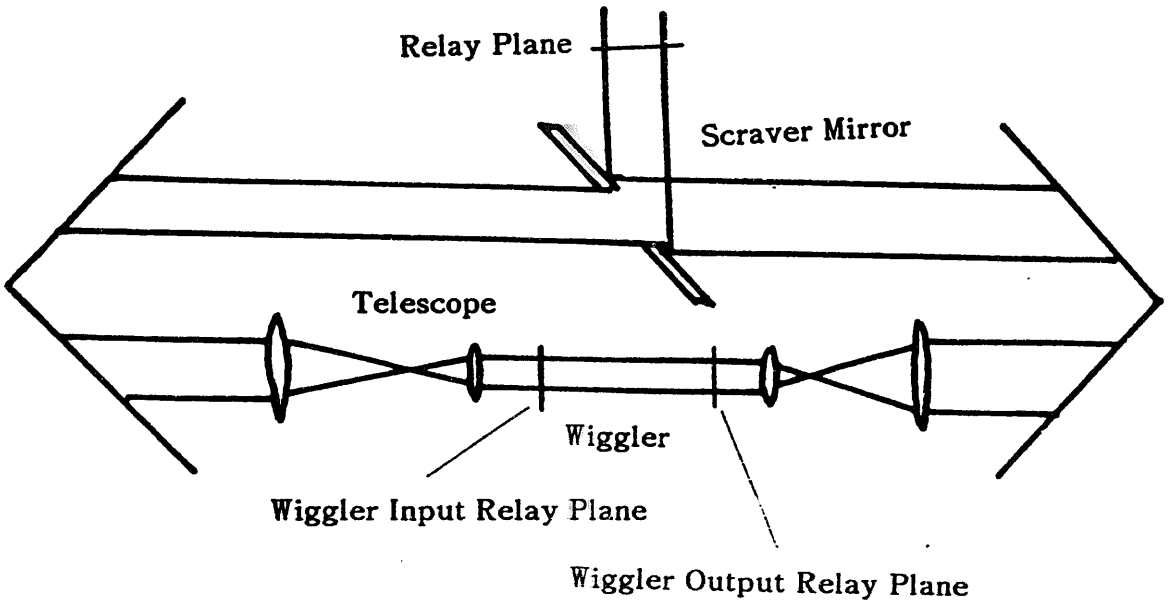

Schematic of Corner Cube Mirror Alignment Apparatus

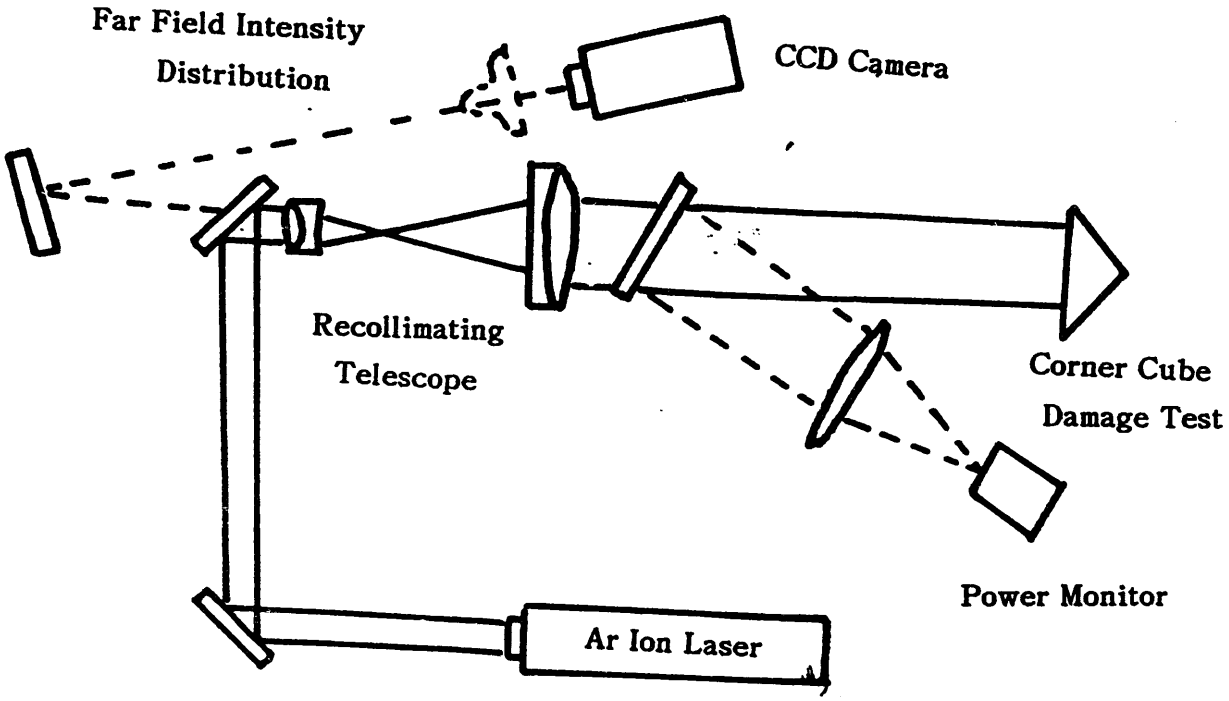

Schematic of Corner Cube Polarization Geometry

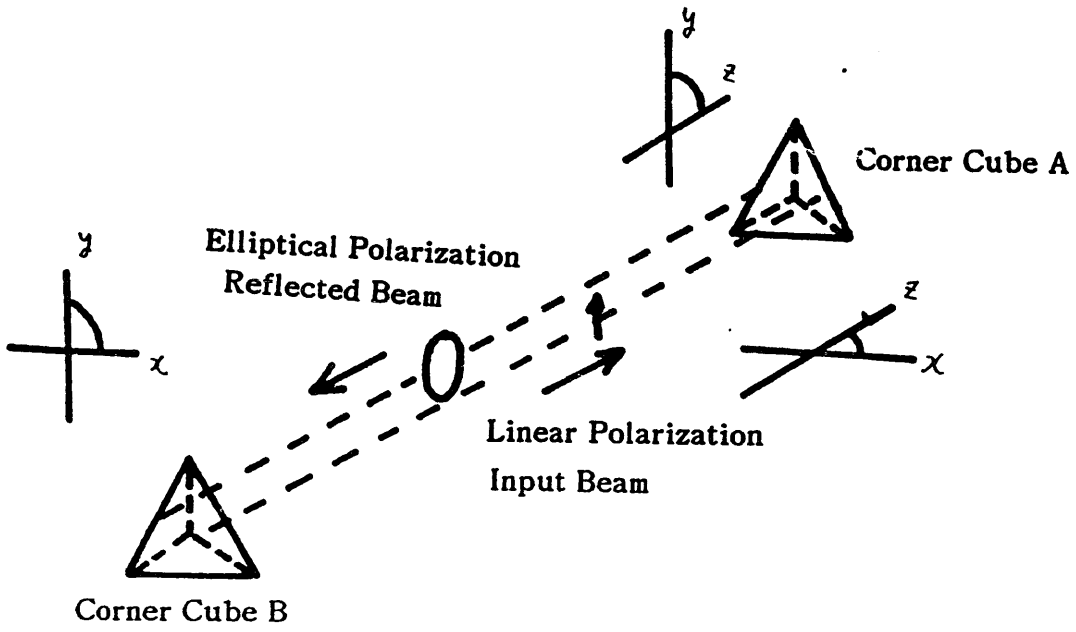

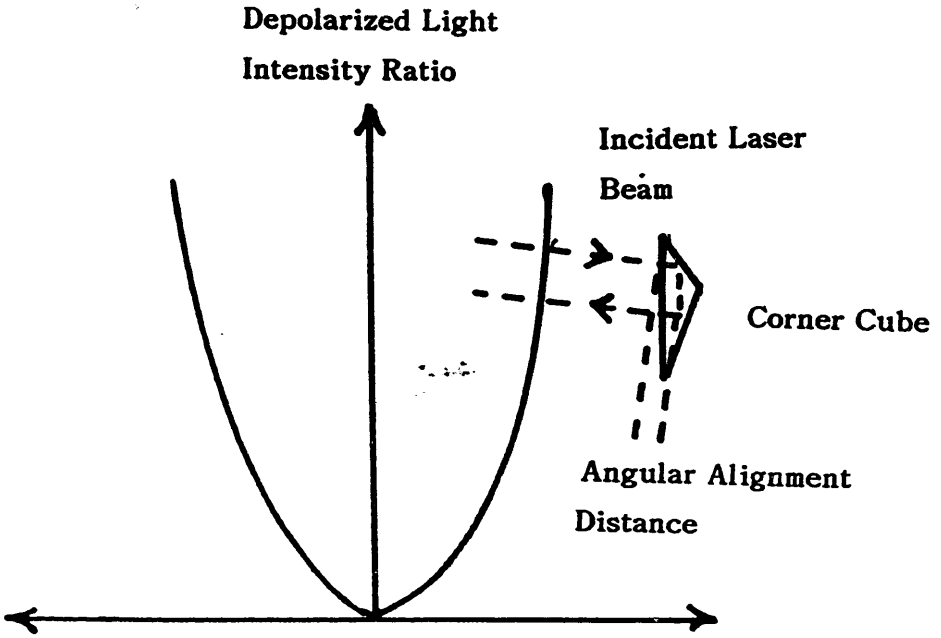

Depolarization of Laser Beam as Function of Alignment

ORCCRR SUMMARY

* Reduced mirror angular alignment sensitivities
* Reduced mirror spatial alignment sensitivities
* Good mode control capabilities
* Reduced optical damage to wiggler and mirrors
* Polarization changes can be cancelled.

付録２　１９８９年高エネルギー粒子加速器国際会議における自由電子レーザーに関係した発表論文

付録２　１９８９年高エネルギー粒子加速器国際会議における
自由電子レーザーに関係した発表論文

from Proceedings of the 1989 IEEE Particle Accelerator Conference
88-647453,89CH2669-0
１９８９年３月２０－２３日、シカゴ、米国

ＲＦライナック型ＦＥＬ

計算機シミュレーション

BOEING 120 MeV RF LINAC INJECTOR DESIGN AND ACELERATOR PERFORMANCE COMPARISON WITH PARMELA

A. Yeremian, J. Adamski, R. Kennedy, W. Gallagher, J. Orthel
Boeing Aerospace Co.
Lloyd Young
Los Alamos National Lab.

INTRODUCTION

The injector for the Boeing 120 MeV L-band RF linac was designed to produce 400 Amp peak current electron beam pulses with minimal emittance growth. PARMELA [1], a mostly three-dimensional matrix ray trace code with a two-dimensional space charge model, was used to determine the optimum setting of the injector elements for tuning purposes. The injector model predictions were used to tune the injector with very good agreement between the model and the experiment.

Beam dynamics modeling from the gun through the sixth accelerating section was done with PARMELA, using experimental settings for the beamline elements. We observed excellent agreement between PARMELA predictions and experimental results.

INJECTOR SIMULATION

As shown in figure 1, the injector consists of a SLAC type thermionic gun, two subharmonic bunchers at 108 and 433 MHz separated by 120cm drift and a tapered phase velocity traveling wave buncher at 1300 MHz for longitudinal bunching to achieve high peak currents. The radial growth of the beam due to space charge and radial electric fields in the traveling wave buncher are controlled by the axial magnetic fields provided by the solenoids. The diagnostics consist of current monitors, pepper pot, profile screens, and a streak camera as shown in figure 1.

The injector design, originally, was done with ORBIT [2], the one dimensional longitudinal bunching code including space charge and OPTIC [3], one dimensional radial confinement code using the paraxial ray equation. This forced us to do the design in piece meal fashion and did not provide emittance information. Eventually the injector design was tested with PARMELA.

The PARMELA simulation was done from the gun to the end of the first accelerator section all in one piece. The code was run on the Cray with 1000 particles and 5 degrees of 1300 MHz time steps.

The simulation starts with a 5.5nc, 1.9ns FWHM, 1.6 cm diameter electron pulse at the cathode. The entire system thru the first accelerator section is optimized to deliver 5.5nc 10 ps FWHM .6 cm diameter beam at the entrance to the accelerator. The 108 MHz and 433 MHz bunchers are running at 40 kV and 35 kV respectively. The 1300 MHz buncher is powered by 11 MW and the cavity parameters are as shown in figure 1. The axial magnetic field varies from 90 gauss in the front end to 1300 gauss over the first three cavities of the TPV buncher where the beam is the most compressed both radially and longitudinally. From this point the field drops down to 1200 gauss up to the first accelerator and then tapers down to 700 gauss over the accelerator. The last solenoid is located at the end of the first accelerator section where the beam energy

1300 MHz buncher

Cavity	β	E, MV/m
1	0.55	5.9
2	0.66	6.9
3	0.78	7.9
4	1.00	16.3
5	1.00	15.8
6	1.00	15.3

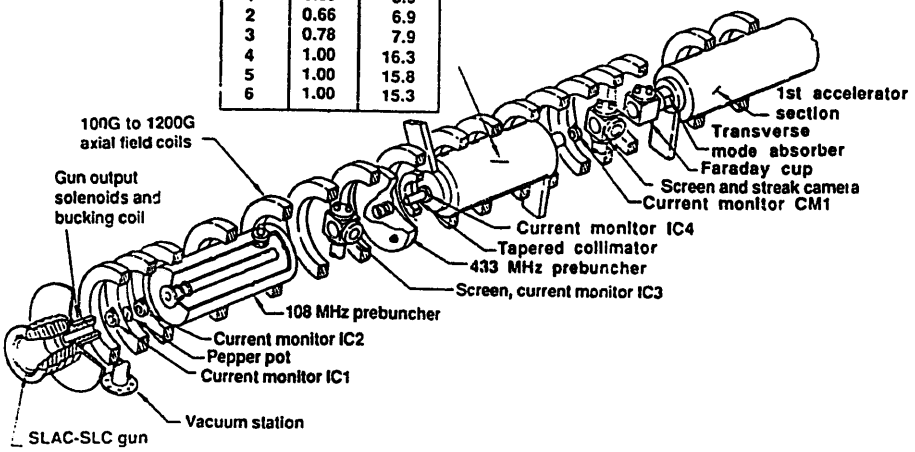

Figure 1. Double subharmonic injector

CH2669-0/89/0000-0657$01.00©1989 IEEE

is 20 MeV. After many PARMELA runs an optimized system of injector parameters were chosen to produce 100% charge transmission of 5.5 nc, at the entrance to the accelerator section. Of this 4.1 nc was within 10 ps pulse width. The beam diameter is .65 cm, the normalized emittance 40 pi-mm-mrad, energy is 2.5 MeV and the energy spread .8 MeV FWHM. PARGRAF, the graphics post processor for PARMELA is set up to produce beam parameter plots at each diagnostic station and some key points in the injector. Table 1 shows a summary of the modeling and experimental results.

Table 1. Injector to experiment comparison.

Location	Charge (nc)		Pulse Width FWHM (ns)		peak current (Amp)		Beam size (cm)	
	mod.	exp.	mod.	exp.	mod.	exp.	mod.	exp.
IC1	5.5	5.5	1.9	1.9	3	3	1.6	1.6
Pep Pot	5.5		1.9		3		1.6	1.6
IC2	5.5	5.5	2.0	1.9	3	3	1.6	
CA27	5.5		.43		10		1.9	1.6
IC4	5.5		.128		43		1.0	
Ent TPV	5.5		.149		40		0.6	
Ext TPV	5.5		.021		230		0.4	
CH1	5.5		.015		250		0.4	
SC1/Strk	5.5		.010	.014	320	414	0.5	0.5
FC	5.5	5.8	.010		350		0.4	
Ent Acc1	5.5		.010		410		0.65	

INJECTOR EXPERIMENTAL RESULTS TO PARMELA COMPARISON

The first experiment was to tune and make beam measurements in the injector. All the parameters except emittance and energy were measured. The code to measurement agreement is excellent.

The experiment started with setting the injector components to values predicted with PARMELA, then making slight adjustments to get the minimum pulse width and diameter at the streak camera station at the entrance to the first accelerator station. The solenoids were set to achieve an axial magnetic field profile as close to the PARMELA prediction as possible but we were limited by space and power supplies in the region from the TPV to the end of the first acceleration section. Figure 2. shows the comparison of the axial magnetic field achievable with the existing solenoid configuration to match the PARMELA prediction versus the field achieved in the experiment given the power supply limitations.

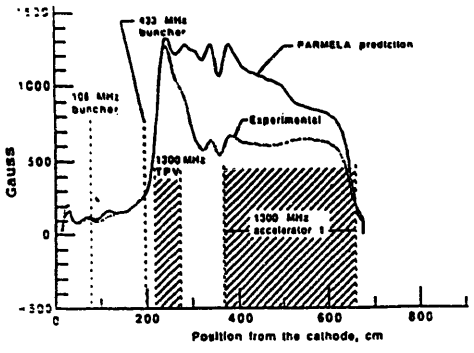

Figure 2. Axial magentic field

The pepper pot,screen combination shown in figure 3 was used to set the beam size at the entrance to the 108 MHz prebuncher. This was done by first turning off the 108 MHz buncher power, inserting the pepper pot and the screen in the beamline and adjusting AF1,2,3 to set the number of holes to 13, which corresponds to 1.6cm beam size as required by PARMELA. Interactive OPTIC is used to zero the axial magnetic field on the cathode using the bucking coil, AF1. The buncher powers were set to 7.5 KW and 4.8 KW respectively for the 108 and 433 MHz bunchers and 11MW for the TPV. At these powers the bunchers should produce the 40 and 35 KV fields respectively as required by PARMELA. Unfortunately the 433 MHz buncher multipactors at 4.8 KW and we had to adjust its power and the neighboring solenoids slightly to avoid multipactoring. The amplitude of the 108 MHz buncher and the phases of all the bunchers were tuned to deliver the minimum pulse width at the streak camera. The power level for the 108 and 433 MHz bunchers after tuning was completed was 8.3 and 6.0 KW respectively which corresponds to gap voltages of 42 and 39 KV. This is in excellent agreement with the model since 10 to 20% errors in power measurements are typical.

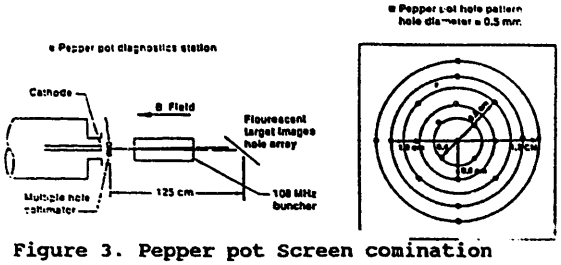

Figure 3. Pepper pot Screen comination

The total charge was measureo with a calibrated current monitor at the output of the gun to be 5.9 nc. The Faraday cup at the entrance to the first accelerator section measured 5.8nc, an agreement better than experimental error. Figure 4. shows 14 ps FWHM (410 Amp) at the streak camera screen at the entrance to the first accelerator. The code to experiment comparison is shown in table 1.

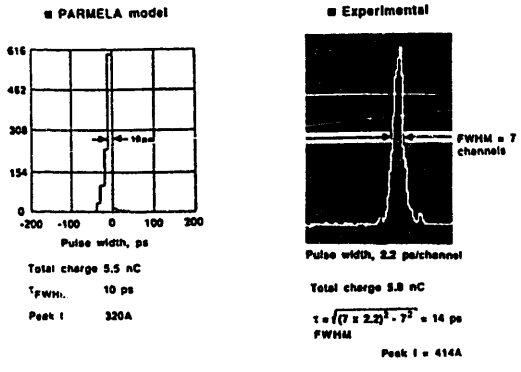

Figure 4. Micropulse structure after TPV buncher

ACCELERATOR EXPERIMENTAL RESULTS TO PARMELA COMPARISON

The purpose of the second experiment was to transport beam thru the entire machine down to the end of the straight ahead leg diagnostics station. At this station we can measure energy, energy spread, charge, position, spot size and the emittance. The experimental settings used in the accelerator elements were put into PARMELA to make a comparison between the model and the experimental results. The energy and energy spread predicted by PARMELA agreed very well with the measured values at 103.8 MeV plus or minus less than .5 MeV FW. Figure 5. shows that PARMELA is in very good agreement with the experiment for the charge transmission from the gun to the end of the sixth accelerator section. 3.5 nc out of the 5.5 nc of charge at the gun made it to the end of the sixth accelerator section and to the diagnostics station. The loss of charge is partly due to running more power in the 433MHz buncher and adjustment of the nearby solenoids to avoid multipactoring, deviating from what PARMELA simulations would require, and partly due to the lack of power to run the solenoids over the region from the exit of the TPV to end of The first accelerator as PARMELA would require. The latter problem was corrected since this experiment.

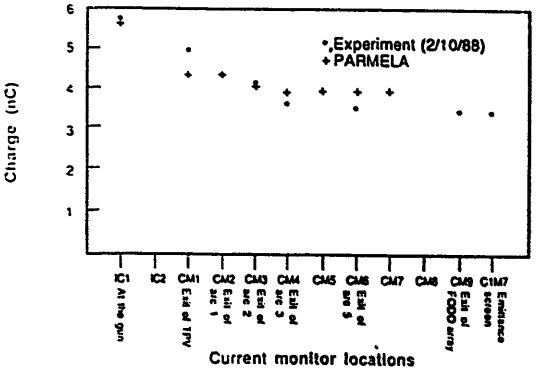

Figure 5. Micropulse charge transmission

Three emittance measurements were made in the X and Y planes. The measurements were made using the size vs - 1/f technique developed at SLAC (Ref 4). The beam phase space at the emittance triplet was varied for each set of measurements and unfortunately the phase space for the Y plane in the second measurement was not right and the data could only produce one leg of the hyperbola. Table 2 compares the predicted normalized emittance and brightness to the measured. PARMELA predicts a normalized emittance of 150 pi-mm-mrad for 90% of the charge, with peak current of about 350 Amps (3.5nc, about 10ps) at the end of accelerator 6. This translates to a brightness of 3.0E9 Amp/m2/rad2. The measured normalized emittance for the same amount of charge is 42 to 73 pi-mm-mrad about 1/3 to 1/2 the value predicted by the PARMELA simulation of the experiment. While we do not have a micropulse width measurement at the end of section 6 it is reasonable to assume that the pulse width is the same or less than that measured at the entrance to the first accelerator section and is somewhere between 10 and 14 ps. For a peak current of 350 Amps the measured brightness is between 4.0E10 and 1.3E10.

Table 2. Emittance and Brightness comparison

	I_p (Amp)	Plane	ϵ_N (π mm-mrad) 93%	$B = \frac{2b}{\pi^2 \epsilon_N^2}\left(\frac{A}{m^2 \cdot rad^2}\right)$ 93%	
PARMELA Calculations	350	Hor. Vert.	150 150	3×10^9 3×10^9	3.5 nc
12:25 P.M.	350	Hor. Vert.	64 64	1.7×10^{10} 1.7×10^{10}	3.5 nc
4:55 P.M.	350		73	1.3×10^{10}	3.5 nc
8:00 P.M.	350	Hor. Vert.	57 42	2.2×10^{10} 4×10^{10}	3.5 nc

2/10/88 Data Runs

CONCLUSION

The injector for the Boeing 120 MeV linac functions very close to its design parameters. PARMELA has been a useful tool for determining the injector tune parameters.

The PARMELA to experiment comparison on the accelerator shows very close agreement with the exception of the emittance which measures a factor of 2 to 3 better than the simulation prediction.

ACKNOWLEDGEMENTS

We whish to extend special thanks to the many scientists and technicians who made these exeriments possible.

REFERENCES

1. K. Crandall and L. Young, "PARMELA: Particle Motion in Electron Linear Accelerators", Los Alamos National Laboratory (private communication)
2. W. J. Gallagher, IEEE Trans.Nucl. Sci., Vol. NS-16, 214 (1969).
3. R. C. Kennedy and A. D. Yeremian, Boeing IR&D Project BAC-938, 1981
4. M. C. Ross et al, "Automated Emittance Measurements in the SLC", SLAC - PUB - 4278, March 1987

High-Brightness Electron Injectors: A Review*

Richard L. Sheffield
MS H825, Los Alamos National Laboratory Los Alamos, NM 87545

Abstract

The last decade has seen increased emphasis on the development of high-brightness electron beams because of rigorous requirements of the new generation of colliders and the advent of free-electron lasers. This talk describes the approaches now being explored for attaining intense, bright electron beams. The methods for producing bright electron beams include photocathode-based, short-pulse injectors; dc electrostatic accelerator sources; long-pulse beams, which are then compressed in time using subharmonic bunching; combining first and third harmonics in an accelerator to attain the equivalent of high-gradient dc fields; and LaB_6 rf guns. For several of the approaches, the temporal length of the electron pulse is decreased after acceleration to relativistic energies by impressing an energy spread on the electron bunch and using a nonisochronous beam-transport system to increase the peak current.

Introduction

Free-electron oscillators require electron accelerators capable of delivering pulse trains of electron bunches of high brightness to a wiggler or undulator.[1] A high brightness implies a high peak current (10 A to 2000 A) and a low transverse beam emittance (2 to 80 π·mm·mrad, determined by matching the transverse size of the electron beam to the optical beam in the wiggler). Electron-beam collider machines also require high peak currents (>2 nC in picoseconds) with extremely small emittances (<10 π·mm·mrad).[2]

Several approaches have been proposed to attain such performance.[3-6] The technology for the production of bright electron beams can be divided into two distinct catagories: long pulse (>1 ns) or dc electron sources and short pulse (<100 ps) electron sources.

In the first catagory, electron guns using a long pulse or a dc beam rely on a well-designed gun producing a beam that has a beam temperature near the thermal limit of the electron source. The beamline design after the gun depends on if the application ultimitely requires a dc beam or a short pulse. For a dc beam (or pulsed beams where the pulse end effects are negligible), very good quality beams can be produced if care is taken in the beam transport design. If the application requires a short pulse, then a bunching system must be designed that preserves the beam quality throughout the bunching and acceleration process. Preserving beam quality is difficult because of the effects of nonlinear rf fields in the bunching cavities and the space-charge forces present at subrelativistic energies.

The second catagory uses a light-activated photoemissive electron source placed directly in the first accelerating cavity (Fig. 1). This design has the advantage of rapidly accelerating the electrons to relativistic energies before substantial degradation in the beam quality caused by space charge can occur. The idea of using photocathodes as high-current electron sources started with lasertrons[7-9] and the production of spin-polarized electrons.[10,11] A light-activated electron source gives unprecedented control over all aspects of the electron

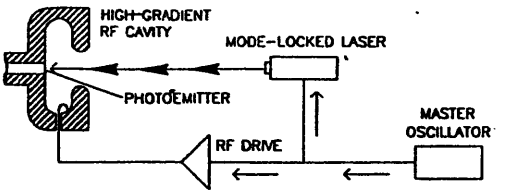

Fig. 1. Schematic of a photoinjector.

distribution: peak current, spatial profile, and temporal profile. This control is possible because the electron distribution is not determined by grids or a cathode, but rather by an incident laser pulse on the photocathode, and lasers have a wide range of variability in pulse format. Pulse lengths can range from femtoseconds to continuous and, for pulses greater than several picoseconds, can have almost any conceivable temporal profile.[12-14]

Intrinsic Source Brightness

The normalized peak brightness is defined as

$$B_n = 2\,I/(\varepsilon_x \varepsilon_y) \quad \text{[units: A/(m}^2 \cdot \text{rad}^2\text{)]} \quad ,$$

where I is the peak current and ε_x and ε_y are the normalized transverse emittances of the beam.[15] For a thermal distribution or a distribution that does not have recoverable correlations in phase space, it is constructive to use the rms emittance formulation, defined to be the area in phase space, which is

$$\varepsilon_x = 4\pi(\langle x^2\rangle \cdot \langle x'^2\rangle - \langle x \cdot x'\rangle^2)^{1/2} \quad ,$$

where x and x′ are the particle's transverse coordinate and angle of divergence from the optic axis, respectively, and <> means an average over the electron distribution f(x,y,z):

$$\langle x^2\rangle = \frac{\int\int\int f(x,y,z)\, x^2\, dx\, dy\, dz}{\int\int\int f(x,y,z)\, dx\, dy\, dz} \quad .$$

Another common definition of emittance is as the area in phase space divided by π, with the π included in the units.

Using the above formulation, the rms emittance is equal to the total phase-space area for a Kapchinskii-Vladimirskii distribution.[16] The normalized emittance is then

$$\varepsilon_n = \gamma\beta\varepsilon \quad ,$$

where for an azimuthally symmetric beam, $\varepsilon = \varepsilon_x = \varepsilon_y$.

The lower limit of the beam's normalized emittance from a thermionic electron source is governed by the emitter size and by the transverse component of the thermal motion of the electrons. The thermal limit of the normalized rms emittance of a beam from a thermionic emitter of radius r_c at a uniform absolute temperature T is

$$\varepsilon_n = 2\pi r_c (kT/m_e c^2)^{1/2} \quad \text{[units: m} \cdot \text{rad]}$$

because $\langle x \cdot x'\rangle = 0$ at the cathode.[17] For a typical thermionic emitter at 1160 K, the average transverse energy of emitted electrons is 0.1 eV. For a uniform current density J, the total current is $I = \pi r_c^2 J$ and the lower limit on the rms emittance

*Work supported by Los Alamos National Laboratory Program Development funds under the auspices of the US DOE.

CH2669-0/89/0000-1098$01.00©1989 IEEE

is

$$\varepsilon_n = 5.0 \times 10^{-6} (I/J)^{1/2}\ \pi \cdot \text{mm-mrad, with } J \text{ in A/cm}^2.$$

The corresponding normalized peak brightness is limited to

$$B_n = 2\, I/\varepsilon_n^2 = 8.2 \times 10^9\, J \text{ [units: A/(m} \cdot \text{rad)}^2\text{]}.$$

The current density from a dispenser cathode is typically not more than 20 A/cm²; therefore, the maximum achievable brightness is 1.6×10^{11}.

Semiconductor photoemitters have an effective temperature of 0.2 eV (Ref. 18). The electron thermal temperature is not simply the difference between the incident photon energy and the semiconductor band gap (a difference of 0.7 eV) because of phonon scattering in the semiconductor crystal lattice. Semiconductor cathodes are capable of delivering[19] over 600 A/cm², giving a brightness of 2.5×10^{12} A/(m · rad)².

The brightness of the source normally does not limit the final brightness of the beam. Instead, the acceleration process and transport through a beamline can decrease the beam brightness by several orders of magnitude.

DC Injectors

The following information on very long pulse (>> 1 ns) and dc injectors is a summary of a paper[6] by W. Herrmannsfeldt. These types of guns are well suited for two applications: first, for electron cooling of ion beams and, second, for electrostatic free electron lasers (FEL).

The design of a dc gun must include the effects of space charge. In the gun, the space-charge self-force in the beam must be cancelled out with a carefully designed focusing electrode (at the Pierce angle[20]), thus maintaining a uniform current density. Also, the exit energy of the beam from the gun should be as high as possible to minimize further space charge defocusing downstream from the gun. If the beam maintains a uniform profile up to relativistic energies, then the beam emittance can be near the thermal temperature of the beam as it was emitted from the cathode. The emittance of the beam caused by thermal effects is discussed in the preceding section.

A gun designed by Herrmannsfeldt for the UCSB FEL and described in a paper[21] by Elias and Ramian is shown in Fig. 2.

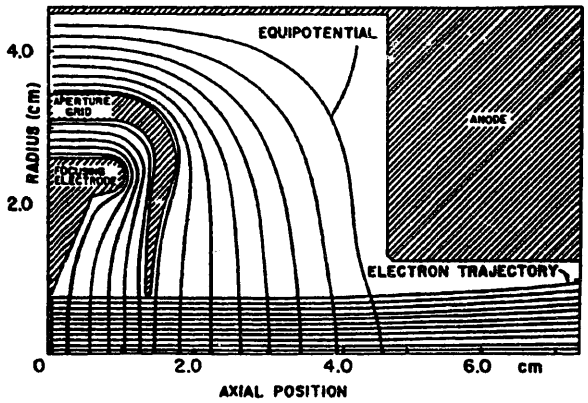

Fig. 2. A dc gun designed for UCSB's electrostatic accelerator.

Injectors Using Third Harmonic Cavities

Bunches accelerated with a dc field do not suffer the emittance growth that is due to time-varying effects typically found in rf accelerators. Harmonics can be used to eliminate this source of emittance growth. A design[4,22] that corrects for the time-varying fields in a radio-frequency (rf) accelerator uses cavities that operate at the third harmonic of the main linac frequency. Two conditions must be met to approximate a dc accelerating field during pulse transit. First, the amplitude of the third harmonic is set to nine times the fundamental frequency's amplitude. Second, the phase of the third harmonic is chosen to decelerate the bunch at the peak acceleration of the fundamental. The amplitude is flat to within 0.1% over 37° of the rf. However, the resulting two-frequency cavity will have increased phase and amplitude control complexity.

For relativistic beams, the harmonic component may be added with separate cavities, considerably reducing cavity design and control complexity. Improved accelerator performance using separated cavities for the first and third harmonic has been verified using PARMELA by Todd Smith.[4] After initial acceleration to several MeV with a long pulse (to minimize space-charge effects), the peak current is then increased using magnetic compression. A schematic of the design is given in Fig. 3.

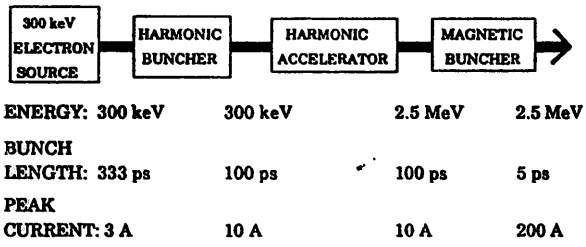

Fig. 3. Injector designed by T. Smith for the Stanford High-Energy Physics Laboratory's Superconducting Accelerator. Calculated emittance using PARMELA is 20 π-mm-mrad.

Photoinjectors

A photoinjector is a photoemissive electron source placed directly in an rf cavity. The photoinjector design depends on the electron bunch produced from a photocathode being rapidly accelerated to relativistic energies in a single rf cavity, hence eliminating the conventional bunching process entirely. The emittance growth of the electron beam is reduced because electron-beam transport at low energies has been significantly reduced.

Los Alamos Experiment

Experiment Design. The Los Alamos experiment uses a laser-driven photocathode electron source situated on-axis in the first rf cavity. The electron-pulse shape is easily tailored in both time and space by appropriately shaping the incident laser pulse. The configuration of the experiment is shown in Fig. 4. The linac has two 1300-MHz rf cavities with independent amplitude and phase controls. Both rf cavities have loops to measure the phase and amplitude of the rf fields present in the cavities. Following the second cell are the diagnostics for bunch charge, beam energy, emittance, and temporal profile. The details of the rf cavity design are presented elsewhere.[23]

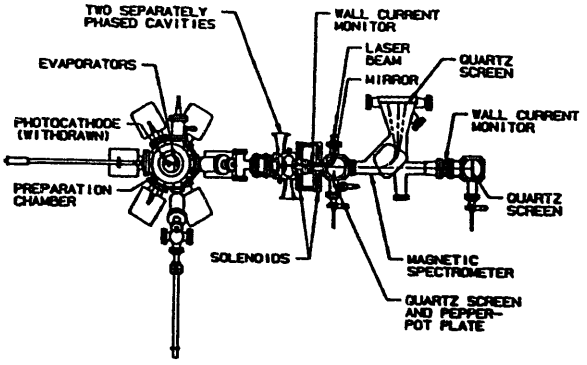

Fig. 4. Two-cavity experiment showing gun, beam transport, and diagnostics.

The photocathodes are fabricated in a preparation chamber vacuum coupled to the rf linac. Following fabrication in the preparation chamber, the photocathode is inserted into the rf cavity. When the quantum efficiency of the photocathode decreases below some arbitrary minimum value, the substrate is pulled back and heat cleaned at 400°C. A new photocathode is then fabricated over the existing substrate without opening the UHV system.

The photocathode is illuminated with a frequency-doubled Nd:YAG laser. The laser is mode locked at the twelfth subharmonic of 1300 MHz, 108.33 MHz. The mode-locking crystal is driven by the same master oscillator that drives the 1300-MHz rf klystron and is phase locked to the rf. The laser generates 100-ps pulses at 1.06 μm that, after frequency doubling to 532 nm, become 70-ps-long pulses. A Spectra-physics pulse compressor was added to the optical train for generation of 4- to 20-ps pulses. The power available at 532 nm is approximately an average of 250 kW over 10 μs.

Experiment Results. The electron energy gain for typical operation was 0.9 MeV in the first cavity and 1.8 MeV in the second cavity. This corresponds to operating both cavities at approximately 2 Kilpatrick (58 MeV/m peak surface field).

The laser pulse length was limited by the gain bandwidth of the Nd:YAG amplifiers to approximately 16 ps. The maximum charge extracted for this pulse was 13.2 nC from 1 cm^2 of photocathode surface. This gives 820 A/cm^2 of current density at the cathode. However, PARMELA simulations predict that a 16-ps electron pulse increases to 22 ps on passage through the first cavity, giving a peak current after the first cavity of 600 A.

The emittance measurements were performed on an earlier experiment that used only a single rf cavity. The experimental parameters were 11 nC (200-A peak), 70-ps Gaussian temporal width, <0.4-cm beam radius at the cathode (was not accurately measured at the time of the experiment and only the upper bound is known), 1.0-MeV beam energy, and a solenoid field of 1.8 kg. The measured emittance was 40 π·mm·mrad. The measured emittance did not agree with a PIC simulation (which gave greater than 150 π·mm·mrad) of the experiment. This disagreement led to a detailed examination of the gun, beamline, and the pepper-pot emittance diagnostic using PARMELA, MASK,[24] and ISIS[25] simulations.

The experimental and simulated electron-beam diameter at the pepper pot and the diameters of the beamlets produced by the pepper pot at the second quartz screen are in close agreement, confirming the accuracy of the simulations. The emittance of the electron beam for that experiment, with 10 nC per bunch, was calculated from the simulations to be 120 π·mm·mrad for 100% of the beam. Simulations[24] show that, if the beam is clipped in time and left with 75% of the original charge, then the emittance of the remaining beam was calculated to be 40 π·mm·mrad in agreement with the experimental results. The results of the MASK calculations are shown in Fig. 5 (Ref. 5). The large decrease in beam emittance with a small decrease in the charge is due to the temporal tails of the long Gaussian pulse used in the previous experiment. Because the focusing solenoid downstream of the cavities can only be properly matched for one space-charge density, the beam is matched only for the peak of the Gaussian pulse, and the head and tail of the electron bunch are overfocused. The low-intensity tails from all the beamlets overlap on the pepper-pot screen; therefore, an individual beamlet's spatial distribution cannot be resolved unambiguously. Hence, an experimental emittance value was obtained for only the temporal core of the electron bunch.

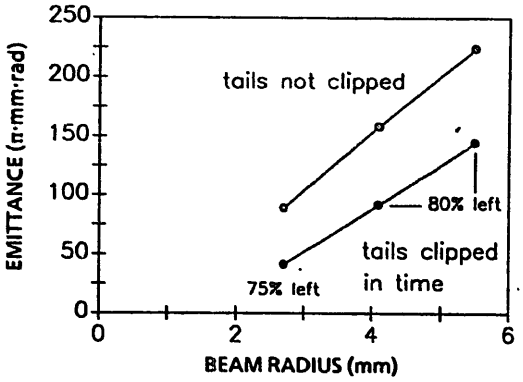

Fig. 5. The beam emittance from MASK simulations (performed by Bill Herrmannsfeldt of SLAC) are within the experimental error in beam radius if the temporal tails of the Gaussian pulse are not included. The two curves show the difference in emittance gained by excluding a small fraction of the charge at the front and tail of the pulse.

Although neglecting the temporal tails of the distribution consequently gives low emittances, most applications of bright electron beams depend upon only the bright central core of the electron bunch. More importantly, the accuracy of the simulation codes have been verified for future linac design.

Duke-Rocketdyne Experiment

The construction of the Mark III accelerator has been described in detail elsewhere.[3] The layout of the experiment is shown in Fig. 6. The machine parameters are as follows: macropulse length of 2 to 5 μs, micropulse length of 2.2 ps, gun energy of 1 MeV, and a magnetic compression of 10 from the alpha magnet. The alpha magnet is a momentum filter and is able to limit the electron energy spread to less than 0.5%.

The electron source in the Mark III is a LaB_6 cathode. Originally the cathode produced electrons by pure thermal emission. However, because the electrons are emitted at all phases of the rf, many of the electrons are accelerated at the wrong phases for matching into the main linac.

The current emission from the cathode is limited by average-power heating; therefore, using the laser to limit the emission to the correct rf phase, higher peak currents can be

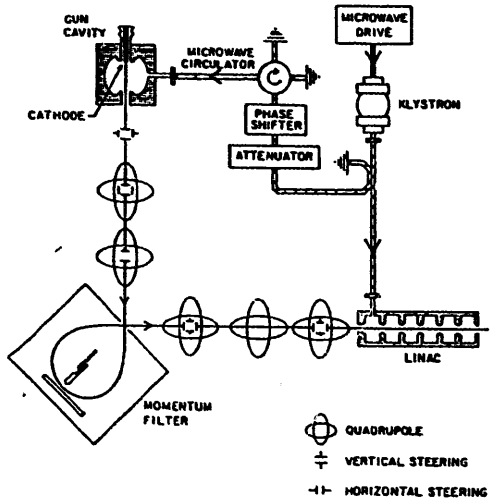

Fig. 6. Schematic of the experiment showing microwave feed system and the path of the electrons from the laser-switched thermionic gun to the Mark III accelerator.

obtained.[26] In this mode, the LaB_6 cathode was operated just below its normal emission temperature, and a laser was used to pulse the cathode. Operation with the laser resulted in an increase in peak current from 33 to 75 A with no observable loss in beam emittance. The gun brightness was approximately 5×10^{12} A/(m-rad)^2.

During operation, the gun pressure was about 5×10^{9}. Not enough operation time has been available to study the cathode lifetime; but based on previous performance, the expected lifetime should be much greater than 1000 hours.

Present Photoinjector Designs

Los Alamos National Laboratory

Two separate initiatives are now underway at Los Alamos based on photoinjector technology.

Design of a Compact Linac. Design of a 20-MeV compact linac based on the photoinjector has been completed. The linac is approximately 1.2 m long and will be operated with a 10-μs macropulse at up to 15 Hz with a 0.5-A average during the macropulse. The design of the linac is based on emittance reduction by reversing the effects of space charge after the photoinjector gun.[27-29] The final electron-beam characteristics from PARMELA simulations are a beam emittance of less than 20 π-mm-mrad and peak currents in excess of 350 A. Magnetic compression of the 16-ps electron pulse can increase the peak current to greater than 500 A. The limit in peak current depends on the application. For instance, a free-electron laser oscillator is very sensitive to the jitter in the arrival time of the electron bunches in the wiggler. Because variations in the electron bunch charge cause variations in the final electron-beam energy, the amplitude stability of the photocathode laser system, which produces the electron bunches, will determine the maximum amount of pulse compression allowed (a change in the electron-beam energy maps into a change in time in the magnetic compressor).

Upgrade of Los Alamos FEL Accelerator. The Los Alamos FEL is now being upgraded to provide electron beams of the quality and intensity required by advanced FELs. The improved electron beam is primarily the result of adding a photoinjector to the accelerator. However, the entire device is being modified to demonstrate that the beam quality can be transported to the FEL without degradation. The facility should provide initial data by summer, 1989. This facility will provide a good benchmark for the computational models used to design advanced FELs because the same models will design the photoinjector, beam transport, oscillator, and amplifier. The design goals of the accelerator are 40 MeV of electron energy, peak currents of 400 A, and a normalized emittance less than 50 π-mm-mrad (90%). An experiment layout is given in Fig. 7.

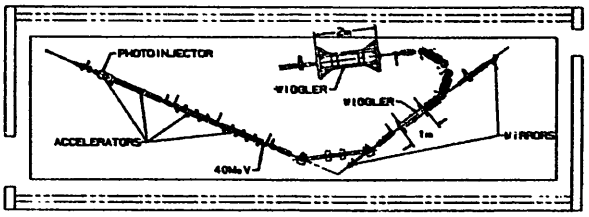

Fig. 7. Upgrade of the Los Alamos FEL with photoinjector.

Brookhaven National Laboratory

The Accelerator Test Facility at Brookhaven National Laboratory (BNL) is being developed into a research facility for laser acceleration and FELs. The design goal for the accelerator is 50 MeV at an emittance of 15 π-mm-mrad. The research team at BNL are building (scheduled for operation in spring of 1989) a 2.856-GHz photoinjector to drive the linac.[30] The S-band, standing wave, disk-loaded structure will operate in the short rf pulse regime (6 μs). The gun is designed for a maximum surface field of 120 MV/m and a pulse repetition rate of 5 Hz.

The surface field at the cathode is 102 MV/m. The energy gain in the 1 1/2-cell structure is 4.9 MeV. The disk-loaded structure was designed to minimize the ratio of the peak surface field to the field at the cathode surface and is not optimized for maximum shunt impedance. To match to the π-mode in the cells, a side-wall coupling scheme is used. In this configuration, the TE_{10} waveguide mode couples strongly to the π-mode and does not, to first order, couple to the zero mode. The π-mode operation was chosen to minimize emittance growth caused by rf defocusing fields in the accelerating gaps.[31]

Lawrence Berkeley Laboratory

A photoinjector design[32] at Lawrence Berkeley Laboratory (LBL) to produce bright beams for linear colliders, compact FELs, propagation of intense bright beams, and coherent x-ray holography has been completed. The rf cavity design is a 1.269-GHz rf cavity consisting of 2 1/2 cells with a peak surface field of 60 MV/m and a cathode field of 30 MV/m. The design goals are to obtain a 3- to 5-ps pulse length and a 1-nC charge at a gun exit energy of 5 MeV.

The photoinjector parameters were obtained by extensive PARMELA simulations[33] and theoretical analysis.[34] The exiting pulse from the gun has an rms length of 6 ps and a 0.6% energy spread. The calculated emittance is 8 to 15 π-mm-mrad.

Bergische Universität-Gesamthochschule Wuppertal

This design for a photoinjector is unique in that the rf gun cavity is superconducting.[35] The design parameters are

1.3 MeV, 5 to 70 ps, and pulse charge of 0.15 to 14 nC. Peak currents range from 2.3 to 200 A. This program will be studying the performance of high QE photocathodes on a niobium surface. A significant advantage to operating a photocathode in a superconducting cavity is that the possiblity of contamination of the photocathode by water or CO_2 will be greatly reduced.

LEL-HF in Bruyères-le-Chatel

This photoinjector design[36,37] has a much lower cavity frequency, 144 MHz, than the previous designs. A lower frequency can reduce the rf effects because the cavity apertures are larger and the fields approximate dc conditions during the electron transit. The design parameters are a beam with 10 to 20 nC, a 1- to 1.5-MeV exit energy from the first cavity, bunch lengths of 50 to 100 ps, an accelerator gap of 7 cm, and a surface field at the cathode of 15 to 20 MV/m.

The design was developed using ATHOS, PARMELA, and OAK. The expected emittance is approximately 20 π-mm-mrad. After initial acceleration to greater than 4 MeV, magnetic compression would be used to increase the peak current.

Summary

The production of high-current high-brightness electron beams has enjoyed considerable progress over the last several years, mainly because of changes in the requirements imposed by free electron lasers. Several approaches show considerable potential for producing very bright electron beams. The concept of placing a photoemissive source in an accelerating structure has been demonstrated. The basic physics of photoinjectors is understood and the technology is now in the initial engineering phases. Several groups around the world are designing bright beams based on this technology and continued improvement in photoinjector design is expected.

Acknowledgments

The author thanks John Fraser with whom the initial work on the photoinjector program was accomplished. The author acknowledges Bruce Carlsten, Bill Herrmannsfeldt, Roger Miller, Charles Sinclair, Todd Smith, Steve Benson, Ken Batchelor, S. Chattopadhyay, and R. Dei-Cas for their helpful discussions and for information on bright electron sources. Also Jerry Watson and Stanley Schriber are acknowledged for their continued support.

References

[1] J. M. Watson, *IEEE Trans. Nucl. Sci.* 32 (5), 3363 (1985).

[2] R. B. Palmer, SLAC-PUB-4295, April (1987).

[3] S. V. Benson, J. Schultz, B. A. Hooper, R. Crane, and J. M. J. Madey, *Nucl. Instr. and Meth.*, A272, 22-28 (1988).

[4] T. I. Smith, *1986 Linear Conf. Proc.*, Stanford Linear Accelerator Center report, SLAC-303, 421-425 (1986).

[5] J. S. Fraser and R. L. Sheffield, *IEEE J. Quant. Electron.* 23 (9), 1489 (1987).

[6] W. B. Herrmannsfeldt, SLAC-PUB-4843, January (1989).

[7] M. Yoshioka, M. Mutuo, Y. Fukushima, T. Kamei, H. Matsumoto, H. Mizuno, S. Noguchi, I. Sato, T. Shidara, T. Shintake, K. Takata, H. Kuroda, N. Nakano, H. Nishimura, K. Soda, M. Miyao, Y. Kato, T. Kanabe, and S. Takeda, *Proc. 1984 Linac Conf.*, Gesellschaft fur Schwerionenforschung, Darmstadt report GSI-84-11,469-471 (1984).

[8] C. K. Sinclair, *AIP Proc. on Advanced Accel. Concepts*, Madison, WI, 156 (1986).

[9] P. J. Tallerico, R. L. Sheffield, W. D. Cornelius, E. R. Gray, M. T. Wilson, D. C. Nguyen, K. L. Meier, and R. L. Stockley, *1988 Linear Accel. Conf.*, Williamsburg, VA, October 2-7 (1988), to be published.

[10] D. T. Pierce, R. J. Celotta, G. C. Wang, W. N. Unertl, A. Galens, C. E. Kuyatt, and S. R. Mielczarek, *Rev. Sci. Instrum.* 51, 478-499 (1980).

[11] C. K. Sinclair and R. H. Miller, *IEEE Trans. Nucl. Sci.* 28 (3), 2649-2651 (1981).

[12] A. M. Weiner, J. P. Heritage, and R. N. Thurston, *Opt. Lett* 11(3), 153 (1986).

[13] M. Haner and W. S. Warren, *Opt. Lett.* 12 (6), 398 (1987).

[14] D. C. Nguyen, D. E. Watkins, and M. E. Weber, *SPIE Proc.*, January 11-16, Los Angeles, CA (1988).

[15] C. LeJeune and J. Aubert, "Emittance and Brightness: Definitions and Measurements," in *Applied Charge Particle Optics*, A. Septier, Ed., *Advances in Electronics and Electron Physics*, Supp. 13A, 159-259 (1980).

[16] P. Lapostolle, *IEEE Trans. Nucl. Sci.* 18 (3), 1101-1104 (1971).

[17] J. D. Lawson, *The Physics of Charged Particle Beams*, (Oxford University Press, 1977), p.199.

[18] P. Oettinger, I. Bursuc, R. Shefer, and E. Pugh, *Proc. 1987 Part. Accel. Conf.*, IEEE Catalog No. 87CH2387-9, 1, 288 (1987).

[19] J. S. Fraser, R. L. Sheffield, E. R. Gray, P. M. Giles, R. W. Springer, and V. A. Loebs, "Photocathodes in Accelerator Applications", Proc. 1987 Part. Accel. Conf., IEEE Catalog No. 87CH2387-9, 3 1705 (1987).

[20] J. R. Pierce, *Theory and Design of Electron Beams* (van Nostrand, 1949).

[21] L. R. Elias and G. Ramian, *Phys. Quant. Elect.* 9, 577 (1982).

[22] T. Energa, L. Durieu, D. Michelson, and R. Worsham, *IEEE Trans. Nucl. Sci.* 32 (5), 2936 (1985)

[23] E. R. Gray and J. S. Fraser, *Proc. 1988 Linear Accel. Conf.*, Williamsburg, VA, October 3-7, 1988, to be published.

[24] W. Herrmannsfeldt, R. Miller, and H. Hanerfeld, SLAC-PUB-4663, June (1988).

[25] M. E. Jones and W. K. Peter, *Proc. 6th Int. Conf. High-Power Particle Beams*, Kobe, Japan (1986).

[26] S. V. Benson et al., Lasers 88, to be published (1988).

[27] B. E. Carlsten and R. L. Sheffield, *1988 Linear Accel. Conf.*, Williamsburg, VA, October 2-7, 1988, to be published.

[28] B. E. Carlsten, "Photoelectric Injector Design Code," these proceedings.

[29] B. E. Carlsten, 10th Int. FEL Conf., Jerusalem, Israel, August 29-September 2, (1988).

[30] K. Batchelor, J. Sheehan, and M. Woodle, Brookhaven Internal Report, BNL-41766 (1988).

[31] K. T. McDonald, Princeton University Report DOE/ER/3072-43, March (1988).

[32] S. Chattopadhyay, Y. J. Chen, D. Hopkins, K. J. Kim, A. Kung, R. Miller, A. Sessler, and T. Young, *Proc. 1988 Linear Accel. Conf.*, Williamsburg, VA, October 2-7, 1988, to be published.

[33] Y.-J. Chen, LBL internal notes, BES 4, ESG Tech Note-74.

[34] K.-J. Kim and Y.-J. Chen, *Proc. 1988 Linear Accel. Conf.*, Williamsburg, VA, October 2-7, 1988, to be published.

[35] H. Chaloupka, H. Heinrichs, H. Piel, C. K. Sinclair, F. Ebeling, T. Weiland, U. Klein, and H. P. Vogel, *Proc. Euro. Part. Accel. Conf.*, Rome, June 7-11 (1988).

[36] S. Joly, R. Dei-Cas, C. Bonetti, F. Cocu, J. P. De Brion, J. Frehaut, G. Haouat, A. Herscovici, H. Leboutet, and J. Siguad, *Proc. Euro. Accel. Conf.*, Rome, June 7-11, 1988, to be published.

[37] R. Dei-Cas et al., 10th Int. FEL Conf., Jerusalem, Israel, August 29-September 2, (1988).

RECENT EXPERIMENTS WITH THE FREE-ELECTRON LASER AT LOS ALAMOS*

Donald W. Feldman and Roger W. Warren

MS H825, Los Alamos National Laboratory
Los Alamos, New Mexico 87545

Abstract

Improvements in the operational characteristics of the Los Alamos free-electron laser have produced experimental results in reasonable agreement with theory and simulation. The results of these experiments will be described.

Introduction

A great deal of effort over the past several years has gone into improving a number of system parameters in the Los Alamos free-electron laser (FEL). The amplitude and timing fluctuations in injector gun pulses and rf power have been reduced by about an order of magnitude; nonlinear optical effects in cavity mirrors have been eliminated with the use of copper mirrors; wakefields, which produced transverse and longitudinal emittance growth at high peak currents, have been eliminated or reduced. These improvements have enabled us to carry out a series of experiments[1-4] in the past year that demonstrated laser performance in gratifying agreement with both qualitative theory and numerical simulations. Each of the following sections briefly describes a set of experiments that demonstrates a significant aspect of free-electron laser operation. The first group involves a uniform wiggler, the second, several tapered wigglers. A description of these wigglers, the accelerator, and optical system can be found in our earlier publications.

Lasing with Uniform Wigglers

Sideband Suppression

Before the recent improvements in the system, we had observed gains as high as 40% in the 1-m uniform wiggler. In recent experiments, we have seen gains as high as 250% at peak currents of ~300-400 A. These gain values are in rough agreement with simulations.[5] The characteristics of the laser now change in a reproducible and predictable way with changes in the length of the cavity resonator. Figure 1 shows a typical experimental detuning curve. One-

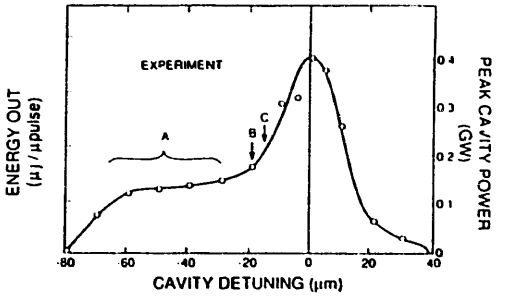

Fig. 1. Experimental in-cavity optical power vs cavity-length detuning.

dimensional pulse calculations for the same conditions yield similar results. A, B, and C indicate the region and points where the spectra are as shown in Fig. 2 a-c. In region A, the spectrum is consistent with the transform limit of our 10-ps electron pulse (Fig. 2a). At B (Fig. 2b), sidebands begin to develop, and at C the spectrum develops into a pattern called the spiking mode (Fig. 2c).[6] This pattern implies a strong

*Work supported by Los Alamos National Laboratory Program Development funds under the auspices of the US DOE.

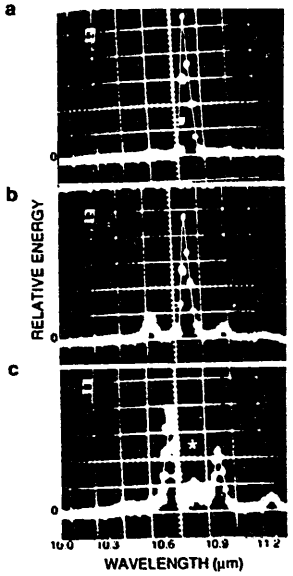

Fig. 2. Experimental spectrum showing (a) narrow spectral shape for large detuning near A; (b) weak sidebands for moderate detuning near B; (c) multiple, evenly spaced sidebands near C.

modulation of the optical pulse, with peak powers 5 times the average, that is, 10-50 GW. The same behavior has been shown in simulations.[5] At larger detuning, the spikes become sharper, narrower, and chaotic, also in agreement with calculations.[5] The spectrum extends over a wavelength range of ~10%, and estimated peak powers exceed 100 GW.

As described above, changing the cavity length by ~30 μm forces the FEL to operate in a single, transform-limited line. The theory explaining such sideband suppression is described in Ref. 7 and is consistent with our observations. Detuning is an elegant way to eliminate sidebands because it requires no additional apparatus. For a uniform wiggler, detuning causes a loss of efficiency. This result, however, is intrinsic to sideband suppression in uniform wigglers because the modulation of the optical pulse by the sidebands is the direct cause of the enhancement in efficiency at zero detuning. In contrast, for tapered wigglers, sidebands reduce efficiency, and detuning has been a completely satisfactory sideband suppression technique for all of those wiggler configurations that we have tested.

The most obvious disadvantage of cavity-length detuning for sideband suppression is that the wavelength is not constrained to a fixed value but changes with beam energy and cavity power. A suppression technique that selects a fixed frequency would be of use. We have experimentally examined one such technique: the use of a diffraction grating ruled on one of the cavity mirrors. The mirror is a spherical grating operated in a Littrow configuration; that is, the desired light, diffracted into the first order, is returned upon itself. Light at the sideband wavelengths is diffracted to the side; it does not interact with the electron beam and is not amplified. Using a grating with a pitch of six lines/mm, we were able to produce transform-limited line widths at cavity powers in excess of 100 MW and simultaneously couple light out of the cavity in an adjacent grating order. The efficiencies observed with a grating were consistent with cavity detuning results; that is, the same efficiency was observed whether the sidebands were suppressed by an active device or by cavity detuning.

CH2669-0/89/0000-1268$01.00©1989 IEEE

Harmonics Generated by Spontaneous Emission

The axial motion of the electrons in the wiggler field contains oscillating components at twice the frequency of the fundamental, transverse motion. The axial motion and its interaction with the transverse motion produces spontaneous emission at all harmonics of the fundamental frequency. We have made a number of measurements of light output at the 2nd, 3rd, and 5th harmonic wavelengths. Harmonics higher than these were too weak to be seen. Measurements were made over a range of micropulse charge. Some spatial symmetry measurements of the modes were obtained, and the effects of cavity feedback on the 3rd and 5th harmonics were measured.

With no appreciable feedback at the harmonic wavelengths, that is, low reflectivity of the mirrors at these wavelengths, the intensities of the 2nd and 3rd harmonics were found to be ~10-5 of the fundamental; the 5th was ~10-7. This is in reasonable agreement with harmonic measurements made at Stanford.[8] When feedback was introduced at the harmonic frequency (either by using copper mirrors or dielectric mirrors with high reflectivity at the harmonic frequency), the 3rd harmonic increased to ~10-4 of the fundamental. We tentatively interpret the large effect of feedback on the spontaneous emission to the following model: The spontaneous emission produced in each successive pass of the coherent fundamental light is coherently related to that of previous passes (over the lifetime of light in the cavity at the harmonic frequency). Because the added light is coherent, the field amplitudes rather than intensities add. If the phase angle between the fields on successive passes is small, this addition produces a large enhancement over what would be expected from simple incoherent trapping of the light in the cavity. We have not yet done a theoretical analysis or numerical simulation that shows that the phase relationship of the harmonic light on successive passes is such as to produce this enhancement.

Measurements of the spatial distribution of the output showed the expected behavior: that is, a single lobe for the fundamental, two for the 2nd harmonic, and three for the 3rd harmonic. We were unable to determine whether the multiple lobes were axially symmetric, that is, doughnut shaped.

Harmonic Lasing

Lasing has previously been observed on the third harmonic by one[9] or two[10] groups at Stanford. We have now been able to lase on the 3rd harmonic of the 10- to 11-μm fundamental by increasing the gain at the harmonic and increasing the cavity losses at the fundamental. The gain at the harmonic was increased by decreasing the wiggler gap from 8.8 to 5.8 mm, thus increasing the wiggler A value from ~0.7 to ~1. A set of various diameter apertures could be inserted into the cavity to increase the losses for the fundamental. With the use of apertures, lasing could be observed on both the fundamental and the 3rd harmonic. The efficiency of the 3rd harmonic lasing is approximately one-third that of the fundamental.

Figure 3 shows the measured detuning curves, with no aperture (Fig. 3a) and two successively smaller apertures (Fig. 3 b and c). Lasing at the 3rd harmonic appeared only when apertures were used and with a very narrow cavity-length tuning range. As the aperture was made progressively smaller, the detuning curve for the fundamental shifted to the short cavity side and no longer overlapped the 3rd harmonic detuning curve. This shift was caused by scraping at the apertures. The admixture of higher order transverse modes produces increased phase shifts for a round trip of the light in the cavity, thus increasing the effective length of the cavity.

Lasing with Tapered Wigglers

Wiggler Characteristics

Early FEL experiments at Los Alamos used a permanent magnet Halbach wiggler with an approximately

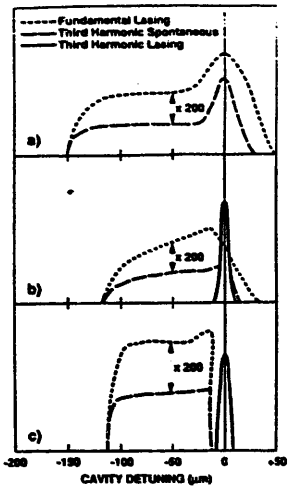

Fig. 3. Measured detuning curves for fundamental and third harmonic with a 5.8-mm-gap wiggler (a, b, and c are successively smaller apertures.)

linear 12% wavelength taper. The experiments during the past year have employed this wiggler and another of similar construction, but with a 30% parabolic taper. This parabolic configuration was chosen because it produced adequate small-signal-gain in the initial flat region and also had a large overall taper. Because the taper is continually increasing, we expected that electrons would not stay in resonance throughout the length, so that trapping would not be as nearly complete as with the linearly tapered wiggler.

The tapered wiggler experiments described here also employed a prebuncher, located ahead of the main wiggler, that produces a velocity modulation that enhances the capture of electrons in the main wiggler. Unlike previous prebunchers or optical klystrons,[11,12] the prebuncher employed here was optimized at high optical power[13] to produce maximum extraction efficiency rather than at low power to enhance small signal gain. It was a ~2.5 period wiggler that could be moved to vary the drift space between the prebuncher and wiggler from about 25-40 cm. Calculations[13] indicated that the prebuncher would produce an enhancement of about a factor of 2 in extraction efficiency at high cavity powers, and this was found to be the case. In agreement with simulations,[14] we found that changing the prebuncher-to-wiggler drift distance had large, periodic effects on the wavelength and the efficiency of the laser. The repeat distance, 3.3 cm, was $\sim\lambda_{LASER}\cdot(2\gamma^2)$, as predicted by slippage arguments.

Electron Trapping

Previous experiments showed that the energy spectrum of electrons that traversed a tapered wiggler had a long low-energy tail,[15] but only a slight sign of electrons trapped in a "bucket" of the ponderamotive potential. The absence of a bucket was caused by the growth of the transverse emittance of the electrons in the beam transport line and large energy loss during transit of the wiggler, both caused by wakefield effects. When these problems were eliminated, the results were different. Figure 4, the results of lasing with the prebuncher and 12% wiggler combination, shows the electron energy distribution in a 100-μs macropulse. Figure 4a is the distribution without lasing; Fig. 4b is the distribution when lasing. The electrons show a well-defined group of trapped particles, which are lowered in energy by an amount consistent with the taper of the wiggler. Similar effects are seen in the 30% tapered wiggler. As expected, the electrons tend to spill out of the bucket with

this wiggler, particularly when the FEL is lasing weakly. When the cavity power is higher, the buckets are deeper, fewer electrons fall out, and a well-defined peak in the energy spectrum appears at an energy loss consistent with the wiggler taper. The experimental energy spectra for both wigglers are in good qualitative agreement with simple physical models of tapered wigglers. In addition, the spectra agree quantitatively with those calculated in end-to-end simulations that modeled the accelerator and beam line with the accelerator code PARMELA and the FEL with the 3D FEL code FELEX.[16]

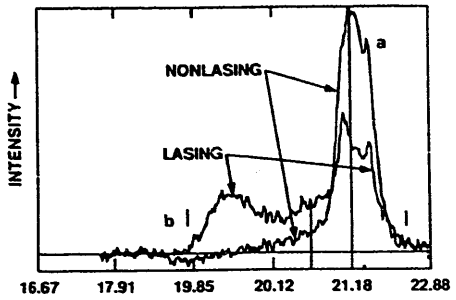

Fig. 4. Trapping and deceleration of electrons by prebuncher-12%-wiggler combination (a) electron spectrometer display without lasing and (b) with lasing.

Efficiency

The highest efficiency that we had previously achieved with the 12% wiggler was ~2.0%. It was probably limited by nonlinear behavior of the dielectric mirrors and emittance growth of the e-beam. The highest efficiency now measured is 4.4%. The measured extraction efficiencies are in reasonable agreement with end-to-end three-dimensional pulse calculations using PARMELA and FELEX.[13]

Detuning

Previously, the 12% tapered wiggler had detuning curves similar to those of the uniform wiggler, not in agreement with simulations. After our improvements to the FEL, both tapered wigglers show quite different properties. The highest efficiencies are now observed when sidebands are suppressed by cavity length detuning, in agreement with simulations. The same qualitative behavior is seen in the 30% taper wiggler. Lasing builds up during the macropulse with a single-line spectrum, then drops as sidebands develop. This behavior is shown experimentally in Fig. 5a. The same behavior is seen theoretically in Fig. 5b, which is a one-dimensional simulation using the code FELPS. As yet, numerical simulations of the effects of detuning with tapered wigglers have not shown a complete correlation with our experimental observations.

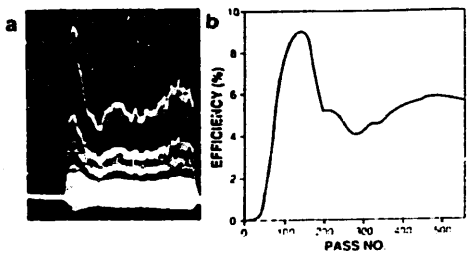

Fig. 5. (a) macropulse of light intensity vs time showing overshoot before sidebands develop; and (b) a simulation of (a).

Conclusions

The experiments at the Los Alamos Free-Electron Laser during the past year have significantly increased our understanding of the physics of rf FEL oscillators and our confidence in both simple physical models and numerical simulations. Although there are still uncertainties in the values of a number of our beam parameters, the FEL performs in qualitative agreement with physical models and in reasonable quantitative agreement with numerical simulations.

The Los Alamos FEL is currently being completely rebuilt with a laser-driven photoelectric injector. This change is expected to enhance its performance and allow new experiments that will extend our knowledge of the physics of these devices.

Acknowledgments

The authors wish to gratefully acknowledge the indispensable help of the staff and operating crew, in particular, Jon Sollid, Bill Stein, Joel Johnson, Alex Lumpkin, Renee Feldman, Roy Norris, Larry Haynes, John Hornkohl, Noel Okay, Scott Apgar, and Richard Martinez.

References

[1] R. W. Warren et. al., "Near-Ideal Lasing with a Uniform Wiggler," Proc. 10th International Free-Electron Laser Conference, Jerusalem, Israel, August 29-September 2, 1988, to be published in *Nucl. Instrum. and Methods.*

[2] J. E. Sollid et. al., "Sideband Suppression in the Los Alamos Free-Electron Laser Using a Littrow Grating," Proc. 10th International Free-Electron Laser Conference, Jerusalem, Israel, August 29-September 2, 1988, to be published in *Nucl. Instrum. and Methods.*

[3] Brian E. Newnam et. al., "Coherent Optical Production in the Los Alamos Free-Electron Laser Oscillator," to be presented in session JJ at the 1989 Quantum Electronics Laser Science Conference, QELs '89, Baltimore, Maryland, April 28, 1989.

[4] D. W. Feldman et. al., "High Extraction Efficiency Experiments with the Los Alamos Free Electron Laser, "Proc. 10th International FEL Conference, Jerusalem, Israel, August 29-September 2, 1988, to be published in *Nucl. Instrum. and Methods.*

[5] J. C. Goldstein et. al., "Simulation Codes for Modeling Free-Electron Oscillators," presented at Conference on Modeling and Simulation of Laser Systems, Los Angeles, California, January 16-29, 1989, to be published in Proc. SPIE 1045, "Modeling and Simulation of Laser Systems."

[6] R. W. Warren, J. C. Goldstein, and B. E. Newnam, "Spiking Mode Operation For a Uniform Period Wiggler," *Nucl. Instrum. and Methods*, A250, 19-26 (1986).

[7] R. W. Warren and J. C. Goldstein, "The Generation and Suppression of Synchrotron Sidebands," *Nucl. Instrum. and Methods*, A272, 155-162 (1987).

[8] D. J. Bamford and D. A. G. Deacon, "Measurements of the Coherent Harmonics Radiated in the Mark III Free-Electron Laser," Proc. 10th International Free-Electron Laser Conference," Jerusalem, Israel, August 29-September 2, 1988, to be published in Nucl. Instrum. and Methods.

[9] Stephen V. Benson and John J. Madey, "Demonstration of Harmonic Lasing in a Free-Electron Laser," Phys. Rev. A (Rapid Communications), 39, pp. 1579-81 (1989).

[10] J. Edighoffer et. al., private communication.

[11] M. Billardon, et. al., "First Operation of a Storage Ring Free-Electron Laser," *Proc. SPIE*, 453, 269-274 (1983).

[12] J. R. Neal, J. Edighoffer, S. W. Fornaca, C. E. Hess, T. I. Smith, and H. A. Schwettman," The TRW/Stanford Tapered Wiggler Oscillator," *Nucl. Instrum. and Methods*, A259, 295-304, (1987).

[13] H. Takeda, B. D. McVey, and J. C. Goldstein, "Theoretical Study of a High-Extraction Undulator for a Free-Electron Oscillator," *Nucl. Instrum. and Methods*, A259, 295-304, (1987).

[14] H. Takeda, private communication.

[15] A. Lumpkin and R. B. Feldman, "On-Line Extraction Efficiency Analysis for the Los Alamos Free-Electron Laser," *Nucl. Instr. and Methods*, A259, 19-25 (1986).

[16] J. C. Goldstein et. al., "Integrated Numerical Modeling of Free-Electron Laser Oscillators," Jerusalem, Israel, August 29-September 2, 1988, to be published in *Nucl. Instrum. and Methods.*

BUNCH LENGTHENING CALCULATIONS FOR THE SLC DAMPING RINGS*

KARL L. F. BANE AND RONALD D. RUTH

Stanford Linear Accelerator Center, Stanford University, Stanford, California 94309

ABSTRACT

The problem of bunch lengthening in electron storage rings has been treated by many people, and there have been many experiments. In the typical experiment, the theory is used to determine the impedance of the ring. What has been lacking thus far, however, is a calculation of bunch lengthening that uses a carefully calculated ring impedance (or wakefield).

In this paper we begin by finding the potential well distortion due to some very simple impedance models, in order to illustrate different types of bunch lengthening behavior. We then give a prescription for extending potential well calculations into the turbulent regime once the threshold is known. Then finally, using the wakefield calculated in Ref. 1 for the SLC damping rings, combined with the measured value of the threshold given in Ref. 2, we calculate bunch lengthening for the damping rings, and compare the results with the measurements.

1. POTENTIAL WELL DISTORTION

The self-consistent beam current distribution in an electron machine, below the turbulent threshold, is given by[3]

$$I(t) = K \exp\left(-\frac{t^2}{2\sigma_0^2} + \frac{1}{\dot{V}_{rf}\sigma_0^2} \int_0^t V_{ind}(t')\,dt' \right) \quad , \qquad (1)$$

with σ_0 the natural bunch length, $\dot{V}_{rf}$ the slope of the rf voltage at the position of the bunch and V_{ind} the transient induced voltage. In our notation a smaller value of t signifies an earlier point in time, with $t = 0$ the synchronous point for a low current beam. The induced voltage V_{ind} is given by

$$V_{ind}(t) = -\int_0^\infty W(t')I(t-t')\,dt' \quad , \qquad (2)$$

with $W(t)$ the longitudinal Green function wakefield. The value of the normalization constant K in Eq. (1) is such that the complete integral of $I(t)$ is equal to the total charge in the bunch Q. If we know the Green function wakefield then Eq. (1) can be solved numerically to give the current distribution of the bunch in the presence of wakefields. Since V_{ind} at time t depends only on the current at more negative (earlier) times, the solution of Eq. (1) is straightforward if we begin at the head of the bunch (where $V_{ind} = 0$) and proceed toward the tail. Taking the derivative of both sides of Eq. (1) yields an alternative form of it:

$$\frac{\dot{I}}{I} = -\frac{t}{\sigma_0^2} + \frac{V_{ind}}{\dot{V}_{rf}\sigma_0^2} \quad . \qquad (3)$$

In what follows, all distances will be given in terms of σ_0. Thus the independent variable becomes $x = t/\sigma_0$. Of particular interest will be the rms length σ_x, the full-width-at-half-maximum x_{FWHM}, and the centroid shift $\langle x \rangle$ of the current distribution. The ratio of the first two quantities is a measure of the similarity of the distribution to a Gaussian. Due to energy conservation, the third quantity, when multiplied by $-\dot{V}_{rf}\sigma_0$, gives the higher mode losses.

2. SOME SIMPLE IMPEDANCE MODELS

Over a frequency interval, the impedance of vacuum chamber elements can often be characterized by a simple electrical circuit element—an inductor, a resistor, or a capacitor. In this section we study the potential well distortion when the whole ring can be characterized by these simple models.

*Work supported by the Department of Energy, contract DE-AC03-76SF00515.

2.1 An Inductive Impedance

The SLC damping ring impedance is dominated by objects—such as shallow transitions, shallow cavities, bellows, or bumps in the vacuum chamber—that can be modelled by an inductor over a range of bunch lengths.[1] For a purely inductive object the induced voltage is given by $V_{ind} = -L\,dI/dt$, with the constant L the inductance. We note that this model is non-physical in that it is lossless. Although the solution of the potential well problem for an inductive impedance is given in Ref. 3, we present it here again in order to complete our picture of bunch lengthening in storage rings.

For a purely inductive impedance, Eq. (3) can be written as

$$y' = -\frac{xy}{1+y} \quad , \qquad (4)$$

with prime denoting the derivative with respect to $x = t/\sigma_0$. The normalized current is given by $y = LI/(\dot{V}\sigma_0^2)$; the normalized charge Γ (the complete integral of y) equals $LQ/(\dot{V}\sigma_0^3)$. The normalized induced voltage $v_{ind} \equiv V_{ind}/(\dot{V}_{rf}\sigma_0) = -y'$.

The numerical solution of Eq. (4), for several values of Γ, is shown in Fig. 1(a). Note that the charge distribution for a perfect inductor is symmetric about $x = 0$ (since there are no losses) and is more bulbous than a Gaussian distribution. From Eq. (4) it is apparent that the solution is parabolic wherever $y \gg 1$. In Fig. 1(b) we display σ_x and $x_{FWHM}/2.355$ (the dashes) as functions of Γ. For large currents σ_x varies roughly as $\Gamma^{1/3}$.

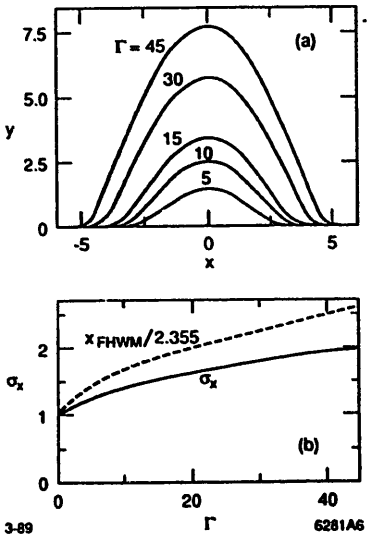

Fig. 1. An inductive impedance: (a) the bunch shape for several values of bunch population, and (b) the bunch length variation as a function of current.

2.2 A Resistive Impedance

Deep cavities, such as the rf cavities of the damping rings, tend to be resistive or somewhat capacitive to a beam over the normal range of bunch lengths. For an ideal resistive object, the induced voltage can be written as $V_{ind} = -IR$, with the constant R the resistance. Note that an ideal resistor is also

CH2669-0/89/0000-0789$01.00©1989 IEEE

not physical; there must be a phase shift, even if slight, between the bunch current and the induced voltage of a vacuum chamber object. For a resistive impedance, Eq. (3) becomes

$$y' = -(x + y)y \quad , \tag{5}$$

with $y = RI/(\dot{V}\sigma_0)$ and $\Gamma = RQ/(\dot{V}\sigma_0^2)$. Note that $v_{ind} = -y$.

Fig. 2(a) displays the solution to Eq. (5) for several values of Γ. As the current is increased the bunch tilts forward (up the rf wave) by an ever increasing amount, in order to compensate for the increased, higher mode losses. Fig. 2(b) shows σ_x and $x_{FWHM}/2.355$ (the dashes). We see that the bunch length increases only very slowly in a resistive machine. The dots give the centroid shift $\langle x \rangle$ of the bunch. It can be approximated by $\langle x \rangle = -\Gamma/(2\sqrt{\pi})$, which is the centroid shift, assuming that the bunch shape does not change with Γ. We note that Papiernik *et al*,[4] have solved the potential well problem for the impedance of a pillbox cavity, and have obtained very similar results.

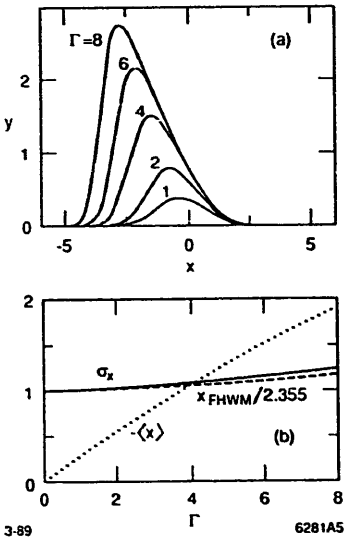

Fig. 2. A resistive impedance: (a) the bunch shape for several values of total charge and (b) the change of bunch length and centroid position (dots) with current.

2.3 A Capacitive Impedance

The wakefield of very short bunches in deep cavities is somewhat capacitive. For an ideal capacitive vacuum chamber object, the induced voltage is proportional to the integral of the current, with constant of proportionality $-1/C$, and C the capacitance. This model is unphysical in that it predicts that the energy loss of a bunch depends only on the total charge Q, and not on the peak current. For a purely capacitive impedance, Eq. (3) becomes

$$y' = -y[x + \int_{-\infty}^{x} y(x')\,dx'] \quad , \tag{6}$$

with $y = I/(\dot{V}_{rf}C)$ and $\Gamma = Q/(\dot{V}_{rf}\sigma_0 C)$. The solution to Eq. (6) closely approximates a Gaussian that has been shortened and shifted. Since the energy stored in a capacitor is $Q^2/2C$, the centroid shift is given by $\langle x \rangle = -\Gamma/2$. Figure 3 shows the bunch length dependence on Γ. By substituting a gaussian into Eq. (6), we can arrive at an analytical approximation of the bunch shortening, which for small current becomes $\sigma_x \approx 1 - \Gamma/\sqrt{8\pi}$. We note that bunch shortening has not been observed in storage rings, except at low currents in SPEAR, when the ring had many rf cavities.[5]

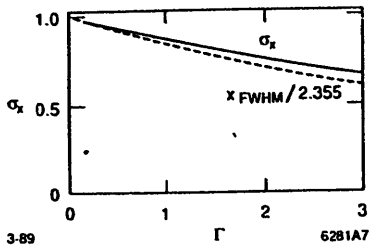

Fig. 3. Bunch shortening for a capacitive impedance.

3. THE INSTABILITY THRESHOLD

At some bunch population, there is an instability. The effect of this instability in an electron storage ring is to increase the energy spread of the equilibrium distribution. This is obviously a nonlinear process. As the bunch length increases, the bunch peak current decreases which decreases the longitudinal forces. Radiation damping then serves to reduce the bunch length. The competition between radiation damping and quantum excitation together with longitudinal instability leads to some equilibrium energy spread. The bunch length is related to this via the rf voltage plus potential well distortion.

Boussard[6] conjectured that the longitudinal instability in a bunched beam is due to a coasting-beam-like instability within the bunch. Qualitatively, the argument goes as follows: Consider an impedance which induces an instability which has a wavelength small compared to the bunch length. If the growth time of the instability is short compared to a synchrotron oscillation period, then the center of the bunch looks like a coasting beam except, of course, that it has a high peak current. Therefore, to estimate the threshold for instability one might use the coasting beam threshold[7] but replace I by I_{peak}.

The issue of the applicability of a coasting beam instability criterion to a bunched beam was studied in detail by J. M. Wang and C. Pellegrini.[8] They found that one obtains a coasting beam like instability condition provided that:

1. The impedance is broad band relative to the bunch spectrum (Fourier transform of the line density).
2. The growth rate is much greater than ω_s (fast blowup).
3. The instability occurs at wavelengths much shorter than the bunch length.

Actually, the threshold which they obtain looks like the threshold for a coasting beam, but it has a different interpretation. It is a sufficient condition for no fast blowup. They also show that one obtains the usual type of coasting beam stability boundary except, of course, the boundary is for fast blowup. The "threshold" condition for a Gaussian bunch is[8]

$$\frac{e^2 N |Z(n)/n|}{2\pi^{3/2}\sigma_\tau \alpha E \sigma_\epsilon^2} \leq 1 \quad . \tag{7}$$

In Eq. (7), we have substituted the peak current for a Gaussian distribution. In this equation, σ_τ must be interpreted as the actual bunch length. Since we have only a sufficient condition for fast instability, we only use Eq. (7) for scaling purposes. Unfortunately, we know of no reliable calculation of the precise threshold, although this should be possible using techniques in Ref. 8.

To proceed, we take the threshold from experimental data, and above the threshold we use Eq. (7) to scale the energy spread as

$$\sigma_\epsilon = \sigma_{\epsilon 0}\left[\frac{N}{N_{th}}\right]^{1/3} \quad . \tag{8}$$

Potential well bunch lengthening is then used to calculate the bunch form in a self-consistent manner.

4. BUNCH LENGTHENING IN THE SLC DAMPING RINGS

The SLC damping rings have many changes in vacuum chamber cross-section. In an earlier paper[1] the longitudinal wakefields of the different vacuum chamber elements were computed for a short—1 mm—Gaussian bunch using T. Weiland's computer program TBCI.[9] All the individual contributions were then added up, giving a pseudo-Green function wake that represents the entire ring (see Fig. 4). By substituting this function into Eq. (1) we can calculate the current distribution up to the turbulent threshold current. Knowing N_{th} we can extend the calculation to higher currents if we replace σ_0 by $\sigma_0(N/N_{th})^{1/3}$ in Eq. (1).

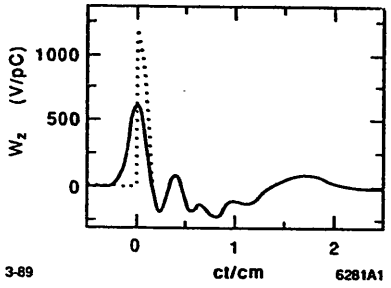

Fig. 4. The wakefield of a 1 mm Gaussian bunch in the SLC damping rings, and our Green function (dots).

We need to keep two things in mind when using our wakefield. First, since it represents the response to a 1 mm Gaussian bunch, it will be unable to resolve variations in bunch shape over distances that are short compared to 1 mm. But this limitation should not be a problem for our calculations because (i) $c\sigma_0$ is large compared to 1 mm, (ii) the bunch becomes even longer at higher currents, and (iii) we expect the bunch forms to be smooth. Second, in order for us to use the wake as a Green function, the front of it needs to be modified so that it is zero for $t < 0$. We have evidence that the results (presented below) are not very sensitive to the details of this modification, provided that the changes are localized near $t = 0$ and that the area under the curve remains unchanged. For our calculations, we have chosen to reflect the leading tail to the back, and then to add it to the existing wake (see the dotted curve of Fig. 4).

Figure 5 displays the bunch lengthening and centroid shift calculation results for the SLC damping rings when V_{rf} = 0.8 MV. (The rf frequency is 714 MHz.) Length dimensions are again given in units of σ_0 (at this rf voltage $c\sigma_0 = 5$ mm). As for the inductive model, the distribution is more bulbous than a Gaussian. If we take the effective inductance of the ring to be 50 nH (see Ref. 1) we find that at $N = 1.5 \times 10^{10}$ $\sigma_z = 1.33$ and $x_{FWHM} = 3.69$ for the inductive model, which compare well with the values of, respectively, 1.38 and 3.93 found here. (To approximate the resistive behavior as well would require a more complicated model.) From Fig. 5(b) we see that there is a significant amount of higher mode losses.

Energy spread measurements performed on the North damping ring found that $N_{th} \approx 1.5 \times 10^{10}$ at $V_{rf} = 0.8$ MV.[2] Taking this threshold value, the bunch lengthening calculations were extended into the turbulent regime (indicated by the dashes in Fig. 5). We see that at $N = 3 \times 10^{10}$ the rms bunch length is increased by 70%. Very precise measurements of the bunch shape as function of current have also been performed at $V_{rf} = 0.8$ MV, using the bunch compressor of the Ring-to-Linac (RTL) transfer line and a downstream digitizable video screen.[2] In addition, the synchronous phase dependence on current has been measured. The results of these measurements are indicated by the plotting symbols in Fig. 5.

Finally, in Fig. 6 we present the bunch shapes for bunch populations of N = 0.7, 1.2, 2.1 and 2.9 × 10^{10}.

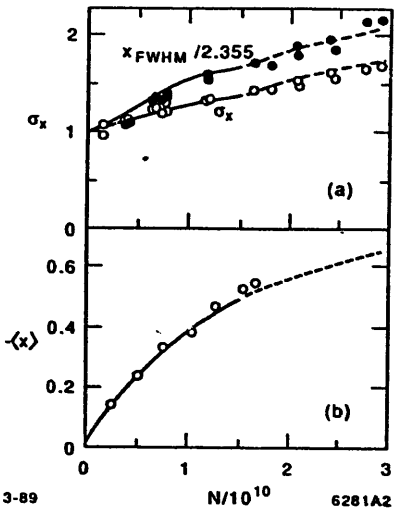

Fig. 5. (a) Bunch lengthening, and (b) the centroid shift calculated for the SLC damping rings at $V_{rf} = 0.8$ MV. The symbols indicate the measurement results.

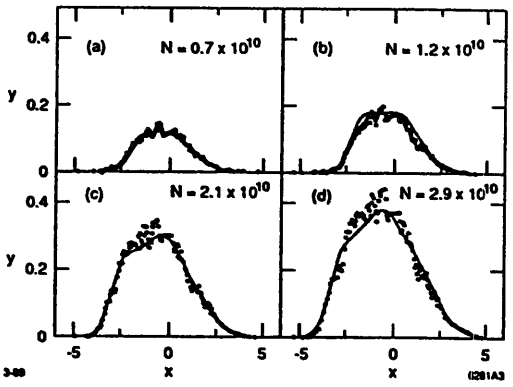

Fig. 6. The calculated damping ring bunch shapes for several current values, when $V_{rf} = 0.8$ MV. Superimposed on the curves are measurement results.

The abscissas give $x = t/\sigma_0$, the ordinates are $y = IZ_0/(\dot{V}\sigma_0)$ with $Z_0 = 377\ \Omega$. Superimposed on the curves are the digitized measurement results. The fluctuations in the data (especially at the peaks) are due to nonuniformity in the response of the screen. Considering that there are no fit parameters, the agreement between the data and the calculations is quite good.

REFERENCES

1. K. L. F. Bane, SLAC–PUB–4618, (1988).
2. L. Rivkin *et al*, SLAC-PUB-4645, (1988).
3. J. Haïssinski, *Il Nuovo Cimento* 18B, No. 1, 72 (1973).
4. A. Papiernik, M. Chatard-Moulin, B. Jecko, Proc. of the 9th Int. Conf. on High-Energy Acc., SLAC, 1974, p. 375.
5. P. B. Wilson *et al*, SLAC-PUB-1894, (1977).
6. D. Boussard, CERN LABII/RF/INT/75-2 (1975).
7. V. K. Neil and A. N. Sessler, *Rev. Sci. Instr.*, 36 429 (1965).
8. J. M. Wang and C. Pellegrini, Proc. of the 11th Int. Conf. on High-Energy Accelerators, CERN, 1980, p. 554.
9. T. Weiland, DESY 82– 015 (1982) and *Nucl. Inst. Meth.* 212, 13 (1983).

STATUS OF LBL/LLNL FEL RESEARCH FOR TWO BEAM ACCELERATOR APPLICATIONS*

D. B. Hopkins and A. M. Sessler
Accelerator & Fusion Research Division
Lawrence Berkeley Laboratory
University of California
1 Cyclotron Road
Berkeley, California 94720

Abstract

We review the status of free electron laser (FEL) research being conducted at LBL and LLNL as part of a broader program of research on two beam accelerators (TBAs). Induction accelerator-driven FELs for use as power sources for high-gradient accelerators are discussed, along with preliminary cost estimates for this type of power source. Finally, a promising new version of an FEL/TBA is described.

LBL/LLNL FEL Research

Figure 1 shows the principal elements of an FEL-driven two-beam accelerator. The TBA has been discussed in detail elsewhere.[1,2] In collaboration with LLNL, our FEL experimental research program got underway in 1982 with the construction of the Electron Laser Facility (ELF) at LLNL.[3] Several papers[4-8] have summarized the FEL performance of this facility when operated at a ~ 35 GHz, > 1.2 GW power level and also at 138 GHz. Recent papers[9,10] discuss strategies for achieving more efficient wiggler tapering and reducing output noise to < 1%.

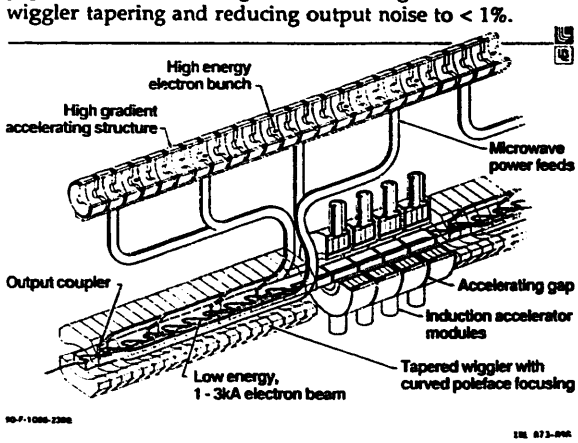

Figure 1. FEL/TBA Configuration

For practical FEL-driven TBAs, a number of troublesome issues have recently been considered. Solutions have been found for some of these while others await further analytical and/or experimental treatment. Early on, wakefield effects in ~ 15-30 GHz high-gradient accelerator sections were thought to preclude their operation at interesting beam brightness levels for linear colliders under consideration. It has been shown[11], however, that the wakefields can be adequately reduced if three things are done. First, the beam apertures, i.e. iris diameters, must be increased about a factor of two over the dimensions arrived at by standard accelerator design procedures. Second, there must be much more transverse beam focusing than in traditional linacs. This can be supplied by external quadrupoles, or, as has been suggested by W. Schnell, by rf in conjunction with elliptical (alternating) gaps. Third, as pioneered in the USSR[12] and extended by Bane at SLAC,[13] an energy sweep along the bunch is required. Another problem initially thought to be serious but later "solved" involves the large potential FEL gain at synchrotron frequency sidebands. Analysis shows[14] that the synchrotron sideband power is dramatically reduced if the FEL interaction waveguide size is chosen properly. This approach has now been experimentally proven successful.[14]

In the TBA, as originally conceived, not all of the microwave power is removed from an FEL section. A significant amount of remaining power crosses the following beam-reacceleration gap, maintaining a sizeable rf bucket in which all of the electrons are trapped, thus establishing the proper phase in the next FEL amplifier. Several difficulties result from this arrangement for which no satisfactory solutions have yet been found. Another difficulty involves rf handling: the extraction of rf power from the FEL. The interaction waveguide is necessarily highly oversized for the operating wavelength. It is found that the usual techniques, e.g. directional coupling, are impractical and convert power into undesirable modes. We experimented unsuccessfully at ELF with a type of coupler which has septa acting as "scoops" for extracting single-mode power.[15] Different approaches are now under consideration. These are mentioned briefly in a later section that discusses a new FEL/TBA version which avoids many of the problems discussed in this section.

A most serious problem with the original FEL/TBA configuration is its phase and amplitude sensitivity to errors in the wiggler magnetic field, beam energy and beam current.[16,17] For practical machines, parameter stabilities of ≤ 0.1 % would be required. The net effect is to limit realistic TBA section lengths to a few tens of meters, at best, with new beam injectors required at these intervals for "starting over". Feedback compensation schemes have been considered but appear to be impractical.

Regarding the high gradient accelerator (HGA) portion of a TBA, our group undertook a program to demonstrate the successful fabrication of HGA sections for 33-35 GHz operation and test them at ELF to determine their ultimate operating gradients. This work has been summarized elsewhere.[15,18] A high-quality 33.39 GHz, 34

*Work performed under the auspices of the U.S. Department of Energy by the Lawrence Berkeley Laboratory under contract No. DE-AC03-76SF00098.

cavity, 10-cm long accelerator, fabricated by the Haimson Research Corporation,[19] is now scheduled to be tested soon at the Massachusetts Institute of Technology, using a developmental cyclotron auto resonance maser (CARM) as a 20-50 MW power source, in a collaboration with G. Bekefi's group.

FEL-Based Accelerator Power Sources

Before the FEL/TBA is fully realized in an actual accelerator, e.g. linear collider, microwave FELs may find an initial application as accelerator power sources. An induction accelerator coupled with a wiggler can readily produce GWs of power. These sources can then be replicated and arranged to periodically drive an HGA in the same manner that multiple klystrons drive long accelerators, e.g. at SLAC. Such sources have been proposed and preliminary cost estimates made, most recently for TeV linear collider applications at 17 GHz[20]. For this study, the assumed collider parameters were as shown in Table 1.

TABLE 1

Linear Collider Parameters

Operating frequency	17 GHz
Collider length	7.41 km
Total rf power required	3.87 TW
Length between rf feeds	1.44 m
rf power/m required	634 MW/m
rf pulse width	50 ns
Repetition rate	180 Hz
Luminosity (single bunch)	5.0×10^{32} cm^{-2} sec^{-1}
Luminosity (21 bunches)	1.0×10^{34} cm^{-2} sec^{-1}

To power this 17 GHz collider, an induction accelerator-driven FEL power source was considered which has the parameters shown in Table 2.

TABLE 2

Power Source Parameters

Beam energy	3.5 MeV
Beam current	3.0 kA
Beam energy stability ($\Delta E/E$)	0.8%
Interaction waveguide size	6.0 x 3.0 cm
Wiggler length	1.7 m
Wiggler period	12 cm
Resonant wiggler field, on axis	4.11 kG
Final wiggler field, after tapering	1.8 kG
Input rf power	80 kW
Output rf power	5.0 GW

For this application, a new, simple, inexpensive permanent magnet and steel wiggler was designed[21]. Also, an "afterburner" was assumed to follow the wiggler to extract a good fraction of the rf energy from the bunched beam before it is dumped. This is a final relativistic klystron stage where the beam threads a few output coupling cavities producing ~ 2 GW of additional rf power, thereby increasing overall efficiency. For the induction accelerator driver, cost estimates were prepared on three different bases: (1) present technology, (2) a newer small-cell design under development and (3) a projected industrialized version. Estimated costs for the induction driver were, (1) \$1.8M, (2) \$1.5M, and (3) \$0.9M, respectively. The wiggler cost is found to be very small, namely ~ \$80K for a 2.1 m length. Since costs are dominated by that of the induction accelerator, efforts are being made to find ways of significantly reducing this cost.

The TBA concept has always incorporated the idea of periodic reacceleration of the drive beam. This would take place to restore the energy to the beam which had been given up to the microwave field in the FEL sections. Induction accelerator cells would be added to accomplish this. Reacceleration can also be of benefit to the power sources being discussed in this section. For the linear collider parameters of Tables 1 and 2 and assuming the small-cell technology mentioned above, the cost and efficiency of power sources has been estimated.[20] These estimates are summarized in Table 3 for four cases having no reacceleration, then one, two, and three reaccelerations. As can be seen, the difference between no reacceleration and three reaccelerations is an impressive cost saving of \$284 M and an efficiency increase to 32% from 25%.

Table 3. Re-Acceleration Various Number of Times

(Assume Small Cell Costs, an RK after burner, and a 3.87 TW total power requirement)

Basic Unit		
Injector (0-1.5 M)	\$ 920k	
Accelerator (1.5-3.5 MeV)	\$ 620k	
W,R,MD and M*	\$ 250k	
Base Unit Cost	\$1790k	
Power Output per Unit (5+2)		7.0 GW
Total Cost (553 units)		\$990 M
Beam to rf Efficiency		67 %
Overall Efficiency		25 %
Single Re-Acceleration		
Base Unit Cost	\$1790k	
Accelerator (+2 MeV)	\$ 620k	
W,M**	\$ 120k	
Unit Cost	\$2530k	
Power Output per Unit (10 +2)		12 GW
Total Cost (323 units)		\$817 M
Beam to rf Efficiency		73 %
Overall Efficiency		29 %
Two Re-Accelerations		
Base Unit Cost	\$1790k	
Accelerators (+4 MeV)	\$1240k	
W,M**	\$ 240k	
Unit Cost	\$3270k	
Power Output per Unit (15+2)		17 GW
Total Cost (228 units)		\$746 M
Beam to rf Efficiency		76 %
Overall Efficiency		31%
Three Re-Accelerations		
Base Unit Cost	\$1790k	
Accelerators (+6 MeV)	\$1860k	
W,M**	\$ 360k	
Unit Cost	\$4010k	
Power Output per Unit (20+2)		22 GW
Total Cost (176 units)		\$706 M
Beam to rf Efficiency		77 %
Overall Efficiency		32 %

*Wiggler, Relativistic Klystron, Microwave Driver, and Microwave Equipment
**Wiggler and Microwave Equipment

Improved Version of an FEL/TBA

Recently, a new version of an FEL/TBA has been proposed which avoids a number of difficulties inherent in the original concept.[22] In the new version, a relatively small, stable rf clock signal is provided at the input of each FEL section. At the end of each FEL section essentially all of the rf power is removed and transported to the HGA power input ports. The bunched electrons of the drive beam go on to the next FEL section through the following reacceleration gaps. There is no longer a need for any remaining microwave power to cross these gaps. The advantages that accrue with this configuration are many. In the original FEL/TBA concept, errors in various parameters were cumulative and resulted in the phase

and amplitude sensitivities discussed earlier. An analysis of the new version has been made and it has been shown that the FEL/TBA can be designed so that errors do not accumulate. In short, the new FEL/TBA "locks on" to the equilibrium state even if the drive beam energy is initially in error. A full study of this subject is now being prepared.[23] In the meantime, we have begun a search for a practical method for extracting all of the rf power at the end of an FEL section. One method which may be workable is to employ a specially-designed magnet at the end of the FEL. This would introduce a short, brief, achromatic jog of the electron beam away from the centerline, separating it from the microwave field[24] In the beam-free region thus created, centered on the machine axis, an angled "mirror" would then reflect the microwave power out of the machine. In a second method being considered,[25] all but several percent of the microwave power is reflected out of the beampipe by a four-faceted reflector. This also serves as a convenient four-way power divider.

Acknowledgements

This paper reports on work conducted by a large number of people over the last several years. Others offered expert advice on various issues. At LLNL, they are W. A. Barletta, R. J. Briggs, F. W. Chambers, J. C. Clark, J. W. Dini, J. C. Farmer, W. M. Fawley, R. A. Jong, R. W. Kuenning, V. K. Neil, T. J. Orzechowski, A. C. Paul, D. Prosnitz, L. L. Reginato, E. J. Scharlemann, R. D. Stever, A. L. Throop, G. A Westenskow, S. M. Yarema and S. S. Yu. At LBL, they are C. L. Chavis, K. Halbach, E. H. Hoyer, G. W. Koehler, H. O. Krapf, F. B. Selph, E. J. Sternbach, G. D. Stover, and D. H. Whittum. At other laboratories, they are G. A. Loew, P. L. Morton and P. B. Wilson of SLAC, J. S. Wurtele of MIT., R. B. Palmer and C. Pellegrini of BNL, B. R. Anderson of the U.S. Air Force Weapons Laboratory at Allbuquerque, N. M., and H. A. Johnsen of Sandia Laboratory, at Livermore Ca. Finally, in private businesses, are J. Haimson and B. Mecklenburg of Haimson Research Corporation and J. R. Bayless of Pulse Sciences, Inc.

References

1. A. M. Sessler, "The Free Electron Laser as a Power Source for a High-Gradient Accelerating Structure", in Laser Acceleration of Particles, P. J. Channel ed. (AIP Conf. Proc. No 91, American Institute of Physics, New York, 1982), p. 154-159
2. D. B. Hopkins and A. M. Sessler, "The Two Beam Accelerator", Proc. 1986 Linear Accelerator Conf., June 2-6, 1986, SLAC, 385 (1986)
3. T. J. Orzechowski, et al., in Free Electron Generators of Coherent Radiation, C. A. Brau, S. F. Jacobs, M. O. Scully, editors (SPIE, Bellingham, WA, 1983) p. 65
4. E. J. Scharlemann, J. Appl. Phys. 58 (1985), 2154
5. T. J. Orzechowski, et al., "High Gain and High Extraction Efficiency from a Free Electron Laser Amplifier Operating in the Millimeter Wave Regime", Nucl. Inst. & Meth. in Phys. Res. A250, 144 (1986)
6. A. L. Throop et al., "Experimental Characteristics of a High-Gain Free-Electron Laser Amplifier Operating at 8-mm and 2-mm Wavelength", Proc. AIAA 19th Fluid Dynamics, Plasma Dyanamics and Laser Conf., Honolulu, Hawaii, June 8-10 (1987)
7. T. J. Orzechowski, et al., "Measurement of the Phase of the Electromagnetic Wave in a Free-Electron Laser Amplifier", Phys. Rev. A355, 2184, March 1 (1987)
8. A. L. Throop, et al., "Experimental Results of a High Gain Microwave FEL Operating at 140 GHz", Nucl. Inst. & Meth. in Phys. Res., A272, 15 (1988)
9. R. A. Jong, et al., "Baseline Design for the IMP Wiggler", Subm. to Journ.. Appl. Phys., April (1988), also UCRL-98214
10. R. A. Jong, et al., "Wiggler Taper Optimization for Free-Electron Laser Amplifiers with Moderate Space-Charge Effects", Nucl. Inst. & Meth. in Phys. Res., A272, 15 (1988), also UCRL-96735
11. F. B. Selph and A. M. Sessler, "Transverse Wakefield Effects in the Two Beam Accelerator", Nucl. Inst. & Meth. in Phys. Res., A244, 323, (1986)
12. V. E. Balakin et al., Proc. of 12th International Conference on High Energy Accelerators (Fermi National Accelerator Laboratory, 1983) pp. 119-120.
13. K.L.F. Bane, "Landau Damping in the SLAC Linac", IEEE Trans. on Nuc. Sci. NS-32, 5, 2389 (1985)
14. J. Masud, et al. "Sideband Control in a Millimeter Wave Free Electron Laser", Phys. Rev. Lttr. 58, 763 (1987)
15. D. B. Hopkins, et al., "Fabrication and 35 GHz Testing of Key Two-Beam Accelerator Components", Proc. 1987 IEEE Part.. Accel. Conf., IEEE Cat. No. 87CH2387-9, 1, 80, Mar. 16-19 (1987)
16. R. W. Kuenning, et al., "Radio Frequency Phase in the FEL Section of a TBA", Proc. of the 8th International Free Electron Laser Conference, Nucl. Inst. & Meth. in Phys. Res. A259, 219 (1987)
17. Y. Goren and A. M. Sessler, "Phase Control of the Microwave Radiation in Free Electron Laser Two Beam Accelerator", Proc. of the Workshop on New Developments in Particle Acceleration Techniques, Orsay, France, July (1987)
18. D. B. Hopkins, et al., "Design and Fabrication of 33 GHz High-Gradient Accelerator Sections", Proc. of European Part. Accel. Conf., Rome, Italy, June 7-11 (1988), also LBL-25368
19. J. Haimson and B. Mecklenburg, "Design and Construction of a 33 GHz Brazed Accelerator Waveguide for High Gradient Operation", Proc. 1987 IEEE Part. Accel. Conf., IEEE Cat. No. 87CH2387-9, 1, 80, Mar. 16-19 (1987).
20. D. B. Hopkins, et al, "An FEL Power Source for a TeV Linear Collider", Proc. 1988 Lin. Accel. Conf., Williamsburg, Va., October 2-7 (1988), also LBL-25936
21. Wiggler designed by K. Halbach and E. H. Hoyer
22. A. M. Sessler, et al., "A New Version of a Free Electron Laser Two Beam Accelerator", Proc. Tenth Int. Conf. on Applications of Accelerators in Research and Industry, Denton, Texas, November 7-9 (1988), also LBL-25937
23. J. S. Wurtele, A. M. Sessler, E. Sternbach, D. Whittum, manuscript for the Proceedings of the Conference on Advanced Acceleration Concepts, Arrowhead, January 1989.
24. Suggested by A. C. Paul
25. Suggested by T. J. Orzechowski.

A FIVE-PICOSECOND, ELECTRON PULSE FROM THE ANL L-BAND LINAC*

G. L. Cox, D. T. Ficht, C. D. Jonah, G. S. Mavrogenes, and M. C. Sauer, Jr.
Argonne National Laboratory
9700 S. Cass Avenue
Argonne, IL 60439 USA

The pulse-compression system of the Argonne National Laboratory Chemistry Division L-Band Linac, presented at the 1986 Linear Accelerator Conference at Stanford, California, has been completed. A five-picosecond-wide electron pulse containing 6 x 10^{-9} coulomb charge has been achieved. Acceleration parameters and the pulse-width measurement technique are discussed, and future plans for the utilization of this pulse in radiation chemistry studies are presented.

Introduction

The description of this system has been presented in Reference 1.

The system was designed to compress the 22-MeV pulse of 30 ps Full Width Half Maximum (FWHM) to pulse lengths of 5 to 6 ps with large peak currents of 1 x 10^3 A/pulse. This system became necessary in order to extend the study of reactive fragments of molecules to the time scale of a few picoseconds and, in particular, to examine the chemistry of electrons and ions before and during relaxation of the surrounding media. The 22-MeV electron linac uses a double gap 12th subharmonic pre-buncher followed by a one-wavelength 1.3 GHz traveling-wave prebuncher and a tapered buncher to produce a single pulse of 30 ps from one rf bucket, with an energy spread of dE/E = ±0.5% (FWHM) as shown in Figure 1. The pulse contains a long tail in the time domain and the same in the energy spectrum. [2]

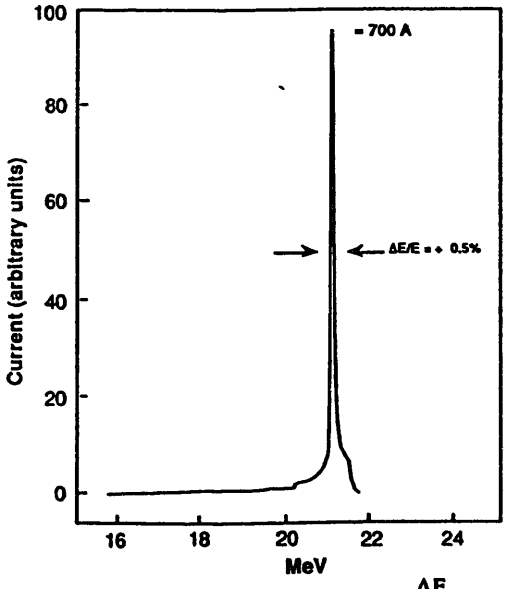

Figure 1. Energy spread of the 30-ps pulse $\frac{\Delta E}{E}$ = ± 0.5% (FWHM).

However, more than 80% of the electrons are within ±35 ps and $\frac{\Delta E}{E}$ of ±1%. The phase compression system required that the energy spread be increased considerably in order to rotate the ellipse, but fortunately the chemistry experiments are not sensitive to the beam energy spread $(\frac{\Delta E}{E})$.

Accelerator Parameters and Beam Measuring

The accelerator was tuned in such a way that the electron pulse was riding on the back slope of the traveling wave so that the front electrons were on the peak of the wave in both accelerating waveguides. The result of such a tune up was that the electrons within the pulse were oriented so that the higher energy ones were in the front and the lower energy ones in the tail of the pulse.

The beam exiting the accelerator is bent 90° by two 45° magnets with adjustable slits between them to control the energy spread of the beam as shown in Figure 2. Following a focusing quadrupole, the beam enters the bunching cavity which is an L-band waveguide identical to the accelerating waveguides of the linac. The value of the isochronous electric field in the bunching cavity is critical, and the rf power fed into it is controlled by a variable power splitter and phase shifter. A six-inch diameter circular magnet is placed just beyond the first 90° bending magnet, and it acts as a crude spectrometer. When the pulse is placed at the peak of the traveling wave in the bunching cavity, the peak field in that cavity is measured by measuring the maximum beam energy gain. Thus, the power splitter has been calibrated, and the readings are accurate and repeat well.

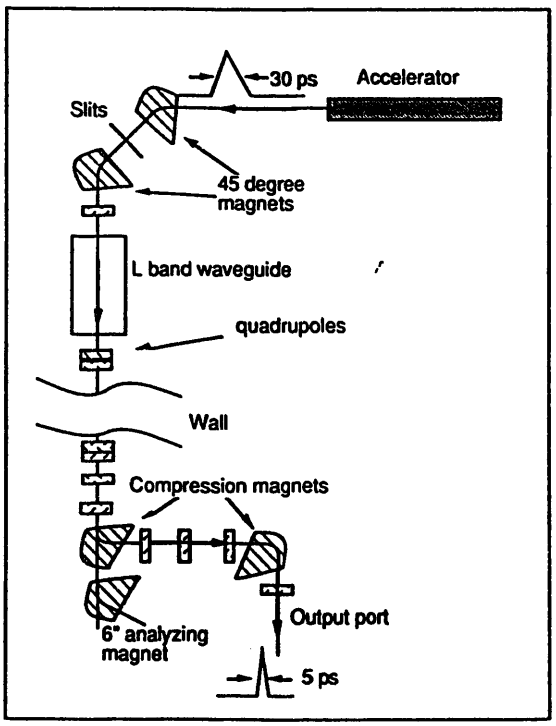

Figure 2. Beam transport system.

*Work performed under the auspices of the US-DOE.

CH2669-0/89/0000-0912$01.00©1989 IEEE

By knowing the peak field in the bunching cavity, a pulse of known width (±15 ps or ±7.5°) placed in such a way that its center is in the 0° phase position, and its front towards the increasing voltage will emerge with an energy spread that is readily calculated $V = V_0 \sin \theta$. In our case, the best results were obtained with a $V_0 = 5.3$ MeV, thus a 30-ps pulse will emerge with $\frac{\Delta E}{E} = \pm 5.3 \sin 7.5° \; z = \pm 0.690$ MeV (FWHM), and this is roughly what it was expected to be.

Optical Measurements

The pulse width was measured using the same technique that has been previously employed in this laboratory [3]. The principle of the measurement is as follows. The electron beam irradiates a 5 cm suprasil cell which contains 1 atm xenon gas. The refractive index of xenon is sufficiently high so that Cerenkov radiation is created and exits the cell in a cone making an angle approximately 2.5 degrees to the beam. This light is then focussed onto the slits of a streak camera. The streak camera is used to measure the width of the pulse. The system is shown in Figure 3.

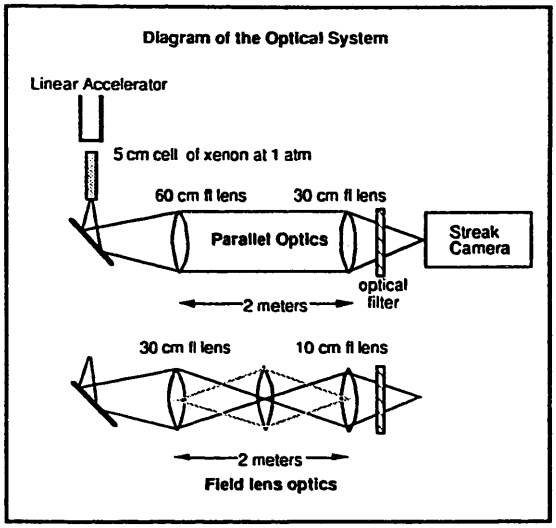

Figure 3. Optical system.

The Cerenkov was generated in xenon rather than in quartz so that most of the light could be collected and used for analysis. In addition, the scattering of the electrons is low in xenon so the angle at which the light comes is defined primarily by the incoming electron beam. Furthermore there is very little velocity difference between the electron beam and the generated light in 1 atm of xenon, which leads to a correspondingly negligible time spread in the the width of the measured Cerenkov pulse. In quartz the generated light travels approximately 30% slower in the quartz than does the electron beam.

Two optical transport systems were used to measure the pulse. Both were able to give good results. For the parallel optics, a defining slit was used at the cell to limit the region of light which can be transported to the streak camera. It was essential to limit the wavelength region of the light which strikes the streak camera. This was done using a 5-58 Corning glass filter which is centered at 410 nm and has a width of approximately 60 nm. If another broad-band filter which is peaked further into the ultraviolet is used or if no filter is used, the measured pulse width is broadened. This was attributed to the variation of the refractive index of the lenses over the wavelength range of light that was detected by the streak camera.

A Hamamatsu C1370-01 streak camera was used for the measurements. This streak camera has a time resolution of better than 2 ps. We used a slit width of approximately 7 μ. This slit width was chosen to keep the intensity low on the streak tube and thus avoid space-charge broadening in the streak tube. (A slit width of approximately 30 μ would not optically have limited our pulse width measurements.) The trigger for the streak camera was obtained from the pulse which triggered the electron gun. The jitter of the pulse detected by the streak camera was approximately 25 ps. This is due to both the jitter in the streak camera trigger and the jitter between the injector trigger and the RF of the accelerator. We did not attempt to improve upon this value.

Because the signal from the streak camera must be limited to avoid space-charge broadening in the measurement, there is considerable shot noise on the signal. To allow signal averaging, a program was written for the Hamamatsu computer to determine the position of the pulse. With this information, several pulses can be shifted and added together. A typical result is shown in Figure 4. Ten pulses were averaged. The slit width was decreased until the measured pulse width was constant. This was done to eliminate the space-charge broadening in the streak camera. Similar results were obtained on different days.

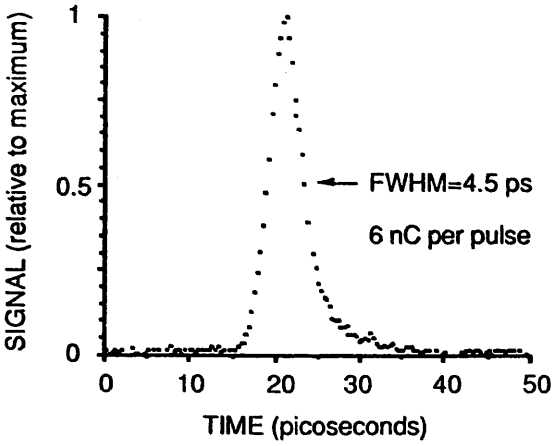

Figure 4. Relative light intensity vs. time for the Cerenkov light pulse created in 1 atm xenon. (Wavelength of light centered at about 410 nm, FWHM ≅ 60 nm.) Average of 10 pulses.

The critical factors for accurately measuring such short accelerator pulses are: (1) controlling the space-charge broadening of the streak camera; (2) controlling the region that is observed by the streak camera using appropriate focussing and field stops; (3) using xenon to tightly confine the light that is measured; and (4) selecting the wavelength that is observed to avoid broadening through wavelength dispersion in the lenses.

Uses of the 5-ps Pulse

The compressed pulse is currently being used to measure the recombination fluorescence which occurs when solutions of aromatic scintillators in dielectric liquids are irradiated. This fluorescence is due to the rapid scavenging of positive and negative charge by the scintillator molecule followed by ion-recombination which yields the lowest excited singlet state of the scintillator. The time dependence of the recombination fluorescence can be used to derive information about the ion chemistry of the solvent and the distribution of distances (from the sibling cation) of the electron ejected in an ionization event. This

work is well underway and will be reported in a future publication. [4]

An apparatus is also being assembled in which the 5-ps pulse will be used in a pump-probe system for measurement of the optical absorbance of transient species in condensed-phase systems. This system is an extension of one used previously for similar measurements with a 30-ps electron pulse, [5] and will be used, for example, to study ultra-fast electron localization and solvation processes in alcohols.

Conclusions

In general, the future of the short pulses (5-6 ps) with high intensity > 1000 A belongs to the laser-excited photocathodes in conjunction with an rf source, but until reliable photocathodes are developed with long life and with reasonable vacuum requirements, the needs of the scientific community for very intense short pulses will be satisfied using the techniques described above.

References

[1] G. Mavrogenes, J. Norem, J. Simpson, "A Pulse Compression System for the ANL 20 MeV Linac," presented at the Stanford Linear Accelerator Conference June 2-6, 1988.

[2] G. Mavrogenes, W. Gallagher, T. Kohe, D. Ficht, "High Charge Picosecond Pulses with a Double Gap Subharmonic Buncher," IEEE NS-30, pp. 2989-2992, 1983.

[3] G. S. Mavrogenes, C. Jonah, K. H. Schmidt, S. Gordon, G. R. Tripp and L. W. Coleman "Optimization of Isolated Electron Pulses in the Picosecond Range from a Linear Accelerator using a Streak Camera-TV Diagnostic" Rev. Sci. Instrum. vol. 47, pp. 187-189, 1976.

[4] M. C. Sauer, Jr. and C. D. Jonah, unpublished results.

[5] C. D. Jonah "A Wide Time Range Pulse Radiolysis System of Picosecond Time Resolution" Rev. Sci. Instrum. vol. 46, pp. 62-66, 1975.

ON USING A SUPERCONDUCTING LINAC TO DRIVE A SHORT WAVELENGTH FEL*

G. A. Krafft and J. J. Bisognano

Continuous Electron Beam Accelerator Facility
12000 Jefferson Avenue
Newport News, VA 23606

Summary

In order to determine the suitability of using a superconducting radio frequency (SRF) linac to generate XUV radiation, the beam dynamics in such a linac have been simulated using a vectorized two dimensional beam breakup code, TDBBU. The energy spread and emittance of the accelerated beam are determined as a function of current for a linac like CEBAF and for a linac optimized for high peak currents. The results indicate that there are significant improvements in transverse emittance growth possible by going to lower RF frequencies and by utilizing BNS phasing in the accelerating cavities.

In the first section of this paper the simulation is described. Next, the transverse and longitudinal wakes typical in superconducting cavities are discussed. The results of the simulations are given, followed by a comparison of a linac driven FEL and a typical storage ring driven FEL. The conclusion of the work is that the former scheme looks promising because higher average power is possible.

Description of the simulations

The simulation code TDBBU[1] has been used to calculate the intrabunch collective effects since they degrade the bunch properties at high peak currents. The code neglects changes in the electron's longitudinal coordinate but follows the transverse phase space coordinates and the longitudinal momentum of the electrons. Electrons are tracked through a linac lattice. In addition, at the cavity and drift positions of the lattice, backward propagating wake functions are used to update the tranverse and longitudinal momenta. The form of the wake function as a function of τ is essentially arbitrary to the simulation.

Macroparticles are loaded with a uniform spacing in the longitudinal direction. A nonuniform bunch is simulated by changing the charge in the macroparticle as a function of the longitudinal coordinate. This approximation is reasonable as long as there is no longitudinal motion within the bunch, i. e. the bunch is relativistic, and as long as the instability generated by the wake occurs on distance scales long compared the spacing of the macroparticles.

In all the results to be reported here, the transverse load is the standard uniform elliptical load with a given emittance, the α and β functions at injection being chosen to match the focusing lattice of the accelerator. In most cases an offset is introduced at injection to initiate the instability.

A run involving 1500 machine elements and 3000 macroparticles takes about 15 CRAY 1 minutes.

Effect of the Longitudinal Wake

The stored energy in the superconducting cavity is

$$U = \frac{QV^2}{R\omega_0}$$

where V is the voltage gained when an electron traverses the cavity on crest, R/Q is the shunt impedance of the cavity, and $\omega_0/2\pi$ is the cavity frequency. The total energy extracted from the cavity by a bunch with total charge q is

$$u = qV.$$

The dimensionless quantity u/U is proportional to qk_f/V where k_f is the loss factor[2] for the fundamental mode

$$k_f = \frac{\omega_0}{4}\frac{R}{Q}.$$

In fact the relative energy spread scales the same way, if the loss factor is generalized to include all the longitudinal modes.

The longitudinal wake function, $W(\tau)$, quantifies the energy change experienced by a test particle following an exciting particle due to the longitudinal modes. By superposition, the energy error induced in the electron at time t is

$$\Delta E(t) = e\int_{-\infty}^{t} I(t')W(t-t')dt' = eq\int_{-\infty}^{t} \hat{n}(t')W(t-t')dt'$$

where $\hat{n}$ is the unit normalized distribution $\hat{n}(t) = I(t)/q$ and e is the electron charge. By performing the proper averages one obtains

$$\sigma_E = \sqrt{\langle\Delta E^2\rangle - \langle\Delta E\rangle^2 - \langle t\Delta E\rangle^2/t_{rms}^2} \qquad (1)$$

where the phasing of the cavities is chosen to minimize the *rms* energy spread. This result may be expressed in terms of the total loss factor as

$$\frac{\sigma_E}{E} = F\frac{qk_{\|}}{V}$$

where F is a form factor depending only on the form of the longitudinal wake and the bunch longitudinal density and $k_{\|}$ is the total loss factor[2]. The F constants for several types of bunch profiles are given in Table 1.

Longitudinal Distribution		F	σ_E
Uniform	$W(\tau) = A$	0	0
Parabolic	$W(\tau) = A$	0.05	$0.03eqA$
Gaussian	$W(\tau) = A$	0.08	$0.09eqA$
Uniform	$W(\tau) = B\tau^{-1/2}$	0.07	$0.09eqB/L^{1/2}$
Parabolic	$W(\tau) = B\tau^{-1/2}$	0.15	$0.15eqB/L^{1/2}$
Gaussian	$W(\tau) = B\tau^{-1/2}$	0.19	$0.20eqB/\sigma^{1/2}$

Table 1 Energy Spread for Various Wake Functions

Accelerator Configurations

Two accelerator configurations were simulated in this study. The first configuration, summarized in Table 2, has parameters corresponding to the present CEBAF accelerator. In addition

*This work was supported by the United States Department of Energy under contract DE-AC05-84ER40150.

to a longitudinal wake of 10 V/pC and a transverse wake of 6 V/pC cm^2 for a CEBAF cavity, the effective wakes in Table 2 include contributions from vacuum chamber discontinuities in the CEBAF design.

The second configuration, given in Table 3, represents a machine designed explicitly for high peak current operation as an FEL driver. The main features distinguishing such a linac from the CEBAF linac are:

- Lower operating frequency (350-500 MHz)
- Smooth vacuum chambers to avoid wake effects
- External termination of Higher Order Mode loads
- No recirculation to avoid multipass BBU instability

In addition, it is likely that some form of energy recovery would be attempted in order to take advantage of the high efficiency of the superconducting cavities and to avoid excessive power usage. Energy recovery does not affect the results of the calculations since bunch properties at the wiggler depend only on wakes generated on the first pass through the linac.

Frequency	1500	MHz
Injection Energy	45	MeV
Final Energy	4	GeV
Injection Emittance	1π	μm rad
Effective Transverse Wake	30.0	V/pC cm^2 per cavity
Effective Longitudinal Wake	41	V/pC per cavity
Bunch Length	2.2	psec

Table 2 Parameters in CEBAF Accelerator Simulation

Frequency	350	MHz
Injection Energy	10	MeV
Final Energy	1	GeV
Injection Emittance	1π	μm rad
Transverse Wake	0.8	V/pC cm^2 per cavity
Longitudinal Wake	7	V/pC per cavity
Bunch Length	22	psec

Table 3 Parameters in Driver Accelerator Simulation

The CEBAF lattice has constant focal length on the first pass and the driver lattice has constant focal length throughout. For concreteness we assume that the driver scenario has single cell 350 MHz cavities which achieve a total gradient of 5 MV/m. The injected normalized *rms* emittance for the beam is $1\pi\times10^{-6}$ m rad (see Eqn. (2) below). Using Eqn. (1) the energy spread is estimated as a function of bunch charge for CEBAF and for the driver. In order to retain an energy spread less than .1% the bunch charge must be limited to 10^9 electrons for CEBAF, but the limit for the driver is about 10^{10} electrons.

Simulation Results

In Fig. (1) the effect of the longitudinal wake is given by plotting the energy error and time of the macroparticles as they leave CEBAF after acceleration. The energy error ΔE is the difference between the actual energy and the energy that the synchronous particle would have at zero current. The phasing of the cavities has been chosen to minimize the *rms* energy spread of the emerging beam. The peak current in the simulation was 300 A, the bunch shape was parabolic, and the longitudinal wake was proportional to $\tau^{-1/2}$. The energy spread is consistent with Eqn. (1).

In Fig. (2) the transverse position and time are plotted for the bunch macroparticles. The transverse wake causes the familiar distortion of the bunch into a banana shape. In Fig. (3) a tranverse phase plot of the emerging particles is presented, along with a zero current result in Fig. (4). The emittance of the bunch has effectively grown with current due to the transverse instability. The growth is quantified in our work by using the normalized rms emittance

$$\epsilon^n_{rms} = \sqrt{\langle P_x^2\rangle\langle X^2\rangle - \langle P_x X\rangle^2}/mc \qquad (2)$$

where P_x is $p_x - \langle p_x\rangle$, X is $x - \langle x\rangle$, m is the electron rest mass, and c is the velocity of light.

In Figs. (5) and (6) emittance is plotted against the peak current for several bunch lengths. In Fig. (5) the plot is for the nominal CEBAF parameters. In Fig. (6) the plot is for the driver configuration. If the cavities are phased in the way recomended by Balakin, Novokhatsky, and Smirnov[3] the effect of the transverse instability is reduced in several simulations that have been performed. Since emittance growth becomes a problem only at currents where energy spread is already excessive, the gains from BNS phasing are helpful only for relatively long bunches ($L > 6$ psec for CEBAF or $L > 60$ psec for the driver). Otherwise, the main limitation on bunch charge is due to the energy spread requirement in the FEL.

Since the maximum bunch charge in the driver is 2700 pC (corresponding to 180 A peak current) and the average power is limited, a maximum bunch repetition rate is obtained. For the overall continuous power into the accelerating cavities to be less than 20 kW, the bunch repetition frequency must not exceed 3 MHz. A storage ring-bypass scheme has been proposed as a coherant x-ray source at Berkeley[4]. The results of this proposal of most interest to us are an average power of .3 W at 400 Å, a peak power of 150 MW, and a radiation pulse length of 50 psec. The rather low average power is due to the fact that the beam is stored for a full damping time of the storage ring before passing through the FEL again. The comparable numbers for the optimized driver are an average power of 400 W, a peak power roughly the same as above, and a radiation pulse length of 20 psec, the main advantage being that the bunches can come much more frequently in the SRF linac case. It seems that the SRF driver compares favorably to the Berkeley proposal. However, without some form of energy recovery, the facility power is quite a bit larger than the storage ring proposal.

Conclusion

In this paper a superconducting linac driven FEL has been considered. It was shown that such a scheme can produce beams suitable for the generation of short-wavelength coherant radiation. The emittance growth from the accelerator and the energy spread of the beam have been computed as a function of current. In contrast to the situation in normal conducting linacs, superconducting linacs are dominated by the longitudinal wake effects instead of transverse wake effects. It should be emphasized that a self-consistent calculation has been done, i. e. the collective effects have been included in the estimates of linac performance, and the resulting beam quality is good in parameter regimes of interest. For radiation source drivers care should be taken to insure that the vacuum chamber is smooth in order to reduce the wake fields.

Acknowledgement

Discussions with B. Yunn are gratefully acknowledged.

References

[1] G. A. Krafft and J. J. Bisognano, *Proc. 1987 Particle Accelerator Conference*, IEEE Catalog No. 87CH2387-9, pg. 1356

[2] P. B. Wilson, *Physics of High Energy Particle Accelerators*, AIP Conference Proceedings No. 87, pg. 450 (1982)

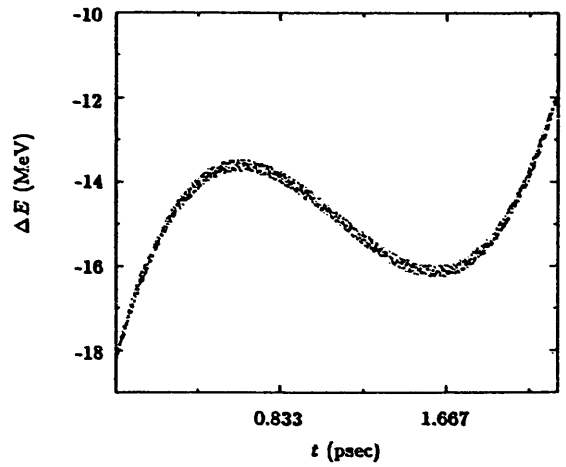

Fig. (1) Macroparticle Energy Error vs. Time at Exit from CEBAF

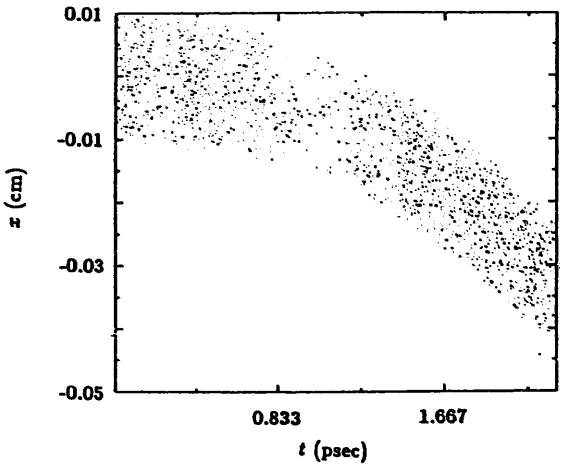

Fig. (2) Macroparticle Horizontal Position vs. Time at Exit from CEBAF

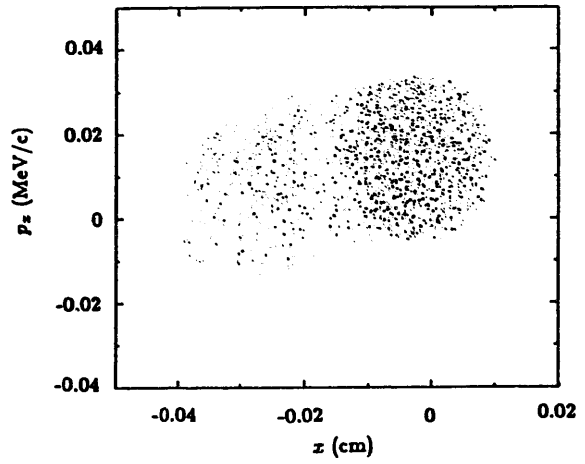

Fig. (3) Macroparticle Phase Space Plot at Exit from CEBAF

[3] V. Balakin, A. Novokhatsky, and V. Smirnov, *Proceedings of the 12th Int. Conf. on High Energy Accelerators*, Fermilab, pg. 119 (1983)

[4] J. Bisognano *et al.*, "Feasibility Study of a Storage Ring for a High-power XUV Free-electron Laser", *Particle Accelerators*, 18, 223 (1986)

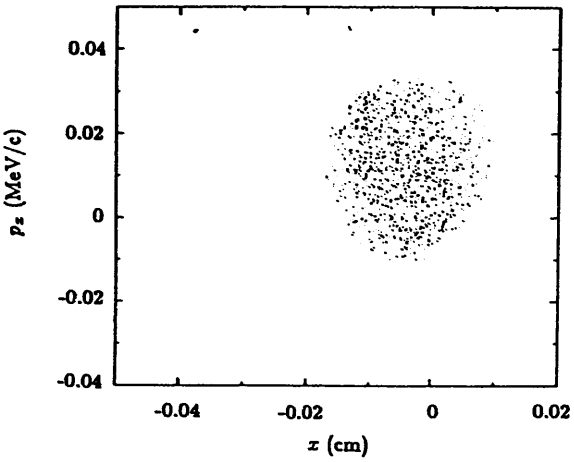

Fig. (4) Macroparticle Phase Space Plot at Exit from CEBAF, $I = 0$

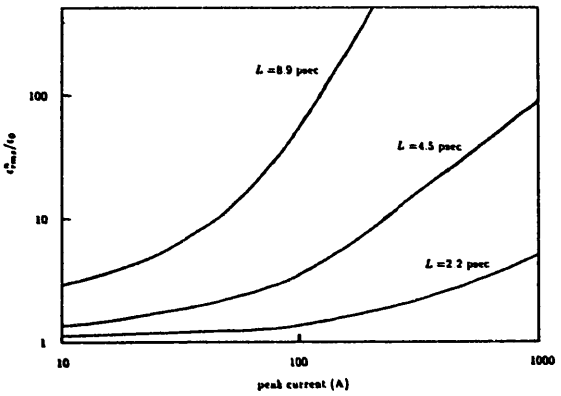

Fig. (5) Emittance vs. Current for CEBAF

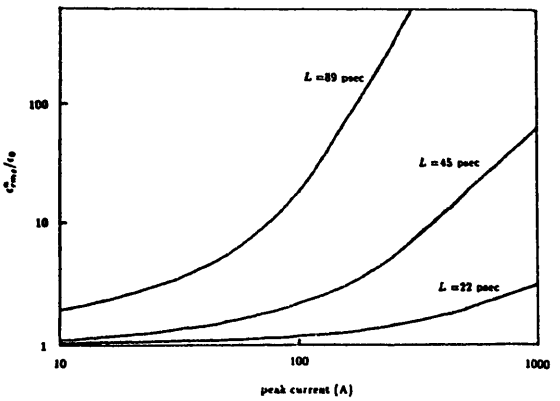

Fig. (6) Emittance vs. Current for Driver

The NIST/NRL Free-Electron Laser Facility

P.H. Debenham, R.L. Ayres, J.B. Broberg, R.I. Cutler, B.C. Johnson, R.G. Johnson, E.R. Lindstrom, D.L. Mohr, J.E. Rose, J.K. Whittaker, N.D. Wilkin, and M.A. Wilson

National Institute of Standards and Technology
Gaithersburg, MD 20899, USA

C.-M. Tang and P. Sprangle

Naval Research Laboratory
Washington, DC 20375, USA

S. Penner, Rockville, MD 20852, USA

ABSTRACT

A free-electron laser (FEL) user facility is being constructed at the National Institute of Standards and Technology (NIST) in collaboration with the Naval Research Laboratory. The FEL, which will be operated as an oscillator, will be driven by the electron beam of the racetrack microtron (RTM) that is nearing completion. Variation of the electron kinetic energy from 17 MeV to 185 MeV will permit the FEL wavelength to be tuned from 200 nm to 10 μm. Performance will be enhanced by the high brightness, low energy spread, and continuous-pulse nature of the RTM electron beam. We are designing a new injector to increase the peak current of the RTM. A 3.6-m undulator is under construction, and the 9-m optical cavity is under design. The FEL will emit a continuous train of 3-ps pulses at 66 MHz with an average power of 10-200 W, depending on the wavelength, and a peak power of up to several hundred kW. An experimental area is being prepared with up to five stations for research using the FEL beam. Initial operation is scheduled for 1991.

1. INTRODUCTION

We are building a free-electron laser at the National Institute of Standards and Technology (NIST) to provide a powerful, tunable source of light for research in biomedicine, materials science, physics, and chemistry.[1] The planned research facility is shown in Figure 1. In a free-electron laser (FEL), the static, sinusoidal, magnetic field of an undulator (or wiggler) causes an electron beam to follow a sinusoidal trajectory and hence emit electromagnetic radiation. Radiation with a particular wavelength, λ, remains in phase with the electrons and stimulates additional emission; i.e., the device lases. The resonant wavelength is given by the expression

$$\lambda = (\lambda_w/2\gamma^2)\cdot(1+K^2), \qquad (1)$$

where λ_w is the wavelength of the wiggler magnetic field, and γ is the electron energy in units of the electron rest energy, E_0. The wiggler parameter, K, that appears in Equation 1 is proportional to the root-mean-square (rms) magnetic field of the wiggler, B_w:

$$K = |eB_w\lambda_w/2\pi E_0|. \qquad (2)$$

Our FEL will be driven by the electron beam of the NIST/LANL racetrack microtron (RTM), a continuous-wave (cw) accelerator that is scheduled for completion in 1990. The FEL can be characterized as a high-power, tunable, picosecond, mode-locked laser. By varying the kinetic energy of the electron beam between 17 MeV (γ = 34) and 185 MeV (γ = 363), we will be able to vary λ between 200 nm and 10 μm, from Equation (1). For our wiggler, λ_w = 28 mm, and B_w can be varied between 0.23 T and 0.38 T by varying the gap. This will allow us to tune λ by ±20% without changing γ. The laser output, like the electron beam, will be a continuous train of 3-ps long pulses at a frequency of 66 MHz. The expected properties of the output radiation are given in Table 1, and the average output power is shown in Figure 2 as a function of λ.

FEL radiation will be available for research applications in the 160-m² FEL user area shown in Figure 1. The photon beam will be transported in vacuum from the FEL to any of up to five experimental stations in the user area. The user area will be shielded from the electron beam and inhabitable at all times. Thus experimenters will be able to make manual adjustments to experiments in progress, as well as set up experiments when the photon beam is delivered to other stations. In the remainder of this paper we discuss the physics of microtrons and the status of our FEL project.

2. MICROTRONS

Racetrack microtrons have several properties that make them excellent sources of electrons for free-electron lasers. In this section we discuss the physics of the racetrack microtron and its predecessor, the classical microtron.

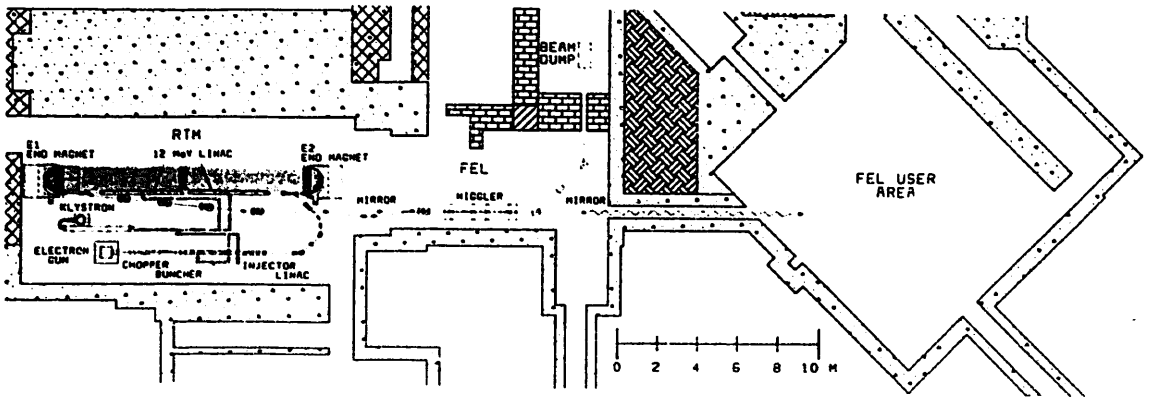

Figure 1. Plan view of the NIST/NRL FEL facility.

CH2669-0/89/0000-0775$01.00©1989 IEEE

Table 1. Output Light Properties of the NIST/NRL FEL

Wavelength	200 nm - 10 μm
Average Power (W)	10 - 200
Repetition Rate (MHz)	16.528 and 66.111
Peak Power (kW)	40 - 1000
Peak Energy (μJ)	0.1 - 3.0
Photon Flux ($cm^{-2} \cdot s^{-1}$)	10^{25} - $2 \cdot 10^{27}$
Photon Fluence (cm^{-2}, 1mm-diam spot)	$3 \cdot 10^{13}$ - $6 \cdot 10^{15}$
Pulse Width (ps)	3
Spectral Resolution	$1.4 \cdot 10^{-4}$ - $7 \cdot 10^{-3}$
Polarization	Linear
Spatial Mode	TEM_{00}
Beam Diameter (mm, at 1/e amplitude)	0.4 - 1.6
Beam Divergence (mrad, full angle)	0.3 - 5

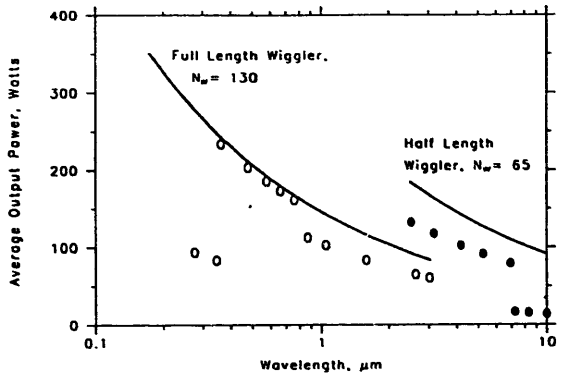

Figure 2. Predicted average output power of the NIST/NRL FEL. The solid curves show the maximum power that can be extracted from the electron beam. The circles are calculated values of output power for realistic values of mirror reflectivity and output coupling.

2.1 Classical microtron

The racetrack microtron evolved from the conventional, or classical, microtron, which was proposed by Veksler[2] in 1944. (Reference 3 provides a thorough discussion of the classical microtron.) As indicated in Figure 3, the classical microtron consists of a *microwave** cavity with an accelerating gap located in a uniform magnetic field, B. An electron that originates at one side of the gap with negligible kinetic energy crosses the gap at rf phase ϕ and in doing so gains energy $\Delta T = V \cdot \cos\phi$, where V is the peak gap voltage. The electron is returned to the gap on a circular orbit with a radius of curvature that is proportional to its momentum. The values of B and ΔT are chosen such that the circumference of the first orbit is an integral multiple of the rf wavelength, λ, and each subsequent orbit is an integral number of wavelengths, $\nu\lambda$, larger in circumference than the one before. This choice of energy gain, ΔT_r, defines a resonant phase angle, ϕ_r, such that $V \cdot \cos\phi_r = \Delta T_r$. Electrons at this phase remain in resonance with the accelerating voltage and

*Hence the name *microtron*.
†These are called end magnets.

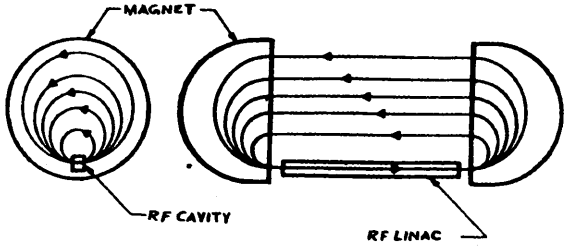

Figure 3. Classical microtron (left) and racetrack microtron.

gain energy ΔT_r each time they cross the gap. The resonant parameters are related by the microtron resonance condition,

$$2\pi \cdot \Delta T_r / c = \nu\lambda B. \qquad (3)$$

Conventional microtrons are used to produce pulsed electron beams at energies of 5 MeV to 45 MeV. The resonant energy gain per pass, ΔT_r, is limited to approximately 1 MeV. The maximum energy is limited by the need to use a relatively large, low-field magnet ($0.1 \text{ T} \leq B \leq 0.3 \text{ T}$). The microwave cavity is limited to operation in the pulsed mode by cooling limitations[4].

2.1.1 Phase focusing. Like other resonant accelerators, the microtron benefits from phase focusing, an important mechanism which results in good energy resolution and stability. Phase focusing comes from operating on the falling side of the microwave, so that an electron that crosses the accelerating gap before the central electron (i.e., with $\phi < \phi_r$) gains more energy than ΔT_r. The extra energy of this electron increases the length of the next orbit, and the extra distance traveled delays its next gap crossing. In this way, the phase is restored toward ϕ_r. The restoring force produces phase oscillations around ϕ_r with an amplitude equal to the initial phase spread in the electron bunch, so the phase spread remains constant as the electrons are accelerated.

Likewise, electrons that begin at the resonant phase with excess energy will arrive at the gap late the next time and gain less than ΔT_r. Thus, the initial energy spread in the beam is preserved.

2.2 Racetrack microtron

Reference 4 is a comprehensive study of the racetrack microtron and other recirculating electron accelerators. The racetrack microtron, shown in Figure 3, can be thought of as a classical microtron with its circular magnet separated into two semicircular ones† and its microwave cavity replaced by a multi-cavity linear accelerating structure, *viz.*, a linac. The electron orbits resemble a nested series of racetracks having a common homestretch and increasingly distant backstretches. The space between the magnets is exploited for several improvements. A linac can provide an energy gain on the order of 10 MeV and can be cooled adequately for cw operation. Focusing elements can be included on the straight sections.

Racetrack as well as conventional microtrons are governed by Equation 3 and benefit from phase focusing. From Equation 3 it can be seen that the increased ΔT_r allows the use of a higher magnetic field (approximately 1 T) and therefore smaller, more efficient magnets.

A racetrack microtron with N passes through a linac of energy gain ΔT_r can be compared with a single-pass electron linac of energy gain $N \cdot \Delta T_r$, to which we will refer as a "straight" linac. The RTM linac is shorter than the straight linac by a factor of N, which is typically between 10 and 50. This can lead to a significant reduction in the initial cost of the linac, its enclosure, and radiation shielding, which more than compensates for the cost of the end magnets and return beam lines. Moreover, the power dissipated in the shorter linac is lower by a factor of N, a saving that can make cw operation affordable. Finally, the straight linac does not provide phase focusing and consequently tends to have a larger beam energy spread and poorer energy stability than the RTM.

3. THE NIST/LANL RTM

The NIST racetrack microtron arose from the need for cw electron accelerators for nuclear physics in the late 1970's. Existing pulsed accelerators were not suitable for doing experiments in which several subatomic particles are detected coming from a nuclear reaction initiated by a single electron. High event rates during the pulse increase the probability of detecting unrelated but coincident particles from separate reactions to the point where the signal from true coincidences is obscured. One solution to this problem is to reduce the peak electron current without reducing the average current (hence the true event rate) by increasing the duty factor of the accelerator.

Existing US cw electron accelerators based on cryogenic, superconducting linacs[5] were limited in average current by the phenomenon of beam breakup, or BBU†. Encouraged by the successful RTM at Mainz[6], we began in 1980 the construction of a high-current, 185-MeV, cw RTM with a room-temperature linac at NIST. This was a joint project with Los Alamos National Laboratory (LANL), funded by the US Department of Energy (DoE), to determine the feasibility of a 1 to 2 GeV, cw, high-current, room-temperature, recirculating electron accelerator for nuclear physics. The design of the NIST/LANL RTM was thus strongly influenced by requirements for a 1 to 2 GeV accelerator. For example, the product of the number of passes (N) and the average beam current ($\bar{I}$) is the same in the two machines, close to the threshold for beam breakup.

†BBU is self-destructive deflection of the beam by unwanted modes of the accelerating structure that are excited by the beam. Superconducting, low-loss structures are especially vulnerable to BBU because the unwanted modes can be excited by relatively low-current beams.

When the DoE project ended in 1987, we realized that the RTM would make an excellent FEL driver and began the present project.

3.1 Design

The NIST/LANL RTM is described in Reference 7. Table 2 gives the design parameters of the accelerator and some measured beam properties. Shown in Figure 4, the accelerator comprises a 5-MeV injector connected to

Table 2. NIST/LANL RTM Parameters

	Original Design	Observed as of 3/89	Modified Design for FEL
Injection energy (MeV)	5	5.5	5
Energy gain per pass (MeV)	12	11.2	12
Number of passes	1-15	1	1-15
Output energy (MeV)	17-185	16.2	17-185
Average current (μA)	10-550	630	10-550
Accelerating frequency (MHz)	2380	2380	2380
End magnet field (T)	1.0	1.0	1.0
Peak current (A)	<0.066	-	2-4
Micropulse length (ps)	3.5	-	3.5
Micropulse frequency (MHz)	2380	2380	66.111 16.528
Macroscopic duty factor	1.0	1.0	1.0
Energy spread (keV)	<40	18	<40
Normalized emittance* (μm)	<10	2.4	<10

*In the two-dimensional phase space of beam size and beam divergence, the emittance, ε, is the area which contains 95% of the beam, divided by π. Normalized emittance = βγε, where β is the electron velocity divided by c.

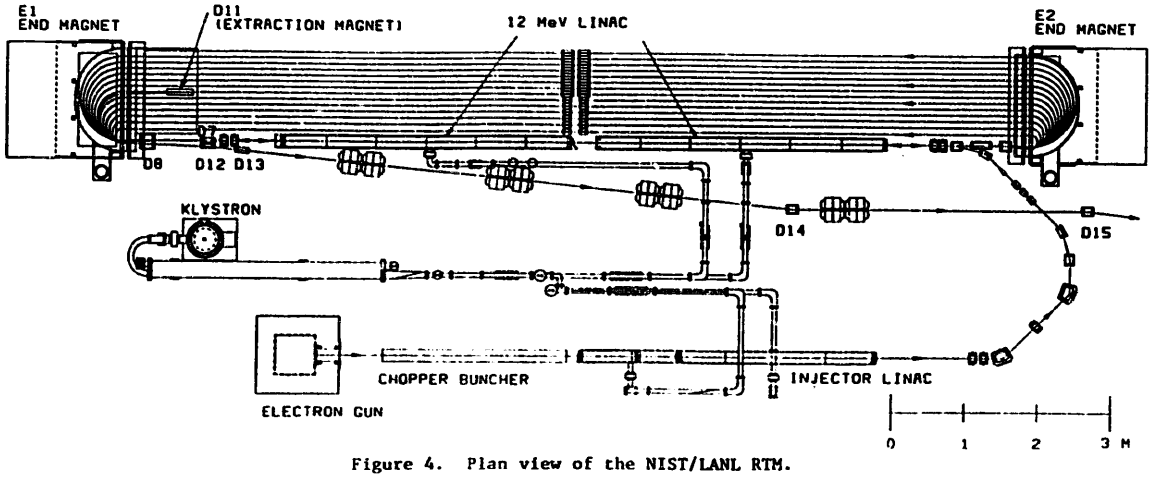

Figure 4. Plan view of the NIST/LANL RTM.

a racetrack microtron by a 180-degree beam transport system. With a floor area of 5 m by 16 m, the RTM is compact for a 185-MeV, cw accelerator. The average beam power at full energy is 100 kW.

The injector consists of a 100-keV, dc electron gun followed by a transverse-emittance-defining system, a chopping and bunching stage, and a 5-MeV, cw linac. In the microtron, 5-MeV electrons from the injector are recirculated for up to 15 passes through an 8-m long, 12-MeV, cw linac for a total energy gain of up to 180 MeV. The first pass is from right to left in Figure 4, following which the 17-MeV beam is given a parallel displacement by dipole magnets D7 and D8, deflected counter-clockwise through 180 degrees by end magnet E1, and returned to the linac axis by D8 and D7. With the length of the 17-MeV orbit adjusted to a half-integral multiple of λ, the 17-MeV beam enters the left end of the standing-wave linac with a 180-degree phase shift and is accelerated to the right. From this point on the beam circulates counter-clockwise through the microtron. Quadrupole magnet doublets are located at the middle of each beam-return line to provide adjustable focussing.

Beam can be extracted from the RTM after any number of passes simply by moving extraction magnet D11 to the appropriate beam-return line. The magnet deflects the beam inward, causing it to emerge from end magnet E1 outside the racetrack orbit. It is then removed from the accelerator by dipole D12 and the ensuing beam line. In this fashion the energy can be varied in steps of 12 MeV by changing nothing in the accelerator but the position and field strength of magnet D11*. Continuous energy variation is achieved by changing ΔT_r and B.

Microwave power from a single, 450-kW-output cw klystron is delivered to the injector linac and the RTM linac through a waveguide distribution system that can be seen in Figure 4. With a dissipation of approximately 50 kW in the distribution system, 100 kW in the injector linac and 200 kW in the 12-MeV linac, there is 100 kW available to accelerate the beam. Overall, the accelerator uses 1.1 MW, of which 9% is converted into beam power. By contrast, an equivalent 185-MeV linac would be 124 m long, dissipate 3.1 MW, and consume roughly 8.8 MW for the same beam power. The power saved by recirculating the beam through a relatively short linac makes cw operation feasible.

3.2 High-Current Injector

The injector produces beam pulses at the accelerating frequency, f_0, of 2380 MHz with a maximum of 0.35 pC per pulse. A peak beam current of 2-4 A is necessary for adequate gain in the FEL, corresponding to 7-14 pC per pulse. We must increase the peak current without increasing the average beam power, which is limited by the amount of rf power available. This will be done by reducing the beam pulse frequency to 66.111 MHz, the 36^{th} subharmonic of f_0. We plan to replace the present, 4-mA, dc, thermionic, electron gun with a 200-mA, thermionic gun pulsed at 66.111 MHz. Subharmonic chopping and bunching will be used to prepare the beam for the injector linac. The new injector, which is also designed to operate at 16.528 MHz, the 144^{th} subharmonic of f_0, is described in detail in Reference 8. Design parameters for the RTM with the new injector are given in the last column of Table 2.

3.3 Status and Plans

The present configuration of the RTM is with a single temporary beam line in place of the 14 beam-return lines in order to study performance with one pass through the 12 MeV linac for a nominal beam energy of 17 MeV. The beam line contains three beam profile monitors (wirescanners[9]) spaced three meters apart. After one pass, the beam is deflected clockwise by end magnet E1 through 180 degrees into the beam line for energy analysis and emittance measurement. Preliminary results are given in Table 2 and in Reference 10. The full, vertical width of the beam at 20% maximum† is about 1 mm throughout the 6-m beam line. The normalized emittance in the vertical plane is less than 2.4 μm, better than the design goal of 5 μm at 17 MeV.

The observed horizontal beam width of 1.6 mm includes the dispersion of electrons with different energies by the magnet. Assuming equal horizontal and vertical emittance, the width from dispersion is 0.8 mm, corresponding to a full energy spread of 18 keV. The observed energy spread is consistent with the measured voltage stability of the linacs of 0.1%[11]. Because the microtron is phase-focused, the energy spread should not increase significantly with recirculation, so we expect to surpass the design goal of 40 keV at full energy. By comparison, the energy spread from a 185-MeV linac with similar voltage stability would be 370 keV. In view of Equation 1, the RTM-driven FEL will have much better wavelength stability than one driven by a linac.

After completion of single-pass beam tests this spring, we will install the microtron beam-return lines. Concurrently, we will install the beam transport line between the microtron and the beam stop shown in Figure 1, without the mirror chicane (dipoles D15-18, shown in Figures 4 and 5) or the following quadrupole doublet. This arrangement will be used to commission the accelerator at full energy with the present injector in 1990. Three wirescanners spaced approximately six meters apart will provide beam size measurements for determining the transverse emittance, and a wirescanner following the 45-degree bending magnet D19 (see Figure 5) will be used to measure energy spread.

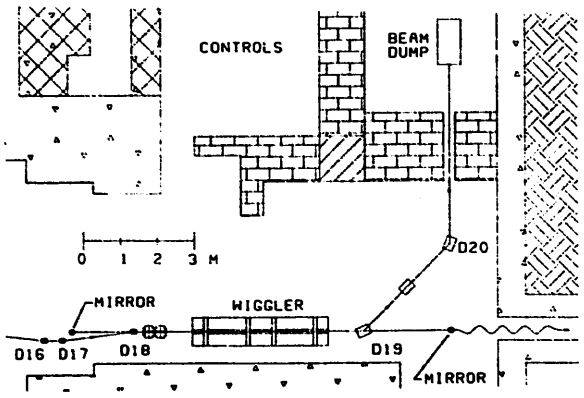

Figure 5. Plan view of the NIST/NRL FEL.

Operation of the RTM for the FEL requires a peak current of up to 40 times the original design value. The stronger wake fields that the increased peak current induces is estimated to have a non-negligible effect on beam quality. We plan to perform more detailed calculations of these effects. Operation with a decreased beam pulse frequency for the FEL could reduce the threshold current for beam breakup, I_t. This is because the accelerating structure may support BBU modes that are resonant with harmonics of the lower frequency that are not harmonics of the higher

*Of course, the magnetic fields in the beam transport line must be changed with the beam energy.

†This includes about 95% of the beam.

frequency. Preliminary calculations indicate that operation at 66.111 MHz will reduce $N \cdot I_e$ from approximately 9 mA (average) to approximately 6 mA[12]. More accurate calculations are underway. Small adjustments in focusing can produce large improvements in I_e. We are developing the high-current injector for installation in 1990, after the RTM is commissioned with the present injector. We plan to commission the new injector in 1991.

4. THE NIST/NRL FEL

4.1 Electron-beam transport

The planned electron-beam transport line from the RTM to the FEL is shown in Figures 1, 4, and 5. Following extraction from the RTM, the beam will be deflected onto the wiggler axis by dipole D14 without dispersion, i.e., with no correlation between electron energy and position or angle. Dipole magnets D15 through D18 will form an achromatic chicane to guide the beam around the upstream mirror of the FEL optical cavity and back onto the wiggler axis without dispersion.

The vertical aperture of the wiggler vacuum chamber will be 8.4 mm. The length of the wiggler will be 3.64 m for optical wavelengths between 200 nm and 2 μm. For wavelengths between 2 μm and 10 μm, we will use only the first 1.82 m of the wiggler to reduce diffraction losses. In both cases we will put the waist of the optical beam at the active center of the wiggler. The size of the waist will depend on λ. The Rayleigh length* will be half the active wiggler length to optimize transmission through the wiggler vacuum chamber. To optimize coupling between the electron and optical beams, we will use the two quadrupole magnet doublets on the wiggler axis to match the size and location of the electron-beam waist to those of the optical beam.

The spent electron beam will be removed from the FEL after the wiggler by an achromatic, 90-degree deflection system consisting of two 45-degree dipole magnets, D19 and D20, and an intermediate quadrupole magnet. The deflection system will focus the beam into a shielded beam dump behind a thick shielding wall. The energy distribution in the spent beam is an important diagnostic for lasing. This information will be obtained from a beam profile monitor located between the 45-degree magnets, where the beam will be dispersed.

4.2 Optical cavity design

The FEL optical cavity, shown in Figure 5, consists of an upstream mirror, the wiggler, and a downstream mirror. We will use a partially-transmissive downstream mirror to extract a small fraction of the optical beam from the cavity. The extracted light will be transported in vacuum to the user area. We have chosen the cavity length to be 9.070 m, twice the distance between electron pulses at 66.111 MHz, so four independent light pulses will build up in the cavity in synchronism with the electron pulses. Because the electron pulse train is continuous, the light pulses will persist in the cavity indefinitely. This eliminates the start-up problems of a pulsed FEL. For the most stable optical output, we will operate at 16.528 MHz to form a single light pulse in the cavity. Approximately four meters of electron-free length will be available for optical devices in the cavity.

ACKNOWLEDGMENTS: This work was supported in part by the US Strategic Defense Initiative Organization through ONR Contract No. N00014-87-F-0066.

4.3 Status and Plans

We have a contract with a vendor to design, construct, install and test the wiggler, including vacuum chambers, supports, controls, and a magnetic-field-mapping apparatus. The design is complete, and the main structure has been constructed. The vendor built a full-scale model of one period of the magnetic structure and performed magnetic field measurements on it to verify the design. The measured field met or exceeded all specifications. Installation of the completed wiggler at NIST is scheduled for the end of this year.

Operation of the FEL is scheduled to begin in 1991. Initially, we plan to operate at visible wavelengths, where good optical components are available. Damage to the cavity mirrors from the relatively high intracavity power is a potential problem. Multi-layer dielectric mirror coatings are available for visible wavelengths that can withstand the irradiance and fluence expected in the cavity. The absorption of these coatings is initially about 10 ppm, but is expected to increase with exposure to harmonic radiation in the FEL. While our situation is somewhat unique, experience at the LURE/ACO FEL[13] suggests that increased absorption will result in mirror failure after several days of lasing.

5. REFERENCES

1. S. Penner et al, Nucl. Inst. and Meth. in Phys. Res. A272 (1988) 73.

2. V.I. Veksler, Proc. USSR Acad. Sci. 43 (1944) 346 and J. Phys. USSR 9, (1945) 153.

3. S.P. Kapitza and V.N. Melekhin, The Microtron, Harwood, London (1978).

4. R.E. Rand, Recirculating Electron Accelerators, Harwood, London (1984).

5. P. Axel *et al.*, IEEE Trans. Nucl. Sci. NS-24 (1977) 1133.

   C.M. Lyneis, IEEE Trans. Nucl. Sci. NS-26 (1979) 3246.

6. H. Aufhaus *et al.*, Proc. of the 1981 Linear Accelerator Conference LA-9234-C (1981) 22.

7. S. Penner *et al.*, IEEE Trans. Nucl. Sci. NS-32 (1985) 2669.

8. R.I. Cutler *et al.*, "Conceptual Design of a High-Current Injector for the NIST-NRL Free-Electron Laser," to be published in Proceedings of the 1989 Particle Accelerator Conference.

9. R.I. Cutler *et al.*, Proc. 1987 IEEE Particle Accelerator Conference (1987) 625.

10. M.A. Wilson *et al.*, "NIST-Los Alamos Racetrack Microtron Status," to be published in the Proceedings of the 1988 Linear Accelerator Conference.

11. R.I. Cutler and L.M. Young, "Performance of the High-Power RF System for the NIST-Los Alamos Racetrack Microtron," to be published in the Proceedings of the 1988 Linear Accelerator Conference.

12. S. Penner, "BBU in Microtrons with Subharmonic Injection," to be published in Transactions of the 1989 IEEE Particle Accelerator Conference.

13. M. Billardon *et al.*, J. de Physique C1 (1983) 29.

*The distance from the waist to the point where the cross section of the optical beam doubles.

DELTA , A LOW-EMITTANCE STORAGE RING AS FREE-ELECTRON-LASER RADIATION SOURCE

Niels Marquardt
DELTA Group
Institute of Physics , University of Dortmund
P.O.Box 500 500, 4600 Dortmund 50, Germany

Construction of the Dortmund 1.5 GeV ELectron Test Accelerator DELTA is expected to start early this summer. The design goals of this new high-brightness photon source are to provide test possibilities for accelerator research and development, to serve as a driver for different FEL experiments, and to represent -to a limited extent- a single-user photon source of very special beam characteristics. The facility consists of a 20-100 MeV LINAC, the booster synchrotron BODO which can also be operated independently as a ramped storage ring, and the main storage ring DELTA. With its circumference of about 115 m the most recent racetrack-shaped version of DELTA has two arcs consisting of 10 separated function triplet cells and two 20 m long straight sections for insertion devices. Three different FEL projects are under development starting with an optical klystron in the visible to FEL's from λ=100 to <20 nm. Design features and status of the dedicated accelerator project are being discussed.

1. Purpose and General Goals of DELTA

The Dortmund Electron Test Accelerator Facility[1] consists of a laboratory building and a 70 m by 40 m large shed, housing the accelerator system, i.e. a LINAC of possibly 100 MeV, the booster synchrotron BODO, and the main storage ring DELTA of maximum energy of 1.5 GeV.

The intention of DELTA is to provide a national test accelerator facility designed for an energy range between 0.5 and 1.5 GeV and optimized for FEL operation[2]. It will not serve as a typical synchrotron radiation (SR) light source for long-term users. Instead, DELTA is planned to develop storage-ring and accelerator physics and to provide SR beams for short-term measurements requiring very special beam qualities and experimental conditions. As a university laboratory it is also best suited for the training of students, technicians, and accelerator physicists.

The main storage ring has a circumference of about 115 m and is designed to have two arcs, each of which consist of 10 separate-function quadrupol triplet cells, and two 20 m long straight sections usable for various insertion devices. The lattice structure with short cells and strong magnetic fields guarantees strong damping and a very low emittance. The ultra-low vacuum pressure and the small impedance of the beam chamber are providing high-current operation.

After a construction phase of three years and commissioning during the following year, routine machine operation and first experiments will start late in 1993.

The main purpose of DELTA is threefold :

(1) Investigation of accelerator physics

(a) Development of mode-damped single- and multi-cell cavities and analysis of cavity modes and of their interaction with high-current particle beams.
(b) Development of different insertion devices and of compact and inexpensive light sources.
(c) Testing of various SR instrumentation and accelerator components.
(d) Investigating the problems related to low-energy injection from LINACs and to the reduction of beam life time caused by ions generated in the storag-ring vacuum chamber.
(e) Theoretical investigation of non-linear phenomena of beam dynamics and comparison with measurements of actual non-linear variations of the beam under the influence of radiation damping. Limitations of the dynamical aperture by sextupolar fields and of the maximum possible beam currents are being investigated by tracking calculations. It will be particularly interesting to compare the results from single-particle tracking with measurements of the time development of oscillations of bunches of many particles coherently excited by fast kicker magnets. Since this has to be done within the first few thousand turns very fast electronics for the beam-position monitors have to be developed. Several theoretical investigations of non-linear beam dynamics have been started already.
(f) Monitor development for low-emittance storage rings. In collaboration with the ESRF, Grenoble, a 4-button beam-position monitor (BPM) with an improved electronics has been designed to obtain a resolution of less than 10 μm and an absolute accuracy of better than 150 μm RMS. This BPM is ready for testing at the storage ring DORIS, DESY. Special monitors to detect fast beam oscillations and non-linear particle motion are also going to be developed. For optimum FEL operation fine adjustment to zero of the dispersion in straight sections, very accurate emittance measurements, and determination of bunch lengths with specially designed monitors and pick-up electrodes are indispensable. Such monitors are going to be developed. The same is envisaged concerning closed-loop, fast feedback systems. Tests with a prototype fast kickermagnet designed as strip-line resonator have been successfully performed.

(2) FEL experiments at DELTA

There is a three-stage project planned at DELTA for the development of FEL's operating at wavelengths from the visible to the XUV, with the long-term goal of realizing wavelengths clearly below 20 nm. These very short wavelengths generated from high-brilliance FEL-radiation sources are of particular interest e.g. for the wide field of X-ray microscopy of non-biological objects and in-vivo examination of biological objects.

For a joint FEL-storage-ring operation very stringent requirements have to be fulfilled by DELTA, like small emittances, short bunches, strong SR damping, large energy acceptance, low total machine impedance, extremely low vacuum pressure, active feedback systems and mode-damped cavities, long straight sections for FEL undulators.

Theoretical studies have been performed to determine the machine parameters optimized for most effective FEL-storage-ring operation and to determine the mutual influence between FEL and accelerator.

To approach the regime of extremely short wavelengths more gradually the following strategy of three steps of FEL development at DELTA is suggested which appears to be less risky and provides various possibilities to get sufficient experience.

CH2669-0/89/0000-0780$01.00©1989 IEEE

(a)**Phase I** : The first rather inexpensive and flexible device, called FELICITA I, is planned to be an optical klystron (OK) of 5–10 % gain which operates in the visible around 400 nm with DELTA running at 500 MeV. It will be made of simple electromagnets with 16 identical periods (λ_u=25 cm) and a total length of 4 m which can be split by extra coils into two undulators and a dispersive section. For this high-gain device of low output power to operate savely, peak currents of 60–100 A will be sufficient, with 4–6 electron bunches, corresponding to an optical cavity of 14.4 m and 9 m lenght, respectively. To reach a higher level of output power, the OK can also be operating in the conventional FEL mode with all sections at the same field. Depending on accelerator performance, however, this mode might not easily reach the oscillator threshold due to its lower gain. On the other hand, FELICITA I in the OK mode should reach the oscillator threshold also at intermediate wavelengths of 200–300 nm or even at 100 nm by either making use of the higher harmonics of the spontaneous undulator spectrum or by running DELTA at higher energies, i.e. 1000 MeV. Gain losses ($G \sim 1/\gamma$) are easily compensated by the higher peak currents possible, due to the reduced influence of Touschek effect and intra-beam scattering at higher energies. The OK will be a very valuable tool for studying laser-beam interaction, for developing mirrors withstanding high-power short-wavelength radiation, and for accurately measuring electron-beam energy and width.

(b)**Phase II** : Using the experience from phase I the next step will be the design of FELICITA II, a high-gain FEL operating in the oscillator mode near 100 nm. To obtain coherent radiation in this regime a much longer undulator with shorter periods on one side and higher peak currents from DELTA operating at higher energies on the other side are necessary. Only in this way reflectivities of mirrors of smaller than 50 % for this wavelength regime can be compensated. The undulator envisaged consists of about 230 periods of 6 cm length each, corresponding to a total length of 14 m. It will be built as hybrid magnet with standard permanent-magnet material and should reach gain values of 3–5. By operating DELTA at energies of around 1 GeV with currents of at least 150 A , this FEL produces radiation between 100 and 25 nm if suitable multi-layer mirrors are available.

(c)**Phase III** : If the mirror problem can not be solved within a few years, one could also think of a single-pass FEL with very high again installed in a by-pass and operating in a pulsed-mode (as was suggested by the Berkeley group). By using about 750 very short periods ($\lambda_u \cong 2$ cm) and an undulator length of 15 m with a few mm gap height, there might be sufficient gain already in one pass to generate a very intense pulse. After a single shot through the by-pass, the beam is deflected again into the storage ring, where it recovers by action of the various damping mechanisms from the severe energy degradation caused by its interaction with the FEL. Due to the short damping time of DELTA frequencies of the laser pulse of 10–20 Hz seem to be realistic.

(3) SR experiments for single users

According to the design concept of DELTA with the possibility of modifying and rapidly changing its beam lines and magnet lattice to satisfy the very special demands of certain test experiments, it also provides an ideal test accelerator for short-term research work with SR in most scientific disciplines. The special diagnostic tools for measuring all beam parameters, the sophisticated accelerator-control system and the methods of accurately stabilizing the beam position with feedback loops, which will be available at DELTA in the future, allow experiments which can not be performed at normal users machines. Of particular interest are those measurements which exploit the very unique time structure of the SR from single-bunch operation for the analysis of rapidly changing dynamical processes and of structural modifications.

2. Lattice and Machine Parameters of DELTA

Since the conditions of strong radiation damping (caused by strong bending fields) and small emittance (better obtained by weak fields) have to be provided simultaneously by the DELTA lattice, a simple FODO structure has been suggested at first. It turned out, however, that the very compact and dense FODO arrangement of 64 strong but short magnets necessary to fulfil these contradictory conditions does not provide sufficient space in between to insert simply formed coil heads, valves, monitor devices, etc.. Therefore, the original FODO lattice has been aban-

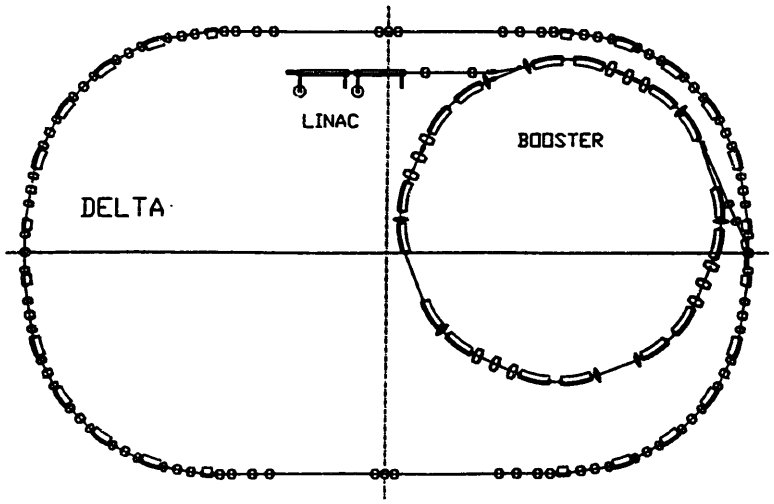

Fig. 1. General layout of DELTA with booster and LINAC

doned in favor of a triplet structure with a similar fourfold symmetry and 6 m long straight sections for insertions in each quadrant as before. The difference is that 3 short bending magnets have been combined in one with the same total strength and bending radius of 3.34 m and a length of 1.05 m, three times longer than before. Instead of alternating focussing and defocussing single quadrupoles between the dipoles, there are now three quadrupole magnets between two dipoles. As before, the most important optics parameters are determined by those of the two arcs which contain an additional straight section of 1.4 m length and extra quads and short dipoles for optical matching. Accordingly, there is more space available between the magnets and for inserting cavities and injection and extraction elements. A layout of the new lattice of the storage ring is shown in Fig. 1.

The total machine circumference has only been slightly increased to 115.2 m. The idea of maximum flexibility has been preserved by keeping the optical configuration of the arcs constant and only changing the two long straight sections according to the requirements of current experiments. With a slightly smaller emittance of 10^{-8} rad m and horizontal damping time and more or less unchanged values of energy spread and chromaticity all attractive features of the FODO lattice are preserved. Chromaticity compensation is made in the arcs where the dispersion is different from zero. As previously, sextupolar field components will be integrated in the quadrupole fields by modifying the pole faces appropriately and introducing extra coils between the upper and lower poles of the quads. A modified prototype quadrupole is under construction. Since FEL operation increases the energy spread and decreases the Touschek lifetime due to the necessary high particle densities, a sufficiently large longitudinal acceptance is important. Various tracking calculations have shown that the dynamic aperture is only slightly reduced by the nonlinear fields of sextupoles and that the energy acceptance of the DELTA triplet optics is of the order of $\Delta p/p = 5$ %. The new optics for one quadrant of DELTA is shown in Fig. 2 together with the dimensions of one triplet cell in more detail. The parameters of the linear beam optics of DELTA as well as the RF parameters are listed in Table 1.

Table 1. *The machine parameters of DELTA at E=1.0 GeV*

Circumference	$L = 115.2$ m
Bending radius	$R = 3.34$ m
Number of dipoles	$n_D = 20$
Tune	$Q_x = 10.217$
	$Q_z = 4.823$
Emittance (1 % coupling)	$\epsilon_x = 4.48 \times 10^{-9}$ m rad
	$\epsilon_z = 4.48 \times 10^{-11}$ m rad
(100 % coupling)	$\epsilon_x = \epsilon_z = 2.24 \times 10^{-9}$ m rad
Momentum compaction factor	$\alpha = 3.94 \times 10^{-3}$
Chromaticity	$\xi_x = -19.49$
	$\xi_z = -6.13$
Damping times (horizontal)	$\tau_x = 26.0$ ms
(vertical)	$\tau_z = 29.0$ ms
Synchrotron damping time	$\tau_E = 15.4$ ms
Energy spread	$\Delta E/E = 4.83 \times 10^{-4}$
Energy loss per turn	$\Delta E = 26.5$ keV
Accelerating frequency	$f_r = 500$ MHz
Harmonic number	$q = 192$
Maximum current (10 bunches)	$I = 500$ mA
(1 bunch)	$I_1 = 100$ mA
Number of cavities	$n_c = 1$
RF power (for I=500 mA)	$P_{RF} = 80$ kW

3. Injection System

The injection system of DELTA consists of a commercially available LINAC of possibly 100 MeV and a synchrotron BODO (BOoster DOrtmund) which can be ramped to the full injection energy of DELTA of maximum 1.5 GeV. Besides its normal preaccelerator mode, it is planned to operate BODO also like a storage ring with low-energy accumulation. The BODO lattice has two-fold symmetry with combined-function magnets.

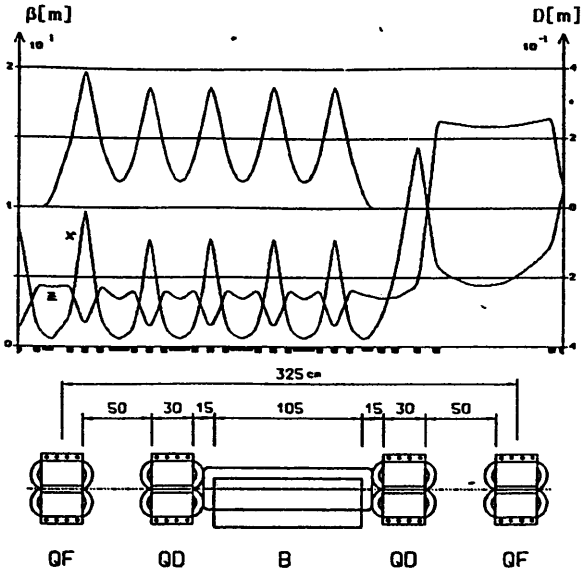

Fig. 2. Dispersion D(s) (upper part) and horizontal and vertical beta functions β(s) (middle part) for one Quadrant of DELTA and layout of a single triplet cell (lower part).

4. DELTA Magnets and Vacuum Chamber

Besides the argument of low costs, the design of the various DELTA magnets is mainly determined by the size of the vacuum chamber and the required field strengths and gradients. A conventional stainless-steel vacuum chamber will be built with one antechamber for continuously pumping with a combination of integrated DIP and NEG pumps. All dipole magnets are of C type with a gap height of 50 mm. Whereas the standard dipoles of the triplet cell have a weak quadrupole strength of $k = -0.3$ m^{-2} and a magnetic length of 1.05 m, there are a few dipoles of half the length and without such gradient which are used for dispersion matching of the straight sections. The DELTA quadrupole magnets with a weak sextupolar gradient of the pole faces and extra coils integrated between the poles to vary the sextupole strength continuously have a pole distance of 70 mm. Magnet specifications are given in Table 2.

Table 2. *Specifications of DELTA dipoles and quadrupoles*

DIPOLES :		QUADRUPOLES :	
magn. length	$l = 1.05$	*magn. length*	$l = 0.3$ m
gap height	$h = 50$ mm	*inner radius*	$r = 35$ mm
gap width	$b = 160$ mm	*max.grad. dB/dx*	$= 26.3$ T m
field strength	$B = 1.5$ T	*max. field*	$B = 0.92$ T
current	$n \times I = 65653$ A	*current*	$n \times I = 13460$ A
cur.density	$dI/dF = 4.1$ A mm^{-2}	*cur.density*	$dI/dF = 2.2$ A mm^{-2}
power	$P = 16$ kW	*power*	$P = 2.7$ kW

References

(1) K.Wille, Nucl. Instr. & Meth. Phys. Res. A272(1988)59; K.Wille,DELTA Report (1986) and Status Report (1988), Univ. Dortmund, (1986), unpublished.

(2) D.Nölle, "Possible FEL Projects at DELTA", Contribution P40 to this Conference.

FEL PROJECTS AT DELTA*

DELTA Group, Dirk Nölle
University of Dortmund
Institute of Physics
P.O. Box 500 500
4600 Dortmund 50, FRG

ABSTRACT

This paper reports on the plans for a new FEL facility at the 1.5 GeV electron storage ring DELTA [1] under construction at the University of Dortmund. First, the concept of this three-stage long-term project is sketched, with FEL's planned in the wavelength regime from the visible to wavelengths below 20 nm. In the following, the first two FEL projects are discussed in more detail.

LONG TERM CONCEPT OF THE DELTA-FEL FACILITY

DELTA is a low-emittance electron storage ring with two about 20 m long straight sections freely available for insertion devices. Working at low energies of about 500 MeV, it is an excellent driver for FEL's from the visible to the XUV. [1]

The project will be started with a simple and inexpensive device producing visible light. Secondly, it is planned to proceed to a high-gain FEL oscillator [2], and finally, with the experience gained so far, FEL operation below 20 nm will be attempted with a single-shot high-gain FEL.

The first device, FELICITA I, has to fulfill the following options. It has to be simple, easy to operate and will work at wavelengths, where all necessary optical equipment is well developed and available. On the other hand, the design of FELICITA I has to be as flexible as possible, but has to provide high gain to guarantee save operation above the oscillator threshold. Therefore, the project will start with an electromagnetic undulator, designed to operate in two different modes, namely as an optical klystron [3] and as a conventional FEL. Using this device it is intended to generate radiation at about 400 nm with DELTA running at 500 MeV. As the next step, it is planned to operate FELICITA I in oscillator mode at wavelengths down to 200 nm by running DELTA up to 700 MeV. Losses in gain due to the higher electron energy beam will be compensated by higher peak currents, since collective instabilities and other current-limiting effects as Touschek effect [4] or intra-beam scattering [5] are not as severe as at low energies. With beam energies of about 1.0 GeV, FELICITA I will produce radiation of wavelengths of about 100 nm, that can be used to test and improve optical components.

From the experience gained so far, DELTA will be optimised, to provide better low energy performance for the second experiment FELICITA II at 100 nm wavelength and below. Since mirrors with more than about 50 % reflectivity are not available [6] at these wavelengths, FELICITA II has to provide gain of 3 or more. As in the case of FELICITA I, this device will operate at energies from 500 MeV up to 1.0 GeV with nearly constant gain. Losses in gain due to the higher energy are compensated by higher peak currents attainable at these energies.

The third FEL project at DELTA is proposed to operate at wavelengths below 20 nm. In this region the operation of a single-pass FEL, installed in a pulsed-mode by-pass is the best solution [7]. The electron beam is kicked once through the by-pass into the FEL, producing a single but very intense laser pulse. Due to this process, the beam quality is degraded seriously. Therefore, the beam has to cool down by synchrotron radiation damping, before it can be reinjected into the FEL by-pass again. Due to the short damping time of DELTA, pused-mode FEL operation with frequencies of 10-20 Hz is realistic.

Besides of better storage ring performance without FEL's, a by-pass dedicated to FEL experiments provides certain advantages. First, the optical cavities can be made shorter, because FEL operation is possible with 3, 4 or 6 electron bunches instead of one- or two-bunch operation only. Moreover, a by-pass with separated beam line for the FEL provides free access for manipulating mirrors etc. during storage ring operation. Inserting an extra chicane in the bypass for FELICITA I, allows to operate with a very short optical cavity.

FELICITA I

FELICITA I will be the first FEL device to be built in a series of storage-ring FEL experiments. It has to be a simple, compact, most flexible and inexpensive device, but has to operate with rather high gain. To avoid problems with optical components, it is designed to operate in the visible first.

These conditions lead to an electromagnetic undulator, made of 16 identical periods. Such an undulator can be split into several sections, simply by exciting the coils of various periods with different currents, the same experimental setup can be used either as an optical klystron (OK) or, alternatively, as a conventional FEL. In contrast to the FEL mode, with all periods held on the same field, in the OK mode the undulator is devided into three sections. The first and the last seven periods are used as two identical undulators, separated by the two central periods driven at higher field and serving as dispersive section.

In the OK mode FELICITA I operates with much higher gain than in the FEL mode, but due to the small linewidth of the gain curve, only low average output power can be extracted [8]. Save ope-

* suported by the Bundesministerium für Forschung und Technologie under contract 05 334AX B 2

UNDULATOR		OK MODE	FEL MODE
Period Length	l_o [m]	0.25	0.25
Peak Field	B_o [T]	0.09	0.09
K - Value	k^u	2.1	2.1
Period Number	n_u	7	16
DISPERSIVE SECTION			
Peak Field	B_o^d [T]	0.69	/
K - Value	k^d	16	/
Period Number	n_d	2	/
Normalised Strength	N_d*	80	/

* optimised for 0.1% energy spread

Tab. 1: Parameters of the electromagnetical Undulator

BEAM PARAMETERS		OK Mode		FEL Mode	
Energy	[MeV]	500	1000	500	1000
Resonant Wavelength	[nm]	418	104	418	104
Average Current*	[mA]	30	60	30	60
Peak Current**	[A]	90	180	90	180
Filling Factor		0.81	0.81	0.81	0.81
Gain Degradation		0.34	0.34	***	
Max. Gain	[%]	10.4	10.3	4.0	3.9
Gain / Peak Current	[10^{-4}]	11.6	5.7	4.5	2.2

* per bunch, 4 bunches
** assuming 1.5 cm RMS. bunchlength
*** working in the Homogenous Broadening Regime [10]

Tab.2: Expected performance of FELICITA I

ration above oscillator theshold is expected for both operation modes and wavelengths about 400 nm. But at a later stage, progressing down to the UV, OK operation will be more favorable, because of the strongly reduced reflectivities of the mirrors of the optical cavity. With the OK-option, oscillator operation down to 200 - 300 nm is expected, which is particularly interesting for chemical, biological and medical applications [9].

Operating DELTA at 1.0 GeV, FELICITA I provides an intense radiation source for testing and developing optical components, suitable for the second experiment.

FELICITA II

Due to the expected high losses of optical cavities at wavelengths below 100 nm, XUV-FELs have to provide much more gain per pass compared to the visible regime [6].

To compensate mirror losses on the order of 50 % per reflection, gain factors of about 3 - 5 are necessary to reach the oscillator threshold. Such high values can only be attained by the use of very long undulators with many periods. Therefore, FELICITA II will be an undulator of 225 periods of 6.2 cm each and total length of 14 m, built in hybrid permanent magnet technology.

With DELTA running at energies up to 1.0 GeV, this device will produce FEL radiation in the range from 100 nm down to 25 nm.

Period Length	l_o	[m]	0.062
Peak Field	B_o	[T]	0.35
K - Value	k_u		2
Period Number	n_u		225

Beam Energy	[Mev]	500	1000
Resonant Wavelength λ_r	[nm]	100	25
Average Current*	[mA]	50	100
Peak Current**	[A]	150	250
Gain Degradation Factor***		0.3	0.3
max. Gain****		5.5	2.1

* per bunch, 2 bunches
** assuming 1.5 cm RMS. bunchlength
*** calculated according to Bizzari et al [9]
**** calculated with a onedimensional FEL simulation code [11]

Tab. 3: Parameters of FELICITA II

REFERENCES

[1] N. Marquardt," DELTA, a Low-Emittance Storage Ring as FEL Radiation Source ", Contribution KA7 to this conference
[2] A. Renieri," Final Report of the FEL working-group ", Proc. of the FEL workshop at the University of Dortmund, Germany, 1988 (in prep.)
[3] P. Elleaume, " Optical Klystrons ", Journ. de Phys. 44 C1, pp. 333-353, 1983
[4] J. Le Duff, Nucl. Instr. and Meth., A 239, p.83, 1983
[5] J. Bjorken, S. Mtingawa, Part. Acc., 13, p. 115, 1983
[6] D.T Attwood, " Short Wavelength Optics for Future Free Electron Lasers ", AIP Conference Proceedings, No. 118, pp. 294-313, (1983)
[7] pulsed by-pass FEL ref. von Volker
[8] G. Dattoli, A. Renieri, " Storage Ring Operation of the FEL: the Oscillator ", Nuovo. Cim., 59 B, pp. 1-39, 1980
[9] T.F. Deutsch, " Medical Applications of Lasers ", Physics Today , p. 56, Oct 1988
[10] Bizzari et al.: " The FEL: Status and Perspectives ", ENEA RT/TIB/85/49
[11] Dirk Nölle," Asymmetries of the gain curve ", presented at the 10th Int. FEL Conference, Jerusalem 1988

THE CCVV HIGH-CURRENT MEGAVOLT-RANGE DC ACCELERATOR

O.A. Anderson, W.S. Cooper, W.B. Kunkel, J.W. Kwan, R.P. Wells, C.A. Matuk, P. Purgalis,
L. Soroka, M.C. Vella, and G.J. De Vries,
Accelerator and Fusion Research Division, Lawrence Berkeley Laboratory
1 Cyclotron Road, Berkeley, CA 94720;
and L.L. Reginato, Lawrence Livermore National Laboratory

We describe a constant-current variable-voltage (CCVV) accelerator, intended to operate in the MeV energy range but tunable down to a few percent of an MeV without loss of beam current. We present experimental results from our 200-keV single-beam prototype system designed to accelerate up to 0.2 A of H^+ or H^- or the equivalent current of heavier ions. The beam is accelerated by a series of stackable 100-keV modules, the number depending on the maximum beam energy required. We discuss a proposed 1 MeV accelerator and a conceptual design for a multiaperture system accelerating 10 A of D^- ions to 1–2 MeV for current drive in a fusion reactor. The use of electrostatic quadrupole focusing allows a conservative design with reduced risk of voltage breakdown and allows us to maintain high currents while varying the beam energy. These features are useful for fusion reactor startup and for industrial applications, such as semiconductor processing and surface hardening.

Introduction

We describe various applications of a constant-current variable-voltage (CCVV) accelerator, and describe recent testing of a prototype. Design details were recently discussed elsewhere [1]. The concept is indicated in Fig. 1. There is an ion source and a preaccelerator [2, 3], which are not relevant here. There is an ESQ matching module and an ESQ-focused main accelerator, which could operate at constant current with variable voltage over a range as large as 20–1000 kV.

The CCVV accelerator is a flexible, pencil-beam version of the sheet-beam transverse-field focusing (TFF) dc accelerator, which we previously developed and tested [4], [5]. The system described here differs from others that have been proposed [6] or built [7] in its CCVV features and in simultaneously offering easily stackable modules and dc operation. Each pair of ESQ rods has a separate electrical connection, allowing independent control of focusing and acceleration voltages; this facilitates CCVV operation, modularity, and flexibility in choice of overall length. The average gradient can be made uniform and the acceleration channel can be lengthened to match the length of the graded insulating column (Fig.1). These features simplify construction and also improve voltage-holding reliability.

Our prototype, shown in Fig. 2, can accelerate a single beam of up to 200 mA of H^+ or H^- or the equivalent current of heavier ions; a multiple-beam system would be used for larger currents. The preaccelerator, which operates at a constant 100 kV, is incorporated into a beam-matching module with high pumping conductance. Preliminary operation of this module was reported previously [8]. We have recently added and tested a 100 keV ESQ-focused acceleration module. This 20-cm long CCVV module can be adjusted to either accelerate or decelerate the beam [1, 8]. For energies above 200 keV, more accelerating modules can be added to the stack, as in Fig. 1, where there are nine CCVV modules. We have proposed to build a facility at LBL to test a 1-MeV system [8]. Three additional modules would produce the maximum beam energy of 1.3 MeV required for the current U.S. baseline design for ITER (the International Thermonuclear Experimental Reactor) [9], as discussed further on.

CCVV Acceleration

Each pair of ESQ rods in the CCVV accelerator (Fig. 1) has separate electrical connections, allowing continuous adjustment of beam energy while maintaining a uniform average voltage gradient if desired. Since the current-carrying capability is independent of the average longitudinal gradient, we can make the accelerator internal length fit the external insulator length. In our designs for experimental facilities [8], we choose a length which allows operation in air rather than SF_6. For lower voltage applications, as in our prototype 200 kV accelerator (Fig. 2), an average gradient of 5 kV/cm is reasonable, so that our 100 kV module length is 20 cm. In the design for a 1-MeV facility, the lengths of most of the stackable modules were increased to 30 cm, giving 3.3 kV/cm [8].

Our freedom to lengthen the accelerator should also increase reliability for voltage holding. It reduces internal gradients and the solid angle accessible for voltage breakdown mechanisms along the beam path. The ESQ focusing forces also remove most secondary ions and electrons generated within the ESQ sections. Long-path breakdown along the pumping space is avoided as discussed in Ref. [1].

A beam envelope simulation for the ten-module, 1000-keV CCVV accelerator of Fig. 1 is shown in Fig. 3. The ESQ voltages for

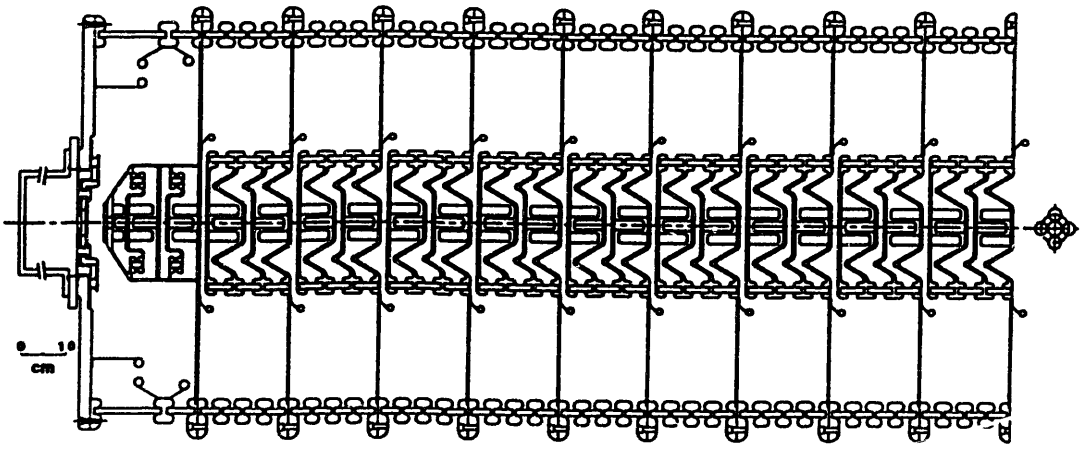

XBL 895-1923

Fig. 1. Conceptual design of 1-MeV CCVV accelerator, showing 100-keV matching/pumping module and nine CCVV accelerator modules of 100 keV each. The overall length is about 2 meters, not counting the ion source.

CH2669-0/89/0000-1117$01.00©1989 IEEE

this structure are determined by the beam current density, the emittance, and an assumption about the acceleration voltage gradient (assumed uniform in this case). The quadrupole transverse voltages were chosen to be proportional to the fourth root of the beam energy. Electrical and mechanical tolerances are discussed in Ref. [1].

200-keV CCVV Prototype

The 200 keV prototype is shown in Fig. 2. The first module contains the ESQ-focused matching/pumping section. The round, nearly parallel beam extracted from the ion source is transported at about 100 keV and converted into a phase-space format that is matched for subsequent ESQ acceleration. Gas pressure from the ion source is rapidly reduced because of the high pumping conductance in the beam extraction region and the open construction of the ESQ cage. A Monte Carlo code was used for the system design [1].

A single 100-keV ESQ accelerating module is shown in Fig. 2; details of the mechanical design are given in Ref. [1]. In the case of H^- or D^- operation, beam stripping produces heat loads and electrical currents to the electrodes; water flow and power supply requirements were estimated with the help of computer simulations [1]. As discussed further on, the measured loads turned out to be smaller than our conservative estimates.

Testing the CCVV Prototype

The matching/pumping module was tested with a 1.4 cm diameter H^- beam (measured at the source aperture) at 100 kV beam energy. Pulse length was up to 3 seconds without any breakdown problems. There was no measurable beam loss. The amount of full energy electrons in the beam was too small to be measured (less than one or two percent). The beam emittances before and after the ESQ module were equal within our 10 percent measurement uncertainty. The envelope parameters of the output beam were in reasonable agreement with those predicted by an envelope code. Using a larger diameter beam (2.9 cm), we transported up to 64 mA of H^- beam through the first module. The current was limited by the performance of the present H^- source.

Because of test stand scheduling conflicts, only preliminary tests of the the CCVV accelerator module have been performed. We used the 1.4 cm diameter beam at about 30 mA, running 70 ms pulses at 200 keV. We will run long pulses and obtain 200 kV emittance data when the test stand is again available (probably in April).

In our design it was difficult to estimate the effect of stray particles from beam-gas collisions. Even though our H^- source was operated at high gas pressure (14 mTorr) in order to maximize its output, our ESQ electrode currents (around 4 mA) were much smaller than our worst-case estimates. Our open-system high pumping conductance design was evidently quite effective.

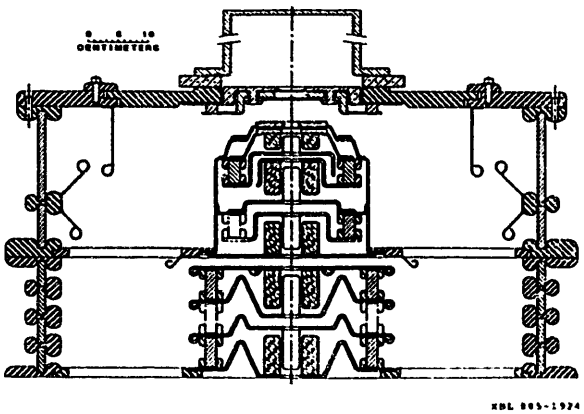

Fig. 2. The 200-kV CCVV prototype, showing matching/pumping module and a single CCVV acceleration module. Small insulating support rods are shown near the ESQ electrodes.

ITER Beamline Design

At present the baseline design for the ITER (International Thermonuclear Experimental Reactor) neutral beam system [9] calls for 70 MW of D^0 delivered to the plasma. To meet this requirement it is proposed to use three ports with a total of 9 beamlines arranged in a vertical stack of three beamlines per port. Each beamline (Fig. 4) contains two vertical arrays of 45 accelerating channels per array and each channel accelerates 0.14 A of D^- to 1.3 MeV. Therefore, each beamline delivers up to 8.75 MW of D^0, so that eight beamlines can deliver the required power while one beamline is on standby.

The proposed system will use improved D^- sources, multiaperture CCVV accelerators, and gas neutralizers. The residual ions remaining after neutralization are swept out by electrostatic deflectors into beam dumps. Cryopanels, located at the accelerator exit and neutralizer exit pump the excess gas.

The 1.3 MeV ESQ-focused accelerator design includes a 100 keV matching/pumping module and twelve 100 keV accelerator modules, with overall length 260 cm. If the energy requirements should change, modules can be added or deleted. The CCVV feature permits varying the beam energy at constant current, avoiding shine through during the low plasma density phase of startup.

The size of the CCVV modules and the number of modules required was determined by the chosen current per channel (0.14 A). If high-current sources become available, the size of the modules can be scaled up and the number reduced. For example, 0.56 A/channel could be handled by ESQ modules operating at the same electric field strengths but scaled up a factor of two in all dimensions. The mechanical construction would be considerably simplified.

Power System

We plan to use a different approach from neutral beam systems based on positive ions, where the low-impedance accelerators handle large currents (~100 A) at relatively low voltage (~100 kV) and fast series and shunt switches, acting in a few microseconds, provide fault damage protection. This type of protection is less practicable for megavolt CCVV applications; fortunately, the increased accelerator impedance favors other types of control, as discussed below.

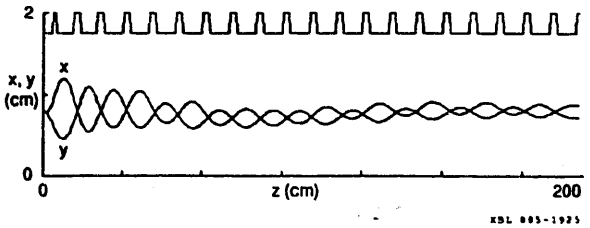

Fig. 3. Beam envelopes and quad locations for a system (see Fig. 1) with standard matching/pumping section and nine CCVV modules, accelerating 200 mA of H^- from 100 keV to 1 MeV.

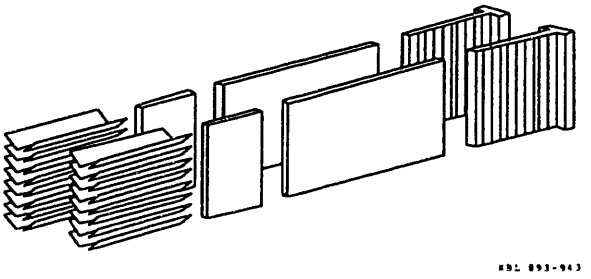

Fig. 4. Schematic of ITER beamline. From right to left are the CCVV accelerator assemblies, the gas neutralizers, the electrostatic ion separators, and the beam dumps.

Accelerator Power Supply for ITER

The high-frequency technology under investigation for generating high voltage (1 MV) for ITER is similar to that adopted widely by the low voltage power supply industry. To reduce the size of the transformer components we propose to use a frequency between 50 and 100 kHz. Although the overall size of a high voltage power supply is mainly dictated by the high-voltage gradients, the use of high frequency reduces the energy storage due to stray capacitance and allows rapid primary control. This should eliminate the need for costly shunt switching fault protection. Switching power supplies using solid state devices have achieved efficiencies approaching 90% in low voltage converter applications [10]. We are also investigating the use of vacuum devices.

To achieve high overall efficiency, we are investigating a modularized step-up technique to generate the high voltage which we call the Cascaded Resonant Transformer Rectifier (CRTR) system (Fig. 5). We maintain high efficiency by minimizing the leakage inductance, maximizing the shunt inductance, and by tuning to cancel the reactive losses. The ferromagnetic materials being tested are the nickel-zinc and manganese-zinc ferrites. We are in the process of constructing a ten stage, 100 kV prototype driven by an advanced MOSFET frequency converter. Details will be given upon completion of the prototype.

Although high frequency technology reduces the energy storage, in the megavolt range the electrodes must nevertheless be protected from the energy in stray capacitance. In the standard way, a lossy inductance will be inserted in series with the stray capacitance. This lossy inductance, which uses toroidal magnetic material, limits the spark-down current and absorbs most of the energy.

CCVV Deceleration for Ion Implantation

A CCVV module can also be used for deceleration. This reduces the design current, but, in fact, applications such as semiconductor processing require relatively small current. Using the same envelope code that we used to design our CCVV accelerators (cf. Fig. 3), we have shown [1] that the output voltage of our CCVV prototype (slightly modified) can be varied between 200 kV and 20 kV at a constant current of 80 mA. The beam energy in the matching/pumping module remains unchanged. We hope to test this type of operation in the near future. A design optimized for low energy flexibility, with quadrupoles shortened to reduce the phase advance, could be tunable from 200 kV to 10 kV or less, depending on the current.

Advanced Semiconductor Applications

Most modern commercial ion implanters for semiconductor manufacturing are multi-purpose machines, operating from 200 kV to less than 20 kV. The lower energies are used to produce fast switching shallow junction devices. Devices have also grown vertically, to three and four metal layers, so that 200 kV performance remains important. Reasonably constant throughput and good divergence are also essential in a production system. In present commercial systems, these requirements are met by two-stage accelerator systems, e.g., a 20 kV injector with a 180 kV boost. Current drop off becomes serious only below 20 kV, and beam divergence of 1° to 2° has been adequate up to now. However, as feature sizes push below 1 micron, future systems may require reduction of beam divergence to 0.5°, or less, for high aspect ratio structures. The CCVV decel structure is capable of meeting these anticipated future requirements.

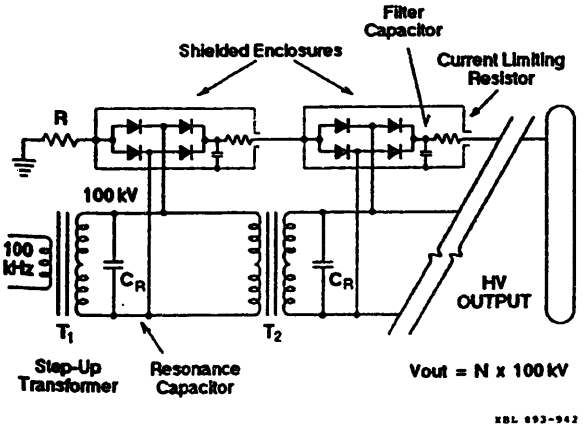

Fig. 5. Proposed power supply concept. Two modules are shown; ten would be required for a 1 MV system.

Our CCVV envelope results described above take the beam emittance into account but not the effect of nonlinearities in the system. Fully self-consistent particle dynamics in the CCVV system will soon be studied using the ARGUS 3D code [11]. Meanwhile, we have estimated the output divergence angle at low energies. Depending on the ion source, beam divergence of less than 0.5° appears to be feasible. Beam expansion can be used to cool the beam to a lower transverse temperature than that in the plasma source.

Acknowledgments

We thank all those who contributed to this project, especially C.H. Kim, D.A. Goldberg and A. Faltens. This work was supported by the Director, Office of Energy Research, Office of Fusion Energy, Development and Technology Division, of the U.S. Department of Energy under Contract No. DE-AC03-76SF00098.

References

[1] O.A. Anderson, L. Soroka, C.H. Kim, R.P. Wells, C.A. Matuk, P. Purgalis, W.S. Cooper, and W.B. Kunkel, IEEE Conference Proceedings, First European Particle Accelerator Conference, Rome, June 7-11, 1988.

[2] O.A. Anderson et al., "Design of a 200 mA DC H^- Injector for an RFQ," Proc. of the 1987 Particle Accelerator Conference, Washington, DC, March 16-19, 1987; IEEE Cat. No. 87CH2387-9, p. 289.

[3] O.A. Anderson, W.S. Cooper, W.B. Kunkel, C.F. Chan, L. Soroka, C.H. Kim, A.F. Lietzke, C.A. Matuk, P. Purgalis, and R.P. Wells, "Accelerator and Transport Systems for High-Current Negative-Ion Beams," Proceedings of the IAEA Technical Committee Meeting on Negative Ion Beam Heating, Culham Laboratory, July 15-17, 1987; also published as Lawrence Berkeley Laboratory report LBL-23748.

[4] O.A. Anderson, D.A. Goldberg, W.S. Cooper, and L. Soroka, "A Transverse-Field Focusing (TFF) Accelerator for Intense Ribbon Beams," 1983 Particle Accelerator Conference, Santa Fe, NM; IEEE Trans. Nucl. Sci. 30, 3215 (1983).

[5] O.A. Anderson et al., "Overview and Status of the Transverse-Field Focusing (TFF) Accelerator," 1985 Particle Accelerator Conference, Vancouver, B.C.; IEEE Trans. Nucl. Sci. 32, 3509 (1985); J.W. Kwan et al., "Transverse-Field Focusing Beam Transport Experiment," Proc. 4th Int'l Symposium on the Production and Neutralization of Negative Ions and Beams, Brookhaven National Laboratory, 1980; AIP Conf. Proc. 158, 507 (1986).

[6] D.A. Goldberg et al, "A Multi-Aperture Electrostatic Quadrupole (MESQ) Accelerator for Neutral Beam Injection," Bull. Am. Phys. Soc. 27, 1142 (1982).

[7] E.A. Abramyan et al., "Transformer Type Accelerators for Intense Electron Beams," IEEE Trans. Nucl. Sci. 18, 447 (1971).

[8] O.A. Anderson et al., "Applications of the Constant-Current Variable-Voltage DC Accelerator," to be published in Nucl. Instr. and Meth.

[9] O.A. Anderson, and 24 co-authors, "A High Energy Neutral Beam System for Reactors," presented at the 15th Symposium on Fusion Technology, Utrecht, The Netherlands, Sept. 19-23, 1988.

[10] A.K.S. Bhat, IEEE Trans. on Industrial Electronics 35 (1988).

[11] A. Mondelli, C. Chang, A. Drobot, K. Ko, A. Mankofsy, and J. Petillo, "Application of the ARGUS Code to Accelerator Design Calculations," presented at this meeting. Modeling of our 200 keV CCVV prototype system is described.

HIGH-AVERAGE-POWER MILLIMETER-WAVE FEL FOR PLASMA HEATING USING THE ETA-II ACCELERATOR*

A. L. Throop, D. P. Atkinson, J. C. Clark, G. A. Deis, R. A. Jong, W. E. Nexsen, A. C. Paul, E. T. Scharlemann, B. W. Stallard K. I. Thomassen and W. C. Turner
Lawrence Livermore National Laboratory, P. O. Box 808, Livermore, CA 94550

M. A. Makowski
TRW, Inc., Redondo Beach, CA

D. B. Hopkins
Lawrence Berkeley Laboratory, Berkeley CA 94720

Abstract

The Microwave Tokamak Experiment (MTX) is under construction at LLNL to investigate the feasibility of intense, pulsed microwave radiation for plasma heating on future ignition tokamaks. A high-average-power free-electron laser (FEL) will use the Experimental Test Accelerator (ETA-II), a linear induction accelerator, in combination with an advanced high-field wiggler, to produce 1-2 MW of power at 1-2 mm wavelengths for periods of up to 0.5 s. The design of the FEL, termed the intense microwave prototype (IMP), is described, along with the status and major issues associated with the experiment.

Introduction

Electron cyclotron heating (ECH) has become an important option for achieving and sustaining ignition in the next generation of tokamaks, such as the Compact Ignition Tokamak (CIT) and the International Thermonuclear Engineering Reactor (ITER).[1] Table 1 lists the major requirements of an ECH source.

Table 1. ECH source requirements.

Frequency (GHz)	140 - 600
Total average power (MW)	10 - 30
Overall efficiency (%)	15-30
Center frequency adjustment(%)	± 25
Rapid frequency tuning over 100 ms(%)	± 3-5

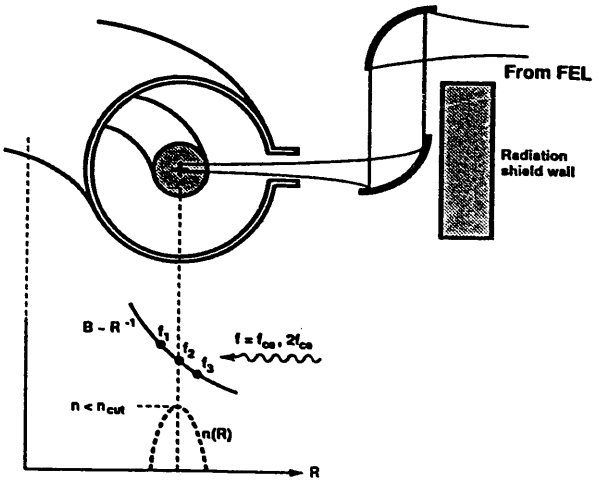

Figure 1. Geometry for ECH heating.

Figure 1 illustrates the geometry of ECH. The coupling structure consists of simple mirrors, which are removed from the plasma edge, thereby reducing impurity influx and minimizing neutron activation issues. High flux densities (100 kW/cm^2) can be achieved with ECH, requiring small port access. The ECH resonance is also highly localized so that by frequency-tuning the source (5% over 100 ms), one can adjust the heating location to improve confinement time and to suppress disruption processes.

There has been considerable interest in using the induction-linac driven FEL (IFEL) for ECH over the past two years. Previous experiments using the ETA and ELF facilities demonstrated peak powers of over 1 GW and conversion efficiencies of over 35% at 35 GHz using a tapered wiggler.[2] The same facility operated at 140 GHz in an untapered configuration and produced peak powers of over 50 MW and total gains of 63 dB.[3] Simulation codes showed good agreement with the measurements. While these experiments operated at low repetition rate (PRF) and, thereby, low average power, the recent developments in high-brightness, high-repetition-rate technology have made a high-average-power IFEL feasible.[4]

For ECH applications, the relativistic beam energies and high currents of the IFEL are well suited for operation at high frequencies and high powers. The high-gain amplifier configuration of the IFEL allows the low-power master oscillator to be frequency swept for rapid tuning. The short pulse length mitigates electrical breakdown issues. The intense nature of the output pulses also offers the unique opportunity for using nonlinear mechanisms for efficient current drive and other applications.[5]

Overview and FEL Simulations

Figure 2 shows the layout of the MTX experiment.[6] Figure 2(a) shows the ETA-II facility, consisting of a nominal 1-MeV injector and 6 to 8 accelerating sections to achieve 6 to 10 MeV of beam energy.[7] The IMP wiggler is located in the ETA-II vault along with FEL microwave diagnostics. An optical train of six mirrors is used to transport the FEL output power to the tokamak, as shown in Fig. 2(b). The MTX uses the Alcator-C tokamak, which has been relocated to LLNL from MIT. Alcator-C produces a high-field (> 9-T), high-density (n > 4 x 10^{20}m^{-3}) target plasma that is relevant to future machines. The toroidal field coils are cooled by liquid nitrogen and can operate at a maximum rate of about twelve shots per hour. The design objectives for the MTX FEL are to produce 1-2 MW of average power at a frequency of 140 or 250 GHz for durations of up to 0.5 s.

Figure 3 shows the results of simulation codes for the IMP FEL operating at 250 GHz where the axial variation of the wiggler magnetic field and the

CH2669-0/89/0000-0770$01.00©1989 IEEE

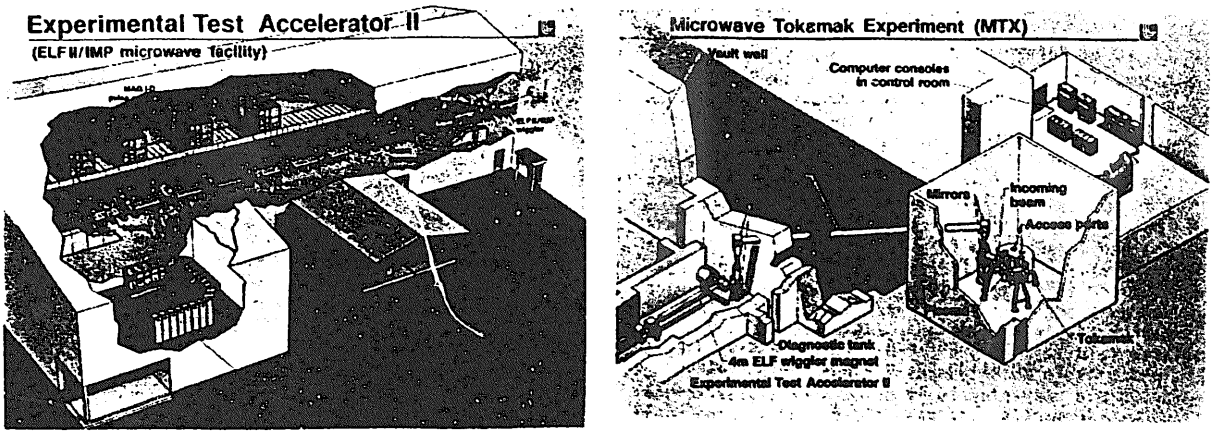

Figure 2. (a) ETA-II accelerator and wiggler for FEL. (b) Schematic of MTX experiment.

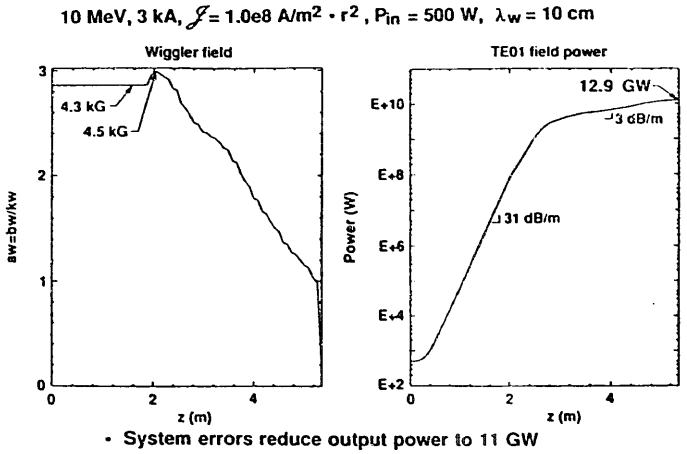

Figure 3. Axial field profile and output power for 250-GHz FEL.

corresponding microwave output for tapered operation are plotted.[8] Exponential gain and saturation occurs over the first 2 m of the wiggler, while an additional 3 m is required for tapering and high extraction efficiency. Table 2 lists the performance predicted at 250 GHz. Over 10 GW of peak power and 2.5 MW of average power is predicted, providing a design margin over the MTX requirements. High mode purity is predicted for tapered operation, along with a wide amplifier bandwidth.

Table 2. Summary of simulation results for 250-GHz FEL.

Peak TE_{01} output power (GW)	> 12 (11)*
TE_{01} mode fraction (%)	> 97
Extraction efficiency (%)	> 40 (37)*
Peak noise power (MW)	3
3-dB amplifier bandwidth (%)	10
Average TE_{01} power (MW)	2.7*

* with system errors: 0.1% wiggler error, 1 mm offset, ± 1% energy sweep; pulse format - 5 kHz, 50 ns.

ETA-II Accelerator and Beam Transport

Table 3 lists the beam parameters required to operate the FEL and compares them with the ETA-II design objectives and present status. The ETA-II is designed to deliver a bright beam at high average power. The brightness required for microwave FELs is 20 to 40 times less than the value measured on ETA-II.[9] Similarly, the energy variation and macropulse length are within the ETA-II design objectives. For higher-current operation, an anode-cathode design will be used that produces 3 kA, but at a predicted brightness of over 1 x 10^8 A/(rad-m)^2.

Figure 4 shows the beamline transport for the FEL. Solenoidal lenses are used to transport and match the electron beam from the accelerator to the wiggler. The design results in less than 10% variation in the diameter of the beam envelope and predicts only small emittance growth. The transport section contains a section for accelerator diagnostics as well as periodic graphite limiters to scatter and remove any halo electrons with a large transverse velocity component.

Table 3. Summary of ETA-II objectives and FEL requirements

Parameter	High-brightness objectives	Microwave FEL 250 (140) GHz	Initial measurements*
Energy (MeV)	6 - 20	9 - 10* (6-7.4)	2.3 - 5.2
Current (kA)	1.5	3.0	1.5 - 2.0
Brightness [x 10^9 $A/m^2 \cdot r^2$]	2.0	0.1	2.0 - 4.0
Pulse width (ns)			
- FWHM	70	70	70
- "Flat top"	50	50	50
Energy variation (%)	±0.4	±1	--
PRF, burst (Hz)	5000	5000	1 - 3 †
Burst length (s)	30	0.5	--

* See paper M24: W.C. Turner et al., this conference.
† Operation up to 5 kHz demonstrated on offline facility.

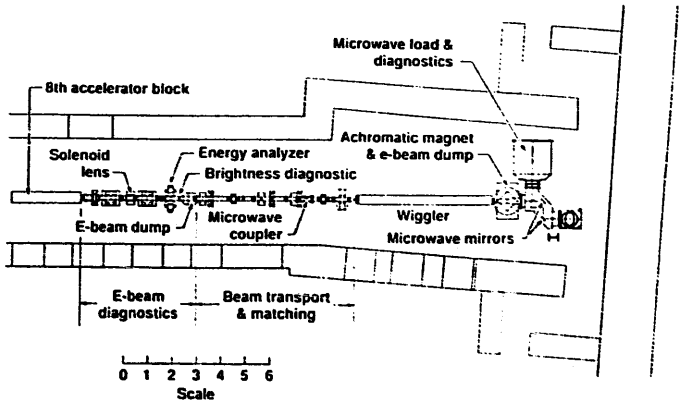

Figure 4. Plan view of beamline for 250-GHz FEL.

The input master oscillator microwave signal is coupled into the wiggler collinearly with the electron beam using a 45-degree mirror in the beamline. The mirror contains an aperture through which the electron beam is focused and couples the input signal with an expected 10-16 dB insertion loss. Except for the graphite limiters, the linear beam fill factor (beam radius / wall radius) has been kept at less than about 50% to avoid potential wall loading. At the output of the FEL, the microwave radiation can either be deflected into an anechoic diagnostic chamber using a movable mirror or it can be allowed to continue into the microwave transmission system to the tokamak.

The FEL interaction causes the electron beam exiting the wiggler to have a large energy spread. An achromatic magnet reimages the beam at nearly right angles to the beamline, where the beam is expanded to reduce the power density. The beam absorber is a simple graphite slab that uses thermal inertia during the 0.5-s macropulse and is cooled between shots.

IMP Wiggler

For operation at millimeter wavelengths and high average powers, the FEL wiggler must operate with steady-state fields (to accommodate high PRF accelerator operation), must allow the wiggler field to be arbitrarily tapered, and must achieve high magnetic fields with small transverse error fields to avoid beam steering. Table 4 lists the wiggler requirements. The wiggler design uses iron electromagnet pole pieces in conjunction with permanent magnets to achieve the required field strength and tunability. A similar design, operating at a lower field, is presently in use in a 25-m wiggler that is part of a 10-μm FEL experiment at LLNL.

Table 4. Requirements for IMP wiggler.

Period (cm)	10
Gap (cm)	3.7
Length (m)	5.5
Peak field (kG)	4.7
RMS field error (%)	0.1
B-field tuning range (%)	>37

Figure 5 illustrates the basis of the high-field design, and Fig. 6 shows the pole piece configuration. The permanent magnets are placed adjacent to the iron pole pieces to bias the B-H curve of the iron to higher field strengths. In the process, the linear range of operation is reduced as indicated in the figure. For the IMP design, the maximum field is operated at an acceptable value of about 85% of the Halbach limit, and a 50% tuning range is achieved. The IMP wiggler is presently in fabrication. Assembly and testing will occur this summer, with installation planned for this fall.

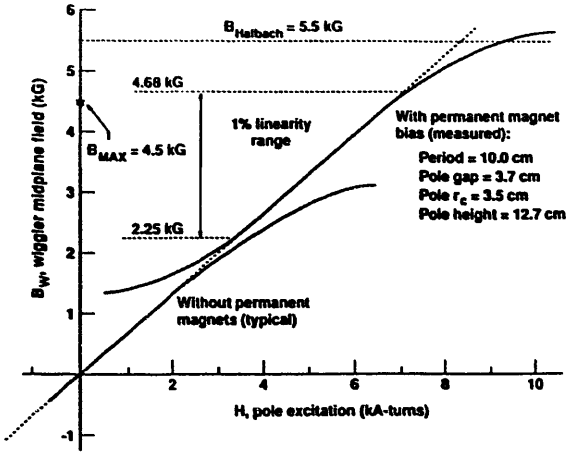

Figure 5. B-H curves for IMP wiggler with and without permanent magnets.

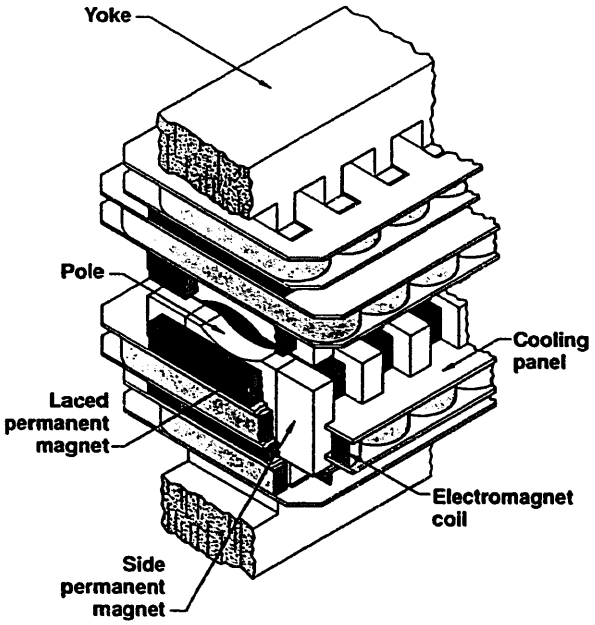

Figure 6. Pole piece design for laced electromagnetic wiggler.

Microwave System

Figure 7 shows an elevation view of the microwave system for the 250-GHz FEL. A 5-kW gyrotron is used as the master oscillator and has been tested off line. A Vlasov coupler is used to launch a free-space Gaussian beam, which is then coupled into the wiggler using the mirror coupler described above.

Four primary mirrors transmit the FEL output to the tokamak over a 20-m distance in a 20-in.-diam evacuated pipe. At millimeter wavelengths and for high peak powers, quasi-optical transport is favored over waveguide methods due to attenuation and surface heating. The transmission system for the IFEL is windowless, thereby avoiding thermal and bandwidth issues associated with using a window at high average power and with a tunable source. The mirrors are approximately 44 x 58 cm in diameter and are being fabricated with a 5-μin. finish. Alignment tolerances are not severe -- about ± 3 mm at each mirror. Simulations predict an overall transmission loss of less than 8% at 250 GHz, with most of the loss (4%) occurring at the first mirror due to loss of sidelobe power in the antenna pattern from the FEL waveguide.

Two major issues in a high-power microwave FEL are surface breakdown and thermal heating in the interaction waveguide.[10] Figure 8 shows the waveguide geometry. The waveguide is highly overmoded ($d/\lambda = 30$) and operates in the TE_{11} mode, as determined by the FEL resonance condition. An elliptical waveguide is shown since it provides additional margin to keep the beam fill factor at less than 50%. The first experiments to be conducted will use a circular waveguide of equivalent area for ease of fabrication.

At millimeter wavelengths, surface heating, rather than surface breakdown, determines the maximum power limit in the waveguide. With 10 GW of peak power, the maximum surface fields will be about 140 MV/m. Based on an extrapolation of Stanford Linear Accelerator Center data for 3-10-GHz, 2.5-μs-wide pulses, the threshold for surface breakdown for a 250-GHz, 50-ns pulse is over 5000 MV/m. A threshold of 360 MV/m measured using the 35-GHz FEL and an unconditioned cavity, extrapolates to a threshold of 1000 MW/m. Thus, surface breakdown is not expected. Multipacting is also of concern, but the experiment operates outside of the range for multipacting in either a field-free region ($0.07 < fd < 10$ GHz-cm; IMP = 750 GHz-cm) or in the presence of the wiggler field ($0.2 < f_c/f < 1$; IMP = 0.04). In addition, the 50-ns pulse length is much less than the volume ionizaton time for the vacuum quality of interest (10^{-6} Torr).

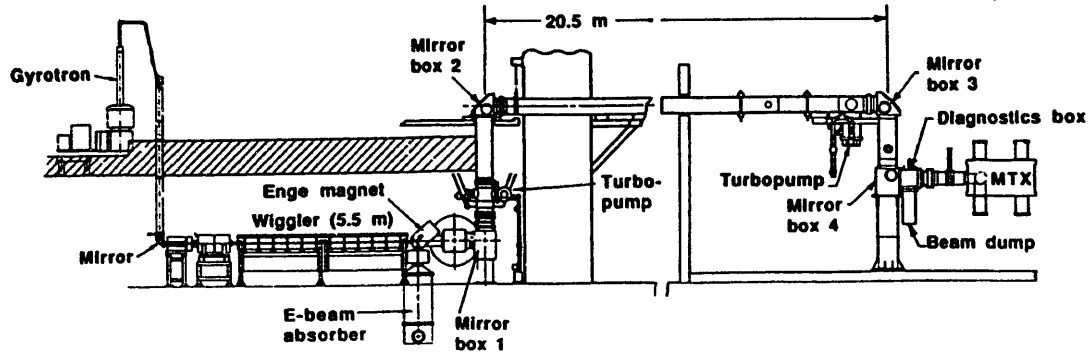

Figure 7. Elevation view of microwave system for 250-GHz FEL.

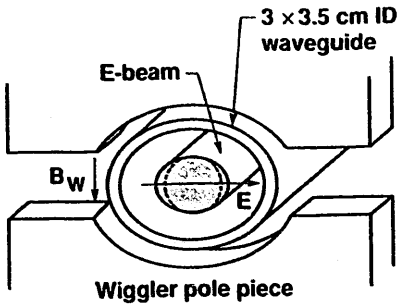

Figure 8. Interaction waveguide geometry.

The peak surface-wall load is a unique issue for the IFEL because of the intense field strengths that occur over the last 1-2 m of the interaction waveguide. At 10 GW of peak power, the peak wall loads are 0.07 J/cm^2 per pulse, which is about 10% of the damage threshold measured for an uncoated copper surface. In general the temperature rise is kept to less than 30°C during the 50-ns pulse to avoid surface fatigue. Thus, for the MTX experiment, the peak wall loads are not expected to be a major issue. For operation at higher average powers in ignition tokamaks, a corrugated waveguide that operates in the low-loss HE_{11} mode will be used.

At 2 MW of average power, the peak wall loading is 300 W/cm^2 near the end of the interaction waveguide. For the 0.5-s shot duration of the MTX experiment, thermal inertia will limit the temperature rise of the wall to less than 80°C so that only low levels of cooling between shots will be required. Again, for higher power devices and long-pulse operation, the use of a corrugated waveguide will reduce the average wall loading to a tractable value.

Plans for Experiments

The first series of FEL and plasma heating experiments is planned for this summer. While the IMP wiggler is in fabrication, the air core wiggler used in the previous ELF experiments will be used for early "single-pulse" experiments at 140 GHz. This will require ETA-II to operate at 6 MeV and 2.5 kA and is expected to produce up to 2 GW of peak power. These experiments will allow first evaluation of the ETA-II beam for driving an FEL, will test the microwave transmission system, and will allow preliminary studies of the coupling of intense microwave pulses to the plasma.

During FY90, after installation of the IMP wiggler, experiments will continue at 140 GHz but with 5-kHz pulse trains of up to 10-ms duration. This pulse train will deliver over 6 kJ of energy to the plasma for bulk heating experiments, and will begin to address issues of high-average-power transport of both the electron and microwave beams.

Operation at 250 GHz for 0.5 s will require an upgrade in ETA-II power conditioning and energy as well as changes in the master oscillator and microwave diagnostics. This is expected to be completed during FY91, allowing ECH experiments at higher tokamak fields and densities, near to those of interest to CIT and ITER.

Summary

The technology for constructing a multi-megawatt FEL operating at millimeter wavelengths appears feasible using the induction linac. The ability to transport and use bright, high-power electron beams for an FEL will be developed on the ETA-II and IMP Facilities. The MTX experiment will investigate the ability to transport intense microwave beams, to couple them efficiently to the tokamak plasma, and to use predicted nonlinear effects for current drive and other advanced concepts.

*Work performed under the auspices of the U.S. Department of Energy by Lawrence Livermore National Laboratory under contract W-7405-ENG-48.

References

1. T. C. Marshall et al., "Electron Cyclotron Heating - Technology Review," U.S. DOE, Germantown, Maryland, DOE/ER-0366 (1988).
2. T. J. Orzechowski et al., Phys. Rev. Lett., vol. 57, (1986).
3. A. L. Throop et al., Nucl. Instrum. Methods Phys. Research, A 272, (1988).
4. R. J. Briggs et al., Proceedings of 1987 Particle Accelerator Conference, p. 178.
5. R. H. Cohen et al, in "Nonlinear Phenomena in Vlasov Plasmas," F. Doveil, editor, Editions de Physique, Orsay, 1989, p. 335.
6. K. J. Thomassen, editor, "Free-Electron Laser Experiments in Alcator-C" (U. S. Government Printing office, Washington, D. C., 1986)
7. J. C. Clark et al., "Design and Initial Operation of the ETA-II Induction Accelerator", presented at Linac 88 Linear Accelerator Conference, Williamsberg, VA., October 1988, available as LLNL report UCRL 99201.
8. R. A. Jong et al., Rev. Sci. Inst., vol. 60, February 1989.
9. W. C. Turner et al., paper M24, this conference.
10. D. B. Hopkins, et al., paper D56, this conference.

STATUS OF THE ETA-II LINEAR INDUCTION ACCELERATOR: HIGH BRIGHTNESS RESULTS*

W. C. Turner, J. K. Boyd, J. C. Clark, and W. E. Nexsen

Lawrence Livermore National Laboratory
P. O. Box 808, L-626
Livermore, California 94550

Abstract

A two-aperture collimator has been used to measure brightness of the electron beam produced by the injector and the first 20 acceleration cells of the ETA-II linear induction accelerator. Osmium alloy dispenser cathodes produce the electron beam. For accelerated currents up to 1.5 kA with 2.0- to 2.7-MeV beam energies the measured brightness is 4×10^9 A/(rad-m)^2, exceeding our design goal by a factor of 2. At the highest current, 2.0 kA, a beam brightness of 2.6×10^9A/(rad-m)^2 has been measured.

Introduction

The Experimental Test Accelerator II (ETA-II) accelerator is the latest in a series of linear induction electron accelerators built at the Lawrence Livermore National Laboratory. The initial objectives of the ETA-II experimental program are to create high-brightness, high-average-power electron beams. Both parameters are related to the usefulness of the induction accerator as a driver for a short-wavelength, high-average-power free-electron laser (FEL). Design parameters for ETA-II are 10-MeV beam energy, 3-kA current, 50-ns pulse flat top, and 5-kHz repetition rate. The accelerator consists of a nine induction cell injector, sixty induction accelerator cells, and four magnetic compression pulse-power modulators. The emphasis in this paper is on measurements of beam brightness. The experiments were done at low repetition rate with the injector plus the first 20 acceleration cells. Beam energy was typically 2.5 MeV, current up to 2 kA, and repetition rate 1 to 3 Hz. Descriptions of ETA-II are given elsewhere.[1,2]

Description of the Experiment

The choice of cathode and the electron optics design of the electrode shapes in the extraction region of the injector are crucial for obtaining high and uniform current density and for minimizing the transverse phase space volume of the electron beam. For the experiments reported here, we use thermionic, osmium-coated dispenser cathodes. Previous experiments have shown the intrinsic brightness of this type of cathode to exceed 1.2×10^{10} A/(rad-m)^2 up to current densities of 140 A/cm^2; the current density and brightness are uniform to within ±10% over the cathode area.[3] Diagrams of the ETA-II cathodes and extraction electrode shapes are shown in Fig. 1. The extraction geometry consists of a curved cathode surrounded by a non-emitting focusing electrode, an intermediate electrode, and the anode pipe through which the beam is extracted. The cathode is mounted on the end of a stalk inserted through the bore of five induction cells, while the anode pipe is inserted from the opposite direction through four additional induction cells. Solenoidal coils incorporated into the anode induction cells focus the beam inside the anode pipe. Axial magnetic field strength is typically 0.5 to 1.0 kG. The cathode is designed to be operated with nearly zero magnetic field component normal to its surface in order to minimize the canonical angular momentum of the extracted electron beam. This is accomplished with two coils placed over the cathode-anode region on the outside of the vacuum chamber. Current in these coils opposes the focusing field in the anode pipe and is adjusted to null the normal magnetic field component on the cathode surface. The electrode shapes and relative locations have been designed with the DPC particle code.[4] For a cathode to anode voltage of 1.5 MV the DPC code predicts a space-charge-limited current of 2140 A for the 8.9-cm-diam cathode of Fig. 1(a) and of 3126 A for the 12.7-cm-diam cathode of Fig. 1(b).

For the experiments reported below, the brightness of the electron beam is measured with a field-free, two-aperture collimator, which is shown schematically in Fig. 2. A sine/cosine coil pair between the collimator apertures corrects for misalignment between the collimator and beam axes. A pair of solenoidal coils at the end of ETA-II and 70 cm in front of the first aperture of the collimator is used to focus the beam to a waist halfway between the two apertures. Experimentally, this is done by adjusting the strength of the solenoidal lens to maximize current through the second aperture. The apertures are holes with radius a = 1.5 mm drilled through range-thick 3.8-cm

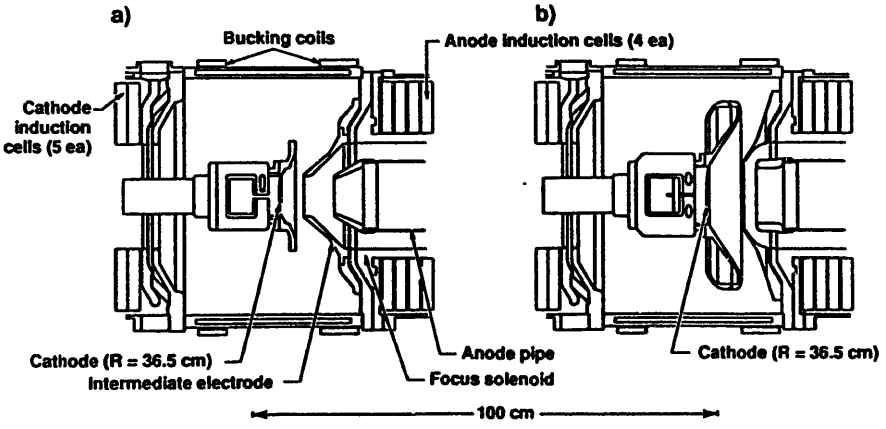

Figure 1. Diagrams of the cathode-anode region of the injector for the (a) 8.9-cm-diam and (b) 12.7-cm-diam cathodes.

* Performed jointly under the auspices of the U. S. DOE by LLNL under W-7405-ENG-48 and for the DOD under SDIO/SDC-ATC MIPR No. W31RPD8D5005.

graphite disks and separated by a distance $L = 61.6$ cm. A gated image intensifier CCD camera is used to observe the beam image on the first aperture. The image is typically about 1 cm in diameter. Steering coils (also sine/cosine wound) over the focus solenoids direct the beam onto the first aperture. Resistive foil-wall return-current monitors measure the beam current before and after each aperture. Referring to Fig. 2 we define I_1 as the current that exits the accelerator and falls on the first aperture, I_2 as the current through the first and incident on the second aperture, and I_3 as the current through the second aperture. The (normalized) beam brightness is defined by

$$J = \frac{1}{(\beta\gamma)^2}\frac{I_3}{V_4}\frac{1}{\delta},$$

where $\beta\gamma$ is the usual relativistic factor, $V_4 = \pi^2 a^4/L^2 = 1.32 \times 10^{-10}$ (rad-m)^2 is the transverse four-dimensional phase space acceptance defined by the collimator, and $\delta = \delta(\beta\gamma, I_2/I_A, I_3/I_2, a/L) < 1$ is a space-charge correction factor. The beam energy, and therefore $\beta\gamma$, is calculated from capacitance probe monitors of voltage applied to the induction cell gaps. The space-charge correction factor accounts for the reduction of phase space acceptance due to space-charge spreading of the beam. For this correction we use a formula derived by Caporaso,[6] which gives an upper bound on δ and therefore a lower bound on the beam brightness estimated from I_3.

Attention to vacuum quality is very important for obtaining the results reported in this paper since the osmium-coated dispenser cathode can be easily poisoned by too high a partial pressure of electronegative compounds such as water vapor, oxygen, and fluorocarbons. The basic requirement is that the desired space-charge-limited current density (10 to 20 A/cm^2) be achieved at a temperature low enough to ensure stable cathode operation for the time required to obtain the data (approximately twenty operating days for measurements with a given cathode). It has previously been shown that a leak-tight, unbaked vacuum system with O-ring seals and base pressure $P < 1 \times 10^{-7}$ Torr is adequate to meet this requirement.[3] In this case the base vacuum pressure consisted mostly of water vapor and residual amounts of methane, carbon monoxide, and their fragments. Although by modern standards this pressure is not too difficult to achieve some attention has to be taken to avoid the sometimes disappointing results obtained with this type of cathode in acclerator environments. For the experiments reported here we avoided materials that contribute high water vapor pressure (i.e., plastic insulators), chose an O-ring (Viton) and dielectric insulation fluid (FC-75 Fluorinert) combination that limits permeation of dielectric fluid into the high vacuum region to very low levels, and also ensured that there were no detectable atmospheric leaks before operating the cathode. Once this was achieved the background pressure—$p = 5 \times 10^{-8}$ Torr with the cathode hot—was routinely obtained, and there have been no indications of cathode deterioration for the duration of our experiments. This vacuum pressure is maintained with two turbomolecular and two cryo pumps mounted over the cathode region of the injector. No high temperature bakeout is required, and all vacuum seals are standard O-rings.

Experimental Results

As a check of basic cathode operation we have measured cathode emission current versus temperature for fixed injector voltage. Cathode temperature is measured with an optical pyrometer and quoted as a brightness temperature ($^\circ C_B$) uncorrected for emissivity of the cathode surface. Temperature varies significantly over the cathode surface: the coolest region is at the center, while the hottest regions are near the outside of the cathode and directly over the spiral-wound heater filament imbedded in the back of the cathode. In this paper we always refer to temperature at the cathode center. At 1000$^\circ C_B$ the temperature differential between hottest and coolest region of the cathode surface is 60$^\circ C_B$ (16$^\circ C_B$) for the 8.9-cm (12.7 cm) diameter

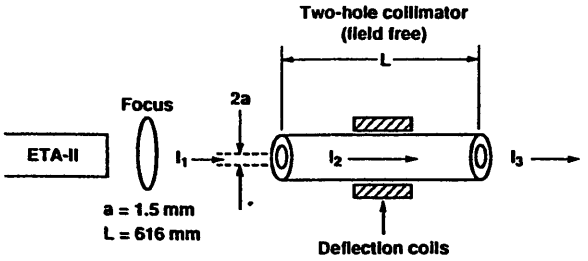

Figure 2. Schematic diagram of the field-free, two-aperture collimator used for electron beam brightness measurements.

cathode. Heater power required to maintain the cathodes at 1000$^\circ C_B$ is 1078 W (17.3 W/cm^2) for the 8.9-cm-diam cathode and 1414 W (11.2 W/cm^2) for the 12.7-cm-diam cathode. Emission current versus temperature is shown in Fig. 3 for the 8.9- and 12.7-cm-diam cathodes. For these two cathodes, the injector voltage was 0.9 and 1.2 MV, respectively, at saturation. Both sets of data show a sharp knee at the transition from emission to space-charge-limited operation. The transition temperature is low enough to ensure very long cathode lifetime in space-charge-limited operation. The larger cathode seems to be superior since, for the data in Fig. 3, the transition occurs at lower temperature (970$^\circ C_B$ versus 1090$^\circ C_B$) even though the saturated current density is somewhat higher (15.8 A/cm^2 versus 12.9 A/cm^2). Application of Richardson's law gives a work function for the 12.7-cm-diam cathode that is 0.2 eV lower than for the 8.9-cm-diam cathode. For measurements of beam brightness we always operate the cathodes in the space-charge-limited region.

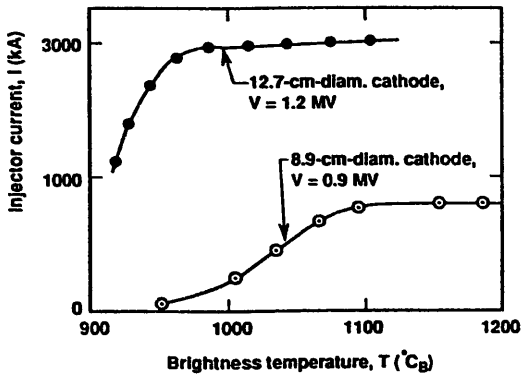

Figure 3. Emission current vs temperature for the (a) 8.9-cm- and (b) 12.7-cm diam cathodes.

In Fig. 4 we show a plot of injector current versus voltage for the 8.9-cm-diam cathode with all data points space charge limited. Relativistic corrections to Child's law are small up to the maximum applied voltage, so the data are in good agreement with a three-halves power law $I \sim V^{3/2}$. The experimental data in Fig. 4 and similar data for the 12.7-cm-diam cathode fall ~15–20% below the DPC predicted current for a given applied voltage.

Electron beam brightness data obtained with the apparatus shown schematically in Fig. 2 are summarized in Tables 1 and 2 for the 8.9- and 12.7-cm-diam cathodes. Brightness is given in the far right-hand column, while beam energy, beam current (I_1 in Fig. 1), currents exiting the first (I_2) and second (I_3) apertures of the collimator, and the space charge correction factor δ are given in the other columns. For both cathodes, data were taken for a range of beam currents and over several run days with slightly different beam transport conditions to verify the reproducibility of the data. For the 8.9-cm-diam cathode, the brightness $J = 4 \times 10^9$ A/(rad-m)^2 is essentially constant within experimental error with beam current varying from 0.85 kA to 1.4 kA.

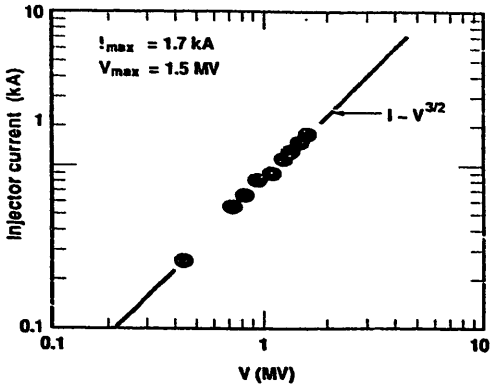

Figure 4. Injector current vs voltage for the 8.9-cm-diam cathode.

At 1.5 kA, the 12.7-cm-diam cathode has a similar brightness [5 × 10^9 A/(rad-m)^2], but at higher currents the brightness values recorded are somewhat reduced: at 1.7 kA, $J = 1.7 \times 10^9$A/(rad-m)^2, and at 2.0 kA, $J = 3.2 \times 10^9$A/(rad-m)^2. Whether this decrease in brightness is a real trend or an artifact of less than optimum tuning of the accelerator is unknown at present.

With the large currents being accelerated in these experiments and the relatively low beam energy, beam transport is dominated by the space charge of the beam rather than by beam emittance. To measure beam brightness with the two-hole collimation scheme and avoid being overwhelmed by space charge it is necessary to use small apertures and sample a relatively small fraction of the total beam current. The question naturally arises whether the brightness values obtained are representative of the whole beam. Earlier measurements of the intrinsic cathode brightness[3] and the DPC simulation results support the notion that beam brightness is uniform. In principle, one could scan the beam across the collimator to obtain a brightness profile, but in practice this method has been impractical because of the spatial beam sweep induced by energy variation and because of the time needed to tune the accelerator for a given data point. Reducing the energy variation of the beam to ±1% for a 50-ns flat top is one of the primary goals of the ongoing experimental program. In addition, after repeating these measurements with the full 60 accelerator cells, we plan to measure the total beam brightness with either the pepper pot method used to study the intrinsic cathode brightness[3] or a collimator with superimposed axial magnetic field.

For the bulk of the data in Tables 1 and 2, beam transport calculations with experimentally measured values of current in the solenoidal focusing magnets predict envelope oscillations with roughly 2:1 ratio because of mismatch. At present, we do not have diagnostic capability to measure these oscillations. One attempt (on 1/31/89 in Table 2) was made to eliminate them by using a set of focusing currents that, in theory, had very small envelope oscillations. Although the result obtained, $J = 3.2 \times 10^9$ A/(rad-m)^2 at I = 1.14 kA, is respectable, it is not quite as good as earlier data.

Discussion

In Fig. 5 we plot brightness versus current for the ETA-II data included in Tables 1 and 2 together with measurements of the intrinsic brightness previously measured for a dispenser cathode. For currents of 1.5 kA or less the ETA-II brightness measured with the two-aperture collimator is 4 × 10^9 A/(rad-m)^2. To our knowledge this brightness is the highest recorded in an induction accelerator, and it has been obtained at a current that is very reasonable for a high power FEL. This brightness value exceeds our original design goal by a factor of 2, and, if maintained during acceleration to the final beam energy required by the FEL resonance condition, is sufficient for efficient production of an FEL beam with a wavelength of less than

Table 1. Summary of brightness results obtained with the 8.9-cm-diam cathode.

Date	Beam energy (MeV)	Beam current (kA)	βγ	I_2 (A)	I_3 (A)	δ	J [10^9 A/(rad-m)^2]
11/22/88	2.54	1.15	5.89	24.8	11.8	0.595	4.3
11/29/88	2.54	1.15	5.89	17.0	11.8	0.645	4.0
11/29/88	2.41	0.85	5.63	23 ±9	11.3	0.583 ±0.058	4.7 ±0.5
11/30/88	2.75	1.26	6.31	52.5	11.2	0.565	3.8
12/1/88	2.70	1.40	6.20	62 ±22	10.7	0.545 ±0.050	3.9 ±0.3

Table 2. Summary of brightness results obtained with the 12.7-cm-diam cathode.

Date	Beam energy (MeV)	Beam current (kA)	βγ	I_2 (A)	I_3 (A)	δ	J [10^9 A/(rad-m)^2]
1/17/89	2.74	1.48	6.28	322	9.7	0.366	5.0
1/20/89	2.22	2.0	5.24	33.0	5.6	0.581	2.6
1/27/89	2.14	1.52	5.09	17	10.2	0.540	5.5
1/27/89	2.14	1.52	5.09	17	9.4	0.554	4.9
1/27/89	2.31	1.72	5.43	22	4.5	0.690	1.7
1/31/89	2.05	1.14	5.11	79	4.6	0.446	3.2

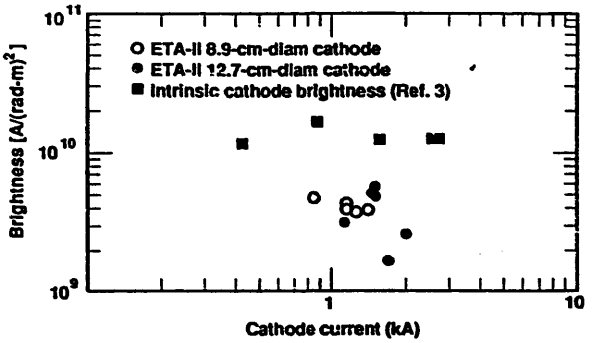

Figure 5. Brightness vs accelerator current.

1 μm. Referring to Fig. 5 the measured ETA-II brightness is about a factor of 3 less than the brightness measured for a dispenser cathode in simple plane geometry without beam extraction. The code calculations suggest that some degradation of brightness occurs in the extraction region because of nonlinear forces on the electron beam as it enters the anode pipe. However the code also predicts brightness about a factor of 2 higher than that experimentally observed. Perhaps some of this discrepancy can be explained by the fact that our measurement can be viewed as a lower bound due to several effects: first, the space charge correction itself is a lower bound; second, it is possible that we have not found the best accelerator conditions for transporting the beam through the two apertures of the collimator; and, finally, the results may be limited by energy sweep of the beam across the collimator, which often results in rather narrow-peaked signals being recorded.

References

1. D.S. Prono, et al., "Engineering Aspects and Initial Performance of ETAII," in *Proc. Beams '88—7th Int'l Conf. High Power Particle Beams*, Karlsruhe, Germany, July 4–8, 1988, Vol. 1, p. 214.
2. J.C. Clark, et al., "Design and Initial Operation of the ETAII Induction Accelerator," in *Proc. Linac 88 Linear Accelerator Conf.*, Williamsburg, VA, October 2–7, 1988; also published as LLNL report UCRL-99201.
3. W.C. Turner, et al., "High-Brightness, High-Current Density Cathode for Induction Linac FELs," in *Proc. Linac 88 Linear Accelerator Conf.*, Williamsburg, VA, Oct. 2–7, 1988; also published as LLNL report UCRL-99042.
4. J.K. Boyd, et al., *IEEE Trans. Nuc. Sci.* NS-32 (5), Oct., 1985, p. 2602.
5. C. Lejeune and J. Aubert, in Applied Charged Particle Optics, A. Septier, Ed. (Academic Press, New York, 1980), Part A, 159–259.
6. G.J. Caporaso, *The Effects of Space Charge on the Acceptance of Brightness Measuring Devices*, LLNL report UCID-20527 (1985).

LOW EMITTANCE IMMERSED AND NON-IMMERSED FOILLESS DIODES FOR HIGH CURRENT ELECTRON LINACS*

M. G. Mazarakis, J. W. Poukey, S. L. Shope, D. E. Hasti,
D. L. Smith, M. D. Haworth+, C. A. Frost,
G. T. Leifeste and J. S. Wagner
Sandia National Laboratories, Albuquerque, NM 87185
+Science Applications International Corporation, Albuquerque, NM 87106

ABSTRACT

A low emittance immersed foilless diode injector was designed and built for the upgraded RADLAC-II accelerator. The design is for a 5-MV, 40-kA annular beam with a 9-cm outer radius. A conical cathode field shaper eliminates the previously observed large cathode shank losses. The non-immersed foilless diode approach was utilized in the design of the Sandia recirculating linear accelerator (RLA) injector. A low energy design (~1.7 MV) and high energy (4 MV) design were carried out in conjunction with a solenoidal vacuum beam transport and injection system.

INTRODUCTION

Foilless diode electron sources are the most appropriate for very high current, high energy linear accelerator. They produce well defined 10 - 100-kA beams that can be easily transported and further accelerated through the post-accelerating gaps of the device. The beam transport can be accomplished either with magnetic lenses and solenoids or with ionized plasma channels operating in the Ion Focusing Regime (IFR).[1]

We have investigated two types of foilless diodes: a magnetically immersed and a non-immersed configuration. The non-immersed diodes are ideally fit for the lower end of the beam current range of interest. Both approaches can produce very low temperature beams with transverse velocities of the order of $\beta_\perp = 0.05$. The immersed diodes are preferred for applications where the beam either does not exit the solenoidal magnetic field such as free electron lasers, x-ray production devices, microwave generators, etc., or is extracted from the accelerator after it has acquired high energies (~20 MV). The reason is that these diodes produce beams with considerable canonical angular momentum (P_θ) which spin quite fast once out of the magnetic field in which they were generated. Consequently, after extraction, an additional term is quadratically added to the transverse velocity equal to the angular velocity v_θ. The non-immersed foilless diode does not have the canonical angular momentum limitations; however, because of space charge in the A-K gap region, it cannot produce larger than 20-kA laminar beams with reasonable size radia (5-10 cm). The beam in the RADLAC-II[2] accelerator is magnetically transported and accelerated up to 20 MV before being extracted from the 20-KG solenoidal magnetic field. On the other hand, in our Recirculating Linear Accelerator (RLA)[1] the beam is extracted from the diode injector at energies between 1.5 - 4 MV and is then injected into a closed geometry racetrack-shaped beam containment vessel similar to a conventional "storage ring." There the beam is recirculated many times through the post-accelerating gaps with the aid of a non-magnetic IFR transport channel. Hence, for the RADLAC-II accelerator, we selected an immersed foilless diode while for the RLA, the non-immersed diode appears to be a more appropriate choice.

In this paper, we report a new immersed foilless diode for the upgraded RADLAC-II[3] accelerator and a non-immersed foilless diode injector for the Sandia Recirculating Linac.

The New RADLAC-II Foilless Diode Injector Design

Figure 1 shows the RADLAC-II injector cavity where the foilless diode and both the cathode and anode field shapers are located. The beam current is monitored by a Rogowski coil located 1.4-m downstream from the A-K gap of the foilless diode. The total current emitted by the cathode shank and by the cathode field shaper (Fig. 1) is measured by a larger Rogowski monitor surrounding the base of the field shaper inside the injector cavity.

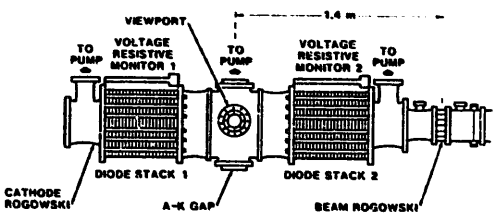

Fig. 1. RADLAC-II injector cavity.

A conical design was chosen for the new cathode field shaper which starts at the cathode end plate with a 10-cm diameter cylinder and tapers off smoothly at the cathode tip. The half angle of the cone is 4° and the radius of the conical surface as a function of the distance from cathode end plate is such that it can provide magnetic insulation against radial emission all along its length. The magnetic field at the A-K gap is 20 kG.

Some radial losses occur in a region where the magnetic insulation would be expected to fail if there were not a self-magnetic field B_θ. On the anode side of the region, magnetic insulation is obtained due to the guiding magnetic field B_z. Figure 2 shows the equipotential surfaces for the conical injector as

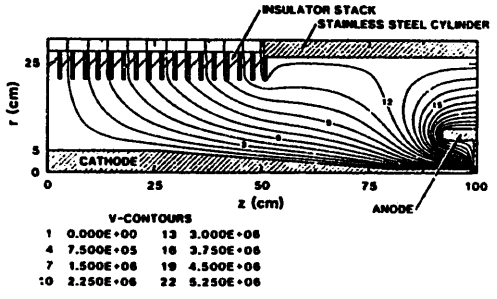

Fig. 2. Equipotential plot for the new conical field shaper.

*This work was supported by the U.S. Department of Energy under contract number DE-AC04-76DP00789, by DARPA/AFWL under Project Order AFWL86-154, and by the U.S. Navy SPAWAR under Space Task 145-SNL-1-9-1.

obtained by the JASON[4] code, and Figure 3 gives the electron map for the new injector geometry. A new version of MAGIC[5] which includes subroutines allowing space-charge limited emission from slanted conducting surfaces was utilized for these simulations. The shank current losses are 7.5%.

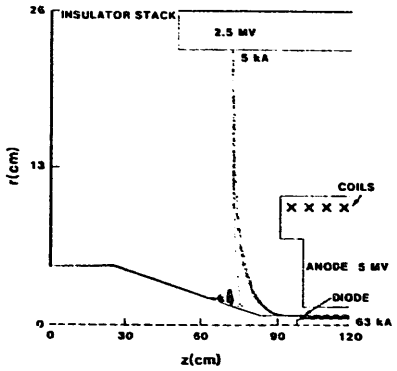

Fig. 3. Electron map for the new injector. The applied voltage to the A-K gap is 4.75 MV. All electron losses occur radially and account only for 5 kA of the 68 kA total shank current.

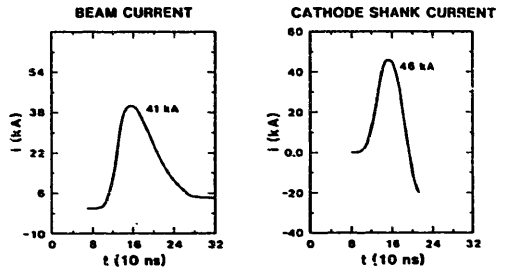

Fig. 4. Total shank and beam current for a 4.1-MV injector voltage. The shank current losses (=shank current minus beam current) are less than 11%.

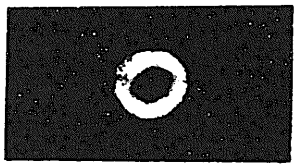

Fig. 5. Time-integrated pinhole photograph of the beam from the new injector. The slight ellipticity is due to a small parallax between the beam and camera axis.

The experimental results indicate good agreement between numerical simulation and measurements. The measured cathode shank current losses are only 5-11%. Beam currents range from 35 kA at 3.6 MV to 41 kA at 4.1 MV (Fig. 4). The cathode shank current for those shots was 37 kA and 45 kA. As shown by the time-integrated x-ray pinhole photograph (Fig. 5), the beam halo is eliminated and the beam is annular without any appreciable filling-in. From Figure 5, we estimate[6] a $\beta_\perp$=0.10.

The superior beam quality produced by the injector has been further verified in the most recent experiments[7]. A very well defined ~40 kA annular beam was generated and transported through the first half of the upgraded RADLAC-II accelerator structure (=5 m downstream from the cathode tip) without any losses or beam quality deterioration. Actually the measured $\beta_\perp$ after the beam had been accelerated by the first two post-accelerating gaps was smaller than that at the injection point and of the order of $\beta_\perp$ =0.08.

The RLA Non-Immersed Foilless Diode Injector and Beam Transport System

The present RLA configuration consists of a 1.7-MV isolated Blumlein injector[1] and one post-accelerating cavity with the accelerating gap located inside the IFR channel. The electron diode of the injector is outside the racetrack and ~1.5 m away. The beam cannot be transported from the injector to the racetrack with a straight IFR channel formed by the same low electron beam (LEEB) ionizing technique as the one utilized for the racetrack IFR. The solenoids of the two IFR channels would not be compatible at the intersection point. The foilless diode design presented here produces a very cold beam which can be magnetically transported into the injection area through a vacuum line with minimum beam temperature increase.

The diode design presented here incorporates the advantages of both a planar and an immersed foilless diode. It produces a fairly parallel laminar beam with small divergence as in the case of the planar diode (Fig. 6). The pinching effect of the anode foil is eliminated along with the canonical angular momentum term of an immersed foilless diode.

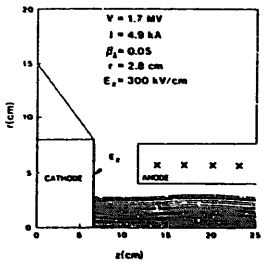

Fig. 6. Non-immersed foilless diodes can produce very cold beams.

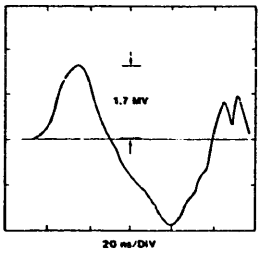

Fig. 7. Injector voltage as measured along the diode stack.

Close to the anode electrode, the beam encounters the magnetic field region of the transport system. The cathode is at zero magnetic field. The electric field at the cathode is kept as low as possible and at a right angle to the cathode surface (E_r = 0). The electron emission region is specified by an area covered with felt which starts undergoing explosive electron emission at as low an electric field as 60 kV/cm. The current density for these configurations scales as

$$j = \frac{3.52\times10^{3}}{d^{2}}\left[\gamma^{2/3} - 1\right]^{3/2} \qquad (1)$$

where $\gamma = eV/mc^2 + 1$. The A-K gap (d) is selected depending on the beam radius and total current required for each diode voltage.

In designing these diodes, we select first the approximate A-K gap and define the emitting area according to the scaling formula (1). Then we define

the shape of the electrodes using the JASON code.[4] Finally, we use the code TRAJ[8] to study the beam production and to design the magnetic transport system. Much care is taken in designing the cathode surfaces to avoid electric fields in excess of 200 kV/cm. However, since the voltage of the present injector is bi-polar (Fig. 7), attention is given to reducing the field on the anode electrode. Figure 8 is a design of the 1.7-MV diode with both cathode and anode electrode shapes optimized. Figure 9 shows the electron trajectories for the 1.7-MV case. Figure 10 shows the magnetic field on axis generated by two solenoids and three focusing coils. It must be close to zero not only at the emitting surface of the cathode but also at the injection point in order to prevent any interference with IFR channel. Figure 11 presents a 4-MV, 10-kA design for our new RLA injector.

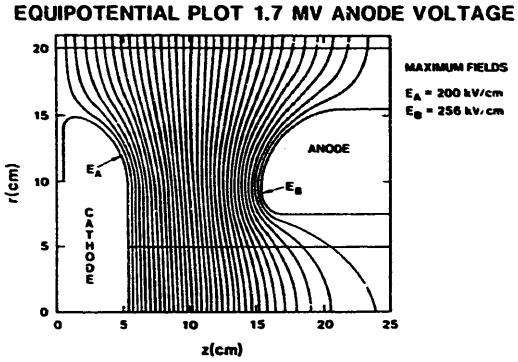

Fig. 8. Both the anode and cathode surface shapes are optimized for minimum electric field stresses.

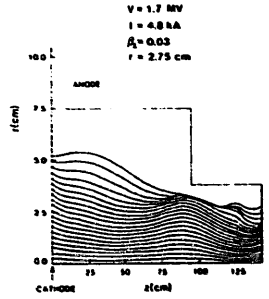

Fig. 9. Electron trajectories. The quoted transverse velocity and radius are at the exit foil (located at z=146 cm).

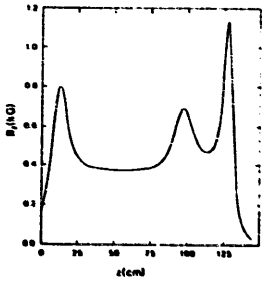

Fig. 10. The magnetic field B_z on axis.

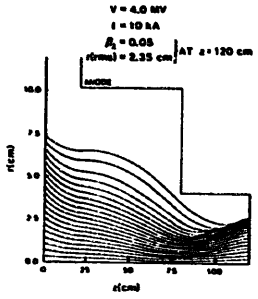

Fig. 11. Electron trajectories for a 4-MV beam.

CONCLUSIONS

A new immersed and a non-immersed foilless diode injector has been recently designed and constructed respectively for the upgraded RADLAC II and the Recirculating Linear Accelerator (RLA). Creedon's model formalism[9], the JASON code and the new version of MAGIC PIC code that includes the slant geometry package was extensively utilized for the immersed diode injector design. The design of the non-immersed diode and beam transport system is simpler, and only the JASON and the trajectory code TRAJ were necessary to simulate this diode.

The new RADLAC-II injector has been installed and very successfully operated. It met and in many instances exceeded all of our design goals. The previously observed excessive electron losses have been eliminated. The total measured shank current is only 5-10% higher than the 40-kA beam current. A high quality annular beam was generated with a $\beta_\perp$ of 0.1 and normalized emittance equal to 0.8 rad-cm. This beam was injected into the RADLAC-II beam line and further accelerated by the first two post-accelerating gaps without losses or emittance increase.

The non-immersed foilless diode injector will be installed in our RLA and experimentally validated in a few weeks. We expect it to produce a very low temperature and emittance electron beam which will be transported in a vacuum beam pipe with no losses and minimum quality degradation. The elimination of the anode foils and of the previously utilized gas cell, wire zones and classical IFR, makes this injector attractive.

REFERENCES

1. S. L. Shope, et al., "Acceleration and Bending of a Relativistic Electron Beam on the Sandia Recirculating Linac," Proc. IEEE Part. Accel. Conf., Washington, DC, March 1987, CH2387-9/87/0000-0908.
2. M. G. Mazarakis, et al., "RADLAC Accelerator Beam Experiments," Proc. of the IEEE Part. Accel. Conf., Washington, DC, March 16-19, 1987, CH2387-9/87/0000-0908.
3. S. L. Shope, et al., "The Upgraded RADLAC-II Accelerator," Proc. of the 1988 Linear Accel. Conf., Williamsburg, VA, October 3-7, 1988, to be published.
4. S. J. Sackett, "JASON-A Code for Solving General Electrostatics Problems User's Manual," LLL Report UCID-17814. Revised by M. L. Kiefer, Sandia National Laboratories, Albuquerque, NM (1984).
5. B. Goplen, et al., "Users Manual for MAGIC/Version-Sept. 1983, MRC/WDC-R/068," Mission Research Corp., Washington, DC, (1983)
6. D. E. Hasti, et al., "RADLAC-II Upgrade Injector Experiments," SNLA SAND88-1032, Albuquerque, NM (1988).
7. S. L. Shope, et al., "RADLAC-II Upgrade Experiments," this Conference.
8. J. W. Poukey, "Trajectory vs. PIC Methods on Diode Design," Proc. of 12th Conf. on Numerical Simulations of Plasma, San Francisco, CA, (9/87).
9. J. M. Creedon, J. Appl. Phys. 48(3), 1070 (1977).

RADLAC-II UPGRADE EXPERIMENTS

S. L. Shope, C. A. Frost, D. E. Hasti, G. T. Leifeste,
M. G. Mazarakis, J. W. Poukey, and D. L. Smith
Sandia National Laboratories
Albuquerque, New Mexico 87185

Abstract

The linear induction accelerator, RADLAC II, is being upgraded to produce a 20-MeV, 40-kA, annular electron beam. Prior to the upgrade, RADLAC II produced a 15-MeV, 15-kA electron beam. Modifications to the pulsed power, injector, and magnetic transport have resulted in a faster rising flat-topped voltage pulse. A high quality, 40-kA, 2.0-cm diameter beam with a low perpendicular thermal velocity, $\beta_\perp c$, has been produced from the injector, $\beta_\perp < 0.2$. The high quality beam has been accelerated through two accelerating gaps. The final four accelerating stages are being added to RADLAC II and transport experiments through the full accelerator are beginning. Simulations show the beam quality will be maintained through the entire accelerator.

Introduction

RADLAC II is a pulsed, high gradient linear induction accelerator. The electron beam is produced in a 5-MeV injector and transported in a 20-kG magnetic guide field through six, 2.5 MeV accelerating gaps that were designed to minimize beam instabilities.[1] The performance of the accelerator has been improved by straight-forward changes to the pulsed power and modifications to the injector.[2,3] The upgrade was performed in three steps. The first step was installation of the modified pulsed power feeding the injector, the second was adding two accelerating stages, and finally, we are going to the full accelerator.

Pulse Power Modifications

In the final upgraded accelerator, four Marx generators rather than two, will be used to drive four Hermes-III intermediate storage capacitors (ISC).[4] The oil-water interfaces were relocated to provide symmetrical, low inductance feeds (Fig. 1). Each ISC charges two pairs of pulse-forming lines (PFL) through low inductance, low jitter, laser-triggered gas switches developed for PBFA II.[5] The PFLs were lengthened to increase the pulse width from 40 to 50 ns. The improved geometry and electrical properties of the new pulsed power configuration provide for faster charging times and enables two self-breaking water switches per line to close, rather than one, resulting in a flat-topped voltage pulse at the diodes. Figure 2 is a comparison of the old and new diode voltage waveforms.

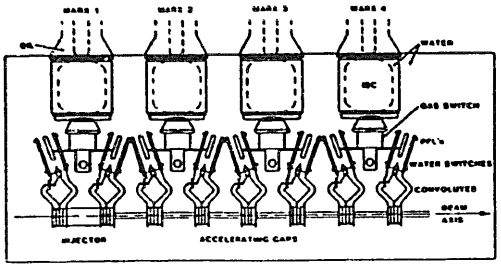

Figure 1. Diagram of the upgraded accelerator showing component layout.

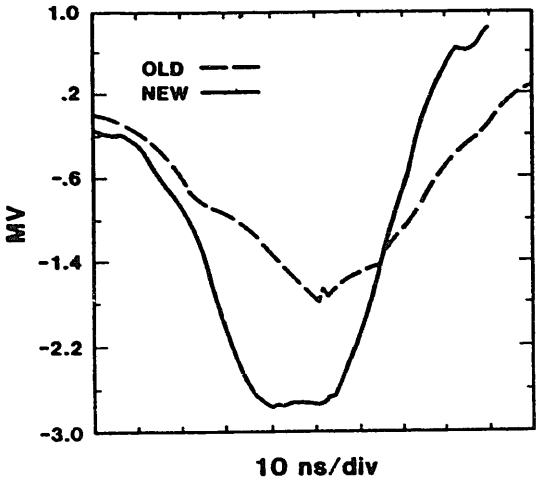

Figure 2. Comparison of the old and new diode waveforms. The Marx charge in both cases was 85 kV.

Injector Experiments

Before the upgrade the RADLAC-II injector produced a 3-MeV, 15-kA, 40-ns electron beam. Time integrated x-ray pinhole photographs of the old injector showed the beam was large and had a halo that was approximately the same diameter as the drift tube, Figure 3(a). Particle simulations for this geometry indicated there was a large loss of shank current (60%) due to the loss of magnetic insulation on the cathode

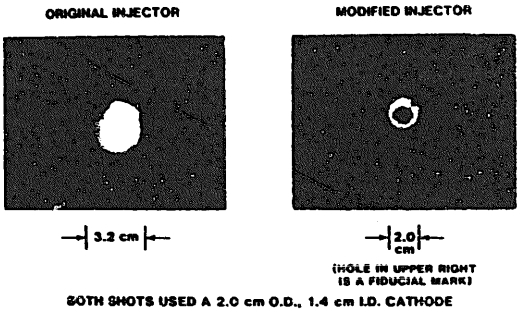

Figure 3. Comparison of x-ray pinhole photographs from the old injector (3a.) and the new injector (3b.)

shank. There was also electron emission from the face of the cathode holder allowing electrons to fill the drift pipe. Nonuniformities of 40% in the magnetic guide field also contributed to the poor beam quality. These coils were replaced by new magnets that produced fields with variations of only 15%.

The cathode shank was redesigned to reduce spurious electron emission and maintain magnetic insulation to minimize electron losses.[3] The modified injector and

CH2669-0/89/0000-1005$01.00©1989 IEEE

the improved magnetic field produced a 2-cm diameter, 5.3-MeV, 47-kA annular beam. Figure 3(b) is a pinhole photograph of a beam produced by the new injector. The $\beta_\perp$ for this beam was 0.16. The maximum perpendicular velocity can be calculated directly from measurements of a time-integrated, x-ray pinhole photograph. The measured annulus width is a function of the cathode dimensions, the applied magnetic field, the beam energy and camera geometry. There are known quantities and can be used to calculate $\beta_\perp$ from Larmor radius effects.[6] Typical measured values for $\beta_\perp$ ranged from 0.1 to 0.19 and agreed with the values obtained from particle simulations.

The measured injector currents are consistent with the space charge limited currents predicted by analytic theory. The space charge limited current is given by:[7]

$$I_{ANAL} = (1-0.3L^*)(\gamma^{2/3}-1)^{3/2}(17\ kA)\ \frac{r_b}{\delta}\ [Ln\ \frac{8\delta}{a}\ ]^{-1}$$

$$\gamma = \frac{V(MV)}{.511} + 1,\ L^* = \text{Dimensionless number equal to the anode-cathode gap in cm}$$

$$r_b = \frac{r_1 + r_2}{2},\ \delta = R - r_2,\ a = r_2 - r_1$$

For the RADLAC injector, $r_1 = 0.7$ cm, $r_2 = 1.0$ cm, $R = 1.6$ cm, and $L^* = 1.0$ cm. A comparison of the predicted current and measured current along with our geometry is shown in Figure 4.

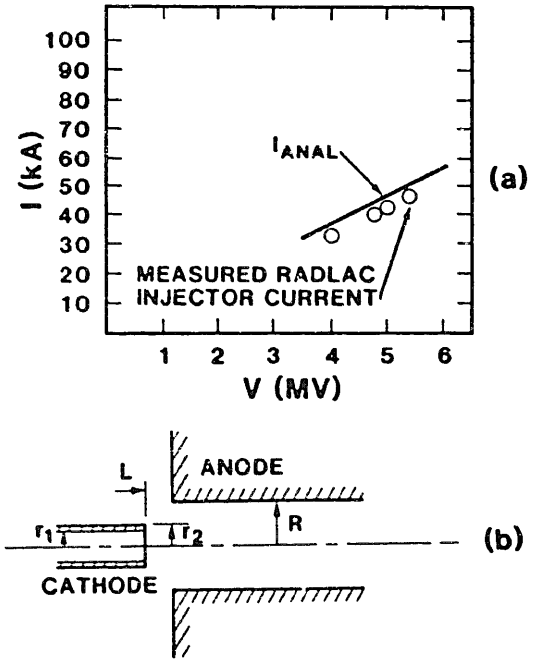

Figure 4. Comparison of analytical and experimental currents is shown in part a. The geometry is shown in part b.

Acceleration Experiments

The next phase of the experiment was to accelerate the beam through one accelerating gap. Hollow electron beams with energies of 3.5 to 4.2 MeV and beam currents of 25-35 kA were produced in the injector and accelerated to final energies of 5.6 to 6.3 MeV. The pinhole photographs indicated there was some expansion of the beam and some thickening of the annulus. The final $\beta_\perp$ for these beams was 0.08-0.12. Figure 5 shows a pinhole photograph of one of the accelerated beams.

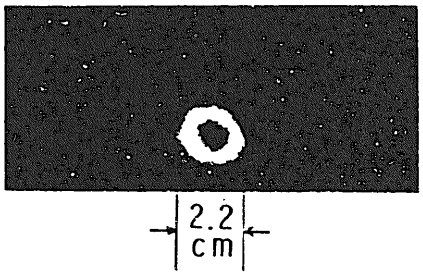

Figure 5. Pinhole photograph of beam after acceleration through one gap.

The beam was then accelerated through two accelerating gaps resulting in final energies of 7.3 to 8.3 MeV and currents of 27 to 36 kA. A pinhole photograph for one of these shots is shown in Figure 6. The final $\beta_\perp$ for these beams was 0.09 to 0.12. Again, these values are consistent with particle simulations.

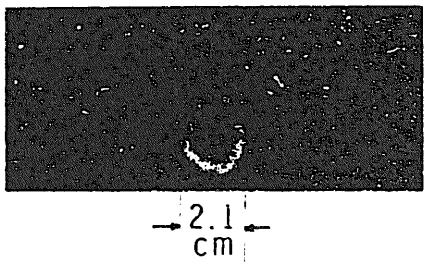

Figure 6. Pinhole photograph of beam after acceleration through two gaps.

The full accelerator has now been installed and experiments have begun. The final accelerator will produce a higher current, higher energy, better quality beam. Table I shows the comparison between the old beam parameters and the predicted parameters for the upgraded accelerator, based on the experimental results.

Table I
Comparison of RADLAC-II Beam Parameters

Parameter	Before Upgrade	After Upgrade
Energy ($(\gamma-1)mc^2$)	14 MeV (1.75 MV/stage)	20 MeV (2.5 MV/stage)
Current (I)	18 kA	42 kA
Beam Radius (r)	1.4 cm	0.9 cm
Perpendicular Thermal Velocity ($\beta_\perp c$)	0.16 c	0.05 c
Normalized Emittance Including Rotation (ϵ_n)	7.5 rad-cm	5.9 rad-cm
Brightness (B_n)	33 A/(rad-cm)^2	123 A/(rad-cm)^2

Parameters from before the upgrade are based on measured output from the accelerator. Parameters for the upgraded beam are based on particle code predictions of accelerator performance using measured input beam parameters from the first step injector experiments. The normalized emittance, ϵ_n, is defined as[8]

$$\epsilon_n = \sqrt{(\gamma r \beta_\perp)^2 + (P_\theta/c)^2} ,$$

$$\text{where } (P_\theta/c) = \frac{1}{2}\frac{1}{mc^2} r_k^2 B_k$$

In the accelerator magnetic guide field, r_k and B_k are the cathode radius and magnetic guide field at the cathode, and $(P_\theta/c) = r\gamma\beta_\theta$ after extraction from the magnetic guide field. The brightness is defined as[9]

$$B_n = \frac{I}{(\pi\epsilon_n)^2} .$$

Conclusions

We have improved the performance of the RADLAC-II accelerator. An injector has been developed that produces a high voltage, high current, high quality annular beam. The beam has been accelerated stably through two accelerating gaps. Simulations and experiments indicate the full accelerator will produce a 20-MeV, 40-kA annular beam with a $\beta_\perp < 0.2$.

Acknowledgements

The authors would like to thank the RADLAC-II technicians: Dennis Bolton, Tom Coffman, Janet Finch, Mike Harden, and Chip Olson. Their efforts have contributed to the success of the experiments. This work was funded by the DOE under contract DE-AC04-76DP00789, DARPA/AFWL under ARPA Order 5789, and DARPA/NSWC under ARPA Order 4395.

References

[1] S. L. Shope, et al., "The Design of the Accelerating Gaps for the Linear Induction Accelerator RADLAC-II," Proc. 1987 IEEE Particle Accelerator Conf., Washington, DC, March 16-19, 1987, p. 978.

[2] D. L. Smith, et al., Sandia Report SAND88-1158, Sandia National Laboratories, Albuquerque, NM, June 1988.

[3] M. G. Mazarakis, et al., "Low Emittance Immersed and Non-Immersed Foilless Diodes for High Current Electron Linacs," Paper M 26 this conference.

[4] J. J. Ramirez, et al., "The Hermes III Program," Proc. of the Sixth IEEE Pulsed Power Conference, Arlington, VA, IEEE Cat. NO. 87CH2522-1, June 1987, p. 294.

[5] D. R. Humphreys, et al., "RIMFIRE, A Six Megavolt Laser-Triggered Gas-Filled Switch for PBFA II," Proc. Fifth IEEE Pulsed Power Conf., Arlington, VA, IEEE Cat. NO. 85C2121-2, June 1985, p. 262.

[6] D. E. Hasti, et al., "RADLAC-II Upgrade Injector Experiments," Sandia National Laboratories Report, SAND88-1032-UC-28, May 1988.

[7] E. Ott, T. M. Antonsen, Jr., and R. V. Lovelace, Phys. Fluids, 20, 1180 (1977).

[8] E. P. Lee and R. K. Cooper, Particle Accelerator, 7, 83, 1976.

[9] T. C. Marshall, Free Electron Lasers, MacMillan Publishing Company, New York, 1985, p. 103.

OPTIMIZATION OF PULSE QUALITY FOR A LINEAR INDUCTION ACCELERATOR

S. Eckhouse and M. Markovits

Maxwell Laboratories, Inc.
8888 Balboa Avenue
San Diego, CA 92123

Abstract

Maxwell Laboratories, Inc. has undertaken an effort to develop and optimize Linear Induction Accelerator (LIA) cells and drivers for these cells. Major emphasis was given to improved pulse quality properties regarding the flatness of the accelerating voltage waveshape. As part of this effort, a LIA test stand was designed, constructed, and tested. This paper presents the major design considerations, description of the test stand, results of circuit modeling the LIA cell and its driving pulse power system, and results of testing this LIA system. The measured pulse waveshapes of the tested Linear Induction Accelerator cell are in good agreement with the numerical circuit modeling, and they exhibit a very high degree of flatness, ±0.4% for 65 ns pulsewidth and ±1.2% for 80 ns pulsewidth, for optimal switching conditions. Additional tests underway are described.

Introduction

Induction Linear Accelerators have the capability of accelerating multi kiloamp electron beams to energies of tens of MEVs. Such electron beams find important applications as potential drivers for high power Free Electron Lasers and as sources for deep penetration flash x-ray radiography. Most Linear Induction Accelerator (LIA) applications require a high brightness beam and a small electron energy spread in the beam. In a LIA, the energy spread of the electron beam is mostly controlled by the pulse power source driving the cells of the LIA. The energy variation of the electrons in the beam is directly proportional to the voltage variation in the accelerating pulse sensed by the beam. Other effects, such as space charge or timing errors, may also contribute to the energy flatness, but it is clear that a poor high voltage pulse quality in each accelerating cell will result in a large value of energy spread of the accelerated electron beam. Maxwell Laboratories has undertaken an effort to develop and optimize LIA cells and pulse power drivers for these cells, with improved pulse quality properties. As part of this effort, a LIA test stand was designed, constructed, and tested.

The Test Stand

The test stand includes a pulse power source that uses a Blumlein pulse forming line and an induction accelerating cell. The cell can be loaded with different types of magnetic materials to investigate the interaction between the cell and the pulse power system.

The pulse power system for the LIA test stand is composed of 10Ω (2 x 5Ω), 100 ns water Blumlein pulse forming line (PFL) that is charged up by a fast 4 stage standard Maxwell Porta-Marx. The Blumlein is switched by a coaxial midplane, low inductance, precision triggered switch that is directly interfaced to the Blumlein PFL. The Blumlein PFL is connected to the cell using two short (3 nsec), parallel rigid 20Ω oil transmission lines that are connected to two HV connector points on the LIA cell. The cell has four identical HV connections. Two of them are used for cable connections, and two for compensating resistors that load the pulse power source in parallel with the cell. The Blumlein, the rigid coaxial lines, and the four HV connectors on the cell are shown in Figure 1. Great care has been taken in the design and construction of the pulse power system and its interface to the induction cell to minimize any pulse distortion effects that may arise as a result of the pulse power system or its cell interface. The main rationale for this "clean" pulse power system design was to try and separate between pulse distortion effects that originate from the pulse power system, from pulse distortion effects that have to do with the induction cell and its magnetic materials. The use of a stiff (10Ω) source to drive

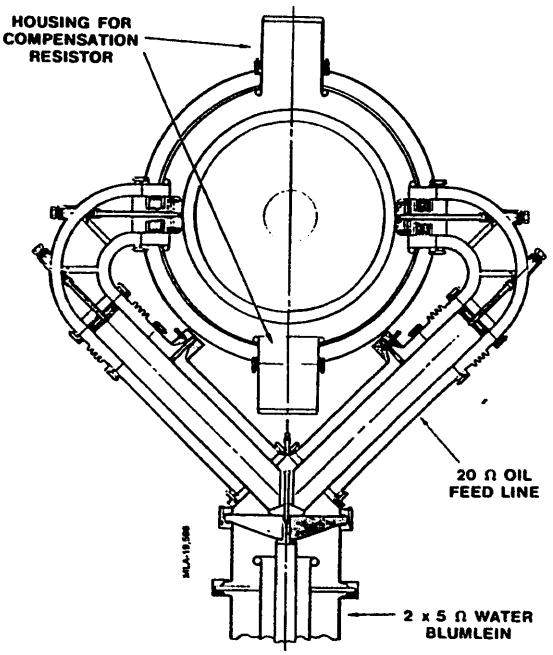

Figure 1. Design of Maxwell Linear Induction Accelerator test stand transmission line.

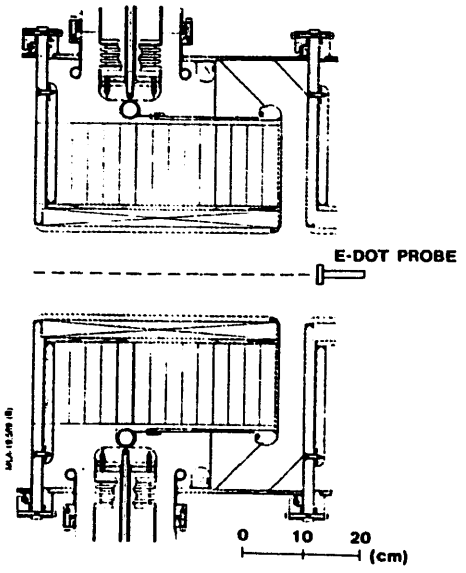

Figure 2. Mechanical layout of test induction cell.

CH2669-0/89/0000-1008$01.00©1989 IEEE

the cell is another significant element in achieving a good HV pulse quality applied to the cell. Such a pulse power source may have limited applications for high repetition rate LIAs where efficiency may be of prime importance, but is an excellent driver for low repetition rate LIAs where the efficiency of the accelerator is not an important issue.

The test induction cell mechanical layout is shown in Figure 2. The space devoted to the magnetic core has an ID of 25 cm , an OD of 50 cm, and a total length of 35 cm. This space can be loaded with a varying number of ferrite cores or Metglass cores. A total axial length of 25 cm in the core volume has a coaxial structure that may behave as a coaxial transmission line loaded with the magnetic material that is tested in the cell. A length of 10 cm does not have this "perfect" coaxial structure. Thus, by comparing the cell electrical behavior with magnetic cores located in these two axial locations, a better understanding of the importance of this type of cell design can be achieved.

The cell uses a radial HV insulator that separates the oil insulated volume of the cell from the evacuated region. The cell and insulator were optimized for minimum HV stresses on the insulator. The cell is also equipped with a water cooled DC focusing solenoid that is part of the cell structure. Great care has been taken in keeping very tight mechanical tolerances in the cell design, in particular in control of the cell axis, the magnetic axis, and the accelerating gap. The cell is constructed in such a way that mechanical control of the cell axis can be achieved without opening the cell or disturbing the accelerator structure when such a cell is integrated into a full LIA structure. The cell can also be conveniently disassembled to facilitate change of magnetic materials for varying test conditions.

Numerical Circuit Modeling

The cell and its driving pulse power system were modeled using Maxwell's MAX-CAP, a simple circuit code, and a Maxwell circuit code equipped with a magnetic material model capability. A simple equivalent electrical circuit model of the cell and its pulse power driver are shown in Figure 3. This simple model models the cell as a lumped constant inductance in parallel with the cell (gap and oil) capacitor and the compensating resistor. The result of the calculated cell voltage signal using this simple model for different switching times of the Blumlein switch are shown in Figure 4. The inductance of the module is based on the use of 14 TDK PE11B ferrites with 25 mm thickness, 50 cm OD, and 25 cm ID. The 35 μH inductance was calculated assuming a constant magnetic permeability of 500 through the full length of the pulse. As can be seen in Figure 4, the flatness of the pulse depends to a large extent on the switching time of the Blumlein switch. By choosing this time, one can achieve a flat pulse, a positive slope pulse, or a negative slope pulse. A more realistic cell electrical model that takes into account wave effects, was also investigated. For the operating conditions of the cell and pulse power system described in this paper, wave effects do not play a very significant role, judging from the experimental pulse quality that is measured on the cell, as presentedbelow.

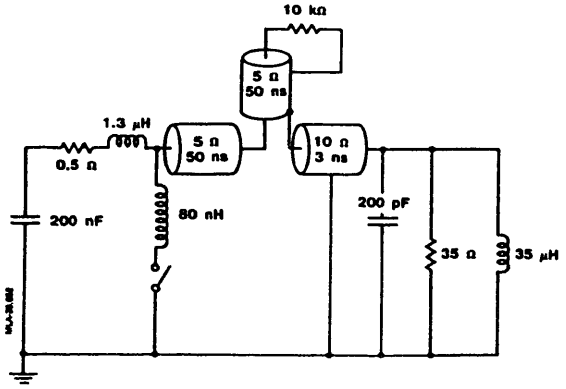

Figure 3. Equivalent circuit of induction cell and its pulse power driver.

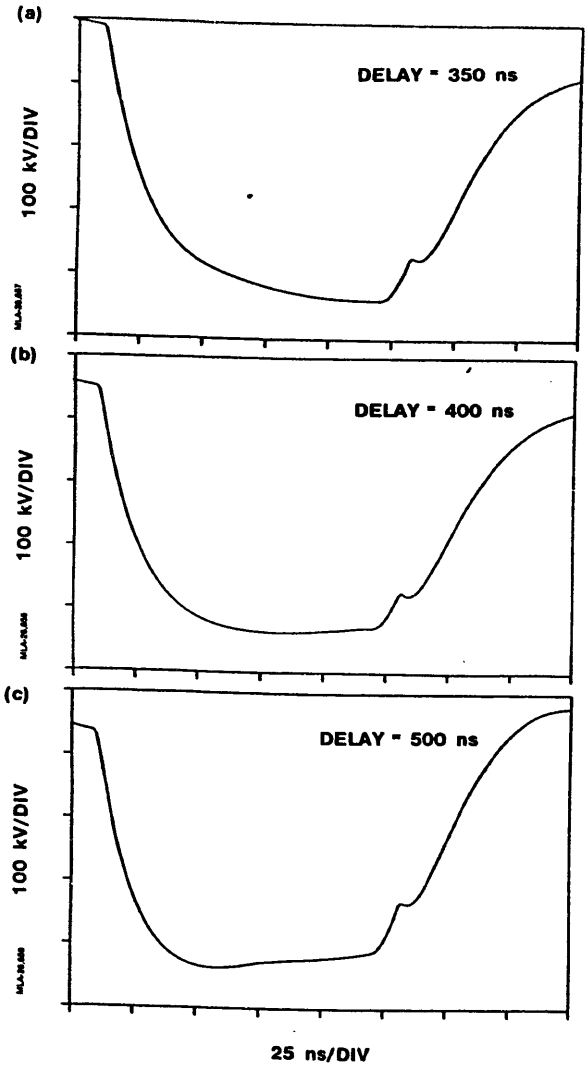

Figure 4. Induction linac module accelerating voltage waveshape simulation for different delay times of the Blumlein switching with respect to the Marx generator erection: (a) 350 ns, (b) 400 ns, and (c) 500 ns.

Measurements Results

For the purpose of diagnosing the pulse propagation into the cell, the cell was equipped with E-dot and B-dot probes that measure local voltages and currents as they propagate into the cell. These probes include a current and voltage measurement probe at the feed to the cell, a current measurement probe that measures the current into the load resistor, and an E-dot probe that measures the induced accelerating electric field at the accelerating gap. This last probe is the most critical one from the point of view of measuring the performance of the induction cell, since it measures the real accelerating voltage that is sensed by electrons when they enter into the accelerating gap. This probe was constructed by wrapping an insulated copper sheet on a rigid coaxial cable that was pushed (see Figure 2) through the drift tube into the gap region. This probe measures the voltage at the center of the accelerating gap.

Figure 5 shows voltage traces as measured by this probe for different triggering times on the Blumlein main switch. As can be seen in Figure 5, the best operating conditions with the "most flat" voltage pulse are achieved for a delay of 410 nsec in the firing time of the main switch with respect to the erection of the Marx generator. This value agrees very well with the value calculated in the numerical circuit modeling. The flatness of the measured pulse is ±0.4% for 65 ns pulsewidth, and ±1.2% for 80 ns pulsewidth. A typical current waveshape measured on one of the ballast resistors is shown in Figure 6, together with the E-dot waveshape as recorded

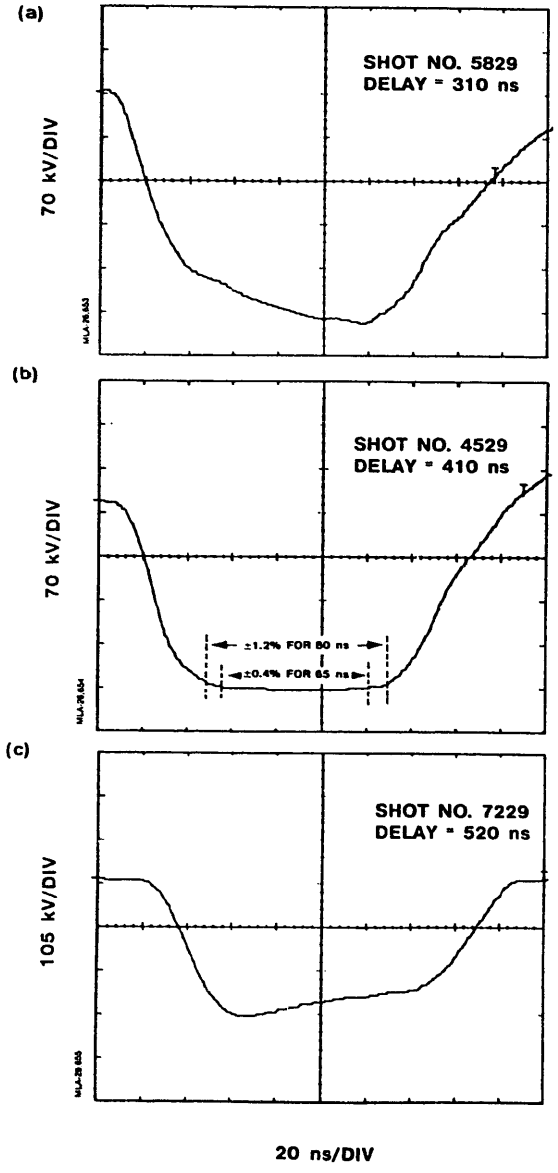

Figure 5. Induction linac module measured accelerating gap voltage waveshapes for different triggering times of the Blumlein switch: (a) 310 ns, (b) 410 ns, and (c) 520 ns.

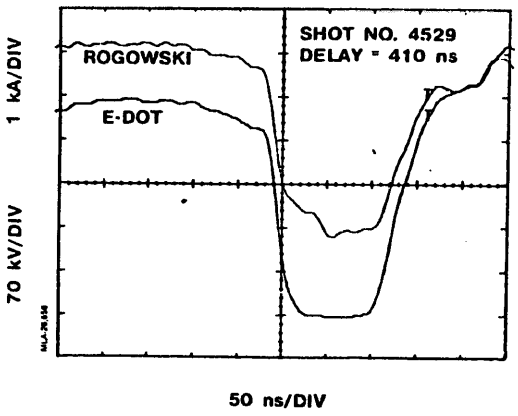

Figure 6. Comparison of compensating resistor current waveshape Rogowski probe measurement to E-dot probe voltage waveshape measurement at the induction cell accelerating gap.

for the same shot as the one shown in Figure 5-b. As can be seen in Figure 6, the current through the (water) ballast resistor has an oscillation superimposed on it. This distortion in the current waveshape is a result of the resonant function of the Rogowski coil used to measure the current, as found during calibration of the Rogowski coil with a square pulse. As can be seen from the measurements in Figure 5, the cell behaves as an ideal inductive load, and no wave effects are observed experimentally.

An additional series of measurements is now underway, where the cell is loaded with a smaller number of ferrites distributed in different locations inside the cell to detect any wave effects that may distort the accelerating voltage pulse shape. We are also planning to carry out a similar series of measurements using high quality Metglass cores that were manufactured and wound by Allied Corporation. These measurements will be done under a joint Allied/Maxwell R&D effort to develop LIAs with Metglass cores that will have superior pulse quality with reduced dimensions. [1]

References

[1] S. Eckhouse, E. Chu, and M. Montgomery, Scaling Laws and Optimization of Linear Induction Accelerator, presented at the IEEE Conference on Particle Accelerators, Washington, D. C., March 16-19, 1987.

A 4-MEGAVOLT, 5-KILOAMPERE PULSED-POWER HIGH-BRIGHTNESS ELECTRON BEAM SOURCE*

R. L. Carlson, L. A. Builta, T. J. Kauppila, D. C. Moir, and R. N. Ridlon
Los Alamos National Laboratory
P. O. Box 1663
Los Alamos, New Mexico 87545

T. P. Hughes
Mission Research Corporation
Albuquerque, New Mexico 87106-4245

Abstract

The REX machine at Los Alamos is being used to generate a 4-MV, 5-kA, 50-ns electron beam. The beam is produced by a planar velvet cathode, accelerated through a foilless anode aperture, and transported by an air core magnetic lens. Extensive measurements of the time-resolved (<1 ns) properties of the beam using a streak camera and high speed electronic diagnostics have been made. These parameters include beam current, voltage, current density, and emittance for a single cathode/anode configuration. Results indicate beam brightness in excess of $10^8 A/m^2-rad^2$. Numerical simulations of the experiment have been performed with ISIS, a time-dependent PIC code, and are in good agreement with the measurements. This electron beam source is being considered as an injector to a linear induction accelerator and can be operated at higher voltages and currents as a stand-alone flash x-ray machine.

1. Introduction

The Relativistic Electron-Beam Experiment (REX) machine at LANL is used to generate a 4-MV, 5-kA, 50-ns electron beam. The generation and transport of this beam is being carefully examined for its potential application as an injector for the Dual Axis Radiographic Hydro-Test Facility (DARHT) accelerators. Measurements of the time-resolved electron beam current, voltage, and emittance produced by a velvet cathode are presented in comparison with ISIS particle-in-cell simulations (Ref. 1). The experimental arrangement is discussed in Section 2 and the data and results are presented in Section 3.

2. Experimental Arrangement

The electron source consists of a 76.2-mm diam velvet cathode mounted on a field forming electrode (Fig. 1). The velvet cloth is inset in the surface of the cathode assembly about 1 mm to keep the fiber tips flush with the metal surface. The aluminum field forming electrode, which is coated with glyptal to suppress emission, is flat in the anode region. The anode/cathode (A-K) gap is 147.6 mm and the anode aperture is 152-mm diam. The field forming electrode is centered on a Lucite-radial insulator with embedded aluminum grading rings. The insulator assembly separates the oil-filled pulse forming line (PFL) from the vacuum diode and contains a 125-Ω radial-liquid resistor. The stainless steel vacuum vessel which includes the anode is cryogenically pumped. Typical vacuum in the A-K region is 3×10^{-5} torr.

The magnetic field used for beam extraction is generated by a 1.7-m-i.d. bucking coil centered 145 mm behind the cathode and a 244-mm-long, air-core, solenoid extraction magnet whose center is located 377.0 mm from the cathode. The inside and outside radii of the solenoid are 114 mm and 216 mm, respectively. Figure 2 is a map of the axial magnetic field as a function of axial position (z) and radius (r) about the axis of the machine. The voltage pulse produced by the Marx generator/PFL is routinely measured with capacitive (E-dot) monitors located in the oil-filled transmission line before the radial resistor and in a plane that is midway across the A-K gap on the vacuum side. The voltage monitors have been calibrated by measuring the electron beam energy with a magnetic spectrometer. The current is measured with four symmetrically located, magnetic sense (B-dot) loops. The current is measured before the radial resistor (I-tube), in the vacuum (I-total), at the anode aperture 211 mm from the cathode (I-diode), and at the drift tube 720 mm from the cathode (I-transport). The four symmetric signals from the B-dot loops are summed passively at the machine and transmitted along with the E-dot signals to a screen room using ~ 30 m of RG214. The pulse currents and voltages are integrated with 1-μs time constant 50-Ω integrators recorded on Tektronix 7103 oscilloscopes. The bandwidth of the measurements is limited by cable attenuation at the higher frequencies.

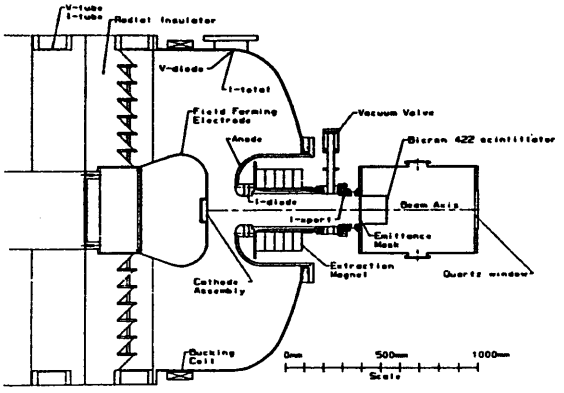

Fig. 1. REX Experimental Hardware.

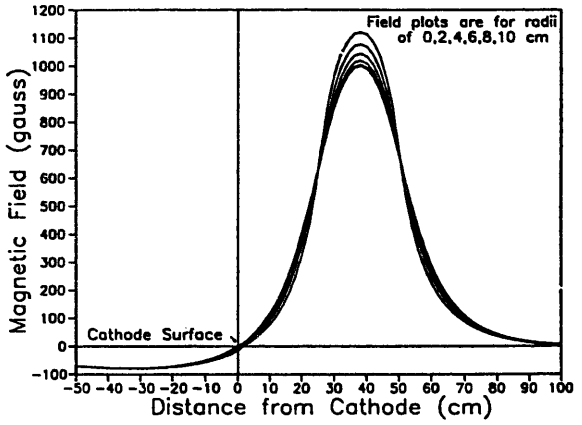

Fig. 2. Magnetic Field Map for Fig. 1.

The emittance of the electron beam is measured by

* Work performed under the auspices of the U.S. Department of Energy.

intercepting the beam with a brass disc (3.2-mm thick, 216-mm diam), which contains a linear array of 17, 1-mm diam holes separated by 10 mm, located vertically along the diameter. The mask is located 817 mm from the cathode. The measurement is made with the electron beam nearly collimated at a diameter of ~ 100 mm. The peak extraction magnet field to produce this beam condition is 850 G. The beam that is transmitted through the holes drifts 204 mm before striking a 0.5-mm-thick strip of Bicron 422 scintillator. Light from the scintillator is imaged onto the photocathode of an IMACON 500 streak camera using a 3.5-inch-diam Questar telescope and two turning mirrors. Typical sweep speed for all of the measurements was 2 ns/mm. Time resolution of the streak camera data was limited by the 1.3-ns FWHM response time of the scintillator. Streak data were recorded on Kodak Royal X-Pan (RXP) film.

3. Data and Results

Oscillograph traces of the voltage (V-tube) and current monitor (I-diode) are shown in Figs. 3a and 3b, respectively. As stated above, the voltage monitor was calibrated using a magnetic spectrometer. The resulting constant is 2.55 ± 0.04 MV/V. The current monitor was inserted in a 50-Ω coaxial pulse line described in Ref. 2 and yielded a calibration constant of 6.05 ± 0.30 kA/V.

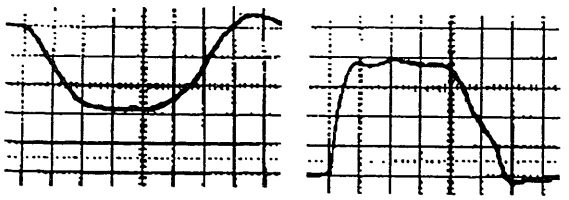

Fig. 3. V-tube and I-diode at 3.8 MV (0.5 V/div) and 4.8 kA (0.2 V/div) Recorded at 10 ns/div.

Figure 4 is a plot of electron beam current versus voltage. Experimental data, obtained by varying the Marx charge voltage, are shown as diamonds with the error bars indicating the current uncertainty. The upper curve with circles is the result of a simulation using the ISIS particle-in-cell code (Ref. 3). Middle and lower curves come from Child-Langmuir (Ref. 4) nonrelativistic planar diode and Jory-Trivelpiece (Ref. 5) relativistic planar diode, respectively. The experimentally measured current is almost twice that expected from a simple planar relativistic diode. Experimental data are in reasonable agreement with ISIS calculations, but are systematically lower.

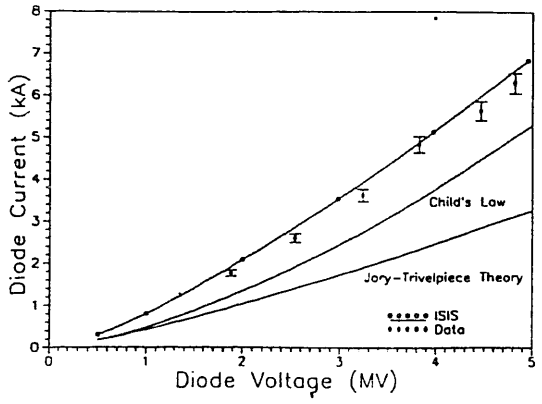

Fig. 4. Beam Current vs Voltage for 76.2-mm-diam Cathode and A-K Gap of 150 mm.

Photographic reproduction of a streak camera emittance measurement is shown in Fig. 5. Time sweep is from left to right and from the start to the end of light is 50 ns, in agreement with electrical measurements. The voltage across the A-K gap is relatively flat across 30 ns of the pulse. The streak record on RXP film is scanned with a 50-μm aperture using a microdensitometer. The subsequent film density is converted to relative light intensity by using the exposure curve obtained for the RXP film with local processing. The analysis is generally performed on the 30-ns flat top of the pulse, where the beam energy variation is ± 1.5%. The data are time averaged over the 30-ns flat top and additionally sampled at the center of the pulse over 1 ns. In either case, the analysis to obtain the emittance is the same. Figure 6 is a plot of relative beam intensity as a function of x obtained from the emittance mask streak record. Each of the distributions represents a sample of the beam that is transmitted through the 1-mm-diam hole in the mask. A beam that is cold (born with no transverse energy) would generate a rectangular distribution 1 mm in diameter. Because of finite temperature, the beams have gaussian distributions. The location of the peaks relative to the mask yields information on beam convergence as well as beam radius. These data are used to produce an x-x' plot, where 90% of the beam is included in the temperature as well as the diameter (Fig. 7).

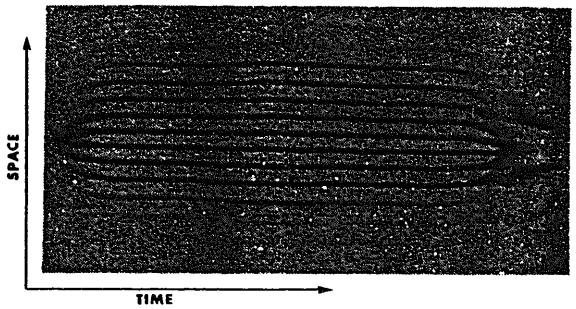

Fig. 5. Streak Record of Emittance Mask.

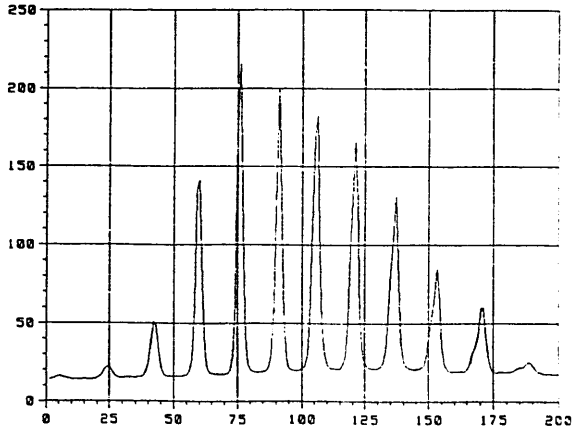

Fig. 6. Relative Intensity of Beamlets Across the Center of the Beam.

Overlayed on the x-x' plot are the x-x' results of cold beam simulations by Mission Research Corporation (Ref. 3) and LLNL (Ref. 6). The simulations include the effect of the emittance mask that shorts the radial electric field. Clearly, nonlinear space-charge affects the measurement, and these simulations included the mask in order to make comparisons with the experimental results. Figures 8a and 8b are ISIS simulations with the radial electric field shorted at

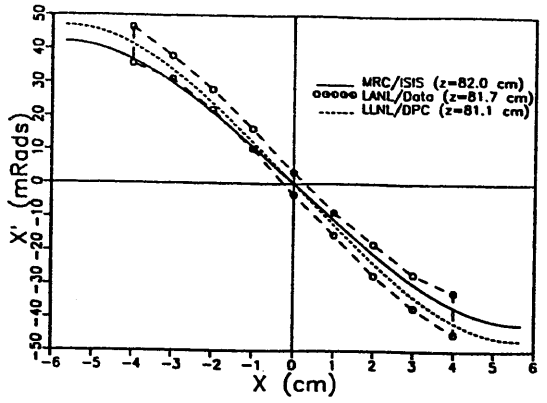

Fig. 7. REX Electron Beam Emittance Integrated over 30 ns at 3.8 MV and 4.8 kA.

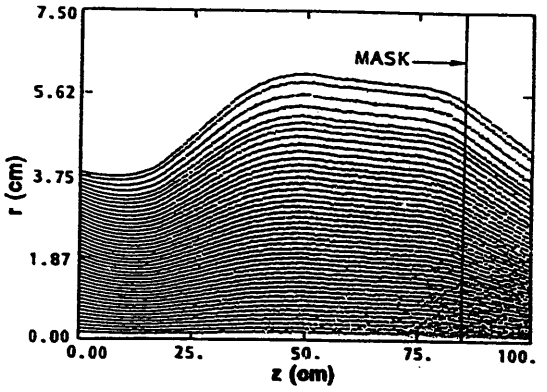

Fig. 8a. ISIS Simulation with Emittance Mask.

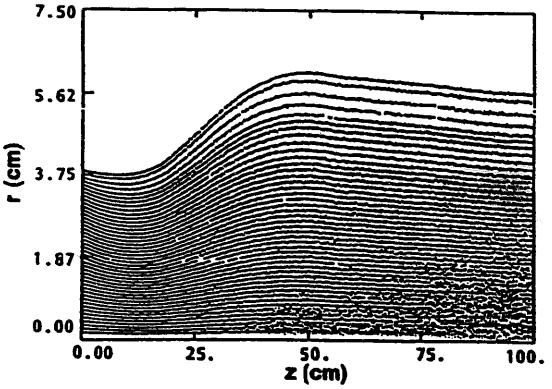

Fig. 8b. ISIS Simulation without Emittance Mask.

the emittance mask location and show the effect of no emittance mask. The edge emittance of the beam for Fig. 7 is obtained by calculating the phase space area of the x-x' plot divided by π, and gives values of 0.12 and 0.058 cm-rad for data integrated over 30 and 1 ns, respectively. The corresponding Lapostolle emittance from ISIS is 0.05 cm-rad for a monoenergetic beam, and therefore, must be compared to the 1-ns data. The brightness of the REX beam at 4 MV and 5 kA integrated over the 30 ns flat top is 3.5 x 10^8 A/m^2-rad^2.

The effective cathode temperature can be measured by examining a single beamlet coming from the center of the mask. The center beamlet produces a gaussian intensity distribution with an x_{rms} = 0.42 mm; the mask hole radius is 0.5 mm. This produces an effective temperature of 130 eV (Ref. 5). The temperature predicted according to Ref. 7 is 18 eV using a cathode radius of 38.1 mm; this discrepancy is not understood at present.

4. Conclusion

Extensive measurements of the time-resolved properties of the electron beam have been presented and compared with simulations. Agreement between simulation and experiment is excellent; therefore, ISIS can be used as a tool to design an electron injector for DARHT. This agreement is exemplified by the x-x' plot, where the only input to the code is the beam energy as measured by the spectrometer and the extraction magnet field $B_z(r,z)$. The remaining beam dynamics issues are completely predicted by the simulation. Therefore, the nonlinear space-charge forces, extracted current, beam transport, and focusing are correctly calculated by the code.

References

[1] ISIS was written by M. E. Jones at Los Alamos National Laboratory.

[2] R. L. Carlson, R. N. Ridlon, and L. E. Stout, RSI Vol. 57, No. 10, 2471 (1986).

[3] C. D. Child, Phys. Rev. 32, 492 (1913); I. Langmuir, Phys. Rev. 2, 450 (1913).

[4] H. R. Jory and A. W. Trivelpiece, JAP 40, 1180 (1977).

[5] T. P. Hughes, R. M. Clark, R. L. Carlson, L. A. Builta, T. J. Kauppila, D. C. Moir, and R. N. Ridlon, Report MRC/ABQ-R-1133, February 1989, pp. 9-18.

[6] DPC calculations were performed by John Boyd of Lawrence Livermore National Laboratory.

[7] Y. Y. Lau, JAP 61, 36 (1987).

A NOVEL SMALL PERIOD ELECTROMAGNETIC UNDULATOR FOR FREE ELECTRON LASERS*

W.Zhou, A.N.Fang and W.Z.Tang
Zhejiang University
Hangzhou, Zhejiang, China

Abstract

A new kind of small-period electromagnetic undulators is proposed in this paper. The concept of this proposal comes from numerical calculation, which shows that optimizing the shape of the current and ferromagnetic area could enhance the field strength of the small-period electromagnetic undulator. A computer code is conducted for calculating the field distribution of the undulator by means of nonlinear finite element method, which shows the alterant concept could also decline the space harmonics of electromagnets. Based on the numerical datas, a model undulator is constructed and measurements (using a Hall probe) is carried out on it. Experimental results have a quite good agreement with numerical calculation.

Introduction

A small period undulator used in the FEL has the advantage of generating shorter wavelength radiation with a given electron energy or conversely reduce the voltage and size, then the cost of accelerator required to achieve a target wavelength. This system is currently a subject of considerable interest.

The main problem of small period undulator application is the magnetic field intensity at beam position will decrease so rapidly with the shorting of the period. It is hard to build physical magnet arrays with very small periods to generate very short wavelength. In this paper, we optimize the shape of the current and ferromagnetic area. It could enhance the magnetic field of small period electromagnetic undulator and also decline the space harmonics of the field distribution. To compare with the structure of general rectangular coil and ferromagnetic core form, the magnetic flux density can be increased by a factor 1.3-1.47. For a electromagnetic undulator with a periodicity of 3.9 mm, at a point 1 mm stands apart from the ferromagnet surface, the radial magnetic flux density B_r per ampre B_r/I value can be increased from 0.9×10^{-3} kG/amp to 1.19×10^{-3} kG/amp.

*This work was supported by the Chinese National Science Foundation.

Calculation of Magnetic Flux Density

If the coil and ferromagnetic core both are rectangular shape and neglect the magnetic resistance, the analytical solution could be derived in this simplest condition. When the magnet is in cylindrical form, the distribution of the inner radial magnetic flux density is found to be

$$B_r(r,z)=\sum_{k=1}^{\infty}\frac{2\mu_0 I}{(2k-1)\pi h}\frac{\sin[(2k-1)\pi h/\lambda_0]}{I_0[2\pi(2k-1)a/\lambda_0]}\sin\left[\frac{2\pi(2k-1)z}{\lambda_0}\right]I_1\left[\frac{2\pi(2k-1)r}{\lambda_0}\right] \quad (1)$$

where I_0, I_1 are the Bessel functions of pure imaginary argument zero and first order respectively. a is the inner radius of the cylindrical form electromagnet. λ_0 is the length of period. h is the half width of coil.

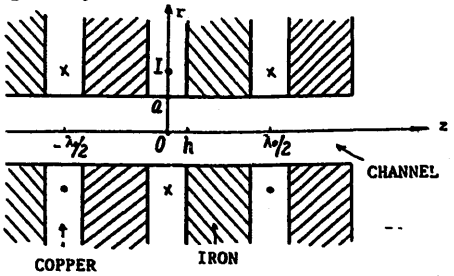

Fig-1. Side view of general electromagnet with rectangular coil and ferromagnetic core form.

From the analytical formula, the radial magnetic flux density B_r will be decreased rapidly with the increase of the distance from the ferromagnet surface and the shorten of the period. On the other hand, the field variation of B_r along Z direction is distributed with significant spatial harmonics.

When the shape of coil and core are not simple rectangular form, we have to calculate the magnetic flux density with numerical calculation method. In this paper, the finite element method is presented. This method can easily adapt to the nonrectangular boundaries and interfaces of medium of those models with complex physical and geometric conditions. Divide the field into triangular meshes and use the automatic zoning successively.

At the same time, if we consider the magnetic permeability μ of the ferromagnetic material is varied with the magnetic flux density B and the relation $\mu=\mu(B)$ is nonlinear and nonanalytical. We use low order interpolation to construct the approximative function of B

CH2669-0/89/0000-0786$01.00©1989 IEEE

sectionally and iteratively compute B several times untill the magnetic potential A(r,z) satisfy the defind accuracy. In this paper, the controlled value of accuracy is:

$$\varepsilon = \frac{A^{(i)} - A^{(i-1)}}{A^{(i)}} < 0.05\% \qquad (2)$$

For the sake of confirming up the accuracy of this calculating code, a theoretically and experimentally known simple form electromagnet was checked at first. The result of calculating was in keeping with the known value very good.

Optimizing Design of the Construction of mm Period Undulator

For optimizing design, we optimize the shape of the current and ferromagnetic area, including the ratio of the core height to the period, the ratio of the coil width at surface to the period, the shape of coil and core, and the shape of the magnet pole.

The configuration of a optimizing design of a magnet element of a 3.9 mm period undulator as an example is shown in Fig-2.

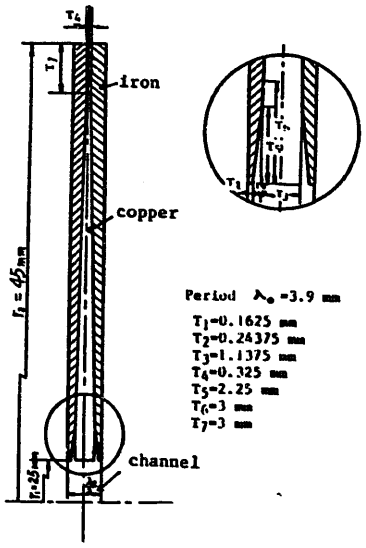

Fig-2. Configulation of optimizing design of an element of a 3.9 mm period undulator.

The construction of a magnet element is composed by two half DT4A soft iron ring. (this kind of magnetic material having saturation value 15.5 kG).

The comparision of the B_r-I relation of the optimizing design and general design (ref. 1) are shown in Fig-3. To compare with the rectangular magnet with the same 3.9 mm undulator and same 1 mm from magnet. The magnetic flux density can be increased by a factor of 1.3-1.47.

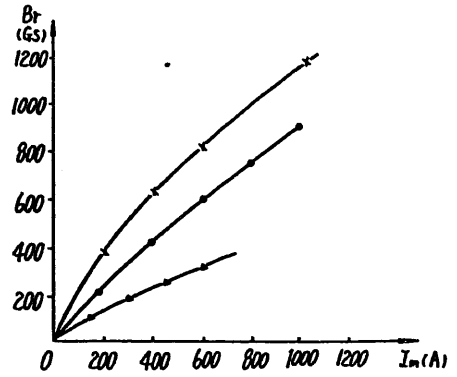

Fig-3. The comparison of optimizing design of a cylindrical electromagnet and a general rectangular electromagnet. (λ_0=3.9 mm; d=1 mm)

- * Computed value of a optimizing design of a cylindrical electromagnet.
- • Measured value of a general rectangular electromagnet double-sided, 2 mm gap. (ref. 1)
- ▲ Measured value of a general rectangular single-sided electromagnet. (ref. 1)

On the other hand, in this paper the designed electromagnetic undulator is in cylindrical form. The magnetic flux density is related more closely with the distance out of magnet surface but is lossely with the inner diameter, so we can wider the inner diameter, then the current channel is wider than that of rectangular form.

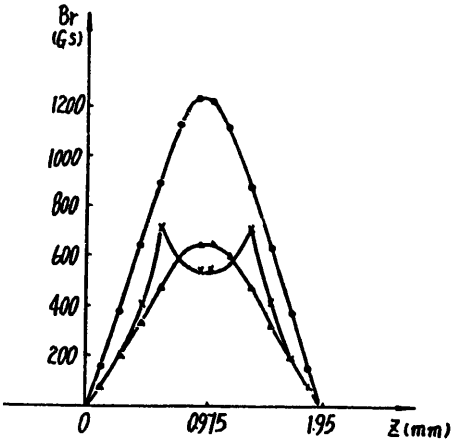

Fig-4. Diagram of field distribution (λ_0=3.9 mm; d=1 mm)

- * General rectangular pole shape, I=400a
- ▲ Optimized pole shape, I=400 a
- • Optimized pole shape, I=1000 a

From Fig-4, it is obviously that the space harmonics is declined by optimizing the pole shape.

Because of the size of the Hall probe is not so small (1.7 mm X 1.7 mm X 0.35 mm) and in order to mill the optimized core easily, an enlarged model λ_u=4.8 cm is constructed and measured. The coils are wound with 124 turns of 0.9 mm diameter wire and formed by hot mould pressing. As shown in Fig-5, the experimental results have a quite good agreement with numerical calculations.

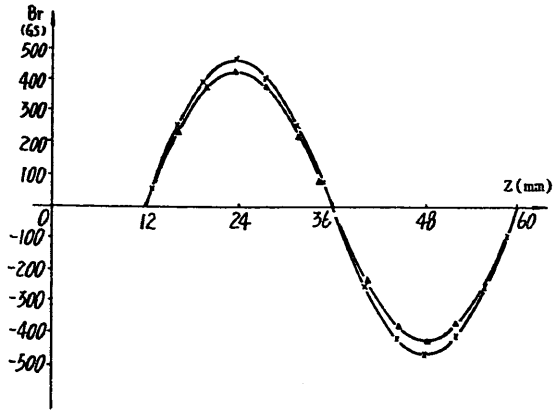

Fig-5. The comparison of computed and measured value.

* λ_u=4.8 cm, d=8 mm. NI=1025 a. (computed result).
▲ λ_u=4.8 cm, d=8 mm. NI=1025 a. (measured result).

Conclusion

To optimize the shape of the current and ferromagnetic area could enhance the field strength and decline the space harmonics of the small period electromagnetic undulator. The construction is simple and practical.

References

[1]. W.W.Destler et al, J. Appl. Phys., 60(2), 521(1986)

[2]. M.E.Gross et al, J. Appl. Phys., 60(2), 529 (1986)

[3]. V.L.Granatstein et al, Appl. Phys. Lett., 47(16), 643 (1985)

[4]. G.Ramian et al, Nucl. Instr. and Meth., A 250, 125 (1986)

[5]. R.M.White, Appl. Phys. Lett., 16(2), 194 (1985)

DEVELOPMENT OF A 10-m WEDGED-POLE UNDULATOR

K.E. Robinson, S.C. Gottschalk, F.E. James,
D.C. Quimby, J.M. Slater, and A.S. Valla
Spectra Technology, Inc.
2755 Northup Way, Bellevue, Washington 98004 USA

Abstract

A 10-m rare-earth permanent magnet hybrid undulator [1] called NISUS (Near-Infrared Scalable Undulator System) is being installed by Spectra Technology, Inc. (STI) for use in the Boeing Aerospace Company (BAC) free-electron laser (FEL) program series. The design has been optimized for operation at a 1-μm wavelength with the BAC accelerator parameters. A remotely-adjustable compound taper is utilized to achieve optimum startup gain and high saturated extraction. Notable improvements include the use of wedged poles for higher field strength and magnetically seamless structure which accommodates frequent two-plane steering correction without drift spaces. An important development is the finding that magnetic field errors can be substantially reduced using thin iron shims attached to the permanent magnets.

Introduction

Performance demands have increased for undulators. Long scalable undulators are becoming necessary for various applications. Modularity, field quality and serviceability are major requirements of an undulator system. A major goal of STI has been to build NISUS from modules which would allow easy scaling to longer lengths without redesign. The NISUS design parameters are listed in Table 1. The on-axis magnetic field strength is 5.6 kG in a 3.89 cm period and 1.44-cm gap.

Table 1
NISUS DESIGN PARAMETERS

UNDULATOR	
Length	10 m
Period	3.89 cm
Peak Field	5.6 kG
Gap	1.44 cm min.
Clear Aperture	1.14 cm
a_w (rms)	1.44 max
Energy Taper	Adjustable to 20%
E-BEAM	
Energy	121 Mev
Peak Current	500 A
Energy Spread	1% FW
Emittance	0.02 cm-rad ($\gamma\pi r\theta$)
PHOTONS	
Wavelength	1.06 μm
Rayleigh Range	3.7 m

The NISUS design includes a number of improvements relative to the technology used in the earlier tapered hybrid undulator (THUNDER) [2]. The use of the wedged-pole configuration [3] has provided a major increase in field strength, has reduced the harmonic content to less than two percent, and assures that no portion of the poles operate near saturation. Another major difference stems from an upgraded method of providing e-beam steering and focusing correction. The new NISUS magnetic structure is seamless, eliminating the drift spaces previously used to accommodate steering stations. This simplifies construction since careful phase tuning of drift spaces is unnecessary.

System Components

An isometric drawing of the assembled undulator is shown in Figure 1. The 10-m, 256 period undulator magnetic structure is built in 16 modules, each consisting of 16 periods. The entire structure rests on an optical table which is firmly mounted to the floor of the accelerator chamber. The optical table provides a rigid, vibration damped, and scalable platform. The modular arrays of vanadium permendur poles and samarium cobalt magnets are supported from above and below on long aluminum box beams. The upper box beam is rigidly held by six strongback support stanchions. The magnetic field may be tapered by varying the gap separation. Each remotely adjustable gap separation mechanism is attached to the box beam and moves an undulator half up and down. The mechanism consists of two rigid threaded-rod actuators driven by a worm-gear and ball nut assembly. Linear variable differential transformer (LVDT) gap sensors with 1-μm resolution provide closed-loop position feedback. The drive accuracy and reproducability are expected to be equivalent to the resolution because the attractive force between undulator halves eliminates backlash. Each magnetic structure section is connected to its nearest neighbor by a tuning fork shaped flexure joint, which allows for angular variation between sections as the gap is tapered. The sides of the undulator are open for easy access to the vacuum chamber components.

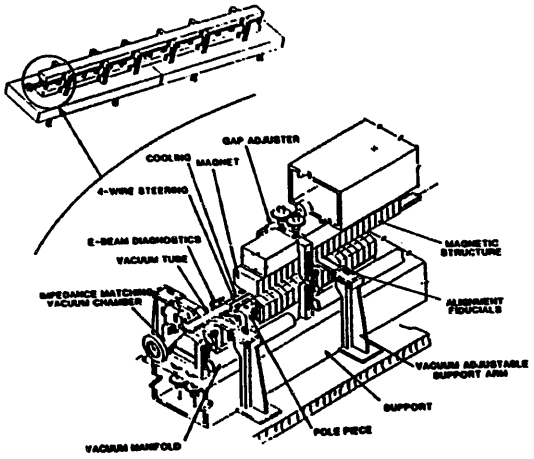

Figure 1

The NISUS vacuum system configuration is depicted in Figure 2. A 1.2-m length of vacuum tube section is shown, together with the associated 2-axis kinematic mount. Commensurate with the undulator section length, each vacuum tube section consists of two subassemblies. One subsection has a set of independently controlled steer-focus wires, the other has a pop-in target mount, and ports for non-

CH2669-0/89/0000-0783$01.00©1989 IEEE

interrupting beam diagnostics and pumping. Both fluorescent screens and non-contact stripline beam position monitors are used for e-beam sensing. Tests have shown that the lead C-rings achieve a leak-free seal tolerant of large misalignments between vacuum-tube sections. Each of the modular sections can be independently removed for servicing. Side contact cooling is provided.

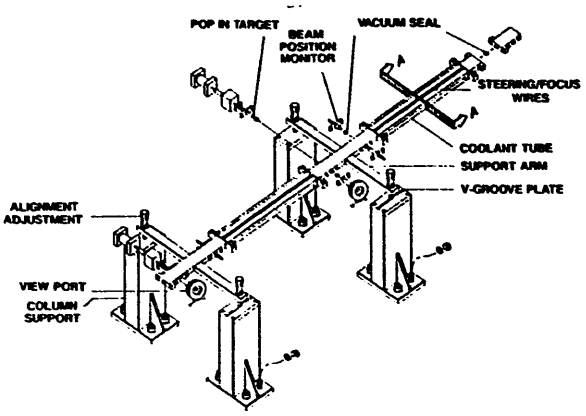

Figure 2

Two-plane steering correction is provided in NISUS by an efficient distributed coil system which is mounted directly on the vacuum chamber. The steering system consists of four wires mounted in close proximity to the pole tips, as suggested by Halbach [4]. Four copper ribbons are oriented at approximately 60 degrees with respect to the horizontal axis. The primary function of the wire ribbons is to supply e-beam steering. By changing the relative symmetries of the currents in each of the wires, steering or focusing fields at any angle can be generated.

A 16-pole mockup has been used to test the 4-wire steering system concept. The strength and field quality produced in both steering and focusing current configurations has been verified. The system is found to produce a horizontal steering field of 1.3 G/amp, which, at 10 A, provides over 300 G-cm of integrated steering field in a 25-cm length. In the mockup the poles are unpowered so that higher order moments in the steer-focus field distribution can be studied without being overpowered by the 5.6-kG primary field. Standard multipole analysis determined that higher order impurities generated by the 4-wire configuration are acceptably small. These moments are expected to contribute less than one percent change in e-beam radius over the 10-m undulator length. The main source of these impurities is wire misplacement.

The basic features of the NISUS magnetic structure were also first verified with a prototype. This mock-up verified achievement of the design 5.6-kG on-axis field strength using wedged poles. This strength for the fundamental field component is at least 15 percent higher than achievable with straight-poles at this gap to period ratio.

The prototype has also shown that two sections can be joined in a magnetically seamless manner and that the tuning fork shaped flexure joint between sections operates correctly when used to achieve a tapered field. The pole alignment, pinning and clamping techniques have been verified and the magnet insertion procedures determined. By replacing some of the poles with canted poles, the cant angle needed for equal two-plane focusing was established.

Canted-pole two-plane focusing has been selected over curved-pole focusing [5] for NISUS primarily because of the higher achievable on-axis field strength. The canted-pole system avoids a field strength limitation imposed by saturation of overhanging pole tips [6]. While curved poles minimize the resonant coupling between the synchrotron oscillations and betatron motion of trapped electrons, this is not a concern for the e-beam brightness and other parameters of interest [8]. Furthermore, canted poles together with the internal 4-wire steering and focusing system allows additional operational flexibility in an adjustable gap undulator. The available focusing trim allows the desired equal two-plane focusing condition to be maintained over all ranges of gap and e-beam energy.

A plot of the measured transverse field gradient produced by the canted poles in the 26-pole NISUS prototype is shown in Figure 3. Comparison with comparable data measured for THUNDER [2] reveals an interesting difference. In THUNDER the gradient is considerably more nonuniform with axial position; the gradient drops nearly to zero between the poles. This difference apparently results because the thickness of the straight poles used in THUNDER takes up a smaller fraction of the undulator period. The thicker NISUS wedged poles are considerably wider at the tip. For a pole tip cant angle of 10.8 mrad, the measured average gradient dB/dx in NISUS is about 100 G/cm and the peak gradient is approximately 130 G/cm.

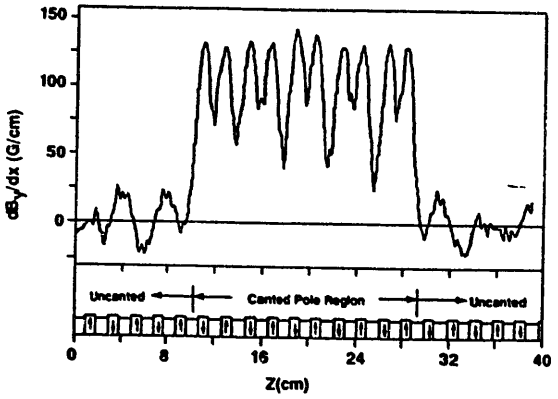

Figure 3

Based on these measurements, the desired nominal equal two-plane focusing condition is provided in NISUS by canting a total of 6 central poles out of 32 in each section. The required average gradient is so small that a subset of poles is canted in each undulator module in order to make the cant angle reproducible in manufacturing. E-beam transport is indistinguishable from fully distributed canting since the discrete canted pole regions occur frequently within the 9-m betatron period.

Field Shimming

In practice, undulator field quality has been limited by the presence of several undesirable factors, caused in part by inhomogeneities in the permanent magnets and pole imperfections. One of the most studied errors is that of the half-period integrals under each undulator pole [8]. Calculations of the effect of field errors in long undulators [9] show that it is highly desirable to improve the rms variation of these integrals from the typical values of 0.5 to 1.5 percent achieved in high field strength permanent magnet undulators. The

techniques used to construct the current generation of undulators for 0.5 and 1-μm operation are not suitable for further extrapolation. These methods consist of tighter mechanical tolerances and higher rejection rates of the permanent magnets with resultant cost penalties. Magnet and pole interchange algorithms for error compensation have not been perfected and will be labor intensive at best. What is needed is a method of tuning an undulator to the desired fields after it has been assembled.

An important result of the NISUS magnetic structure prototype work is the finding that field errors can be dramatically reduced by a straightforward field tuning method. The basic concept is that thin iron shims are used to selectively shunt a small fraction of the field lines from regions where the field is higher than desired. The shims are placed on the surface of the magnets in the shallow recess between pole tips, thereby shunting field lines from one pole to another.The shims are easily placed or adjusted by hand, and are therefore a preferable tuning technique compared to magnet or pole interchange. With the large scalar potential difference between the poles, the shims are completely saturated and the number of field lines shunted is determined simply by their thickness. The field modification induced by the shim is largely confined to the region of two poles, and it has been shown experimentally that it is approximately linear in the shim thickness and additive with that of shims on neighboring poles.

Given that the field reduction is predictable, one can generate algorithms that modify the field in a predetermined way. Thus far, the shims have been applied to the problem of reducing the rms level of half period dipole field errors. By symmetry, the field modification has no integrated dipole component. However, the shims are still useful for correction of these steering errors. Shims allow a redistribution of any arbitrary dipole errors to a new distribution, which can be simply a constant (independent of axial position) error. This constant error can be canceled with an externally applied field of large spatial extent. Thus, the shims are a means for converting high spatial frequency errors to lower spatial frequencies where they can be dealt with by a simple bias field provided by the steering coils.

The capability of magnetic shims for correcting the primary field component has been demonstrated in the central region of the 26-pole NISUS mockup. Shown in Figure 4 are the half-period field integrals under the 18 central poles. Only the residual errors are shown, that is, the contribution of the best fit sine wave has been removed. The initial kick errors are shown as the points connected by the dotted lines. The quality of construction of this initial prototype was not as well controlled as NISUS itself, and prior to shimming the rms value of residuals compared to the underlying field is 1.3 percent. Following placement of appropriately chosen shims and one iteration, this value is reduced to 0.11 percent.

Conclusion

NISUS has achieved the goals of scalability, modularity, serviceability, and high field quality need for advanced FEL and Synchrotron radiation application. At the time of this writing, all of the undulator modules have been assembled and the last 5 meters are undergoing magnetic field testing. The first 5 meters were installed following its magnetic certification, in the fall of 1988, complete installation is anticipated by the fall of 1989 prior to full system operation. NISUS rms errors in the half-period field integrals can be substantially reduced using thin iron shims attached to the permanent magnets. A shimming algorithm has been demonstrated which allows arbitrary dipole steering errors to be redistributed into a constant dipole error which can be easily canceled by the internal steering coils in NISUS.

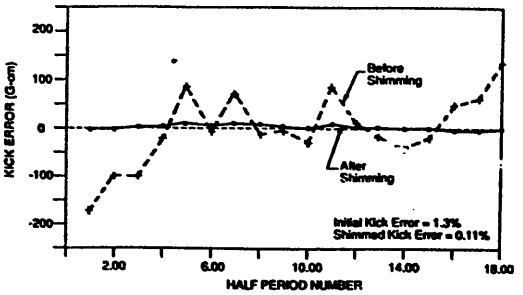

Figure 4

Acknowledgements

The authors would like to acknowledge the contributions of M. Brown, D. Jander, R. Rudeen, and D. Van Ess to the construction and measurements of NISUS. This work was supported in part by the U.S. Army Strategic Defense Command through Boeing Aerospace Company contracts GR5166 and GT8052.

References

[1] K. Halbach, J. Phys. (Paris) 44, C1-211 (1983).
[2] K.E. Robinson, D.C. Quimby, and J.M. Slater, IEEE J. Quantum Electron. QE-23, 1497 (1987).
[3] D.C. Quimby and A.L. Pindroh, Rev. Sci. Instr. 58, 339 (1987).
[4] K. Halbach, presented at Eighth International Free Electron Laser Conference, Glasgow, UK, 1-5 September 1986, unpublished.
[5] E.T. Scharlemann, J. Appl. Phys. 58, 2154 (1985).
[6] D.C. Quimby, K.E. Robinson, R.G. Berger, S.C. Gottschalk, A.L. Pindroh, J.M. Slater, and A.S. Valla, Nucl. Instr. and Meth. Phys. Res. A272, 192 (1988).
[7] D.C. Quimby, Nucl. Instr. and Meth. A250, 456 (1986).
[8] B.M. Kincaid, J. Opt. Soc. Am. B 2, 1294 (1985).
[9] B.E. Newnam, Proc. SPIE 738, 155 (1987).

A SECOND SUPERCONDUCTING WIGGLER MAGNET FOR THE DARESBURY SRS

M.W. Poole, V.P. Suller and S.L. Thomson
SERC Daresbury Laboratory, Warrington WA4 4AD, U.K.

Abstract

A second superconducting wiggler magnet will be installed in the SRS as a wavelength shifter, adding a 6T radiation source to the present 5T one. A warm bore design with a short central pole will minimise the tune shift and emittance blowup of the electron beam. Relocation of a chromaticity-correcting sextupole magnet to provide space for the wiggler has potentially serious effects on the dynamic aperture that are examined.

1. Introduction

A 5T superconducting magnet has been operating as a wavelength shifter on the SRS since 1982; its design has been previously described[1,2] and its effect on the SRS beam properties has also been discussed[3]. The five existing experimental stations, together with two additional ones under development, have become heavily oversubscribed with the demand for synchrotron radiation in the range 10-50 keV and even higher energies are sought by some users. A second wiggler facility has now been fully funded and detailed planning and construction is in progress.

The scientific case for the new facility is based on the needs of x-ray diffraction, protein crystallography, small angle scattering and EXAFS (biological and dilute) and implies the utilisation of a wide fan of radiation to gain maximum advantage. For this reason a wavelength shifter with a single high field region and an opening angle of at least 50 mrads has been chosen, allowing its utilisation simultaneously by five major experimental stations. Recently it has been decided to add an extra high flux density station as close in to the storage ring as possible: when in use this Laue station will block off all other users of the line. It appears possible that this unique facility can be placed about 7.5 m downstream from the wiggler source point, where the power density will be several Wmm^{-2} and peak fluxes of more than 10^{11} photons $s^{-1}mm^{-2}$ per 0.1% band can be obtained. The normal stations will have a brilliance ~ 10^{13} photons $s^{-1}mm^{-2}mrad^{-2}$ per 0.1% band.

With beam lines already planned or in use from eleven of the sixteen dipoles or adjacent straights of the SRS it has become increasingly difficult to include further expansion of the facilities. Efficient exploitation of the new wiggler will demand considerable floor area and this will only be possible if the wiggler is installed in the straight immediately upstream of the injection one: the implications of this choice are addressed in this paper.

2. Cryogenic Requirements

The existing superconducting wiggler runs from a large, closed circuit refrigeration system supplied by Sulzer with surplus capacity for a second wiggler. A two-stage compressor about 100 m from the storage ring feeds helium gas to a local cold box which liquefies it using heat exchangers, two high speed turbines and the usual J-T expansion valve. The system is fully computer controlled and automates the cool-down of the wiggler over 3-5 days, maintaining tolerable temperature differentials. A short (~ 10 m) helium transfer line connects to the magnet cryostat in the storage ring, which contains only about 30 ℓ of liquid helium.

Although the refrigerator has at least 30 W available for the new wiggler differences in magnet design philosophy have required careful assessment of operations with two wigglers at the same time. As will be described in the next section, in order to achieve the highest magnetic field level a low pressure (~ 2 bar) cryostat has a clear advantage, whereas the present wiggler operates at 3.8 bar during cool-down. To avoid excessively long cool-down the new magnet will therefore employ liquid nitrogen precooling and include the possible addition of liquid helium directly from a dewar where necessary. Use of a much larger helium volume will also give the second wiggler an attractive endurance, perhaps in excess of one week when not energised. Not only does this make it relatively immune from compressor trips but it gives time for liquid helium to be siphoned off before planned maintenance, or alternatively to be topped up when the refrigerator returns to its gas mode during cool-down of the first wiggler. It is hoped that simultaneous cool-down of the two magnets can be achieved in about seven days.

The large volume of helium in the new system makes it undesirable to invest in a recovery/storage system for helium gas as employed at present. In any event, the present wiggler has not quenched during its seven years of operation so a gas pressure surge seems unlikely. However the opportunity will be taken to replace the refrigerator control system by a more modern option. The new transfer line for the second wiggler will need to be routed to the opposite side of the storage ring, a distance of at least 35 m.

3. Wiggler Magnet Design

An outline design of the new wiggler has been carried out in order to confirm the feasibility of a 6T specification. Preliminary conclusions can be reported here but it should be noted that a final design has yet to be chosen. Conservative design criteria are preferred and, for example, it has been assumed that the Nb-Ti conductor will operate well below its notional rating. Warm bore operation has been selected to avoid complicated interaction with the adjacent storage ring UHV environment: with a beam-stay-clear vertical aperture of 34 mm the inter-coil gap is unlikely to be much less than 70 mm even in the absence of provision for in-situ bakeout of the beam chamber. Use of magnetic steel poles is therefore essential to achieve 6T on the beam centre line, and a return yoke is necessary both to enhance the useful field and to reduce unwanted leakage fields.

The preliminary design has been made with both 2D (PE2D) and 3D (TOSCA) electromagnetic design codes. The focusing effect of such a wiggler magnet depends on the second field integral[4], $\int B^2.dl$, but this can be adequately compensated by adjustment of other storage ring lattice magnets; a local compensation scheme has been adopted recently on the SRS to minimise the increase in vertical source size[5] and also has the advantage that the second wiggler effect no longer depends strongly on its exact location in the ring. However a serious effect remains in a lattice such as the SRS where no zero dispersion locations exist: the beam emittance is increased by the wiggler contribution to the third field integral, $\int |B|^3.dl$, in the storage ring[6]. To a good approximation the emittance change can be represented as follows in SRS-2:-

CH2669-0/89/0000-1250$01.00©1989 IEEE

$$\epsilon_x = \epsilon_x^0 \left[\frac{1 + 0.03 \int |B|^3 . dl}{1 + 0.02 \int B^2 . dl} \right]$$

In the case of the existing 5T wiggler the measured field integrals were 4.4 T^2m and 14.1 T^3m and the above formula predicts an emittance of 1.4×10^{-7} m-rad, an increase of 34% which is in good agreement with the lattice computations[5]. Scaling these integrals to 6T operation would suggest an emittance blow-up of more than 60% due to the second wiggler alone and this is considered to be unacceptable. It is therefore very important to minimise $\int |B|^3 . dl$ in the new wiggler magnet and this will be achieved by adopting a short central pole together with end poles as long as can fit within the available space of a little over 1 metre. The resultant field distribution in one half of the magnet is illustrated in fig. 1, together with the existing wiggler for comparison; such a design should limit the emittance increase to about 50%.

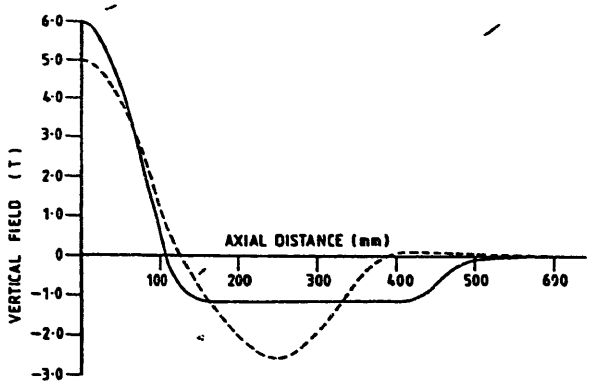

Fig. 1. Vertical field distribution on beam axis through half of wiggler magnet, for existing (5T) and proposed (6T) magnets.

The design example shown in fig. 1 is characterised by a major coil excitation on its centre pole with only a smaller trim coil being necessary on the end poles, about 5% of the ampere-turns assisting the production of the required 1T field level and ensuring a zero field integral through the magnet. The peak field on the central pole coils should be less than 7T, and these coils will probably adopt a graded current density mode of operation. The three-dimensional field studies suggest that a field integral homogeneity of about 0.5 mT-m should be attainable within the good beam aperture of ± 15 mm, leading to a transverse field harmonic error much smaller than the installed non-linear correction capability (for example, of the chromaticity correcting sextupoles).

In order to avoid the need for a water-cooled synchrotron radiation absorber within the wiggler a horizontal aperture of 160 mm has been selected for the beam pipe (the electron beam-stay-clear is 135 mm). The vertical attraction between the coils will be reacted by a stainless steel plate in the mid-plane whose thickness must be minimised at the beam centre line: however, its stiffness will be assisted by the coils themselves and the deflection should be acceptable with a steel thickness of 2-3 mm. Axial pre-stressing of the coils, probably using tie bolts, will also be necessary to overcome the axial magnetic forces of up to 1 MNm^{-1}.

4. SRS Modifications

The selection of a straight section so close to the SRS injection area has serious implications that will necessitate additional modifications. The radiation beam line must cross the injection transfer line from the booster synchrotron close to the storage ring. The UHV environment of the ring is at present protected by differential pumping stages and this isolation factor will reduce significantly when the new beam pipe is in place. At present it is hoped that it will not prove necessary to convert the whole transfer line to bakeable, UHV quality. However the opportunity will be taken to make a series of other improvements, such as a better beam position monitoring system.

There is a general problem that will also arise due to shortage of space. For example the septum pulsed power supply, located immediately adjacent to its magnet, will need to be made smaller and the septum drive mechanism may need to be modified for similar reasons. The problem is exaggerated by the need to accommodate the new high flux density station as close to the ring as possible. The proposed scheme has a shield wall very close to the ring components and careful design will be required to ensure acceptable access to this part of the storage ring. The existing labyrinth access to the ring tunnel will also have to be relocated.

Within the ring itself space for the new wiggler can only be found by removing some existing components. Each SRS straight has immovable upstream (D quadrupole and vertical steering magnet) and downstream (F quadrupole and multipole corrector) modules which leave little space for insertion devices. Furthermore this straight has one of the vacuum sector valves whose movement would have major consequences for the control system philosphy. The two components that can be more readily relocated are the beam scraper, that only needs shielding reinforcement wherever it goes, and the D sextupole, one of four used to control the SRS vertical chromaticity. The resultant space thereby made available is about 1.2 m, and it is within this allocation that the second wiggler is being designed.

Although mechanically easy, the sextupole magnet movement is causing some concern over its effect on the SRS beam properties. In a series of accelerator physics experiments in recent months it has been demonstrated that injection and subsequent accumulation of beam is very difficult if this magnet is shorted out. This investigation has been accompanied by dynamic aperture computations seeking to explain the poorer SRS performance. Figure 2 shows the results of some tracking calculations, illustrating a significant aperture reduction on breaking the four-fold symmetry of the sextupoles. The beam-stay-clear aperture at this location is ± 20 mm horizontally and ± 8 mm vertically. Replacement of the sextupole to a nearby straight achieves some advantage compared with a complete removal. It is already known[7] that the betatron tune working point in SRS-2 is sensitive to a number of resonance lines, for example the structure resonance $Q_R - 2Q_v = 0$, but the sextupole move results in beam loss on the following:

$$\begin{aligned} 3\,Q_R &= 19 \\ Q_R + 2\,Q_v &= 13 \\ Q_R - Q_v &= 3 \\ 2Q_R - Q_v &= 9 \end{aligned}$$

This considerably reduces the available tune space and may well explain the experimental injection results. Theoretical and experimental studies are now receiving high priority in order to find the optimum solution to this problem.

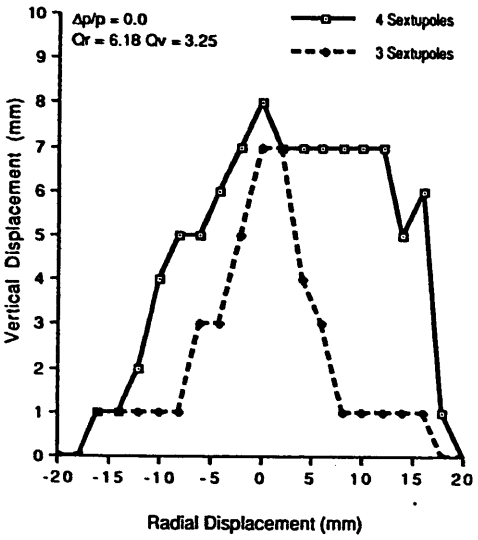

Fig. 2. Dynamic aperture comparison before and after sextupole magnet removal from one straight.

5. Conclusion

Design of the second superconducting wiggler magnet is now well advanced and it is planned to place a contract for manufacture later in the year. Preparations for the modifications to the storage ring and transfer line are also under way and detailed assessments of the implications for SRS performance are in progress. It is hoped to instal the new magnet in the second half of 1991.

Acknowledgements

Many Daresbury staff are involved in the planning and preparation of such a large project and we thank them all for their efforts. We also acknowledge the assistance of Kevin Smith and John Ross.

References

1. D.E. Baynham and B.E. Wyborn, "A 5 Tesla Superconducting Wiggler Magnet", IEEE Trans. Magnetics MAG-17 (1981) 1595.
2. N. Marks et al, "Initial Operation of a 5T Superconducting Wiggler Magnet in the SRS", Nucl. Instrum. Meth. 208 (1983) 97.
3. V.P. Suller et al, "SRS Behaviour with a Superconducting 5 Tesla Wiggler Insertion", IEEE Trans. Nucl. Sci. NS-30 (1983) 3127.
4. R.P. Walker, "Electron Beam Focusing Effects and Matching Conditions in Plane Periodic Magnets", Nucl. Instrum. Meth. 214 (1983) 497.
5. M.W. Poole et al, "Wiggler Tune Shift Compensation on the Daresbury SRS", this conference.
6. R.H. Helm et al, "Evaluation of Synchrotron Radiation Integrals", IEEE Trans. Nucl. Sci. NS-20 (1973) 900.
7. V.P. Suller et al, "SRS-2: Performance and Achievements", this conference.

EFFECT OF TAPERING ON OPTICAL GUIDING AND SIDEBAND GROWTH IN A FINITE-PULSE FREE-ELECTRON LASER

B. Hafizi*, A. Ting, P. Sprangle and C. M. Tang

Plasma Theory Branch
Plasma Physics Division
Naval Research Laboratory
Washington, DC 20375-5000

Abstract

The development of an optical pulse of finite axial extent is studied by means of a numerical code. It is found that increasing the tapering rate reduces refractive guiding, causing the optical wavefronts to become more convex, thus spreading the optical field into a larger cross-section. This increases the output power and efficiency. Concomitant with this, there is a significant reduction in the sideband modulation of the optical field.

I. Introduction

We present the results from a numerical study of a high-current (~ kA), high-pover (~ GW), short wavelength (~ μm), tapered-wiggler free-electron laser (FEL). The results indicate that tapering, in addition to enhancing the extraction efficiency, has the further benefit of improving the quality of the output by suppressing sideband modulation of the optical field. The results are used to illustrate the transition between refractive guiding and gain focusing as the tapering rate is varied.

II. Formulation

The vector potential of the optical field is given by

$$A_s = \frac{A}{2}\exp\left[i\left(\frac{\omega}{c}z - \omega t\right)\right]e_x + \text{c.c.},$$

where A is the slowly-varying envelope, ω is the radian frequency, and e_x is the unit vector along the x axis. We assume that A may be expanded as

$$a(r,z,t) = \sum_{n=0}^{\infty} a_n(z,t)\, L_n\left(2r^2/r_s^2\right) \times \exp\left[-(1 - i\alpha)\, r^2/r_s^2\right], \qquad (1)$$

where $a = |e|A/mc^2$, $-|e|$ is the charge on an electron of rest-mass m, and L_n is the Laguerre polynomial of order n. In (1) $r_s(z,t)$ is the spot-size, α(z,t) is proportional to the curvature of the optical field, and $\{a_n(z,t)\}$ are the transverse optical mode coefficients. Substituting (1) into the well-known parabolic wave equation and employing the source-dependent expansion technique of Ref. 1, one obtains the set of equations given in Ref. 2 for the evolution of r_s, α, and $\{a_n\}$. The code includes betatron motion in a planar wiggler with parabolic pole faces. [3] The synchrotron motion is generalized from that given in Ref. 2 by the addition of the betatron terms in the equation for the electron phase.

The electron beam is taken to have a parabolic density distribution in the transverse plane and a Gaussian distribution in the transverse velocities. The normalized edge emittance for such a distribution may be defined by:

$$\varepsilon_x = 2\sqrt{6}\left[\langle x^2\rangle\langle\gamma^2\beta_x^2\rangle - \langle x\gamma\beta_x\rangle^2\right]^{1/2},$$

and similarly for ε_y. Here <...> indicates an average over the entire beam.

The relativistic factor for a synchronous electron with no betatron motion is given by $\gamma_r^2 = (\omega/2ck_w)(1 + a_w^2/2)$, where $a_w = |e|B_w/k_w mc^2$, B_w is the induction and $2\pi/k_w$ is the wiggler period. The form of tapering employed in the computations is obtained simply by prescribing a constant rate of decrease of energy $d\gamma_r/dz < 0$ for a synchronous electron.

The parameters for the computations presented herein are listed in Table I. The effective energy spread due to emittance is given by

$$\left[\frac{\delta\gamma_r}{\gamma_r}\right]_{emit} = \frac{\left(\varepsilon_x^2 + \varepsilon_y^2\right)/2}{\left(2r_{bo}\right)^2\left(1 + a_w^2/2\right)^2},$$

where r_{bo} is the electron beam radius. The full ponderomotive bucket height for electrons on axis is given by

$$\left[\frac{\delta\gamma_r}{\gamma_r}\right]_{bucket} = \left\{\frac{2a_w|a|f_B}{\left(1 + a_w^2/2\right)} \times \left[\cos\xi_r - \left(\frac{\pi}{2}\,\mathrm{sgn}\,\xi_r - \xi_r\right)\sin\xi_r\right]\right\}^{1/2},$$

where $a = |a|\exp(i\phi)$, $\xi_r = \psi_r + \phi$, and the phase $\psi_r = (\omega/c + k_w)z - \omega t$ of the synchronous electron is related to the rate of change of γ_r in the tapered FEL by

$$\frac{d\gamma_r}{dt} = -\frac{a_w|a|\omega f_B}{2\gamma_r}\sin(\psi_r + \phi).$$

Table I. Parameters for a high-pover, rf-linac FEL

Electron Beam	
Energy, γmc^2	175 MeV
Current, I_b	450 A
Normalized edge emittance, $\varepsilon_x = \varepsilon_y$	153 mm-mrad
Radius, r_{bo}	1 mm
Wiggler	
Pulse length	6.7 ps
Induction, B_w	6.4 kG
Period, $2\pi/k_w$	4.7 cm
Length	42 m
Input Radiation	
Wavelength, $2\pi c/\omega$	1 μm
Spot size, $r_s(0)$	1.25 mm
Pulse length (FWHM)	31.4 ps
Peak input power	450 MW

Table II lists the full bucket height for the various tapering rates $d\gamma_r/dz = c^{-1}\, d\gamma_r/dt$ employed in the computations. Note that for the input pover of 450 MW essentially all the electrons are initially trapped. Also listed in Table II are the initial resonance phases ξ_r.

CH2669-0/89/0000-1234$01.00©1989 IEEE

Table II. Resonance phases and tapering rates

$d\gamma_r/dz$ (m^{-1})	Initial Resonance Phase ξ_r(°)	Full bucket height $[\delta\gamma_r/\gamma_r]_{bucket}$ (%)	Energy spread due to emittance $[\delta\gamma_r/\gamma_r]_{emit}$ (%)
-0.1	2.5	0.96	
-0.3	7.6	0.89	
-0.5	12.7	0.82	
-0.7	17.9	0.75	
-0.9	23.3	0.67	0.12
-1.1	28.9	0.6	
-1.3	34.5	0.52	
-1.5	41.2	0.44	

III. Results and Discussion

Herein we shall present the results for two tapering rates only. The two cases discussed in detail suffice since there is a gradual change in the physical characteristics in going from one tapering rate to the next.

(a) Sideband Instability and Pulse Modulation

The tapering rate has a dramatic effect on the profile of the output optical pulse. This is illustrated rather well in Figs. 1 (a) and (b) which display the normalized radiation field amplitude $a_o(z)$ for the fundamental optical mode at the wiggler exit. The two cases correspond to initial resonance phases $\xi_r = 2.5°$ and 34.8°. In the presence of the sidebands, the optical field will be modulated at a period λ_{mod} given by

$$\lambda_{mod} = \left(\frac{1 + a_w^2/2}{2a_w|a_o|f_B}\right)^{1/2} \lambda.$$

Taking $|a| = 1.4\times10^{-4}$, one finds $\lambda_{mod} = 0.09$ mm which is within 10% of the period of the prominent oscillations observed in Fig. 1(a). On the other hand, when the tapering rate $d\gamma_r/dt$ is sufficiently fast the synchrotron motion of the electrons is nonadiabatically distorted. This tends to suppress sideband growth. [2] For the parameters considered here and the tapering rate for Fig. 1(b), one finds that, if Ω_{syn} is the synchrotron frequency,

$$\left|\frac{d\gamma_r/dt}{\Omega_{syn}(\gamma - \gamma_r)}\right| \sim 1/5,$$

whence the synchrotron motion is marginally nonadiabatic. The distortion of the synchrotron motion is responsible for reduced sideband growth.

(b) Optical Guiding

Optical guiding may be shown to arise from two distinct features of the FEL mechanism. [4] Refractive guiding, which is described by the reactive (real) part of the refractive index, is due to the phase shift of light. A distinguishing characteristic of this type of guiding is that the optical wavefronts are plane under the conditions of perfect guiding. The other type of guiding, gain focusing, is described by the resistive (imaginary) part of the refractive index. In this case, under the conditions of perfect guiding, the wavefronts are convex, corresponding to the fact that there is a net power flow, due to diffraction, away from the electron beam.

Figure 2 shows $\alpha(z)$, which is proportional to the curvature of the wavefronts, at the end of wiggler. The significant feature of Fig. 2 is that the curvature is less for the less rapidly tapered case. In particular, in the vicinity of $z \approx 1.2$ mm in Fig. 2(a), the curvature is negative, indicating that the wavefronts in this region are in fact concave. On the other hand, in the case of rapid tapering, Fig. 2(b), the wavefronts are convex all through the pulse, indicating a flow of power away from electron beam throughout the pulse. Consistent with this, Fig. 3 indicates a larger spot size for the more rapidly tapered case.

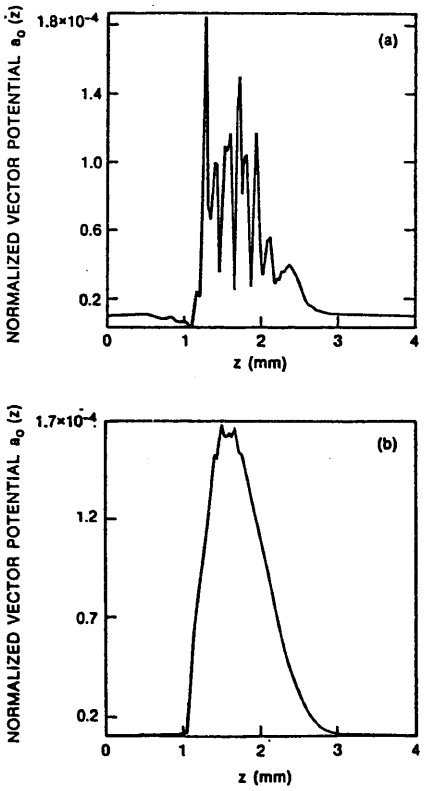

Fig. 1 Normalized vector potential of the fundamental optical mode $a_o(z)$ at the end of the wiggler. (a) slow tapering rate, initial resonance $\xi_r = 2.5°$; (b) rapid tapering rate, initial resonance phase $\xi_r = 34.8°$.

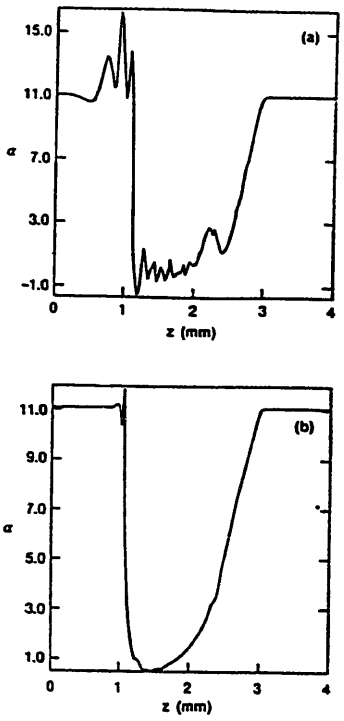

Fig. 2 Curvature α(z) at end of wiggler. (a) slow tapering rate; (b) rapid tapering rate

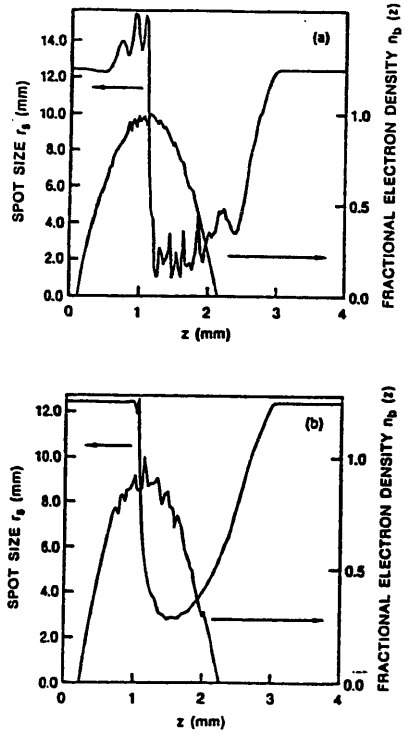

Fig. 3 Spot size $r_s(z)$ and fractional electron density $n_b(z)$ at end of wiggler. (a) slow tapering rate; (b) rapid tapering rate.

IV. Conclusions

Summarizing the results, it is found that in addition to enhancing the efficiency, tapering improves the quality of the output by suppressing sideband growth. Further, it is found that as the tapering rate is increased there is a gradual transition from a refractive-guiding regime to one where gain focussing dominates, with optical power diffracting laterally along the convex wavefronts. The increased transverse extent of the optical field, rather than an increase in the field amplitude is the major reason for efficiency enhancement as the tapering rate is increased.

Acknowledgment

This work was supported by ONR and SDIO through ONR.

References

[1] P. Sprangle, A. Ting and C. M. Tang, 'Radiation Focusing and Guiding with Application to the Free-Electron Laser,' Phys. Rev. Lett., Vol. 59, pp.202-205, 1987; 'Analysis of Radiation Focusing and Steering in the Free-Electron Laser by use of a Source-Dependent Expansion Technique,' Phys. Rev. A, Vol. 36, pp.2773-2781, 1987.

[2] B. Hafizi, A. Ting, P. Sprangle and C. M. Tang, 'Development of Sidebands in Tapered and Untapered Free-Electron Lasers,' Phys. Rev. A, Vol. 38, pp.197-203, 1988.

[3] E. T. Scharlemann, 'Wiggle Plane Focusing in Linear Wigglers,' J. Appl. Phys., Vol. 58, pp.2154-2161, 1985.

[4] E. T. Scharlemann, A. M. Sessler and J. S. Wurtele, 'Optical Guiding in a Free-Electron Laser,' Nucl. Instrum. Methods Phys. Res. A, Vol. 239, pp.29-35, 1985.

*Permanent address: Science Applications Intl. Corp., McLean, VA

COMPUTER SIMULATION OF FEL SIDEBANDS IN A STRONGLY DISPERSIVE WAVEGUIDE

E.J. Sternbach*
Lawerence Berkeley Laboratory
1 Cyclotron Rd.
Berkeley, CA 94720

Abstract

With the development of high power FEL's, it is necessary to consider the development of sidebands in the radiation spectrum. These sidebands can considerably widen the bandwidth of the FEL output and if sufficient power is developed, this can lead to the detrapping of electrons. It has been noted previously that the effects of waveguide dispersion can affect the sideband gain and location[1][2]. In this report the author describes a set of coupled equations suitable for the study of the radiation spectrum of an FEL. These equations include all the effects of waveguide dispersion. A computer simulation that numerically integrates these equations is used to study sideband growth and saturation in the regime of strong dispersion.

Introduction

Many instances of high power FEL's have been demonstrated in recent years. In the regime where powers are high and electron bunching is strong, the development of sidebands to the fundamental FEL frequency is likely. These sidebands broaden the radiation spectrum and under certain conditions can cause detrapping of the electrons from the FEL bucket. It has been noted previously that in a waveguide FEL, the dispersion caused by the waveguide will have a significant effect on the sideband physics. Of particular interest is the regime where the group velocity of the radiation becomes equal to the parallel velocity of the electrons[1]. These conditions cannot be properly described by the usual FEL equations since the major assumption, that of slowly varying amplitude and phase, breaks down. In this paper, a formalism previously developed to deal with waveguide FEL's is briefly described. A computer simulation based on this formalism is used to illustrate some aspects of general sideband physics, particularly the regime of strong dispersion.

Basic Equations

In this section the equations used in the computer simulation are described. The derivation of these equations are described in great detail elsewhere[3][4].

If we assume that the radiation field consists of a finite number of discrete frequencies, then we can derive a pair of first order linear differential equations for each frequency. It is assumed that only forward traveling radiation is important and that nonlocal effects are negligible. The equations that result are

$$\frac{da_{aj}^{mn}}{dz} = \mathcal{J}_j^{mn} \sin\theta_{pj} \quad , \tag{1a}$$

$$\frac{d\phi_{aj}^{mn}}{dz} = \frac{\mathcal{J}_j^{mn}}{a_{aj}^{mn}} \cos\theta_{pj} \quad , \tag{1b}$$

with

$$\mathcal{J}_j^{mn} = \frac{4\pi e^2}{m_e cab} a_w \lambda_{0j} \frac{\cos\frac{m\pi}{2}\sin\frac{n\pi}{2}}{(1+\delta_{m0})} \quad , \tag{2}$$

Here a_a and ϕ_a are respectively the amplitude and slowly varying phase of the radiation. The superscripts mn refer to the transverse waveguide mode and the subscript j refers to the particular frequency being followed. The quantity θ_p represents the difference in phase between the peak of the current component at that frequency and the bottom of the pondermotive well defined by radiation at that frequency. The quantity $\mathcal{J}_j^{mn}$ depends on the FEL geometry and is given here for a linear wiggler in a rectangular waveguide. The terms a and b represent respectively the x and y dimensions of the waveguide. The term λ_0 is the Fourier amplitude of a quantity that goes like the number line density of electrons divided by γ, the relativistic energy factor. The term a_w is the wiggler vector potential normalized by e/mc^2.

The evolution of the current, and therefore the factors θ_p and λ_0, can be obtained by following the motion of individual particles. In terms of γ and t, the particle motion in a linear wiggler is given by

$$\frac{dt}{dz} = \frac{1}{v_z} \quad , \tag{3a}$$

and

$$\frac{d\gamma}{dz} = \frac{\omega}{c} v_x \sum_{\substack{m,n \\ j}} a_{zj}^{mn}(z,t) \quad , \tag{3b}$$

where a_z is the normalized vector potential of the radiation field. Each term in the sum of (3b) will move at a different speed in a waveguide. Since the vector potential of the wiggler field is much larger than that of the radiation field it is a quite good approximation to assume that v_x and v_z do not depend on the magnitude of the radiation field. Thus they are

$$v_x = \frac{a_w(z)}{\gamma} \quad , \tag{4}$$

and

$$v_z = c\sqrt{1 - \frac{1 + a_w^2(z)}{\gamma^2}} \quad . \tag{5}$$

The Computer Simulation

The computer simulations described in this paper were performed on a CRAY 2 supercomputer. Eqns. (1) and (3) were integrated using a version of the GEAR integration package. Since following an entire electron pulse would require too much memory, a length of the electron beam is followed with periodic boundary conditions. The radiation equations follow a particular Fourier component so the longer this length is, the more resolution one can achieve in the simulation. For the simulations done here the length of beam in the simulation was 32 times the bucket length of the fundamental frequency. This gives 3.1% resolution in the radiation spectrum calculations.

The sidebands in these simulations are assumed to start from noise. This noise is assumed to have a flat power spectrum and the total noise power is an input parameter. The simulations in this paper have an input noise power of 5 watts.

Basic Sideband Physics

The sideband instability is seen only when the FEL approaches

* Work supported by the U.S. Department of Energy, at the Lawrence Berkeley Laboratory under contract #DE-AC03-76SF00098.

CH2669-0/89/0000-1239$01.00©1989 IEEE

Table I. Simulation parameters		
Relativistic energy γ	7.1	
Wiggler peak field	3.80	kG
Wiggler wavelength	9.8	cm
Radiation frequency	34.6	GHz
Beam current	800	amps
Waveguide size	9.8 × 2.9	cm
Equilibrium radiation power(TE^{01})	200	MW

saturation and the electron beam is tightly bunched. Thus for this section we will use a simulation where there is one macroparticle per bucket to study sideband gain. This is good model as long as sideband power is small compared to the power in the fundamental. This will allow us to understand some aspects of sideband physics without being confused by complexities due to the electron distribution.

The simulations of this section use the parameters of Table I. These are similar to the parameters of the ELF experiment at Livermore. The plots in Fig. 1 were started from an equilibrium where the particle was started in the center of the bucket. Thus the equilibrium exhibits no synchrotron oscillations. Normally both the upper and lower sidebands grow. Contrary to expectations from the simple theory to date, the lower sideband has significantly higher gain than the upper sideband. When only the lower sideband is allowed to grow, it exhibits a spectrum nearly the same as the simulation with the full spectrum. However, if only the upper sideband is allowed to grow, there is no amplification at frequencies higher than the fundamental.

The observed features can be explained if one considers the creation of FEL sidebands as stimulated scattering. The lower sideband is the Stokes wave and the upper sideband is the anti-Stokes wave. The scattering medium is the tightly bunched electrons which

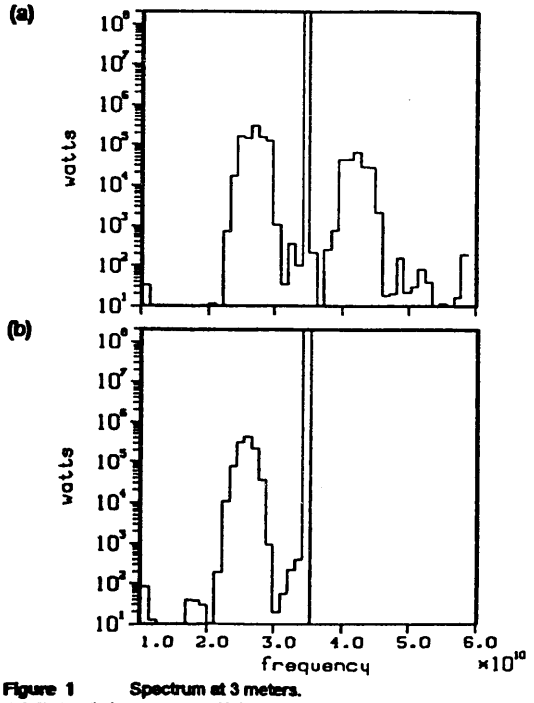

Figure 1 Spectrum at 3 meters.
(a) Full radiation spectrum. (b) Only lower sideband is allowed to grow. Not shown is a case where only the upper sideband was allowed to grow. No amplification of the upper sideband was seen at all in that case.

naturally oscillate at the synchrotron frequency. If one starts with an equilibrium where there is initially no synchrotron oscillation, then the upper sideband cannot grow in a two wave process since it must grow at the expense of the synchrotron oscillation. Fig. 2 illustrates that if one starts from an equilibrium with a large synchrotron oscillation, and if only the upper sideband is allowed to grow, then one does observe amplification at the upper sideband frequency and the synchrotron oscillation decays in amplitude.

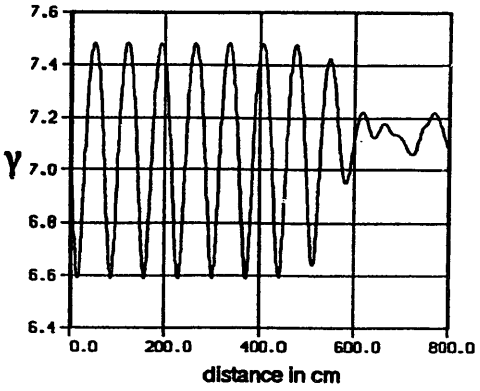

Figure 2 When only the upper sideband is allowed in the simulation, it must grow at the expense of the synchrotron oscillation.

Effect of Dispersion on Location and Gain of Sidebands

In this section we examine some one particle per bucket simulations of FEL sidebands for different levels of dispersion. The parameters used are basically that of Table I except that for different waveguide sizes the wiggler field needed for resonance is changed. For each of these simulations, only a TE^{01} mode is followed. The dispersion then depends only on b, the y dimension of the waveguide. The x dimension, a, in these simulations are adjusted to give the same cross sectional area for the waveguide in each simulation.

Fig. 1a and Figs. 3a through 3c represent simulations in successively narrower waveguides. This represents increasing the amount of dispersion. The final plot in Fig. 3c represents a case where the group velocity of the fundamental frequency in the waveguide is equal to the parallel velocity of the electrons. This "no-slip" condition can be written most simply as

$$(\gamma_t^{mn})^2 = k_w k_s \quad , \tag{6}$$

where for each waveguide mode

$$\omega^2 = (\gamma_t^{mn})^2 + k_s^2 \quad . \tag{7}$$

Here k_w is the wiggler wave number and k_s is the radiation wave number. Since k_s depends on ω through γ_t, the three dependent quantities are the radiation frequency, the wiggler wavelength, and the waveguide size.

The effect of dispersion on sidebands can be summarized as follows. Dispersion causes the sidebands to occur at a greater distance from the fundamental frequency. Even for the simulation in Fig. 1a where dispersion is relatively small, this is a significant effect. An analysis ignoring dispersion would predict a separation of the sideband from the fundamental for Fig. 1a to be about 3.5 GHz. It can be seen that the actual separation is closer to 7GHz. This separation can be seen to increase for smaller waveguide heights in Fig. 3. Also the gain can be seen to decrease for smaller waveguide heights. When the "no-slip" condition is satisfied as in Fig. 3c, the

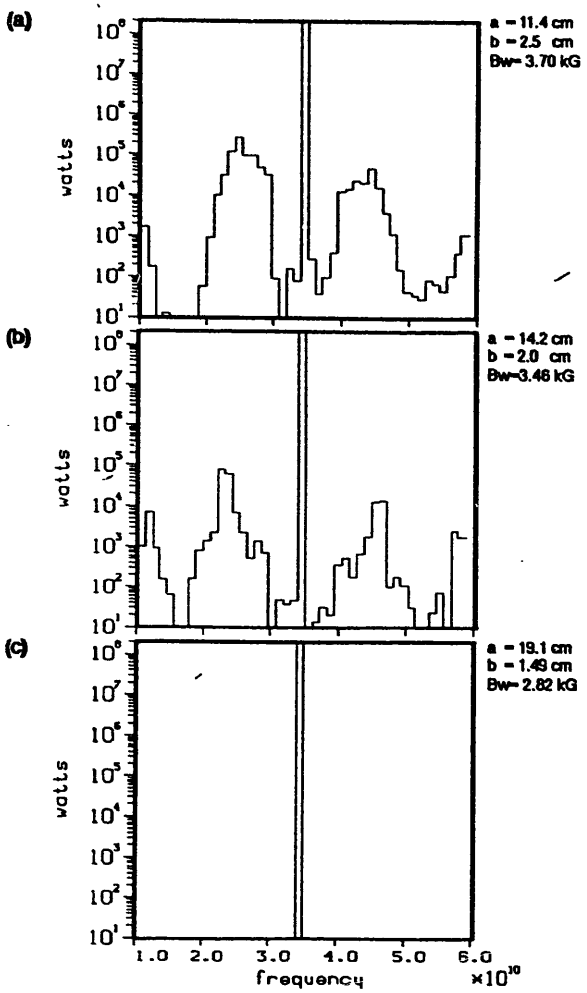

Figure 3 Radiation spectra at 3 meters distance.

sideband gain can be seen to be suppressed entirely. For a sideband frequency to grow, it must modulate the current over a region of many FEL buckets. If the radiation group velocity and the electron parallel velocity are identical, then no information can travel along the electron beam and therefore sidebands cannot grow.

Nonlinear Sideband Simulations

In this section we examine a full many particle sideband simulation where the sideband power is allowed to grow until it is of the same order of magnitude as the fundamental frequency. In this regime, the one particle per bucket simulation is no longer relevant. The parameters used are once more those of Table I with the exception that the FEL is started from an input signal of 60kW and the peak wiggler field is 3.59kG to start the FEL at the peak of the gain curve.

The radiation spectrum in Fig. 4 is taken at 6 meters where there is sufficient sideband power for the system to be highly nonlinear. Four upper sideband peaks are clearly visible. The first lower sideband peak is clear and is nearly as high as the fundamental. Other sideband peaks exist below this, but as waveguide dispersion becomes more prominent the spectrum becomes more complicated. As the buckets for the lower sidebands become large enough for these

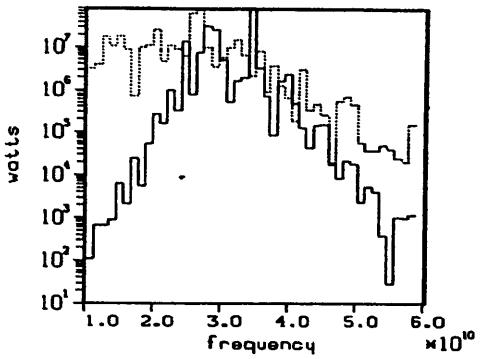

Figure 4 Radiation spectrum at 6 meters for full FEL simulation. Dotted line represents the results of a one particle per bucket simulation and can be seen to be quite far from the many particle simulation in the nonlinear regime.

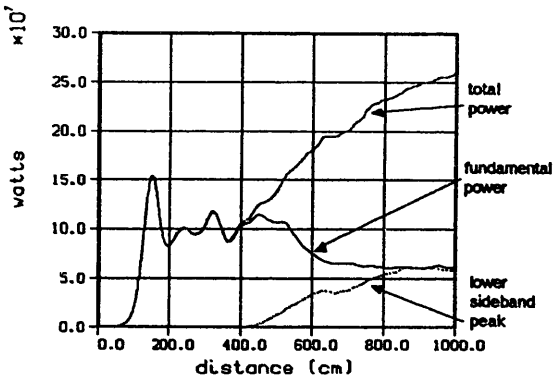

Figure 5 Power vs. distance for full FEL simulation

frequencies to become self- amplifying, the electrons "leak" out of the fundamental frequency bucket to interact with the lower sideband bucket and therefore are decelerated. Thus if an untapered FEL is long enough, power will continue to be produced by electrons cascading into lower buckets and this process will continue to widen the FEL spectrum into lower frequencies.

Conclusion

Computer simulations can give many insights into the behavior of FEL sidebands. They seem to confirm that the sideband instability is a process similar to stimulated scattering. Simulations performed in highly dispersive waveguides show that dispersion can have a large effect on the location and gain of FEL sidebands. In the case where the electron velocity and the radiation group velocity become equal, the sideband instability is completely suppressed.

References

[1] S.S Yu et al., *Nuclear Instruments and Methods*, A259, 219(1987).

[2] J. Masud et al., *Phys. Rev. Lett.*, 58, 763(1987).

[3] E.J.Sternbach, *Nuclear Instruments and Methods*, A272,323(1988).

[4] E.J. Sternbach, "Formalism for the Study of Multiple Frequency Effects in a Waveguide FEL," Lawrence Livermore National Laboratory Research Memo #88-27.